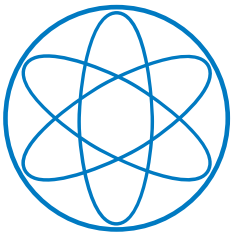

Fakultät für Physik

Fundamental physics with neutrons

High Precision Physics in Low Magnetic Fields: Implementation of a Sub-Nanotesla Field with Femtotesla Temporal Stability

Tobias Lins

Vollständiger Abdruck der von der Fakultät für Physik der Technischen Universität München zur Erlangung des akademischen Grades eines

Doktors der Naturwissenschaften (Dr. rer. nat.)

genehmigten Dissertation.

Vorsitzende:	Univ.-Prof. Dr. Martin Beneke
Prüfer der Dissertation:	
1.	Univ.-Prof. Dr. Peter Fierlinger
2.	Univ.-Prof. Dr. Elisa Resconi

Die Dissertation wurde am 02.02.2016 bei der Technischen Universität München eingereicht und durch die Fakultät für Physik am 16.3.2016 angenommen.

Abstract

The Standard Model (SM) of particle physics is a well-established model that describes three of the four fundamental forces very well. However, it does not include gravity, dark matter, dark energy or the asymmetry between matter and antimatter in the universe. Hence new models are necessary to explain physics beyond the SM.

Very precise determination of SM particle properties or of phenomena that are forbidden in the SM offers a possibility to find new physics complementary to high-energy accelerator-based experiments. For example, the discovery of a non-zero electric dipole moment (EDM) of a fundamental particle would indicate the existence of underlying processes that violate the time reversal symmetry (T). According to the CPT theorem, T-violation is equivalent to CP-violation. Such new sources of CP-violation are needed to explain the asymmetry of matter and antimatter in the universe.

For decades physicists have been using neutrons to study T-violating properties of nature. Every new neutron EDM measurement approach aims to improve statistical and systematic uncertainties, of which the latter contains dominating contributions from magnetic field related effects. Hence measurement and control of magnetic fields is essential. The main part of this thesis will cover various magnetic field sources that produce systematic errors. Strategies on how to measure and control magnetic fields will be discussed and demonstrated.

First, gradients and local dipoles inside the neutron storage chamber are discussed which are the main sources of such systematic errors. A magnetometer arrangement concept is presented that is able to measure both sources with a precision corresponding to the envisaged sensitivity goal of $\sim 10^{-28}$ ecm for neutron EDM.

Second, ways of shielding external distortions are presented. The experiment is protected from external fields by one active and two passive shields. The active shield consists of 24 coils and 180 field probes. Temporal changes of the magnetic field are measured and an algorithm is used to determine optimal currents to dynamically compensate for field changes. The passive shields are made from an alloy with a very high magnetic permeability so that magnetic field lines are guided around the EDM experiment. The magnetic field inside the shield is stable to $\sim$10 fT for typical EDM run times of 250 s, fulfilling the requirements for a 10^{-28} ecm measurement.

Next to EDMs, the excellent magnetic properties of the EDM instrument yield the possibility to search for other exotic physics. As an example for the capability of the magnetic shield, two methods to detect magnetic monopoles have been implemented and demonstrated. The proof of principle measurement shows that both methods are an order of magnitude more sensitive than the previous comparable monopole experiment. The first method is a new technique enabling the determination of the direction of the monopole for velocities $v < 10^{-4}c$. The second method is based on the state of the art experiment and is sensitive to the monopole charge. Both methods are complementary and give the possibility to measure the parameter space of monopoles in a not-yet covered region.

Zusammenfasssung

Das Standard Model (SM) der Teilchenphysik ist ein etabliertes Model, das drei der vier Grundkräfte sehr gut beschreibt. Jedoch beinhaltet es nicht die Gravitation, dunkle Materie, dunkle Energie oder die Asymmetrie zwischen Materie und Antimaterie. Deshalb sind neue Modelle nötig, um die Physik jenseits des SM zu erklären.

Die sehr präzise Bestimmung von SM Teilcheneigenschaften oder von Phänomenen, die im SM verboten sind, bietet einen komplementäreren Ansatz zur Hochenergiephysik, die auf Beschleunigerexperimenten basiert. Würde zum Beispiel das elektrische Dipolmoment (EDM) eines Elementarteilchens mit einem von Null verschiedenen Wert gemessen, würde dies auf Prozesse hinweisen, die asymmetrisch bezüglich der Zeitumkehr sind. Laut dem CPT-Theorem ist eine T-Verletzung gleichbedeutend mit einer CP-Verletzung, von der neue Quellen benötigt sind, um die Materie-Asymmetrie im Universum zu erklären.

Seit Jahrzehnten benutzen Physiker Neutronen, um T-verletzende Eigenschaften der Natur zu studieren. Jede neue Neutronen-EDM-Messung versucht dabei die Statistik und Systematik weiter zu verbessern, wobei der dominierende Beitrag des Letzteren aus Effekten, die mit Magnetfeldern verbunden sind, besteht. Dadurch ist die Messung und Beeinflussung von Magnetfeldern von größter Bedeutung. Zum Großteil behandelt diese Arbeit verschiedene Quellen von Magnetfeldern, die systematische Fehler produzieren. Strategien zu deren Messung und Beeinflussung werden diskutiert und demonstriert.

Im ersten Teil werden Gradienten und lokale Dipole innerhalb der Neutronenspeicherkammer behandelt, welche den Hauptanteil der systematischen Fehler darstellen. Ein Anordnungskonzept von Magnetometern wird präsentiert, welches beide Fehlerquellen mit einer Präzision messen kann, die dem angestrebten Sensitivitätsziel von $\sim 10^{-28}$ ecm entspricht.

Im zweiten Teil werden Methoden zur Abschirmung von externen Störfeldern vorgestellt. Das Experiment wird durch ein aktives und zwei passive Schilder von externen Feldstörungen abgeschirmt. Das aktive Schild besteht aus 24 Spulen und 180 Magnetfeldsensoren. Die zeitliche Änderung des Magnetfeldes wird gemessen und mit Hilfe eines Algorithmus werden optimale Ströme bestimmt, wodurch die Feldänderungen dynamisch kompensiert werden. Die passiven Schilder sind aus einer hochmagnetisierbaren Legierung gefertigt, wodurch magnetische Feldlinien um das EDM-Experiment geführt werden. Für typische Experimentzeiten von 250 s ist das Magnetfeld im Inneren des Schildes zu $\sim$10 fT stabil, was die Voraussetzungen für eine 10^{-28} ecm Messung erfüllt.

Die ausgezeichneten Magnetfeldeigenschaften des EDM-Instruments bieten darüber hinaus die Möglichkeit nach anderer, exotischer Physik zu suchen. Um das Potential des magnetischen Schildes zu demonstrieren, wurden zwei Methoden zur Detektion von magnetischen Monopolen umgesetzt und charakterisiert. Messungen zur Bestätigung der Konzepte zeigen, dass beide Methoden um eine Größenordnung sensitiver sind als vergleichbare, frühere Monopoleexperimente. Die erste Methode

ist eine neue Technik, die die Bestimmung der Geschwindigkeit von Monopolen für Geschwindigkeiten $v < 10^{-4}c$ ermöglicht. Die zweite Methode basiert auf der bisherigen Technik und ist sensitiv auf die Monopolladung. Beide Methoden ergänzen sich und ermöglichen den Parameterraum der magnetischen Monopole in einem bisher unerforschten Bereich zu vermessen.

Contents

1. Introduction

1.1. Physics beyond the Standard Model

In 2012, the last missing ingredient of the Standard Model (SM) of particle physics was found, the Higgs boson. Being one of the most important discoveries in fundamental physics, Peter W. Higgs and Francois Englbert, who both predicted the existence of this particle, were rewarded with the Nobel Price in 2013. In 1964, both independently introduced a mechanism which gives particles their masses [1, 2]. A further consequence of the theory is the existence of a new particle, colloquially referred to mainly as the "Higgs" boson, though other names have also been used to emphasize the contributions of other physicists [2, 3].

The SM is one of the most successful theories in physics, as its predictions of new particles and their properties have been verified in a huge number of experiments [4, 5]. It includes three of the four fundamental forces (the electromagnetic, the weak and the strong interaction) and has predicted many particles with their properties, which have been found later, e.g. the top quark [6].

While the SM is a very solid theory and is able to describe particle physics experiments very well, it has flaws. A few of these shortcomings are described below. For more detailed information see e.g. [7, 8, 9]

The SM requires 18 parameters that must be experimentally determined. It is very "unsatisfactory" that these free parameters do not arise from the theory. In addition, the SM as a quantum field theory is unable to include gravity (described by general relativity). Intrinsically this is not a flaw of the SM, but it shows that additional critical pieces are missing. At very high energies it is assumed that all fundamental forces unite and are described by a more general theory, usually called the theory of everything. The SM is an low-energy field theory that consequentially fails to describe high-energy processes. Hence the SM is considered the low-energy limit of more fundamental theory.

But the SM does not only break down at high energies, it also fails on galactic scales. The measurement of rotation curves of galaxies, which are attributed to gravitational effects, indicate a mass distribution that is significantly different to that which one can detect by measuring its luminosity [10]. In other words, there must be some sort of invisible mass, which interacts very weakly or not at all with electromagnetic waves. All potential particles that can contribute to this hidden mass are referred to as dark matter [5, 11]. Dark matter also plays an essential role in galactic development [12] and is an important component to models explaining the so-called "large-scale structure" of the universe [13]. Other astrophysical observations hint that there is more than just visible and dark matter. The measurement

of the accelerated expansion of the universe [14, 15] points to an energy density, which behaves like a "repulsive" gravity pushing the universe apart. This concept is commonly referred to as dark energy, but almost nothing is known about it. At this point in time, our universe consists of 73% dark energy, 22% dark matter and 5% visible baryonic matter.

The SM predicts an asymmetry between matter and antimatter, usually expressed in the ratio of baryons to photons, which is many orders of magnitude smaller than what is observed [16, 17]. In other words, this large discrepancy represents one of the most fundamental questions: the origin of matter. In general, a few conditions which Sakharov pointed out have to be fulfilled to explain the matter-antimatter asymmetry in the universe [18]: new sources for CP violation (CP = combined symmetry under charge conjugation (C) and parity operator (P)), the deviation from the thermal equilibrium [19] in the early universe and baryon number violation. This topic will be discussed further in the next section.

All these facts very clearly show that there has to be more than the SM. Due to the high precision with which the SM describes known processes, it is generally believed that the SM is just the low energy limit of a superordinate theory and will not be replaced by totally different theory. All models that extend the SM and try to describe the above shown phenomena are summarized by the term *Beyond Standard Model* (BSM) theories [20]. *Dynamical symmetry breaking*, *extra dimensions* and *super symmetry* (SUSY) are examples of such approaches to extend the SM, either by introducing additional fundamental symmetries, resulting in new particles, or by modifying fundamental forces for certain distance regimes.

With the discovery of the Higgs boson, the Large Hadron Collider (LHC) at CERN (Conseil Européen pour la Recherche Nucléaire) made an essential contribution to fundamental physics, but it provides no evidence for new BSM particles. SUSY models are the most prominent models of all BSM theories and they predicted particles with masses in the energy range of the LHC [21, 22, 23]. So while the Higgs particle is an essential discovery for the verification of the SM, the non-discovery of any BSM particle leaves the high energy physics community in some state of uncertainty.

Even near-future upgrades of the LHC might not have the potential to extend its reach to energy regimes needed to directly produce new particles [24, 25]. However, there are other methods to look for new physics. BSM theories often predict small changes of particle properties compared to the SM expectation, or even new properties which have to be zero according to the SM. Indirect searches offer complementary approaches to the direct (accelerator-based) searches. The very precise measurement of SM processes or the search for phenomena forbidden in the SM have the potential to probe physics beyond the reach of colliders [26]. However, to fully understand a new process or a particle, indirect searches alone are not sufficient. For example, electroweak baryogenesis (EWBG), a prospective model describing the origin of matter, needs to be tested at high energies, high precision and using cosmology [27]. Here the focus is on high precision.

1.2. High precision experiments in low magnetic fields

A selection of high-precision experiments are now presented to show the concepts behind them and the technical challenges that are connected to them. A focus will be put on the requirements for magnetic fields, in order to emphasize the contribution of small and stable magnetic fields in searching for new physics beyond the SM.

1.2.1. Clock comparison

The conservation of the combined symmetry under C, P and time reversal (T), CPT symmetry, is a direct consequence of Lorentz invariance, which is a basic concept of the SM and general relativity. Assuming CPT is a symmetry of a local relativistic quantum field theory [28], its spontaneous symmetry breaking should yield observables. According to Mach's principle, the inertial mass of a body is determined by the matter distribution of the universe [29]. A non-isotropic matter distribution then causes that the mass of a body to be dependent upon its direction of acceleration in respect to the center of the galaxy [29]. The mass of a body is then expressed by a scalar and a tensor component, of which the latter is angle dependent. Due to the rotation of the Earth, any process depending on the mass, e.g. the Zeeman transition frequency, should show a sidereal modulation.

The highest sensitivity in Lorentz invariance searches has been achieved using a two species maser of ^{3}He and ^{129}Xe [30], while the latter is used as a co-magnetometer. A co-magnetometer is a secondary magnetometer that occupies the same space as a primary magnetometer and acts as a reference. Both species are co-located inside a magnetic field and their polarizations are oriented in the same direction. The Zeeman transition frequency is defined by a valence neutron and hence a sidereal variation of this frequency can be translated into a tensor component of the neutron mass [31].

As both masers do not have a perfect spatial overlap, an external magnetic field change can not completely be corrected for by the co-magnetometer. The present best experiment showed a stability of the clocks of about 50 nHz, which corresponds to a 10^{-31} GeV tensor component of the neutron mass. (The upper limit for free neutrons is 10^{-29} GeV and was determined by an experiment using the spin precession of ultracold neutrons [32].) Compared to other systematics the field drift of 20 nT (8 nHz) over a 24 hour period is negligible [30]. The measurement showed a sidereal modulation that is consistent with zero.

Any future approach of this measurement technique to improve the current limit by more than one order of magnitude will be limited by magnetic field drifts. Hence improvements in magnetic field stability for semi-sidereal and sidereal drifts are necessary for next generation experiments [30].

1.2.2. Anomalous magnetic moments

Charged particles (e.g. electrons) can be stored inside Penning traps and their movement can be described by three characteristic frequencies, the cyclotron, the anomaly and the axial frequency [33]. The cyclotron and the anomaly frequency are mainly connected through the magnetic moment $\mu = \frac{g}{2}\mu_B$, with μ_B representing the Bohr magneton. Classically g would be exactly 2, but quantum electrodynamics (QED) slightly change its real value. These corrections are caused by virtual particles and with increasing loop level their contributions decrease. QED calculations allow a very precise prediction of g [34, 35]. QED is a classic application of perturbation theory and therefore a theoretical uncertainty can be extracted which is in same order as the experimental sensitivity.

Any difference between the measurement and the calculation of g would indicate that there are additional – not yet known – particles involved. Consequently a very precise determination of g is an indirect search for new particles. The current results of these experiments however are consistent with theory and therefore give no indication for the presence of new particles. Also sidereal modulation of g can be studied to search for CPT violation [36].

The current best experiment features a relative field stability of 10^{-9} in 1 hour. Slower field drifts have been averaged out, as symmetric field fluctuations only broaden the signal, but do not change its mean value. As the broadening also could have arisen from mechanical vibrations and a clear identification was not possible, it is difficult to determine a potential improvement of the experiment by solely improving the magnetic field stability.

Currently a new approach is in the planning phase using muons instead of electrons [37]. The mass of the muon is about 200 times larger than that of the electron, making the system a highly promising candidate system for the observation of BSM physics.

1.2.3. Axion and Axion-like particles

The axion arises from a specific solution to the strong CP problem [38], which refers to a CP violating term in the QCD (Quantum Chromo Dynamics) Lagrangian. This term – commonly called $\bar{\theta}$ – is naively expected to be on the order of 1, but constraints extracted by electric dipole moments (EDMs) give an upper limit of $\bar{\theta} < 10^{-11}$ [39]. Peccei and Quinn introduced a global chiral $U(1)$ symmetry and its spontaneous breakdown leads to a Nambu-Goldstone boson, the axion. This new symmetry dynamically counteracts the $\bar{\theta}$ term and therefore effectively sets it to 0 [40].

Although Peccei-Quinn axions have a coupling constant f_a which is inversely proportional to its mass m_a and proportional to a known scaling factor [40], scientists also look for particles with other scaling factors. Except for the strength of coupling constant, these particles interact with matter similarly to axions and hence are usually called axion-like particles (ALPs). There are several ideas how to search for axions and ALPs based on dark matter axions (uniformly distributed in the

universe), solar axions (produced in the sun) and laboratory experiments (direct production) (see e.g. [41] for an overview of these experiments), each covering a different segment of the relevant parameter space. Most of the experiments rely on strong magnetic fields, though some (including the CASPEr experiment) also require very stable magnetic fields.

The CASPEr [42] experiment combines solid-state EDM and nuclear magnetic resonant (NMR) techniques. ALPs are assumed to induce a time-varying EDM [43] with a characteristic frequency connected to the ALP mass. The experimental approach uses a spin-polarized sample inside static magnetic ($\mathbf{B}$) and electric ($\mathbf{B}$) fields with $\mathbf{E} \perp \mathbf{E}$. The magnetization of the sample precesses around the static B field with the Larmor frequency. Similarly for a non-vanishing nucleon EDM, the spin of the particle also precesses around the E field. A superconducting quantum interference device (SQUID) is used to measure the transverse magnetization. While a static or a non-resonant ALP-induced oscillating EDM does not build up a transverse magnetization, the resonant case, in which the frequency corresponds to the axion, produces a net signal.

The Larmor frequency is varied through the magnetic field and the stability of the field determines the width of the resonance. The sensitivity of the proposed technique therefore is dominated by the temporal stability of the magnetic field and the sensitivity of the magnetometer, on the order of $10^{-16}\,\mathrm{T}/\sqrt{\mathrm{Hz}}$ for frequencies $f \geq$ kHz [42].

1.2.4. Particle oscillation

Particle oscillations are the manifestation of processes that transform a particle into its antiparticle or from one mass eigenstate to another. They are very interesting, as they cover many aspects in fundamental physics. The observation of neutral kaon oscillations [44] led to the complex phase in the CKM matrix, the first measurement of CP violation. The CKM matrix is the quark mixing matrix, which is named after Cabibbo, Kobayashi and Maskawa. Oscillations in neutral B-meson systems have also been observed [45], but they are caused by the already known complex phase of the CKM matrix and hence are no new sources for CP violation (first Sakharov criterion).

The third Sakharov criterion, baryon number violation, might be found in particle oscillation. The observation that neutrinos oscillate between their family flavor (see e.g. [46, 47, 48]), proves that neutrinos have a non-zero mass, which is not part of the SM. The Seesaw mechanism is able to explain this non-zero mass, but requires the neutrino to be a Majorana particle. Neutrinos consequently would be their own antiparticle and hence would violate lepton number conservation. The nature of this process is studied in experiments that search for the neutrinoless double β decay (see e.g. [49, 50, 51]).

Although based on different mechanism, similar oscillations could be expected in the neutron system, in this case resulting in the violation of the baryon number. Free neutrons generated in nuclear reactors or by spallation sources are guided through an

evacuated tube with length $l \approx 100\,\mathrm{m}$ neutrons to a beam stop. The time available for a potential oscillation to an anti-neutron is proportional to the velocity v of the neutrons and l. The beam stop is surrounded by a 4π detector. In the beam stop anti-neutrons would annihilate with a neutron of the beam stop resulting in an event with a characteristic energy with double the rest mass of the neutron.

In 1994 an upper limit of $\tau_{n\bar{n}} > 0.86 \cdot 10^8\,\mathrm{s}$ was set [52] and a new approach is currently in the planning phase [53]. These experiments require very good magnetic shielding over an extended volume, as any magnetic field suppresses the transition to the anti-neutron, caused by energy conservation ($E \propto \mu_n B$, with μ_n the magnetic moment of the neutron). A residual field of $B < 10\,\mathrm{nT}$ suppresses the oscillation probability by only 1.6% and thus the technical challenge for these kinds of experiments lies more in the large size of the magnetic shield than in the ultimately small residual field.

1.2.5. Torsion pendulums

Probing physics to high energy scales is not only made possible by observing the relic effects of hypothetical particles on well known quantities like the anomalous magnetic moment. Searches for long-range interactions also offer a general technique to study arbitrary new interactions as long as they mediate through monopole-dipole or dipole-dipole interactions [54]. In general, the higher the energy scale of the symmetry breaking, the weaker the coupling constant.

Torsion pendulums are able to measure torques with a precision of about $10^{-17}\,\mathrm{Nm}$. A recent experimental implementation uses a spin-ring (pendulum) connected with a mechanical fiber [55]. The ring consists of 20 segments of alternating materials with different spin densities, but the same magnetization. Due to the ring structure, the field of the magnetized segments cancels, but a net spin distribution is left. A second similar ring (attractor) is fixed to a position below. Both rings are shielded with 17 thin sheets of an alloy with a high relative magnetic permeability to reduce any residual magnetic field, caused by imperfect geometry of the individual segments, to below 200 pT penetrating to the outside of the shield.

An interaction between the spins of the upper and lower ring would result in signal in the 10th harmonic of the rotation. The result of the measurement is consistent with zero on the 38 aNm level, indicating that the symmetry breaking of any hidden symmetry involving electrons is above the 70 TeV scale [55].

Currently the measurement is dominated by temperature-induced mechanical noise in the fiber. The thickness of the magnetic shielding was chosen to be large enough to make the systematic error connected to it negligible. Nevertheless a more efficient shield (in terms of shielding factor per unit thickness) would decrease the achievable distance of the pendulum to the attractor. Any interaction involving a boson with a non-vanishing mass m_B follows a Yukawa potential [56] and hence decreases rapidly with increasing distance r ($\propto e^{-m_\mathrm{B} r}$). Even an infinite range interaction will decrease proportionally to r^{-3} due to the dipole form of the interaction. A smaller distance between attractor and pendulum consequently increases

the sensitivity.

1.2.6. Electric Dipole Moments (EDMs)

One of the most prominent groups of experiments in precision physics is the search for EDMs (see e.g. [25, 26, 57]). Until now, no EDM in any fundamental system has been observed. Although particle EDMs are predicted by the SM, their expected value is far away from the reach of current and next generation experiments (see table 1.1). However, many BSM theories predict larger EDMs and may therefore also be constrained or excluded by current EDM limits. A non-vanishing EDM would be the manifestation of a time-violating process, which is equivalent to CP violation.

For decades EDMs have been searched for in different nuclear and atomic systems, but all attempts to date have only produced upper limits on particle EDMs. The conventional dipole moment, which is a non-isotropic charge distribution $d = \int \rho(r) r d^3r$ and which is known to exist, e.g., in many molecules like H_2O, is not of interest here. Permanent EDMs are directly coupled to quantum mechanical properties. Just as the magnetic moment of an electron cannot be interpreted as a rotating charge distribution of the electron, these particle attributes are more abstract and directly linked to the spin $\boldsymbol{\sigma}$ of the particle [58]

$$\mathbf{d} = \int d^3r \langle \overline{\Psi} | \sum_i q_i \mathbf{r}_i | \Psi \rangle \equiv e d_n \boldsymbol{\sigma} \,. \tag{1.1}$$

i indicates the charge constituents. If the ground state $|\Psi\rangle$ is invariant in respect to P, the EDM is zero.

Analogous to the magnetic moment, the EDM of neutrons and protons arise from the quark EDMs, and consistently, the EDM of atoms arise from the nucleon EDMs. With increasing complexity of the systems, more interactions have to be taken into account and therefore it is harder to predict an EDM. Due to this consideration, EDM searches are mainly performed in relatively simple systems (electrons and neutrons) or atoms with one valence nucleon (^{199}Hg and ^{129}Xe). From the theoretical point of view, the direct measurement of the quark EDMs would be preferred, but quark confinement excludes this possibility. With searches, one probes the hadronic, nuclear and atomic matrix elements [25] but does not directly probe the underlying CP-violating interactions. To be able to single out any of the BSM theories, it is therefore necessary to search for EDMs in many different systems. The most prominent among them are listed in table 1.1.

An EDM d is aligned to the spin of the system and couples to an external electric field $\mathbf{E}$. Together with the magnetic moment μ and an external magnetic field $\mathbf{B}$ the whole system can then be described by the Hamiltonian

$$\hbar\omega = -(d\mathbf{E} + \mu\mathbf{B}) \cdot \mathbf{S}/S \,. \tag{1.2}$$

In general, at least two experiments with a parallel and an antiparallel $\mathbf{E}$ and $\mathbf{B}$ field configuration are necessary to determine d. Assuming that the magnetic

	Experimental limit [e · cm]	SM prediction (in e · cm)
Electron	$8.7 \cdot 10^{-29}$ (90% Cl) [59]	10^{-31} [60]
Neutron	$2.9 \cdot 10^{-26}$ (90% Cl) [61]	$10^{-33} - 10^{-31}$ [25]
^{199}Hg	$3.1 \cdot 10^{-29}$ (95% CL) [62]	

Table 1.1.: The most important experimental EDM limits and their theoretical predictions

field stays constant for both experiments, the measurement of the spin precession frequency shift $\delta\omega = \omega_{\uparrow\uparrow} - \omega_{\uparrow\downarrow}$ can extract the EDM

$$d = \frac{\hbar\delta\omega}{4|\mathbf{E}|}\,. \tag{1.3}$$

The key feature for all experiments of this kind therefore is the control of the magnetic field and the measurement of the Larmor frequency ω. A concrete example for EDM searches is given below in a more detailed way compared to the previous examples, as a predominant portion of this work covers the next generation neutron EDM experiment in Munich.

1.3. The Munich neutron EDM (nEDM) experiment

In the following section a short introduction to the nEDM instrument which is currently being set up at the Technische Universität München in Garching bei München (Germany), will be given. In addition, an estimate for statistical and systematic errors are derived.

1.3.1. The apparatus

The experiment itself is located at the site of the Forschungs-Neutronenquelle Heinz-Maier-Leibnitz (FRM II) in the new experimental hall (Neutron Guide Hall East). A strong ultra-cold neutron (UCN) source is currently being set up very close to the reactor core of the FRM II [63, 64]. The kinetic energy of UCNs is lower than the Fermi potential of most materials, therefore the UCNs are reflected under any angle of incidence. This feature gives the possibility to store UCNs inside bottles. Typically they behave more like a gas than a particle beam, which is why the benchmark for UCN production is specified in the UCN density. The extracted UCNs are transported via UCN guides with a transmission of > 0.99 per meter into the UCN storage cells, which are around 30 meters away from the UCN source. Efficient UCN transport is enabled with NiMo coated tubes [65]. The source of the FRM II should be able to provide a density of $> 3000\,\mathrm{cm}^{-3}$ of polarized neutrons inside the EDM chamber [66].

Figure 1.1 shows the schematic overview of the experiment. A non-metallic vacuum vessel houses four cylindrical cells, of which the central two serve as UCN

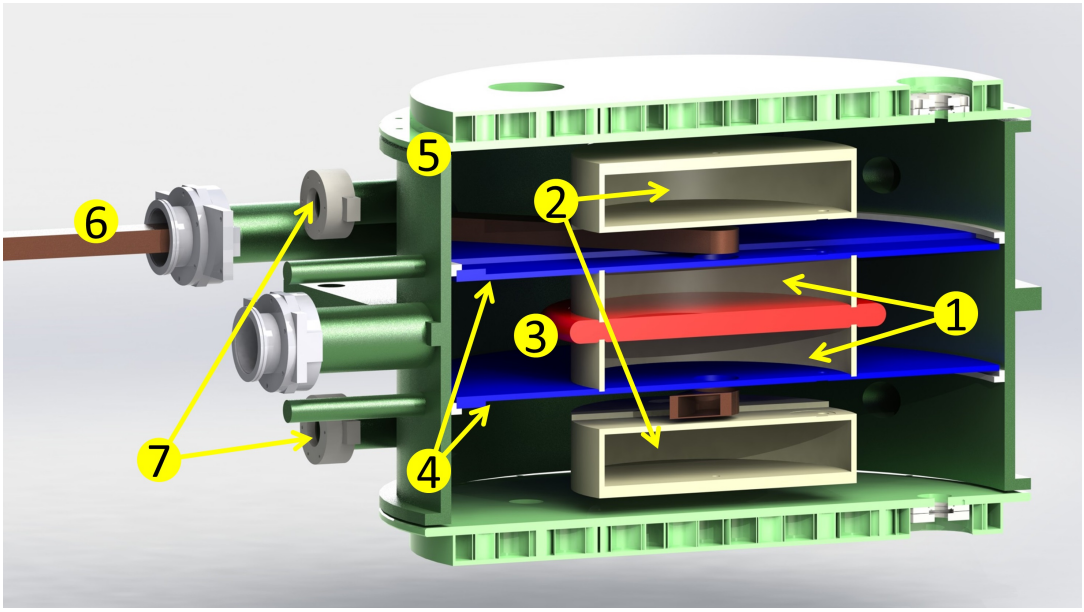

Figure 1.1.: Cutaway view of the Munich nEDM apparatus: two UCN storage chambers (1) are separated by a HV electrode (3). Neutrons are filled in the chambers through UCN guides (6). In addition to the neutrons, these chambers are filled with ^{199}Hg as a co-magnetometer. Two additional ^{199}Hg magnetometers (2) below and above the UCN chambers are used to measured the magnetic field gradient. The HV electrode and the two ground electrodes (4) produce the electric field. The amplitude is the same for both chambers, but the direction of the fields are opposite. All components are mounted inside a vacuum chamber (5) which also features online access channels (7) for the application of various magnetometer systems.

storage chambers. ^{199}Hg is added to them as a co-magnetometer and two additional cells above and below only contain ^{199}Hg acting as regular atomic magnetometers. The cells are separated by the high voltage electrode and the ground electrodes. A 200 kV high voltage supply is used to generate the electric field. Combined with a very homogeneous magnetic field B_0 this double chamber approach realizes the simultaneous measurement of $w_{\uparrow\uparrow}$ and $w_{\uparrow\downarrow}$. The temporal stability of B_0 is therefore less crucial for the determination of $\delta\omega$, but gradients become the major sources for systematic errors.

The key to controlling magnetic fields is the precise measurement of them and the capability to shield from external field changes. Next to the four ^{199}Hg magnetometer [67] there are so-called online access channels to position various other magnetometers near the EDM chambers. The access channels are vented and allow a dynamic positioning of the magnetometers during operation of the nEDM experiment. SQUIDs [68] attached to long cold fingers and ^{133}Cs magnetometers [69] are suitable for this application.

Though the measurement of the field with high precision is important, it is also necessary to provide a magnetically clean and stable environment. The nEDM instrument features a multi-stage shielding strategy with the individual parts listed below. A illustration is shown in figure 1.2.

- **Non-magnetic environment (EDM hole)**: The hall floor at the experiment position has been removed and rebuilt with non-metallic and non-magnetizable materials. It is a 9 m long, 6 m wide and 1 m deep hole and features electrical and vibrational decoupling from the experimental hall.

- **Active compensation system (ACS)**: A 9 m long, 6 m wide and 6 m high aluminum construction (hereafter referred to as the "field cage") carries 24 remotely controllable coils and 60 3-axis fluxgates of the type Mag-690[1]. The fluxgate signals are used to calculate optimal currents for the coils to compensate for external fields. Chapter 3 covers this part of the instrument and its application in detail. Transparent and non-transparent PVC panels form an enclosed shell, which protects the outer passive shield from direct sunlight (see appendix C), but provides sufficient light for working. Direct sunlight could produce temperature gradient-induced currents, which consequently generate stray magnetic fields. In combination with a large air conditioning system, the field cage also provides an environment separated from the experimental hall, allowing a nominal level of cleanliness to be maintained.

- The **outer passive shield** is built of two shells of a very high permeability-alloy (Magnifer®[2]) and one shell of aluminum. The shells form a cuboid structure with inner dimensions of 2.78 x 2.50 x 2.30 m^3 and a 1.92 x 2.00 m^2 large door to bring in large pieces of equipment. This structure is referred

[1]Bartington Instruments, `http://www.bartington.com/mag690-low-cost-three-axis-magnetic-field-sensor.html`

[2]Krupp Magnifer 7904 is used in the presented shield

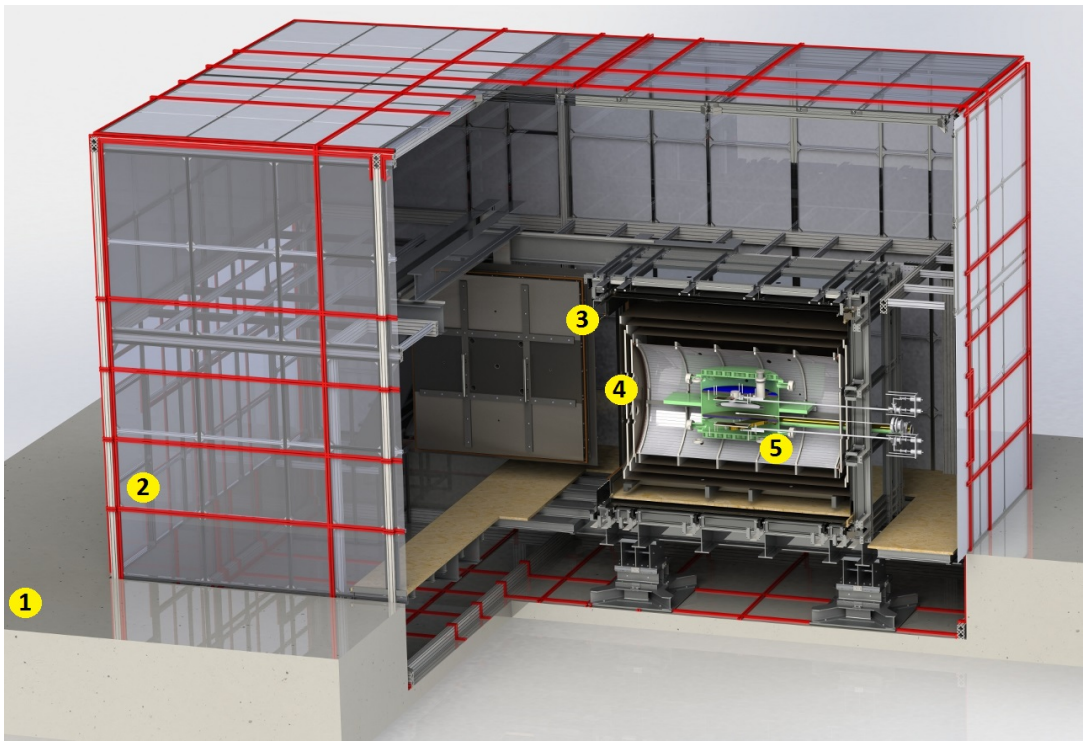

Figure 1.2.: Overview of the magnetic shield for the nEDM experiment: The whole shield is placed in the EDM hole made from nonmagnetic concrete (1). The coils (red) of the ACS are mounted to aluminum support structure (2) Inside of it are the outer (3) and inner (4) passive shields. The vacuum vessel (5) housing the nEDM experiment is at the center of the passive shields. A detailed description can be found in the text.

to as the "magnetically shielded room" (MSR). The MSR shields its interior from external field changes with a factor of $\gtrsim 350$ in the low frequency regime ($f > 1$ mHz). The shielding properties are usually quantified by the shielding factor (SF), which is ratio of the expected unshielded field change to the measured field change at the center of the shield. After degaussing [70] the residual field is in the sub-nanotesla range. A more detailed description of the MSR can be found in [71].

- **Inner passive shield**: Similar to the outer passive shield it is made of multiple layers of Magnifer®: three cuboid-shaped and one cylindrical-shaped. It features $SF \gtrsim 4700$ by itself and in combination with the MSR, $SF \gtrsim 6 \cdot 10^6$ [72]. The innermost layer is cylindrical and is used in conjunction with a cosine-theta coil [70] to produce the inner magnetic fields B_0 and B_1. Both fields are necessary to perform the actual neutron nEDM experiment, which is a conventional Ramsey experiment [73] with stored particles at room temperature.

- The **vacuum vessel** is made of glass fiber reinforced plastic and houses the nEDM experiment (shown in 1.1). It is of great importance that the parts closest to the UCN have a very low residual magnetic field. In chapter 2 a method to track magnetic disturbances, e.g. local dipoles and gradient fields, is presented.

With the exception of the EDM hole all parts of the shield are individually deployable and movable.

1.3.2. Sensitivity considerations

In this section the key ingredients for an EDM measurement based on Ramsey's method of oscillatory fields [74] are described, to outline the requirements to improve the current limit by almost two orders of magnitude (a sensitivity of a few 10^{-28} e $\cdot$ cm). The presented approach features a double chamber experiment which enables the simultaneous measurement of $w_{\uparrow\uparrow}$ and $w_{\uparrow\downarrow}$. Therefore any homogeneous field change shifts the Larmor frequencies equally and drops out in the corresponding frequency difference. Consequently, the requirement of temporal field stability is shifted from homogeneous field to gradient fields, as gradients can shift the Larmor frequency with opposite sign for both chambers. The Larmor frequency is measured using Ramsey's method.

Spin polarized UCNs are filled simultaneously in both UCN chambers and stored for $\sim$100 seconds. In three steps the initial polarization ($\mathbf{P} \parallel \mathbf{B}_0$) is manipulated and afterward analyzed by spin-sensitive neutron counters. The polarization $\mathbf{P}$ is initially aligned parallel to $\mathbf{B}_0$.

First, a so-called $\pi/2$ pulse is applied, which flips $\mathbf{P}$ to the plane perpendicular to $\mathbf{B}_0$ when the $\pi/2$ pulse is resonant to the Larmor frequency $\omega_L = \omega$ and the pulse length fulfills $T_{\frac{\pi}{2}}$ the $\pi/2$ requirement ($\gamma B_1 T_{\frac{\pi}{2}} = \frac{\pi}{2}$, with the gyromagnetic ratio γ of the neutron). The $\pi/2$ pulse is an oscillatory field in the x direction generated by the B_1 coil ($\mathbf{B}_1 \perp \mathbf{B}_0$).

In the second step the amplitude of the B_1 coil is reduced to zero, so that the relative phase between the two "clocks" (ω_L and ω) is conserved. The Larmor frequency of the neutron and the B_1 coil can be considered here as two clocks. For a certain time T (called storage time), the polarization precesses freely and in the case of a small off-resonant case ($\omega_L \neq \omega$) a phase difference accumulates.

The last step of the polarization manipulation is to apply a second $\pi/2$ pulse, which is identical to the first one. In resonant case the second $\pi/2$ pulse flips $\mathbf{P}$, so that it is antiparallel to $\mathbf{B}_0$. In the off-resonant case a relative phase Φ between ω and ω_L accumulates and $\mathbf{P}$ is not flipped completely by $\pi/2$. The result is an angle between $\mathbf{P}$ and $\mathbf{B}_0$, which ranges from 0 to 2π. For example, if $\Phi = \pi$, $\mathbf{P}$ is parallel to $\mathbf{B}_0$ after the second pulse.

In the end the UCNs are spin-analyzed and counted in detectors. In the case of the UCNs, this is performed by the transmission of the UCNs through a highly magnetized foil. Due to the spin-dependent magnetic potential, the foil acts like a barrier for one spin component, while the other component can pass. The polarization is determined by the ratio of UCNs parallel ($N_{\uparrow\uparrow}$) to UCNs antiparallel ($N_{\uparrow\downarrow}$) to $\mathbf{B}_0$

$$P = \hat{\mathbf{B}}_0 \cdot \mathbf{P} = \frac{N_{\uparrow\uparrow} - N_{\uparrow\downarrow}}{N_{\uparrow\uparrow} + N_{\uparrow\downarrow}} \,. \tag{1.4}$$

Hence the measurement of P as a function of ω yields the Larmor frequency ω_L.

The statistical sensitivity for this technique is given by [75]

$$\sigma_{d_n} = \frac{\hbar}{2E\alpha T\sqrt{N}} \,. \tag{1.5}$$

α is the "quality factor". It is derived from the peak-to-peak amplitude of P. The applied electric field E and T are limited by the geometry of the storage chambers and the particle species used inside the chambers [67]. The total number of neutrons N which is counted in the detectors is determined by the UCN density ρ and the volume V_{UCN} of the storage chambers. For reference, the currently best operating UCN source achieves $\rho = 55\,\mathrm{cm}^{-3}$[76].

Systematic errors are related to the magnetic field changes and their measurement, the electric field and the velocity distribution of the UCNs and other contributions. An overview can be found in [61]. For the envisaged sensitivity goal the dominant systematics are field gradients and so-called "geometric phases".

In the presence of a magnetic gradient field, geometric phases arise from the movement of the UCNs inside the storage chamber and can be expressed [77] by

$$\delta\omega \sim \frac{\delta \mathbf{B}_0}{\delta z}\alpha \cdot \frac{\mathbf{E} \times \mathbf{v}}{c^2} \,. \tag{1.6}$$

As this effect is linear in E, it mimics a false EDM signal. Simulations using the real geometry of the experiment are a common tool to study the behavior of this systematic; they show that local dipoles with a strength of ∼pT at a distance of 2 cm distance or magnetic field gradients on the order of 0.3 nT/m would already consume the total error budget [78].

On the other hand a temporal drift of the gradient field produces a shift in the Larmor frequencies of both chambers:

$$\delta\omega = \frac{\mu}{\hbar}\frac{\partial B}{\partial z}dz\,. \tag{1.7}$$

Applied to equation 1.3, this yields a systematic error of

$$d_{\mathrm{sys}} = \frac{\mu}{2E}\frac{\partial B}{\partial z}dz \tag{1.8}$$

In chapter 4 the magnetic field stability is determined and the corresponding expected systematic error derived.

2. Semi-analytical modeling and reconstruction of magnetic fields

In order to get a better understanding of the sources of systematics errors, it is necessary to measure magnetic fields with very high precision. The ^{199}Hg co-magnetometer is an ideal tool for this purpose, as it measures the magnetic field in the volume which also contains the neutrons. However, the center of mass of the neutrons is on average a few centimeters below that of the ^{199}Hg, due to the differences in temperature of the two species. UCNs have a very low kinetic energy (they do not thermalize with the environment) and therefore are noticeably affected by gravity [66]. This shift can be accounted for, and a correction was developed in previous EDM experiments [79]. By applying this correction, the ^{199}Hg precession frequency is then a direct measure of the magnetic field at the position of the UCNs and can be used to measure geometric phases.

The downside of using a co-magnetometer is the limitation on electric fields and UCN storage time and hence future EDM experiments could require either an alternative or complement approach to co-magnetometers. To generate the electric field, high voltage is applied between the high voltage (HV) and the ground electrodes. Residual gases like Hg reduce the breakdown voltage to 200 kV. Also, ^{199}Hg co-magnetometers require a special wall coating to achieve high spin polarization times T_1, which are essential for good magnetometer sensitivity. Due to the lack of suitable coatings for both particle species (UCN and Hg), a compromise must be made, which is not optimal for each of them individually. As a result, the UCN storage time is reduced by a factor of 2-3 compared to an experiment without a co-magnetometer.

In this chapter an alternative approach to measure the magnetic field is described.

2.1. 4π magnetometer concept

The precise measurement of the magnetic field around the EDM experiment sets an upper bound for the local field at the position of the experiment. This statement is valid, only if magnetically screened components are installed inside the EDM chambers and therefore "magnetic field sources" are avoided. The term *magnetic field source* represents any magnetic contamination (dipole or higher-order magnetic fields). The remaining external magnetic fields at the position $\mathbf{r}$ can then be

expressed in a Taylor series

$$\mathbf{B}(\mathbf{r}-\mathbf{r_0}) = \sum_{n=0}^{\infty} \frac{1}{n!} \sum_{i=1}^{3} \Big(\mathbf{dB_i}^n(\mathbf{r0}) \cdot \mathbf{R}^n \Big) \hat{\mathbf{r}}_i. \tag{2.1}$$

$\mathbf{dB}^n$ represents a (3×3^n) matrix, containing the partial derivatives of $\mathbf{B}$, and $\mathbf{R}^n$ represents a vector with a length of 3^n, containing the linear combination of the spatial coordinates (e.g. $\mathbf{R}^2 = (x^2, xy, xz, yx, y^2, yz, zx, zy, z^2)$). Using Gauss' theorem

$$\oint \mathbf{B}\mathbf{dA} = \int \nabla \cdot \mathbf{B} dV \tag{2.2}$$

and $\nabla \cdot \mathbf{B} = 0$ gives

$$\oint \mathbf{B}\mathbf{dA} = 0\,. \tag{2.3}$$

As this is valid in general for any closed surface independent of its shape, the field around the volume of interest can be approximated by a sphere. The linear superposition of a large amount of different field sources can become arbitrarily complex, but this does not affect the following concept.

Because of the assumed spherical symmetry, the Taylor expansion also should be expressed in spherical coordinates (see chapter G for the detailed calculation of the expansion) and the magnetic field can be expressed as

$$\mathbf{B}(\mathbf{r}) = \sum_{n=0}^{\infty} \frac{\mathbf{b}_n(\theta', \phi')}{(r-r_0)^{n+2}}\,, \tag{2.4}$$

with $\mathbf{r}_0 = (r_0, \theta_0, \phi_0)$ the position of the magnetic field source and θ' and ϕ' represent valid combinations of θ, θ_0, ϕ and ϕ_0. The order of the magnetic field source is denoted here by n. ($n = 0$ corresponds to a magnetic monopole, which would contradict $\nabla \cdot \mathbf{B} = 0$.) Therefore dipoles ($n = 1$) are the first order to take into account. For simplicity only one field source is assumed.

Expanding the magnetic field now in series of r gives an approximation for the magnetic field within the experimental volume:

$$\mathbf{B}(\mathbf{r}) = \sum_{m,n=0}^{\infty} \left(\frac{r}{r_0}\right)^m \mathbf{B}_{m,n}(\theta', \phi') \tag{2.5}$$

with all angle dependencies absorbed in $\mathbf{B}_{m,n}$, where n again is the order of the magnetic source and m is the order of the Taylor expansion.

The nEDM experiment is performed in a chamber with a maximal radius of $R_{EDM} = 30$ cm. External field sources can be divided into two types: inside (1.5 m $< r_{\text{in}} <$ 5 m) and outside ($r_{\text{out}} >$ 5 m) of the nEDM instrument. Hence these sources are then at least suppressed by a factor of $(r_{\text{in}}/r_{\text{EDM}})^m \cdot SF \gtrapprox 5^m \cdot SF$ and $(r_{\text{out}}/r_{\text{EDM}})^m \cdot SF \gtrapprox 17^m \cdot SF$. Internal sources ($< r_{\text{in}} <$ 1.5 m) are avoided by magnetically screening all devices and components before installation.

Homogeneous field changes (m=0) affect both EDM chambers identically and therefore cancel out. First-order fields (gradients) consequently are the dominant source for field-induced errors (gradients and geometric phases). Only the z-component of the gradient is important, as the frequency shift due to the x- and y-component (radial components) is symmetric and also later cancels out. The radial components also do not contribute to the geometric phases, because all field lines that penetrate perpendicularly to the barrel of the storage chamber do not a generate geometric phase [80]. Consequently field gradients in the z-direction are most critical.

The systematic effect of a second-order field (quadrupole) can be handled similarly. Due to the cylindrical symmetry, radial components (as well as z components, arising from the double chamber approach) produce the same frequency shift. Hence the contribution of a second-order field arises only from geometric phases which are currently under investigation. Higher-order fields (m >2) are already suppressed to a high level, as shown before. In summary, false EDM signals will mainly arise from linear gradients and geometric phases.

The gradient field can be expressed in many different forms. The only requirement is that it fulfills the Maxwellian equations and that is a linear function of the spatial coordinates. The most general expression for a linear gradient field is

$$\mathbf{B}(\mathbf{r}) = \mathbf{B}(x,y,z) = \begin{pmatrix} G_{1,1} & G_{1,2} & G_{1,3} \\ G_{2,1} & G_{2,2} & G_{2,3} \\ G_{3,1} & G_{3,2} & G_{3,3} \end{pmatrix} \begin{pmatrix} x \\ y \\ z \end{pmatrix} . \tag{2.6}$$

By fulfilling Maxwell's equations $\nabla \cdot \mathbf{B} = 0$ and $\nabla \times \mathbf{B} = \mu_0 \mathbf{j} + \mu_0 \epsilon_0 \frac{\partial \mathbf{E}}{\partial t} = 0$ (in the case of vanishing currents and time invariant electric fields), the parameter space is reduced from nine to five. The expression for the gradient field follows then as

$$\mathbf{B}(x,y,z) = \begin{pmatrix} G_{1,1} & G_{1,2} & G_{1,3} \\ G_{1,2} & G_{2,2} & G_{2,3} \\ G_{1,3} & G_{2,3} & -(G_{1,1}+G_{2,2}) \end{pmatrix} \begin{pmatrix} x \\ y \\ z \end{pmatrix} . \tag{2.7}$$

This matrix fulfills Maxwell's equations for independent combinations of $G_{i,j}$ and therefore can be separated into five parts

$$\mathbf{B}(x,y,z) = G_{1,1} \begin{pmatrix} x \\ 0 \\ -z \end{pmatrix} + G_{1,2} \begin{pmatrix} y \\ x \\ 0 \end{pmatrix} + G_{1,3} \begin{pmatrix} z \\ 0 \\ x \end{pmatrix} + G_{2,2} \begin{pmatrix} 0 \\ y \\ -z \end{pmatrix} + G_{2,3} \begin{pmatrix} 0 \\ y \\ -z \end{pmatrix} . \tag{2.8}$$

This expression will be used for all gradient field calculations.

Even by avoiding magnetic contaminations in the construction of the EDM chambers, internal magnetic fields cannot be excluded, since they can arise during the operation of the experiment. For example, high voltage breakdowns can damage the surface of the electrodes, producing either spots that are directly magnetized or ejecting electrode material that deposits on the insulator rings or another electrode. In both cases a local magnetic dipole could be generated.

In comparison to the typical length scale of the experiment these dipoles are much smaller and can be described in the far field approximation

$$\mathbf{B}(\mathbf{r}) = \frac{\mu_0}{4\pi r^2} \frac{3\mathbf{r}(\boldsymbol{\mu} \cdot \mathbf{r}) - \boldsymbol{\mu}\, r^2}{r^3} \,. \tag{2.9}$$

To produce a magnetic field of 10 pT at a distance of 2 cm, distance the absolute value of the magnetic dipole moment $\boldsymbol{\mu}$ has to be on the order of $4 \cdot 10^{-10}\,\mathrm{A\,m^2}$ ($\mathrm{Tm^3}$). This is the most conservative assumption ($\boldsymbol{\mu} \parallel \mathbf{r}$). Such a dipole is chosen as a benchmark, as it generates a false EDM signal on the order of the sensitivity goal of the experiment [81].

The goal of a 4π magnetometer is therefore to track the external magnetic gradient fields and to check for local dipoles occurring during or following a high voltage breakdown event (which is also separately monitored [82]).

The field can be measured with Cs- and Hg-based magnetometers. Both types are cells containing Cs or Hg gas at a low pressure (<mbar). The light absorption of a laser beam operated at the transition wavelength of the fine (hyperfine, for the Hg) level splitting is measured at a photo diode. The temporal modulation of the laser amplitude then yields the magnetic field. Cs magnetometers are usually smaller in size and exist as fiber coupled versions [83]. In other words, the laser beam is guided to the cell and back to the photo diode. They can be operated with a sensitivity of $\approx 10\,\mathrm{fT}/\sqrt{\mathrm{Hz}}$ and measure the magnitude of the magnetic field (scalar mode). The measurement of field direction (vector mode) is also achievable with Cs magnetometers, but they require a different mode of operation. They can be placed inside the online access channels of the vacuum vessel or around it. Due to their small size, they measure the magnetic field of a point.

Hg magnetometers are about the same size as the UCN storage chambers and two of them are below and above the double UCN chamber. As the Hg atoms occupy a large volume, their precession frequency yields a volume-averaged magnetic field measurement (only scalar mode). They achieve a comparable sensitivity, but are less versatile than Cs magnetometers, as they are larger and read out with a free space laser. Therefore their readout beam needs a free path through the passive shields, which limits the possible deployment of the magnetometers.

An array of these magnetometers enables the reconstruction of the field inside the EDM chamber. Due to the huge parameter space of this problem (position, amount of magnetometers, etc.), the optimization of the magnetometer array is separated into multiple parts. The positions of the magnetometer are quantized through a grid of points with a spacing of about $R_{\mathrm{mag}} = 5\,\mathrm{cm}$. This enables a numerical treatment optimization. In the following sections, gradient and dipole fields will be treated separately and in the end the results are compared.

2.2. Geometry of the magnetometer array

Depending on the technological development of a few components there are three different possible scenarios for the nEDM experiment. The *room temperature EDM*

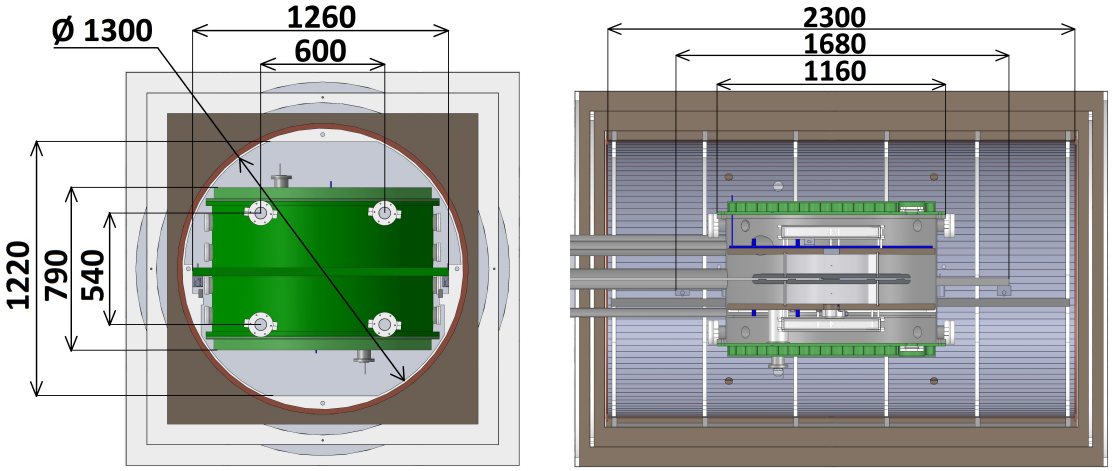

(a) Front view (b) Side view

Figure 2.1.: Vacuum vessel and the inner passive shield with dimensions (in mm).

chambers scenario is basically the setup shown before. In the *minimal vacuum configuration* scenario a special gel is used to make the EDM storage chambers vacuum tight and therefore the vacuum chamber is not necessarily needed, except for mounting other equipment. The *cryogenic* scenario is much different to the previous ones. Here the EDM storage chambers are positioned inside a liquid helium dewar. The positions of the magnetometers are limited by the particular selected scenario, for example the operation of some of the magnetometers is impossible in vacuum or liquid helium.

The cryogenic scenario is the most limiting in terms of available magnetometer positions. Due to temperature shielding, the performance of a cryogenic chamber increases with increasing size. Therefore the feasibility of a 4π magnetometer is studied as a function of the magnetometer distance to the center. For the room temperature EDM chambers scenario the above specified positions are valid. For a minimal vacuum configuration experiment without an evacuated vacuum vessel, positions inside the vacuum vessel are also suitable.

2.2.1. Cryogenic EDM chambers

This scenario is based on the idea to perform an EDM experiment inside a cryogenic storage chamber filled with liquid helium (LHe). This approach to measure the EDM has been proposed in the past [84]. Although the technical implementation is difficult, it also provides some benefits. For example the UCN may be produced inside the LHe and hence there are fewer UCNs transportation losses. Another advantage is the possibility to apply a higher electric field, because high voltage breakdowns occur at higher voltages in LHe than in a vacuum.

The dimensions and spatial orientation are defined by the geometry of the magnetic shield. To study the performance of the 4π magnetometer for this application, a cylindrical shape of the cryogenic chamber is assumed. The maximum available

space is then given by the dimension of the innermost layer of the passive shield (see figure 2.1, for this calculation the green vacuum chamber can be neglected). Due to design reasons, the glass-fiber reinforced holding structure is not perfectly cylindrical, but for the following calculations a cylindrical shape is assumed, using as dimensions the mean diameter of $D_{\max} = 1.30\,\mathrm{m}$ and the maximum length of the shield $L_{\max} = 2.30\,\mathrm{m}$.

Two cylindrical grids of points are chosen to model the UCN chambers (UCN grid) and the potential sensor positions (sensor grid). According to the cylindrical symmetry and the demand of an equidistant point distribution, the two grids are parametrized as follows:

$$(x, y, z)_{UCN} = (r_{\mathrm{UCN}} \cdot \cos(\phi_{\mathrm{UCN}}),\, r \cdot \sin(\phi_{\mathrm{UCN}}),\, z) \tag{2.10}$$

$$(x, y, z)_{\mathrm{sen}} = (r_{\mathrm{sen}} \cdot \cos(\phi_{\mathrm{sen}}),\, y,\, r_{\mathrm{sen}} \cdot \sin(\phi_{\mathrm{sen}})) \tag{2.11}$$

with the spacing $dy = dr_{\mathrm{UCN}} = 1\,\mathrm{cm}$, $dz = dr_{\mathrm{sen}} = 5\,\mathrm{cm}$ and

$$d\phi_{\mathrm{UCN,sen}} = \frac{2\pi}{\left\lfloor \frac{2\pi}{2\arcsin(\frac{dr_{\mathrm{UCN,sen}}}{2r_{\mathrm{UCN,sen}}})} \right\rfloor} \tag{2.12}$$

and the minimum and maximum values resulting from the dimensions of the corresponding parts. $\lfloor\,\rfloor$ symbolizes the floor function, which rounds its argument down to the next integer value. All points of the sensor grid have at least a distance of $R_{\mathrm{mag}}/2 = 2.5\,\mathrm{cm}$ to next closest part (e.g. the cryogenic storage chamber). The resulting grids are shown in figure 2.2a.

2.2.2. Room temperature EDM chambers

For the room temperature EDM chambers experiment a vacuum vessel is needed to house the UCN storage chambers. Collisions with gas atoms or molecules (e.g. H_2O) thermalize UCNs and therefore the loss rate of the UCNs at atmospheric pressure would be extremely high. For this reason ,the vacuum vessel is usually evacuated to $\sim 10^{-6}\,\mathrm{mbar}$ to achieve storage UCN times of a few hundred seconds.

The vessel itself has a few optical windows reserved for the operation of two Hg co-magnetometers and two Hg magnetometers. However, the co-magnetometers are however excluded from the 4π calculations.

The vacuum vessel does not feature feedthroughs for the operation of the Cs magnetometers. Hence the only available positions for the Cs magnetometers are outside the vacuum vessel and inside the online access channels. The arrangement of the sensor positions is done in a Cartesian (C), a spherical (S) and a cylindrical (Cy) grid pattern. The patterns are generated by following the corresponding coordinate convention:

$$(x, y, z)^{\mathrm{C}}_{\mathrm{sen}} = (x,\, y,\, y)\,, \tag{2.13}$$

$$(x, y, z)^{\mathrm{S}}_{\mathrm{sen}} = (r_{\mathrm{sen}} \sin(\theta_{\mathrm{sen}}) \cos(\phi^{\mathrm{S}}_{\mathrm{sen}}),\, r_{\mathrm{sen}} \sin(\theta_{\mathrm{sen}}) \sin(\phi^{\mathrm{S}}_{\mathrm{sen}}),\, r_{\mathrm{sen}} \cos(\theta_{\mathrm{sen}})) \text{ and} \tag{2.14}$$

$$(x, y, z)^{\mathrm{Cy}}_{\mathrm{sen}} = (r_{\mathrm{sen}} \cos(\phi^{\mathrm{Cy}}_{\mathrm{sen}}),\, r \sin(\phi^{\mathrm{Cy}}_{\mathrm{sen}}),\, z)\,, \tag{2.15}$$

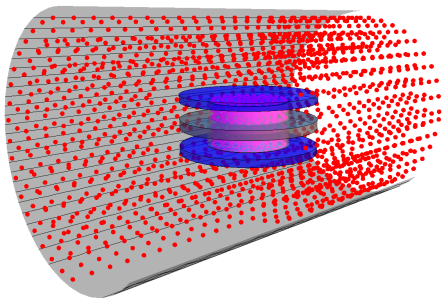

(a) Cryogenic EDM chambers setup (cylindrical)

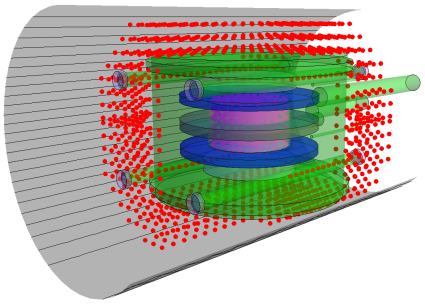

(b) Room temperature EDM chambers setup (Cartesian)

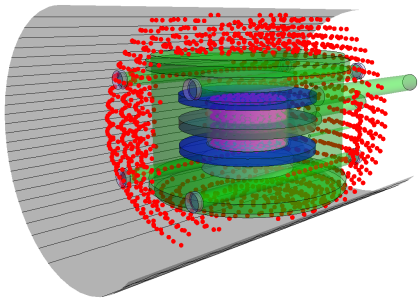

(c) Room temperature EDM chambers setup (spherical)

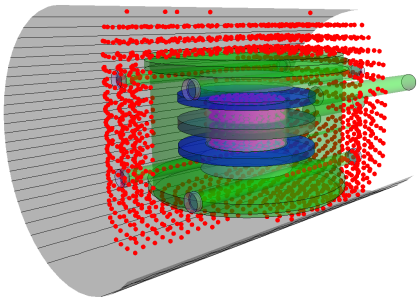

(d) Room temperature EDM chambers setup (cylindrical)

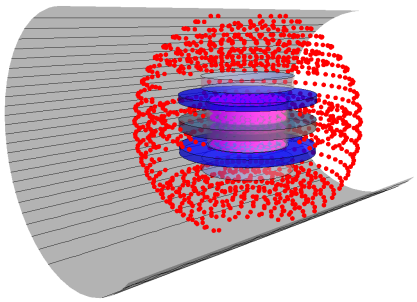

(e) Minimal vacuum configuration setup (spherical)

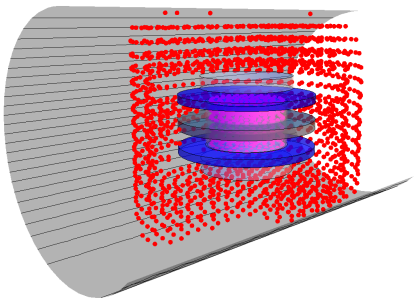

(f) Minimal vacuum configuration setup (cylindrical)

Figure 2.2.: Sensor (red dots) and UCN (magenta dots) grids for the 4π magnetometer calculations for various cases: Sensor positions are arranged following a certain symmetry (not all are shown here). Details can be found in the text. For illustrative reasons the density of the grid is reduced and the front quarter is cut out. For reference, the UCN chambers with the electrodes, the vacuum vessel and the innermost shell of the passive shield are indicated.

with $dx = dy = dz = dr_{\mathrm{sen}} = 5\,\mathrm{cm}$ and $d\phi_{\mathrm{sen}}^{\mathrm{S,Cy}}$ and $d\theta_{\mathrm{sen}}$ equivalently defined to equation 2.12. The optimization of the sensor positions should be unbiased and hence parametrization of the sensor grid is calculated exemplarily for the three grids. All points that overlap with experiment parts within a distance of $R_{\mathrm{mag}}/2$ are removed. The same UCN grid employed in the cryogenic scenario (section 2.2.1) is used here. The resulting grids are shown in figures 2.2b - 2.2d.

2.2.3. "Minimal vacuum" configuration

Special types of silicones with very good electric insulation capabilities are used for the construction of high voltage applications (e.g. transformers). They are also potentially vacuum-tight. The potential use of these materials for the EDM chamber is promising, as it would fulfill two purposes: prevention of high voltage break downs and replacement of the vacuum vessel.

With the vacuum chamber no longer being used, sensor positions inside the former volume of the vacuum chamber become available. The reduced distance to the EDM chamber will yield an increased performance of the 4π magnetometer for the dipole detection.

Similar to the room temperature EDM chambers scenario, all calculations are done independently in a Cartesian, a spherical and a cylindrical grid pattern (the parametrization is equivalent to section 2.2.2). The removal of the vacuum chamber would also remove the online access channel, but the positions inside the online channel overlap anyway with the regular grids for this scenario. The result is shown in figure 2.2e and 2.2f. The Cartesian grid is not shown, but it is also used for the calculations. The cylindrical grid is obviously the most reasonable of the three, but calculations are run for all patterns to have an unbiased approach. The calculation can be parallelized and works in general for arbitrary grids.

By design, the two UCN chambers are separated and evacuated separately. Therefore the inside of the HV electrode may be at atmospheric pressure and it may be possible to place additional magnetometers inside of it. The center of the HV electrode would however not be available, as the HV supply there is attached to provide a homogeneous contact for the electrode. Limited space inside the HV electrode and especially the very limited space for the glass fibers – which are needed for the operation of the Cs magnetometers – restrict the total number of magnetometers inside the HV electrode. It is obvious that the performance of the system increases with the amount of magnetometers, but the sensitive glass fibers connected to the cells make the deployment of too many magnetometers very difficult. Hence here it is reasonable to set the amount to four magnetometers.

The magnetometers are symmetrically placed inside the HV electrode at $(\pm R, \pm R, 0)$. The radius R is determined by using a geometrical argument, which is explained in the next sentences. The main purpose of magnetometers inside the HV electrode is to track magnetic dipoles. Dipoles can be located on the surfaces of the electrodes and of the insulator rings. Positions of the sensors should therefore be arranged in a way that the mean distance from any point to the one of the sensors is minimized.

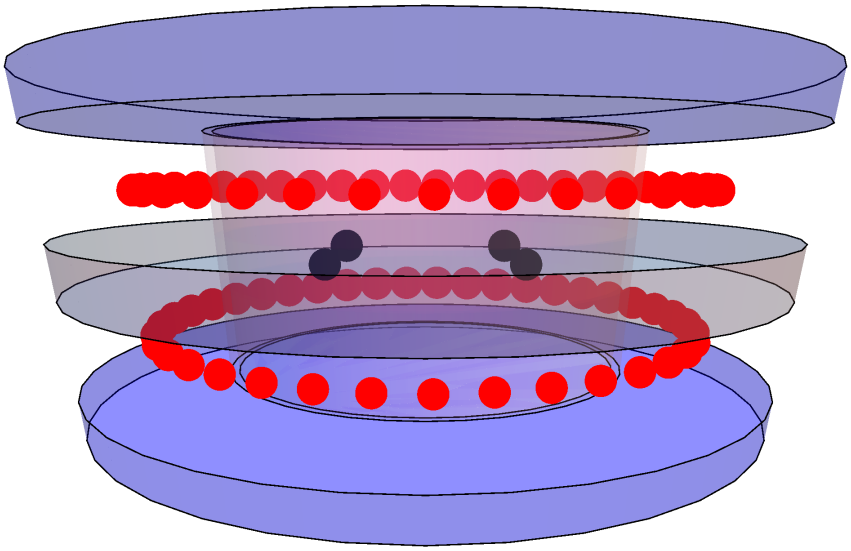

Figure 2.3.: Sketch for the optimization of the magnetometer position inside the HV electrode. The black points represent the HV positions and the red points the closest of the conventional positions.

The optimization is performed for two different cases. First, it is assumed that there are only the four magnetometers inside the HV electrode. Second, there are also magnetometers positioned around the insulator ring in a cylindrical pattern. In figure 2.3 the situation for both scenarios is shown. For the second scenario the only positions taken are those which are closest to the insulator rings.

In order to quantify the optimization of the sensor positioning in regard to the magnetic dipole reconstruction quality, a preliminary figure of merit is defined by the relative strength of a standard dipole (10 pT at a distance of 2 cm distance)

$$s_2(\mathbf{r}_{\mathrm{dip}}) = \sqrt{\sum_{\mathbf{r}_{\mathrm{sen}}} \left(\frac{(2\,\mathrm{cm})^3}{|\mathbf{r}_{\mathrm{dip}} - \mathbf{r}_{\mathrm{sen}}|^3} \right)^2}. \tag{2.16}$$

Due to symmetry, only dipole positions $\mathbf{r}_{\mathrm{dip}}$ on the upper surface of the HV electrode are considered. In addition, the insulator rings and the ground electrodes are neglected to optimize the sensor positions inside the HV electrode. The goal of the optimization is to maximize the integrated relative signal strength $\int s_2(\mathbf{r}_{dip}) d\mathbf{A}$.

It turns out that for the nEDM experiment the ideal radius is $R = 0.14\,\mathrm{m}$, if allowing only sensors inside the electrode, and $R = 0.13\,\mathrm{m}$ when including the outer sensor positions. The result is shown in figure 2.4. With the outer positions (see figure 2.4a) the s_2 is more homogeneous than without them. The minimal value of s_2 is $7 \cdot 10^{-3}$ at the center (x=y=0 cm). This number has to be compared to the sensitivity of the sensor relative to the field of a standard dipole $s_{\mathrm{crit}} = 10\,\mathrm{fT}/10\,\mathrm{pT} = 10^{-3}$.

Without the outer sensors (see figure 2.4b) the minimal value is $2 \cdot 10^{-3}$ at the outermost edge at $\theta = \pm\frac{\pi}{4}, \pm\frac{3\pi}{4}$. At the center the relative signal strength is $5{\cdot}10^{-3} > s_{\mathrm{crit}}$, which for now is considered to be sufficient to detect a standard dipole. The addition of sensors outside the electrode will further improve dipole detection in the electrode, and will be added in the next step of the optimization. Because the outer sensors will be optimized separately in a later calculation, the position of the inside sensors will be fixed to the result of the only-sensor-inside optimization ($R = 0.14\,\mathrm{m}$).

2.2.4. Comparison

The simplest way to directly compare the different scenarios is to look at the spatial distribution of the sensors. Figure 2.5 shows the radial sensor distribution (relative to the center of the nEDM experiment) of the previously introduced scenarios. By comparing the different arrangements among each other, no large difference can be seen except for a minor shift to smaller distances in the minimal vacuum configuration case (MV).

Nevertheless, these will be treated separately, as the dipole reconstruction strongly depends on the distance between the dipoles and the magnetometers. The minimal vacuum configuration setup enables the closest sensor arrangement and is expected to show in general the best scenario for a 4π magnetometer operation. The overlap

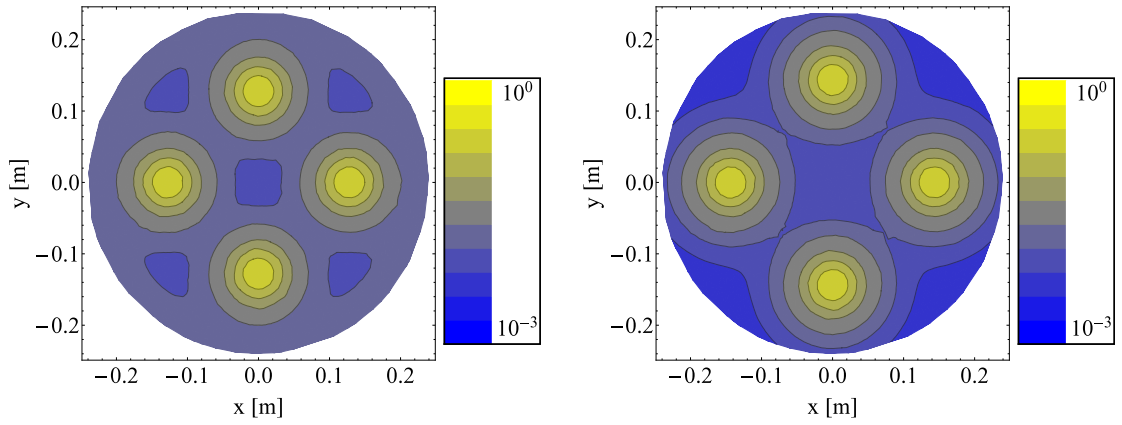

(a) With outer sensors (b) Without outer sensors

Figure 2.4.: Relative dipole strength on the surface of the upper HV electrode.

of the MV distribution and the dipole (Dip) distribution is just an artifact of the presentation in radial distribution.

2.3. Gradient field reconstruction

Now that the geometries and some basic ideas are defined, different issues can be studied, starting with linear gradient fields. Compared to the tracking of local dipoles, linear field gradients at the critical level for an EDM experiment are much easier to handle due to the larger fields. As it has been described in section 2.1, a linear field gradient has five degrees of freedom, and combined with the three degrees of freedom for a constant field, eight parameters have to be determined to reconstruct a gradient field. Therefore the operation of three independent vector magnetometers is sufficient for the reconstruction process. Obviously a larger number of sensors increases the performance of the system. A quick estimation of the gradient field sensitivity can be done by putting the magnetometer sensitivity of 10 fT in relation to the minimal distance of two magnetometers $d_{\min} = R_{\mathrm{mag}}$. The result of 200 fT/m indicates the minimal gradient sensitivity, but with increasing distance the gradient determination improves significantly.

In order to reconstruct the gradient field, it is sufficient to reconstruct the five parameters $G_{i,j}$ that describe the gradient. Two vector magnetometers form a system with six equations and five unknowns. The analytical solution requires only five equations and consequently one component of a magnetometer can be neglected for the pure analytical solution. As there should be no bias in the choice of which channel to discard, six analytically calculated solutions per magnetometer pair are extracted (see appendix H). The average of all magnetometer pair combinations then gives a numerical solution for $G_{i,j}$.

In practice, the three parameters of the homogeneous field $B_{0,i}$ also have to be taken into account. This is done by applying the above described method on three magnetometers. For both cases the analytical solutions are too complex to be shown

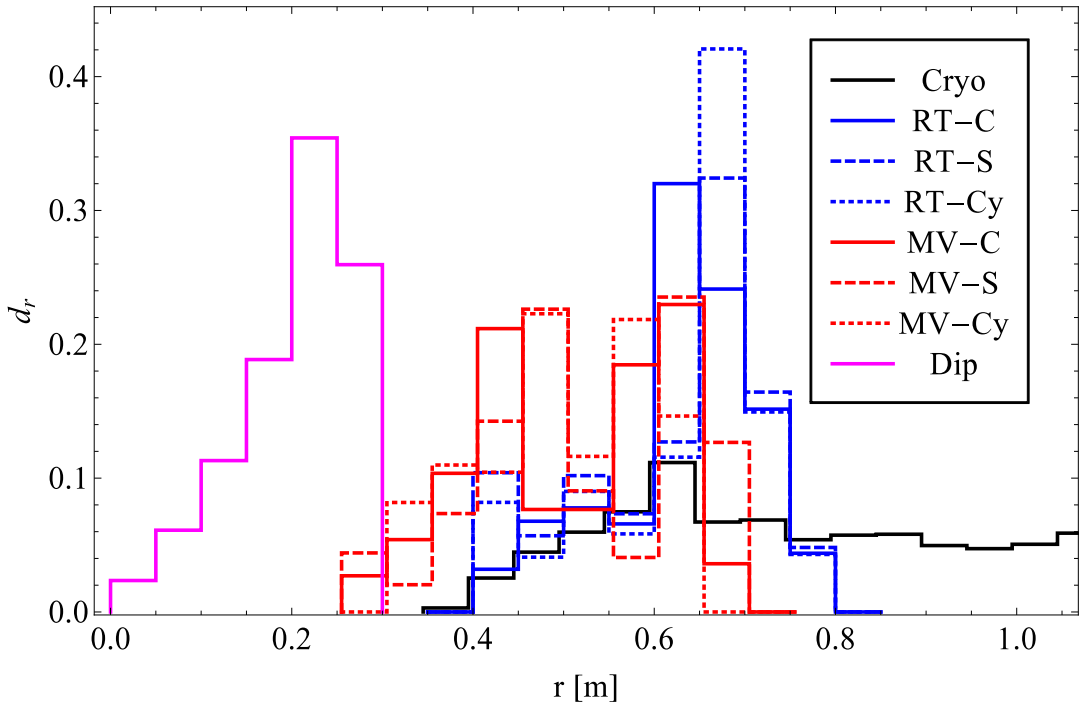

Figure 2.5.: Radial sensor distribution of the cryogenic EDM chambers (Cryo), the room temperature EDM chambers (RT) and the minimal vacuum configuration (MV) setup with Cartesian (-C), spherical (-S) and cylindrical (-Cy) position arrangement. The model dipole (Dip) distribution is shown for comparison reasons. The vertical axis is normalized and indicates the sensor density as a function of the distance from the center of the setup. The radial distribution is a simplified representation of the sensor positions and indicates the expected performance relative to the other scenarios.

here, but easily obtained by computer-based calculations (here Mathematica[1]).

To characterize the reconstruction quality, the relative difference ΔR_p between calculated parameter set ${G^\mathrm{calc}}_{i,j}$ and the randomly generated set G^gen is determined by

$$\Delta R_\mathrm{p} = \frac{\|\mathbf{G}^\mathrm{calc} - \mathbf{G}^\mathrm{gen}\|}{\|\mathbf{G}^\mathrm{gen}\|} \,. \tag{2.17}$$

$\mathbf{G}^\mathrm{calc}$ and $\mathbf{G}^\mathrm{gen}$ represent a vector with five elements ($G^{(\mathrm{calc,gen})}_{1,1}$, $G^{(\mathrm{calc,gen})}_{1,2}$, $G^{(\mathrm{calc,gen})}_{1,3}$, $G^{(\mathrm{calc,gen})}_{2,2}$ and $G^{(\mathrm{calc,gen})}_{2,3}$, see equation 2.8) This determination via the norm $\|...\|$ is preferred over the singular parameter determination

$$\|(\frac{{G^\mathrm{calc}}_{1,1} - {G^\mathrm{gen}}_{1,1}}{{G^\mathrm{gen}}_{1,1}}, ..., \frac{{G^\mathrm{calc}}_{2,3} - {G^\mathrm{gen}}_{2,3}}{{G^\mathrm{gen}}_{2,3}})\| \,, \tag{2.18}$$

as small ${G^\mathrm{gen}}_{i,j}$ can boost the ΔR_p through the normalization. The normalization is required to compare the different reconstruction events, which vary in magnitude due to the random generation of G^gen.

In order to study the performance in a general way, different magnetometer arrays are randomly chosen and for each of them different gradients are randomly chosen. A random number generator determines a random value with an uniform distribution between zero and 100 pT/m for each $G_{i,j}$. As an example, figure 2.6 shows the reconstruction quality for the cryogenic scenario with 20 magnetometers, with an average distance to the center of 50 cm and a magnetometer noise of 10 fT, exposed to a gradient field of the order 100 pT/m.

Except for one sensor configuration, all events show a very good reconstruction quality better than 0.01%. Magnetometer arrays with positions packed very dense to each other or positions that are connected by a straight line, usually result in lower performance. These configurations are not excluded from the random selection process, but in a real implementation they are easy to avoid. The reconstruction quality is mainly dominated by the signal-to-noise ratio SNR which is in this case $5 \cdot 10^3$. By neglecting the bad sensor configurations and averaging over all events, the reconstruction quality for a design parameter set (N_{sen} , $\overline{\mathbf{r}_\mathrm{sen}}$) is extracted. In general, the reconstruction quality is limited by the SNR and scales linearly with it, as shown in figure 2.7.

In the next step, the dependency of the number of applied magnetometers and their positions relative to the center is studied. High sensitivity magnetometers are difficult to operate and expensive to build, therefore finding the lowest number that achieves the experimental requirements is desirable. For the characterization, all potential positions are grouped in spherical shells with radii of $r - R_\mathrm{mag}/2$ to $r + R_\mathrm{mag}/2$. Then N_sen positions are randomly chosen out of a shell. For every sensor configuration N_grad individual runs are performed, with a new gradient to reconstruct being randomly generated each time.

Figure 2.8 shows the result of the sensor number and sensor position variation. By increasing the number of sensors and the distance to the center the performance

[1]Wolfram Research Inc, Mathematica v.10.0, `https://www.wolfram.com/mathematica/`

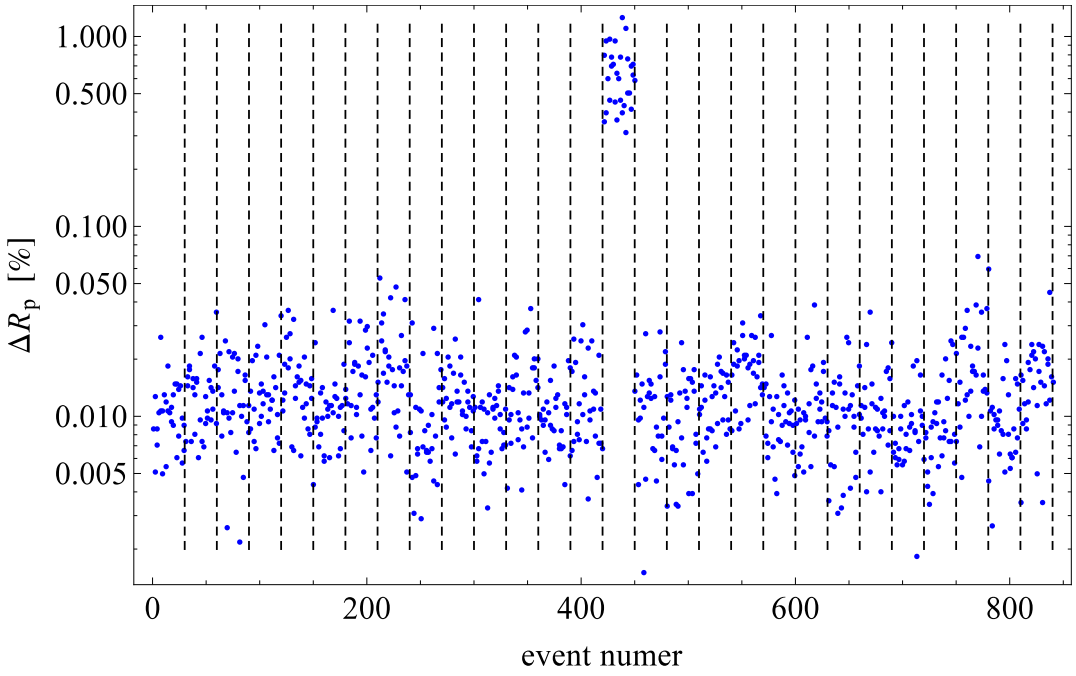

Figure 2.6.: Gradient field reconstruction quality with 20 magnetometers at 50 cm distance to the center with 10 fT and a gradient strength of 100 pT/m: The black dashed lines indicate a new array of magnetometers. In total 30 arrays with 30 different gradients each are shown. The array with the event numbers from 421 to 450 shows a poor reconstruction quality, due to bad magnetometer positions. The black dashed lines enclose event numbers where the positions of the magnetometer array are unchanged.

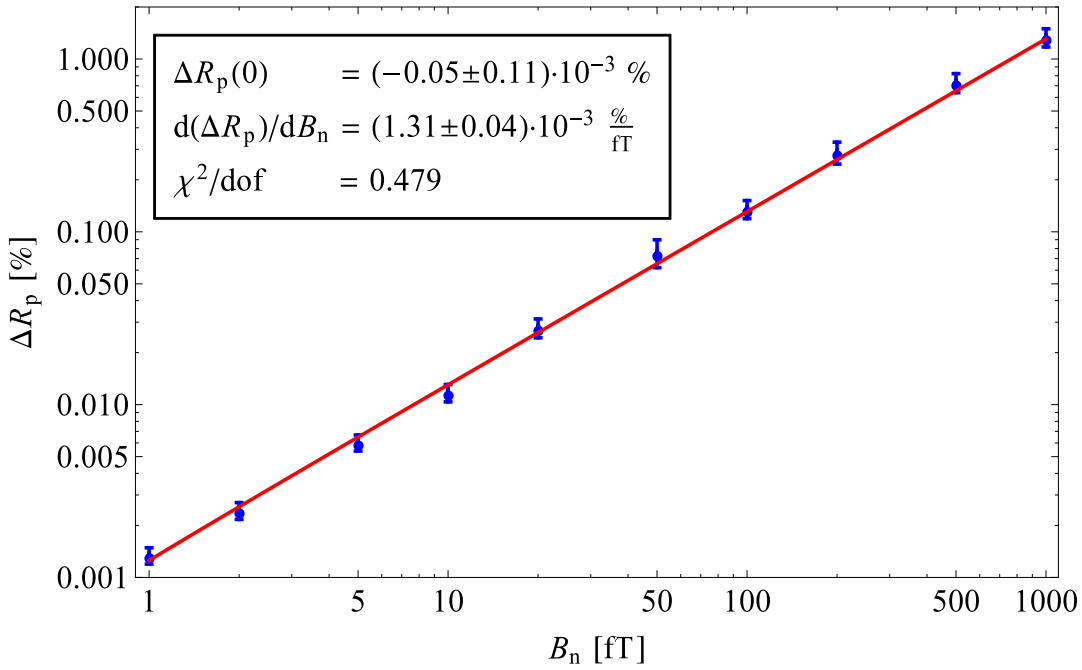

Figure 2.7.: Field reconstruction quality for gradient fields of 100 pT/cm as a function of the magnetometer noise B_n. The red line shows a linear fit ($\Delta R_p = R_p(0) + d(\Delta R_p)/dB_n \cdot B_n$) to the result. As expected, the reconstruction quality worsens linearly with the noise.

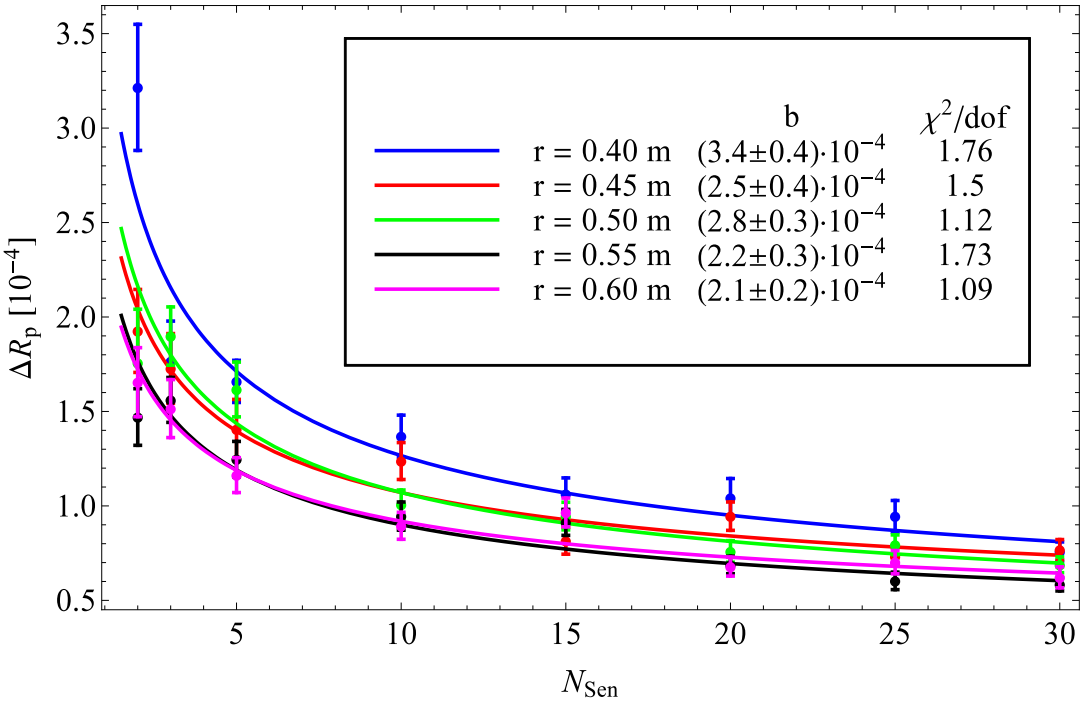

Figure 2.8.: Field reconstruction quality for gradient fields of 100 pT/cm as a function of distance r to the center and the number of sensors. The solid lines are $b/\sqrt{N_{\text{sen}}}$ fits to the data. The choice for the $1/\sqrt{N_{\text{Sen}}}$ functionality is based on the expected statistical behavior. The error bars are determined by the standard deviation spread of the simulation results for different magnetometer arrays.

improves. Both dependencies can be simply explained. A larger number of sensors yields increased statistics and therefore the reconstruction quality is proportional to $\frac{1}{\sqrt{N_{\text{sen}}}}$. On the other hand, an increased distance improves the signal-to-noise ratio.

As shown here by the example of the cryogenic scenario, a 4π magnetometer will easily detect gradients that are even smaller than the detection goal of 100 pT/m. In addition, the difference of the outer part of the grids for the different scenarios (see section 2.2) are small, and hence the results for the cryogenic scenario can also be applied to the other scenarios.

2.4. Local magnetic dipoles

The second and more difficult task of the 4π magnetometer is to detect magnetic dipoles, which could appear during the operation of the experiment inside the UCN chambers. As the relative field strength rapidly decreases with distance, only magnetometer positions very close to the UCN chambers are used for the optimization. The maximal radial distance of a potential dipole is 27 cm, corresponding to the contact line of the insulator ring and the ground electrodes. The critical relative field strength of 10^{-3} is reached at a distance of 20 cm. Combining both values gives a typical distance scale of 47 cm for the sensors.

As only very few positions would be left over for the cryogenic and the room temperature EDM chambers scenarios (see figure 2.5), this maximal distance for magnetometer positions is extended to 60 cm. The remaining positions are referred to as the "reduced sensor grid". Though the relative field strength at this distance is only $2 \cdot 10^{-4}$, the lack of signal might be compensated for by a larger number of magnetometers.

In order to speed up the calculation, the cylindrical symmetry was exploited and only the upper half ($z > 0$) was considered. Further simplification through symmetry arguments were applied, because this would discretize the number of sensors to 8, 16, etc. The symmetry reduction was only used for the sensor position determination. For the calculation, the identical set of positions was used for the lower half, by mirroring the chosen position through $\mathbf{r} \rightarrow -\mathbf{r}$. It might seem to have no large effect, but the variation of the sensor positions gives a very large parameter space in the Monte Carlo optimization and therefore any possible reduction is very useful.

The optimization is based on the idea that the relative signal strength s_2 (in comparison to the previously defined standard dipole) for all surfaces inside the EDM chambers has to be maximized. As a starting point, a grid of points $\mathbf{r}_{\text{dip}}$ in the relevant surfaces is defined. The distribution of the points follows the cylindrical symmetry of the EDM chamber and features a constant point density. In other words, the number of points on each surface is proportional to its area, and, in addition, the distance of a point to its next neighbor is nearly the same for all the points on that surface. The grid is shown in figure 2.9.

The relative signal strength s_2 (see equation 2.16) is calculated at each point. It can be interpreted as a measure as to how well the ensemble of sensors can detect the standard dipole at position of the point. As there are no preferred points, the

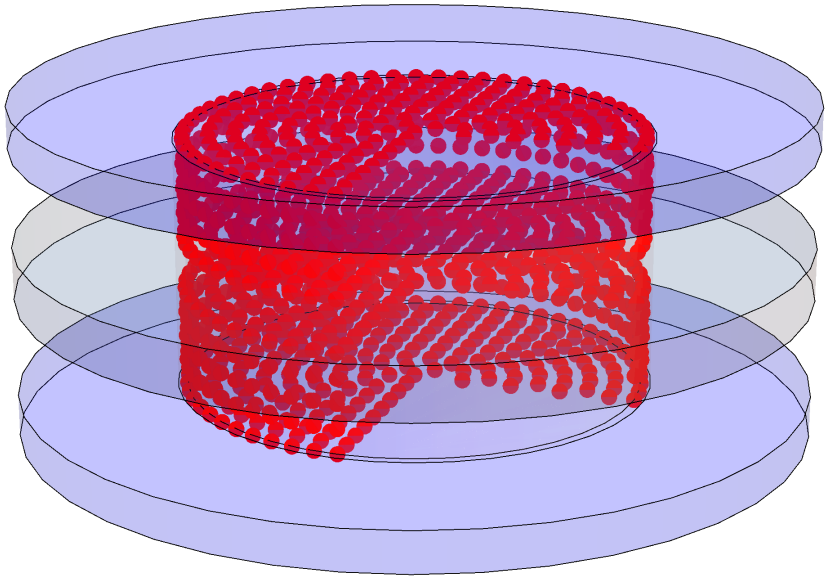

Figure 2.9.: Grid for the numerical treatment of the potential positions for local dipoles on the interior surface of the UCN storage chambers. For illustration reasons one quarter of the points is not displayed.

ratio of points S_C with $s_2 > s_{\mathrm{crit}} = 10^{-3}$ is the figure of merit for the optimization, henceforth called "detectability ratio":

$$S_C = \frac{\sum\limits_{\mathbf{r}_{\mathrm{dip}}} \Theta(s_2(\mathbf{r}_{\mathrm{dip}}) - s_{2,\mathrm{crit}})}{\sum\limits_{\mathbf{r}_{\mathrm{dip}}} 1}\,, \tag{2.19}$$

with $\Theta(x)$ the Heaviside function.

As the parameter space is too large to perform an analytical optimization, a Monte Carlo simulation method is used here. The first step of the optimization algorithm is to randomly chose N_{sen} positions of the sensor grid and calculate S_C. In the next step, one randomly chosen position is replaced by a new one, with the condition that it is not already a part of the ensemble. Again S_C is determined and compared to the previous value. If S_C increases, which means that now a larger area is sensitive for dipole detection, the new position is kept. Otherwise the previous position is chosen.

Using this method, the detectability steadily improves and usually converges to a specific value. As it is not possible to estimate at which value the convergence takes place, the iteration is not stopped after reaching a specific limit, but rather ends after a fixed number of iterations N_{max}.

The downside of this kind of optimization is that it can end in a local minimum and therefore gives false results. This issue is handled by running the optimization

multiple times, each with completely new starting positions. If the majority of the results converge to the same value, it is very likely that a solution is found that is close to the optimum.

For all scenarios N_{sen} is varied and the optimization algorithm reruns multiple times and the results are analyzed.

2.4.1. Cryogenic EDM chambers

For the case of the cryogenic EDM chambers the individual steps of the optimization algorithm will be described. For the other two scenarios and their various sensor grids based on the different underlying symmetries, only the results will be shown.

Before applying the optimization on the cryogenic scenario, the parameter space can further be reduced. As the relative signal strength s_2 strongly decreases with rising distance between the sensor and dipole position, all positions that have a next neighbor between them and the dipole positions are neglected. In other words, only the innermost shell of the cylindrically arranged sensor grid is used for the optimization.

After applying both cuts (innermost shell and $r < 60\,\text{cm}$), the number of positions reduces from around 15000 to 400. Assuming 5 independent sensor positions have to be chosen, already $\gg 10^{11}$ different combination are possible, and the number of combinations rises very quickly with each additional sensor position. Looking at the large number of combinations, it becomes clear that reducing the relevant sensor positions and the corresponding parameter space is very important. The Monte Carlo simulation-like approach would in fact also work for the larger parameter space, however it would need much more time to calculate a result.

In order to get a scale on how fast the optimization speed is – or more importantly how many iterations steps are needed – the evolution of the detectability ratio for 30 sensors is shown in figure 2.10 – for an ensemble of 20 positions. The optimization is based on around 300 starting position sets, but for illustrative purposes only 20 randomly chosen ones are shown. They start at some arbitrary value of S_C, but all converge at around 47.5% after > 150 iterations. The RMS-spread of the different runs is only $\pm 0.5\%$. This is a clear indication that the extracted solutions are very close to optimal solution.

By changing N_{sen} the solutions converge to another final S_C, but the spread of the final S_C remains comparable to the spread shown in figure 2.10. Figure 2.11 shows S_C as a function of N_{sen}. With the fewest number of sensors only $< 10\%$ of surface can be monitored for dipoles. With an increasing number of sensors S_C rises also (here up to around $(67.4 \pm 0.6)\%$). The least possible amount of sensors is 2, due to the mirror symmetry, and the largest is set arbitrarily to 50. It is likely that S_C would continue to improve with additional sensors, but a 4π magnetometer with 50 sensors might already be beyond what is practically and economically feasible.

For $N_{\text{sen}} = 50$ the optimal configuration S_C is shown as a function of the position on the EDM chamber surfaces in figure 2.12. The plot is divided into six parts, each corresponding to one of the six surfaces of the EDM chambers.

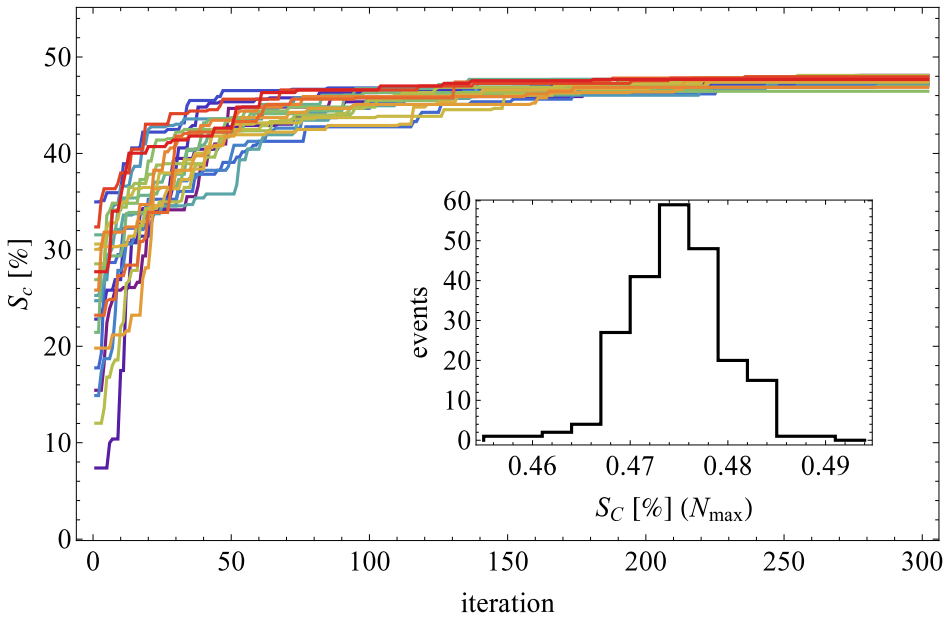

Figure 2.10.: Optimization progress of the Monte Carlo algorithm: 20 randomly chosen runs of the cryogenic EDM chambers scenario are displayed. In all runs S_C (equation 2.19) converges after around 150 iteration steps at around 47.5%. Runs with another amount of sensors N_{sen} converge to a different final S_C, but the spread of the results is comparable to the shown example.

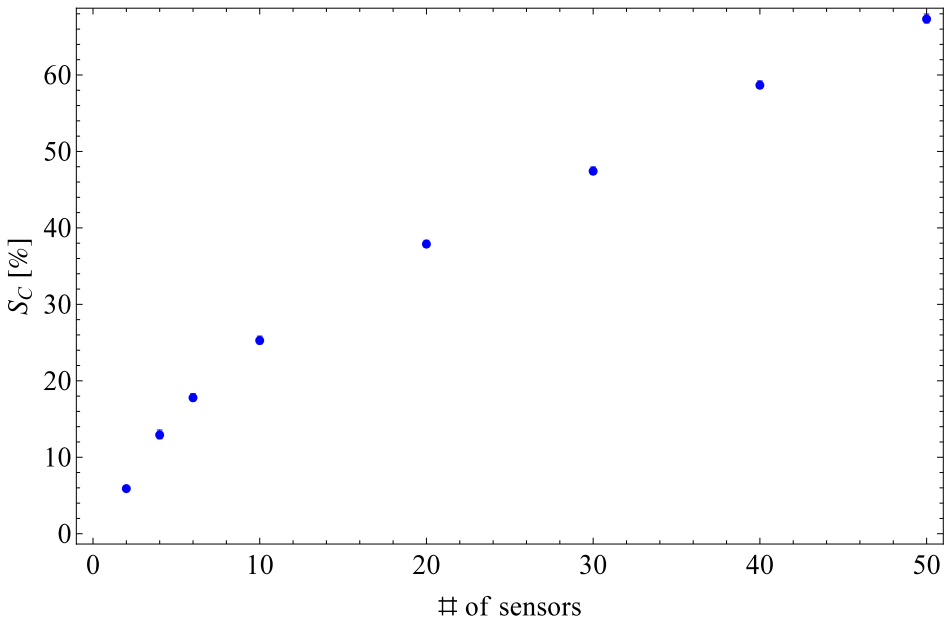

Figure 2.11.: Dipole detectability ratio as a function of the number of applied sensors. Error bars derived from the RMS-spread of final solutions at each particular number of sensors are shown, but are generally smaller than the point size.

It is clearly visible that dipoles on the upper and lower ground electrode surfaces may be detected more easily than on other surfaces. This result is expected, as here the sensors are closer to the position of potential dipoles. The detectability ratio is 94%. The other 4 surfaces are closer to the center and therefore have only a detectability ratio of 69% for the insulator rings and 44% for the HV electrode. The symmetry between the upper and lower halves is caused by the applied mirror symmetry.

There is also a line of minimal values along the y-axis ($\Phi = \pm\pi$), which can be attributed to the convolution of the cylindrical symmetries of the sensor arrangement and the EDM chamber geometry, tilted by 90° with respect to each other. The minimum of s_2 is in the center of the HV electrode and has a value of $6 \cdot 10^{-4}$.

Other good sensor configurations exist which have a better detectability ratio for the HV electrodes, but which demonstrate a worse S_C overall. Though S_C of the HV electrode surface is increased for these configurations, the dipoles on the HV electrode surface are still the most difficult to detect compared to the other surfaces.

It is important to note that the cryogenic scenario is just a future or alternative version of the nEDM experiment, without any fixed experimental dimensions. Therefore the optimization could be fine-tuned to the actual geometry, as soon as there were to be an implementation of this scenario. It is also possible to modify the optimization procedure to prioritize some surfaces. This may be done, for example, by introducing a weighting factor in the calculation of S_C.

2.4.2. Room temperature EDM chambers

In the room temperature EDM chambers scenario three different sensors grids are compared. As a quick reminder, these grids are based on Cartesian, spherical and cylindrical orientations. From the beginning it is impossible to tell which one is more suitable to be used as the starting point of the optimization. Even though the cylindrical grid more closely resembles the geometry of the vacuum chamber, the radial distribution (blue lines in figure 2.5) features a higher number of positions in comparison to the spherical grid, which are closer to the dipole positions.

This closer vicinity directly translates into an improved detectability, as shown in figure 2.13. The spherical scenario has a slightly higher detectability than the cylindrical for 30 and 40 sensors, but the Cartesian scenario differs strongly for $N_{\text{sen}} > 30$. Applying 50 sensors yields a detectability of ∼50% for the Cartesian scenario and almost 60% for the other two scenarios.

Especially for $N_{\text{sen}} \geq 20$, the spread of the results becomes significant (shown in the plot by the error bars). This is a clear sign that the optimization process should have run longer, or that the maximal iteration steps should be increased. However, the results are close to the point of convergence and therefore do not strongly affect the conclusions made in comparison to the other scenarios.

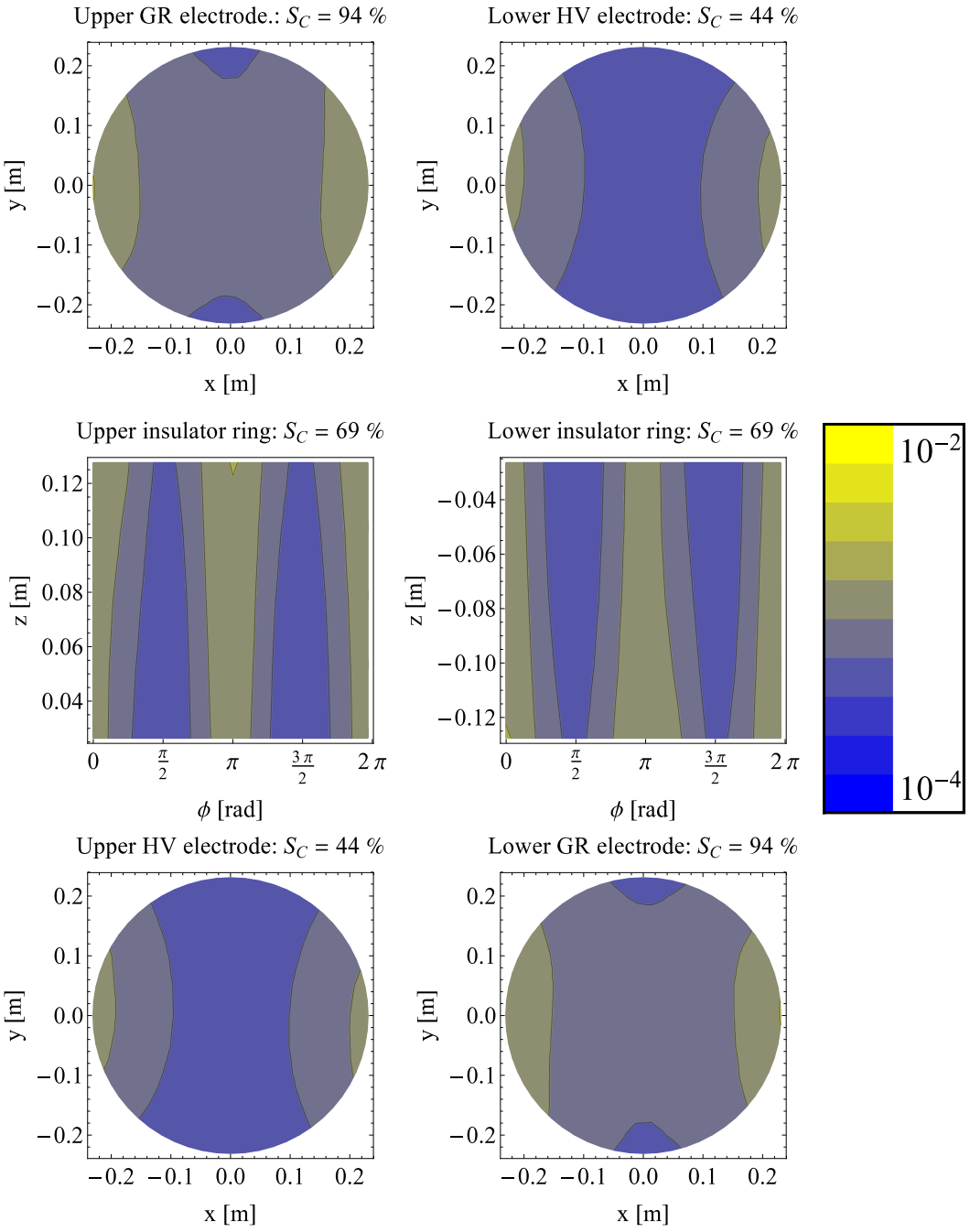

Figure 2.12.: Surface map of the relative dipole strength for the cryogenic EDM chambers scenario with 50 sensors. Dipoles on the ground electrodes can be detected with a probability of 94%. The detectability ratio S_C shows along the y axis (x=0 cm) a minimum which is explained by the two underling cylindrical symmetries (oriented to the y direction (sensor grid) and to the z direction (UCN grid)).

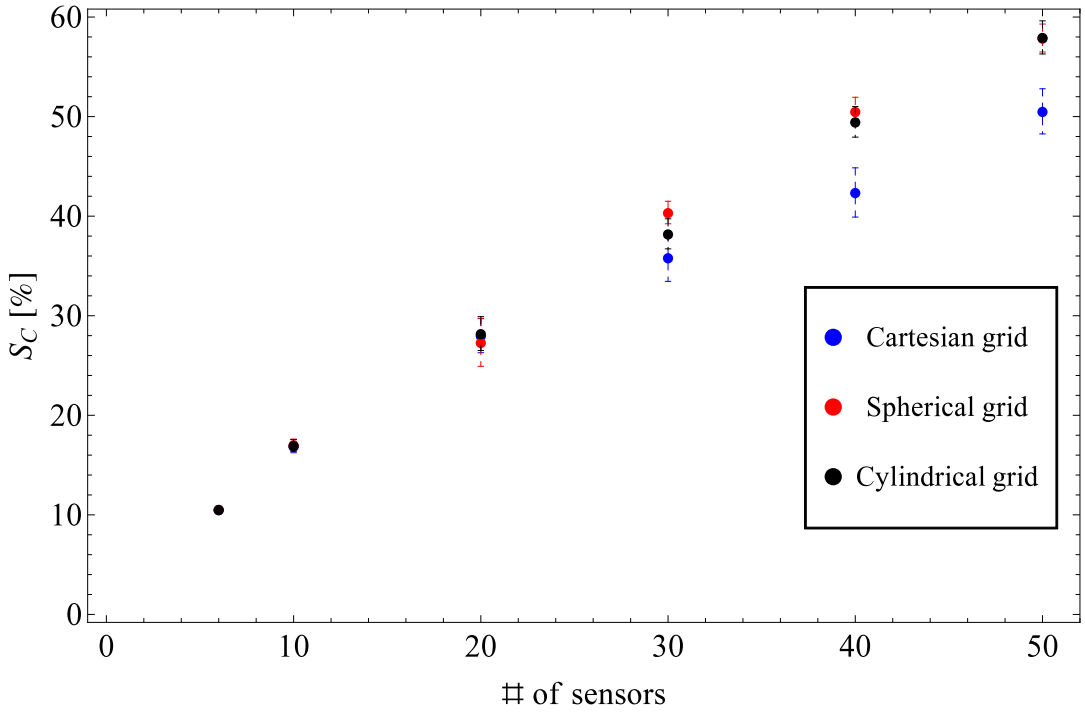

Figure 2.13.: Dipole detectability as a function of the amount of sensors for the Cartesian, the spherical and the cylindrical scenarios of the room temperature EDM chambers setup. The error bars indicate the spread of the optimization results. The spherical and cylindrical grids show with nearly 60% detectability, an almost 10% better detectability than the Cartesian grid.

2.4.3. Minimal vacuum configuration

The minimal vacuum configuration setup not only has the advantage of closer sensor positions, but also has the possibility to operate sensors inside the HV electrode (HV sensors). Just by using the four HV sensors, a full detectability ($S_C = 1$) is achieved. As a reminder, S_C is the detectability ratio of dipoles on surfaces inside the UCN storage chamber (insulator rings, HV and ground electrodes). The relative signal strength has a minimum of $s_2 = 2 \cdot 10^{-3}$. Without increasing the critical signal strength s_{crit}, the optimization would stop directly after it started. Consequently the sensor positions would not be optimized. Therefore s_{crit} is increased to 10^{-2} for the minimal vacuum configuration scenario.

As this new threshold is chosen arbitrarily, the results will only be used as an intermediate step. For comparison, the detectability maps will be shown with the previous threshold of 10^{-3} (see sections 2.4.1 and 2.4.2). The detectability with the new threshold is denoted by S_C^*.

Figure 2.14 shows the modified detectability for three sensor grids as a function of the amount of sensors. The monotonic rise of S_C^* with the number of sensors behaves similar to the room temperature EDM chambers setup. The absolute values are here not of interest, as S_C^* is just an arbitrary value. Hence only the three sensors grids can be compared. The first four sensors are the sensors inside the HV electrode and therefore the grids are identical for $N_{\text{sen}} = 4$. The Cartesian grid has the highest detectability compared to the other two.

The superior performance of the sensor configurations following the Cartesian grid is explained by the radial distance distribution of the positions (see figure 2.5). On average, it has a higher position density compared to the other two scenarios for $r < 0.4$ m.

Compared to the room temperature EDM chambers and the cryogenic EDM chambers experiments, the minimal vacuum configuration setup has an order of magnitude higher detectability. Figure 2.15 shows the best sensor configuration that the optimization process determined. The detectability has a minimum of $3 \cdot 10^{-3}$ at the middle of the ground electrode and a maximum of 0.48 directly above the HV sensor positions.

Next to the sensors inside the HV electrode, only the positions between the HV and the ground electrode – or near to the insulator rings – are found to be the best choice. Positions above the Hg magnetometers are too far away to have a valuable contribution to the detectability. This result therefore allows an undisturbed operation of the Hg magnetometers next to the Cs magnetometers. In addition, the Hg magnetometers can contribute to the performance of the 4π magnetometer.

2.5. Dipole tracking algorithm

The next step is to test if this sensor configuration is actually able to detect the position of a dipole. In other words, is there a correlation between the detectability s_2 that is based on the distance of potential dipoles and the detectability of real dipoles?

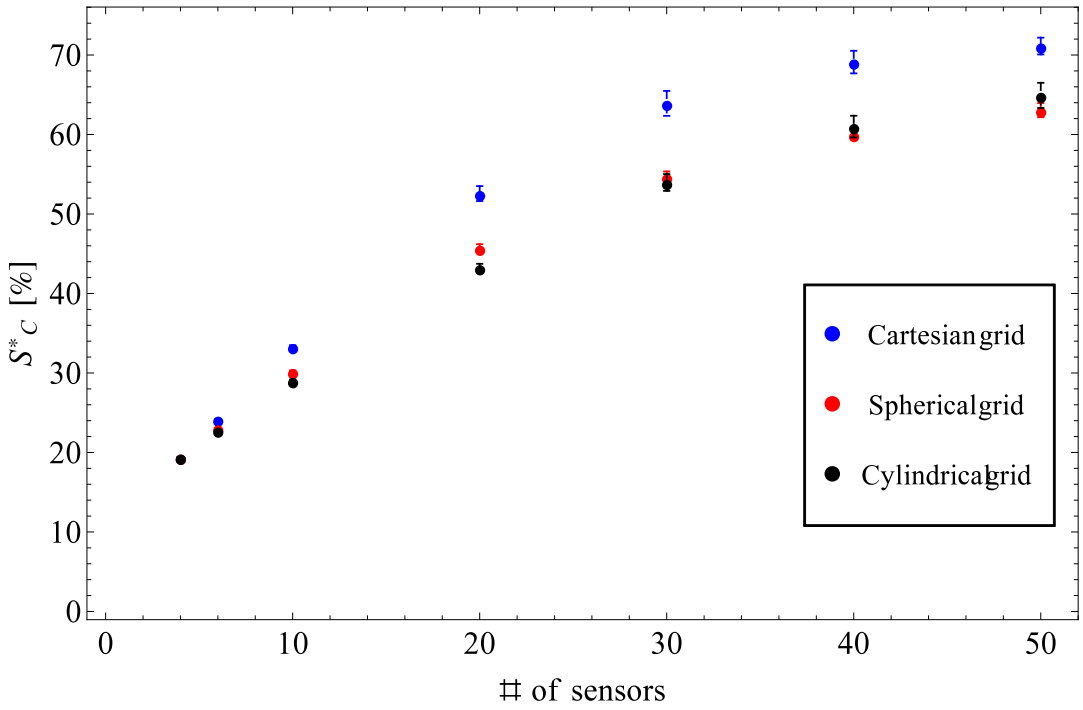

Figure 2.14.: Modified dipole detectability as a function of the amount of sensors for the minimal vacuum configuration setup. The notations and means of representation are equivalent to figure 2.13.

Therefore the best sensor configuration is taken and dipoles are randomly placed at one of the surfaces. The random selection is based on a uniform distribution.

A dipole is described by six parameters (position $\mathbf{r}_{\mathrm{d,gen}}$ and moment $\boldsymbol{\mu}_{\mathrm{gen}}$). In contrast to the gradients, these parameters do not enter linearly, and making an analytical solution almost impossible.

In order to locate potential dipoles a semi-numerical approach is used. First of all, the six parameters of an arbitrary dipole are reduced to five, as they are constrained to the inner surfaces of the storage chambers. The positions are discretized by the equidistant grid (introduced previously). The downside of this simplification is that the spatial dipole location resolution is limited by the grid: the best resolution is given by the minimal distance between two points on the grid.

For each of these points an artificial dipole is modeled ($\mathbf{r}_{d,\mathrm{art}}$, $\boldsymbol{\mu}_{\mathrm{art}}$) and three remaining parameters ($\boldsymbol{\mu}_{\mathrm{art}}$) are numerically determined by minimizing the difference between field of the artificial and initially generated dipole:

$$\Delta B = \frac{1}{B_{\mathrm{norm}}} \sqrt{\sum_{i=1}^{N'_{\mathrm{sen}}} |\mathbf{B}_i(\mathbf{r}_{\mathrm{d,art}}, \boldsymbol{\mu}_{\mathrm{art}}) - (\mathbf{B}_i(\mathbf{r}_{\mathrm{d,gen}}, \boldsymbol{\mu}_{\mathrm{gen}}) + \mathbf{B}_{i,n})|^2}\,, \tag{2.20}$$

with a Gaussian distributed noise field $\mathbf{B}_{i,n}$ for each magnetometer and the norm of

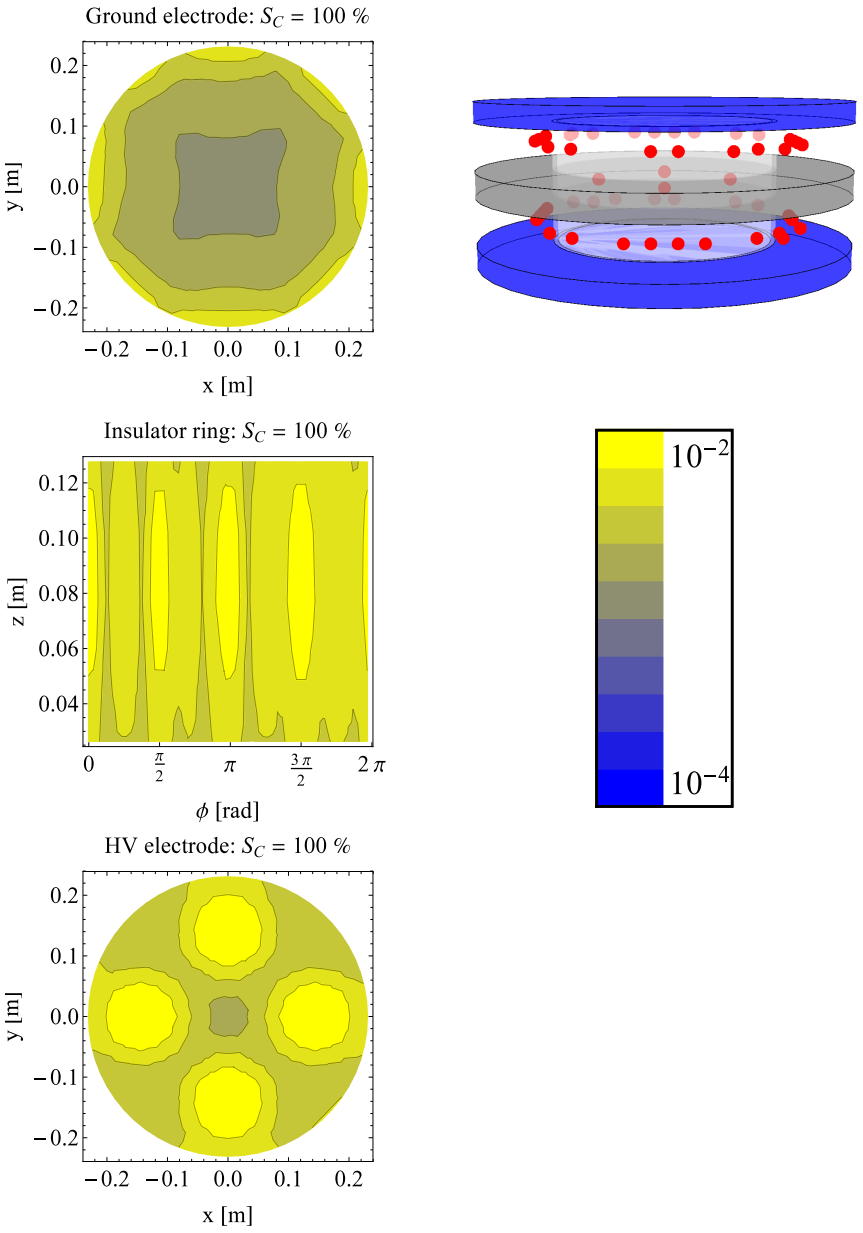

Figure 2.15.: Dipole detectability map for the best sensor configuration of the minimal vacuum configuration scenario with 50 sensors. The notation is equivalent to figure 2.12. Due to symmetry reasons only the upper surfaces are shown. The presented sensor array achieves a homogeneous detectability distribution on all surfaces. With the assumption that the threshold $s_{2,\mathrm{crit}}$ is sufficient, dipoles an all surfaces can be detected. In the right top corner is an illustration of the sensor positions (red dots) around the EDM chamber. They follow an almost cylindrical distribution which implies that the cylindrical sensor grid was not chosen perfectly.

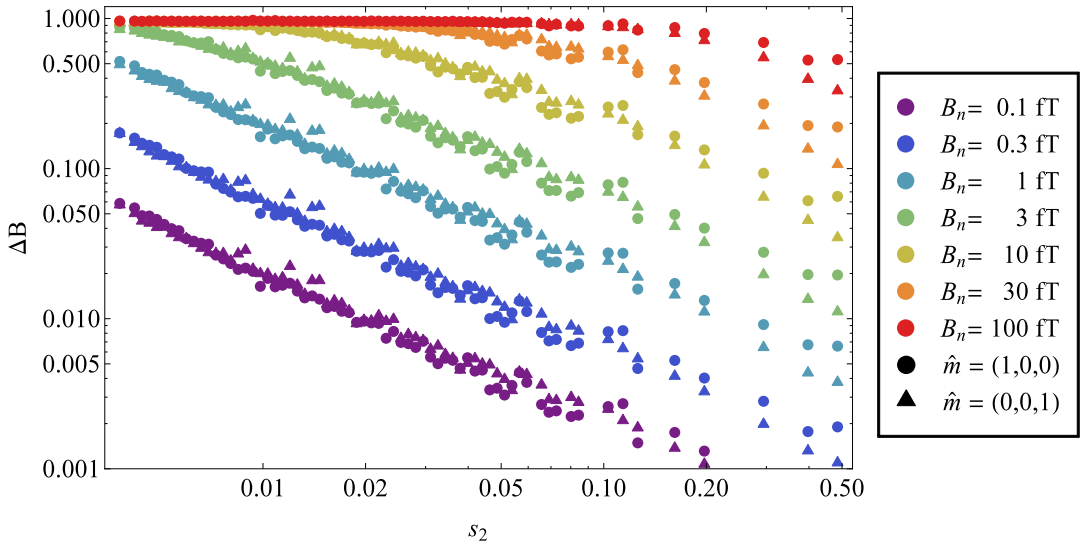

Figure 2.16.: Combined difference field as a function of s_2 for the minimal vacuum configuration (see e.g. figure 2.15) for different sensor noise levels B_n: with increasing s_2, the field of the extracted dipole matches more and more to that of the preset dipole. The normalized difference between the measured and the reconstructed field ΔB (see equation 2.20) shows a linear proportionality to the sensor noise. In addition, there is no significant difference for axially (triangle) and transversely (disk) aligned dipoles. Each point represents the average value of an ensemble of positions with similar s_2.

the generated field

$$B_{\text{norm}} = \sqrt{\sum_{i=1}^{N'_{\text{sen}}} |\mathbf{B}_i(\mathbf{r}_{\text{d,gen}}, \boldsymbol{\mu}_{\text{gen}}) + \mathbf{B}_{i,n}|^2}\,. \tag{2.21}$$

Here only the N'_{sen} sensors are used that measure a field change excessing the noise level.

The extracted values for the magnetic moment $\boldsymbol{\mu}_{\text{art}}$ are then used to calculate the field difference of all sensors. The one $\boldsymbol{\mu}_{\text{art}}$ resulting in the lowest difference field is accepted as the result of the optimization.

In the minimal vacuum configuration ($N_{\text{sen}} = 50$, Cartesian grid) the outcome of the optimization is illustrated and the correlation to the relative signal strength s_2 is drawn (see figure 2.16). As expected, reduced noise and increased s_2 yield a better match of the preset dipole field and the one extracted from the optimization.

Bad field reconstruction is achieved if ΔB is very close to 1. In order to get a criterion for a successful dipole localization, the correlation between the found dipole parameters and the optimization results has to be drawn.

As the position of the dipoles are restricted by the localization algorithm, they are considered as second-order parameters. Therefore the magnetic moment $\boldsymbol{\mu}$ will

be used primarily to define a metric for a successful localization event. In figure 2.17 the results for $\boldsymbol{\mu}$ are shown. To express the dipole reconstruction quality the auxiliary quantities

$$\Delta m = \frac{|\boldsymbol{\mu}_{\mathrm{art}} - \boldsymbol{\mu}_{\mathrm{gen}}|}{|\boldsymbol{\mu}_{\mathrm{gen}}|} \tag{2.22}$$

and

$$\Delta \mathbf{r} = |\mathbf{r}_{\mathrm{d,gen}} - \mathbf{r}_{\mathrm{d,art}}| \tag{2.23}$$

are introduced. A good dipole reconstruction is achieved when Δm and $\mathbf{r}$ are small ($\Delta m = 0$ and $\Delta \mathbf{r} = (0,\ 0,\ 0)$ cm would be a perfect reconstruction). While $\Delta \mathbf{r}$ is limited to the size of the UCN storage chamber, Δm can reach values beyond 1. For example, if the sensor noise is much higher than the field of the dipole, the best of the solutions for $\boldsymbol{\mu}_{\mathrm{art}}$ may yield a field that only matches well for the sensor that determined $\boldsymbol{\mu}_{\mathrm{art}}$. The field of the found solution may be able reproduce the noise dominated field by overestimated dipole strength and hence it is as if the noise of the one sensor is transferred to the other, resulting in an increased field difference at these magnetometers. Consequently Δm can be larger than 1, indicating a very poor dipole reconstruction.

For almost all noise levels and Δm <1% (good dipole reconstruction) ΔB is direct proportional to Δm. Focusing on the previously assumed sensor noise of 10 fT (yellow points) and fixing the criterion of a successful reconstruction to $\Delta m = 0.2$, the critical $\Delta B = \Delta B_{\mathrm{crit}}$ can be approximated to 0.7. As the $\Delta m = 0.2$ criterion is arbitrarily set and has no uncertainty, it is unreasonable to specify an uncertainty for ΔB_{crit}. The majority of the events (except one) match to this confinement and therefore the further calculations will be based on $\Delta B = 0.7$ for 10 fT noise case.

With this result the secondary parameters now can be used to check the validity of the previous argument. Figure 2.18a shows an enlarged part of figure 2.16. By setting the requirement that the majority of the events has to fulfill $\Delta B < \Delta B_{\mathrm{crit}}$, the critical value for s_2 is set to $s_{2,\mathrm{crit}} = 0.024$ (again shown on the example of the 10 fT noise case). The right part of the figure illustrates the correlation between s_2 and the dipole position reconstruction quality Δr. A relative field strength of $s_2 < s_{2,\mathrm{crit}}$ corresponds to a position reconstruction quality of 2.5 cm (denoted in figure 2.18b).

Both Δm and Δr prove that s_2 is a good quantity to study the detectability of dipoles with the use of a 4π magnetometer. But it turns out that the previous assumption of the critical value for $s_{2,\mathrm{crit}} = 10^{-3} = \frac{10\,\mathrm{fT}}{10\,\mathrm{pT}}$ is too naive and should in fact be increased by about a factor of 20. Nevertheless the minimal vacuum configuration setup enables sensors placed close enough to the center to still yield a sufficient dipole detectability.

Reducing the noise by a factor of three would already improve the situation significantly. The 10 fT sensitivity limit is based on a 5 minute long measurement. Temporal drifts do not strongly disturb the measurement, as homogeneous fields affect all magnetometers equally and gradient fields can be corrected with magnetometers that have an larger distance to the EDM chamber. Hence the field can be

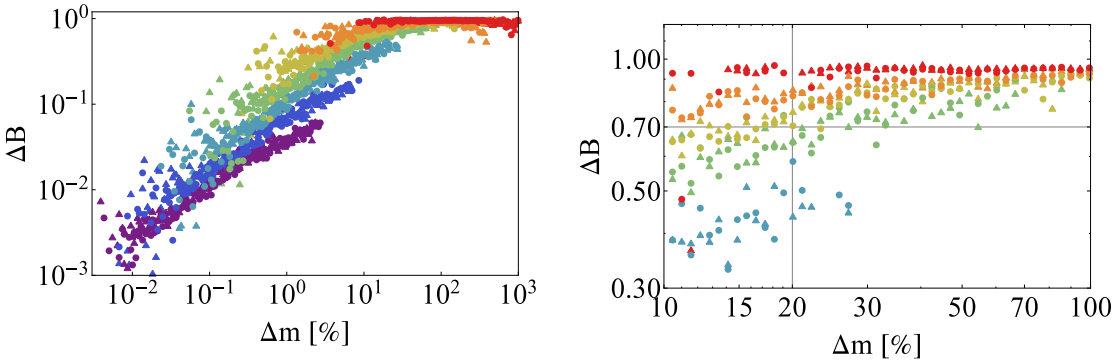

(a) full range (b) zoom

Figure 2.17.: Correlation between the field reconstruction and the dipole moment reconstruction. The almost linear correlation of Δm (equation 2.22) and ΔB (equation 2.20) indicates that ΔB can be used as a measure for the dipole reconstruction quality (a). Setting the threshold to $\Delta B = 0.7$, all simulations results for $B_n = 10$ fT show Δm <20%, which is here defined to be the threshold for a successful dipole reconstruction (b). The color and symbol code is equivalent to that used in figure 2.16. See text for more information.

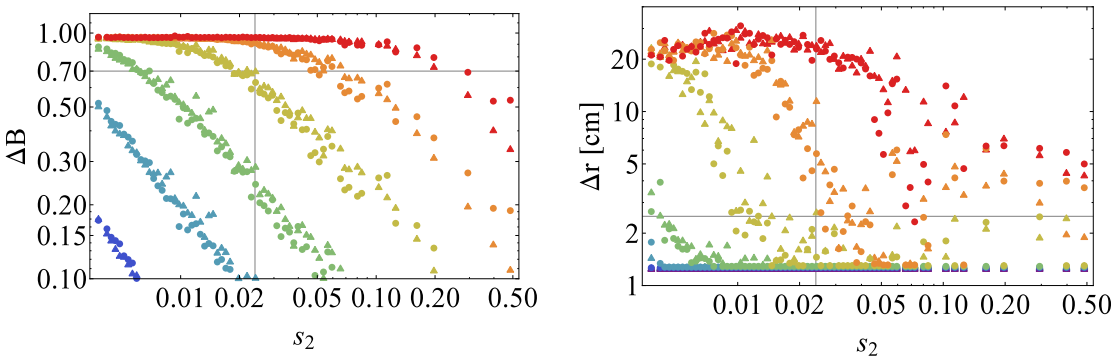

(a) (b)

Figure 2.18.: s_2 threshold determination: The requirement of $\Delta B < 0.7$ sets a critical value for s_2, which is dependent on the magnetometer sensitivity B_n (a). In (b) the resulting position reconstruction accuracy is shown. For B_n =10 fT follows $s_{2,\mathrm{crit}} = 0.024$ and $\Delta r = 2.5$ cm. This means that with the defined thresholds, magnetometer arrays can be determined that are able to detect dipoles within 2.5 cm. The color and symbol code is equivalent as figure 2.16.

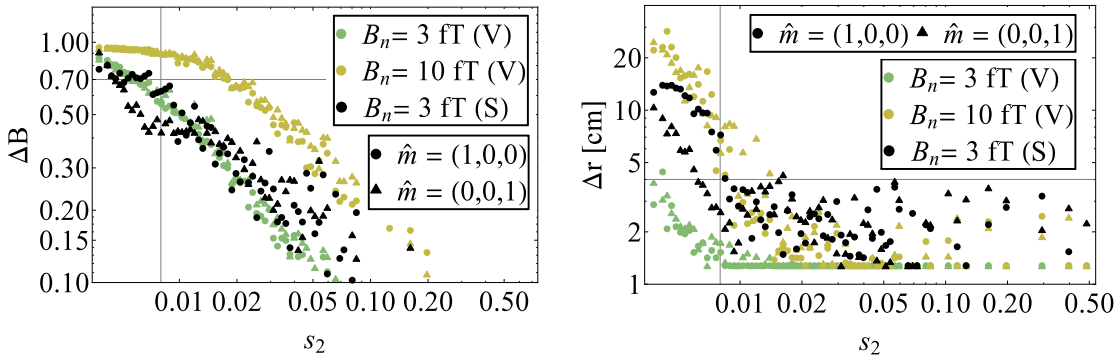

(a) field reconstruction (b) position reconstruction

Figure 2.19.: Usability of scalar (S) and vector (V) magnetometers for the dipole reconstruction. The field difference ΔB (equation 2.20) of an array using scalar magnetometers (black) is comparable to an array with vector magnetometers (green) for an equivalent noise level B_n (a). However, the position reconstruction quality $\Delta\mathbf{r}$ (equation 2.23) of a purely scalar magnetometer based array is worse (∼4 cm) than the vector magnetometer array (∼1.8 cm) for dipoles that are aligned along the z-axis (disk, longitudinal). However, dipoles with a transverse (triangle) alignment are detected more accurately (∼3 cm).

averaged in ∼1 hour, yielding ∼10 field measurements. This improves the sensitivity from 10 fT to 3 fT, yielding $s_{2,crit} \approx 0.008$. Up to this point only the usability of vector magnetometers has been studied. However, since their construction and operation is more difficult than that of scalar magnetometers, a 4π magnetometer is more likely to be implemented using scalar magnetometers. To provide an appropriate metric for scalar magnetometers, equation 2.20 is modified from the absolute value of the magnetic field to just its absolute component. As this also reduces the content of information, two additional magnetometers are included in the calculation. The three magnetometers that measure the highest field excess form three equations with three unknowns (the components of $\boldsymbol{\mu}$). Due to quadratic terms of $\boldsymbol{\mu}_i$ in the semi-analytic expression of the dipole field, now 8 solutions for $\boldsymbol{\mu}$ are extracted, instead of 1 in the vector magnetometer case. All real results are used for the subsequent calculations, which are equivalent to the previous case.

Figure 2.19a shows that the field reconstruction quality of a scalar mode based 4π magnetometer is comparable to a vector mode based one with the same sensitivity level. The difference between both modes can be seen by taking a look at the dipole position reconstruction quality (figure 2.19b). Dipoles aligned along the z-axis show a much higher reconstruction quality than the transversely aligned dipoles. Compared to the vector mode operated magnetometer the detectability is reduced, but for the $s_{2,\mathrm{crit}} > 0.008$ level a position sensitivity of 4 cm is feasible.

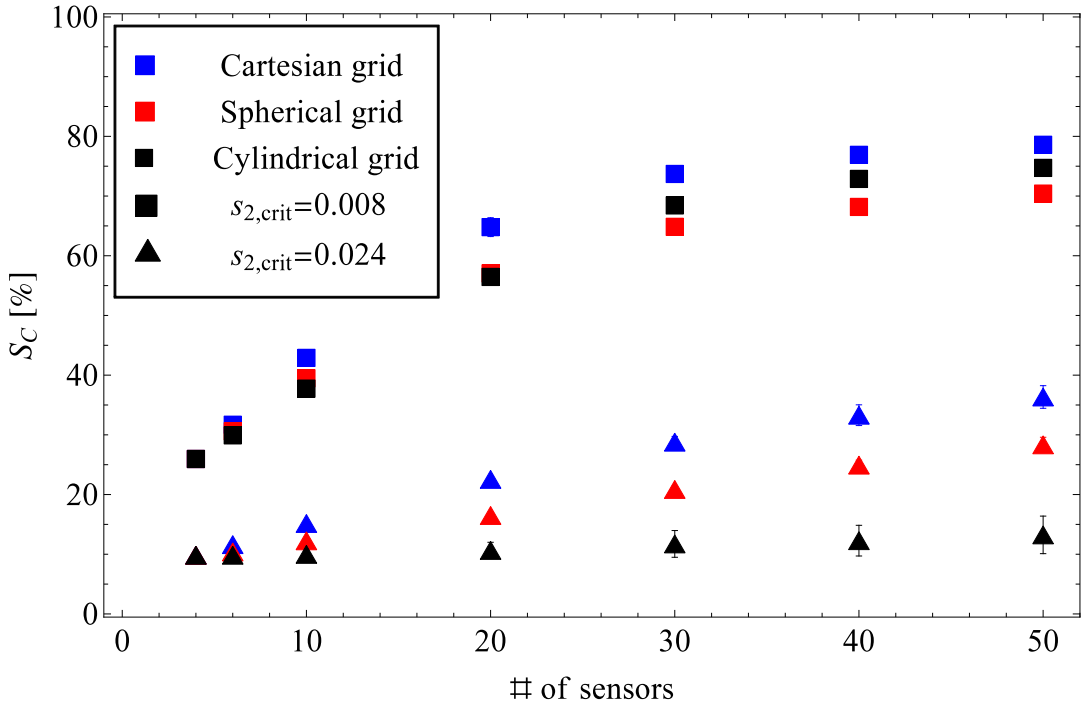

Figure 2.20.: Results of the Monte Carlo-optimization for $s_{2,\mathrm{crit}} = 0.008$ and $s_{2,\mathrm{crit}} = 0.024$. The detectability ratio S_C (equation 2.19) is shown as a function of the number of applied magnetometers. By averaging over longer times, the effective magnetometer sensitivity can be increased, resulting in an improvement of S_C from ∼35% to ∼80%. The relative difference between the grids is equivalent to the previous results (see figure 2.14).

2.6. Feasibility study of the 4π magnetometer

All information (especially the new $s_{2,\mathrm{crit}}$) can now be applied to the calculation of the minimal vacuum configuration setup, in order to get a preliminary result (see figure 2.20). As before, the sensor grid based on the Cartesian distribution yields the highest detectability (79% for $s_{2,\mathrm{crit}} = 0.008$ and 36% for $s_{2,\mathrm{crit}} = 0.024$). The relative difference between the various scenarios is equivalent to the previous result (see figure 2.14), indicating that $s_{2,\mathrm{crit}}$ and N_{sen} can be treated individually.

Up to $N_{\mathrm{sen}} = 20$, S_C increases linearly and afterward saturates at a final value. This behavior is caused by the fact that the surfaces of the HV electrodes and the insulator rings are completely covered, but there are no sensor positions that enable a dipole detection on the ground electrodes. The sensor distribution of the best result shows a symmetric order, with positions closest to the insulator rings. The fact that the cylindrical sensor grid, which was chosen in the beginning, gives worse results shows that it was too general and the sensor positions near the insulator rings are too far away from the insulator rings.

It is, however, intuitive that a cylindrical sensor distribution provides the optimal

result. Similar to the sensor positions inside the HV electrode, the placement of magnetometers inside the ground electrodes may be feasible. As in the HV electrode, 4 sensors are used per electrode and these are placed in a radially symmetric pattern with the same radius as in the HV electrode. The insulator ring sensors are arranged with radial symmetry. The number of sensors is a free parameter.

The ground electrode sensors are not treated individually, but their influence on the detectability S_C is investigated by comparing sensor position ensembles with and without them (see figure 2.21). As long as the total amount of installed sensors is small, there is no large dependence on where the additional sensors are actually placed, e.g. inside the ground electrodes or next to the insulator rings (the solid and dashed lines almost overlap). With a sufficient number of sensors around the insulator, surfaces of the insulator rings are very well covered, and further increasing the number of sensors does not yield an improvement. The surfaces of the ground electrodes can only be efficiently covered by placing sensors in them, as the space above them is occupied by the ^{199}Hg magnetometers.

For the case where the sensors noise is reduced, the detectability reaches 98% when also placing sensors inside the ground electrodes, otherwise only 84% detectability is achievable. If the operation of magnetometers next to the insulator rings is impossible, the detectability drops to 54% (26% if ground electrode are also omitted). The standard noise case obviously has much lower detectability in these situations, respectively 66%, 53%, 21% and 10% for all positions, without the ground electrode positions, without the positions next to the insulator ring and for positions only inside the HV electrode. The preliminary results are also shown in figure 2.21 as a comparison. The deviation for $N_{\text{sen}} > 20$ is explained by the non-optimal coverage of the insulator ring surfaces.

In conclusion, the 4π magnetometer concept has an interesting application for the search for a nEDM, though the construction and operation of such an array may be difficult. Only for experimental setups like the shown minimal vacuum configuration scenario, in which sensors can be placed closely to the critical surfaces, is the concept of the 4π magnetometer feasible. The reduction of the noise level of the deployed sensors should be the preferential task, especially for the scalar magnetometers, given the observation that improved noise has a strong effect on the reconstruction results.

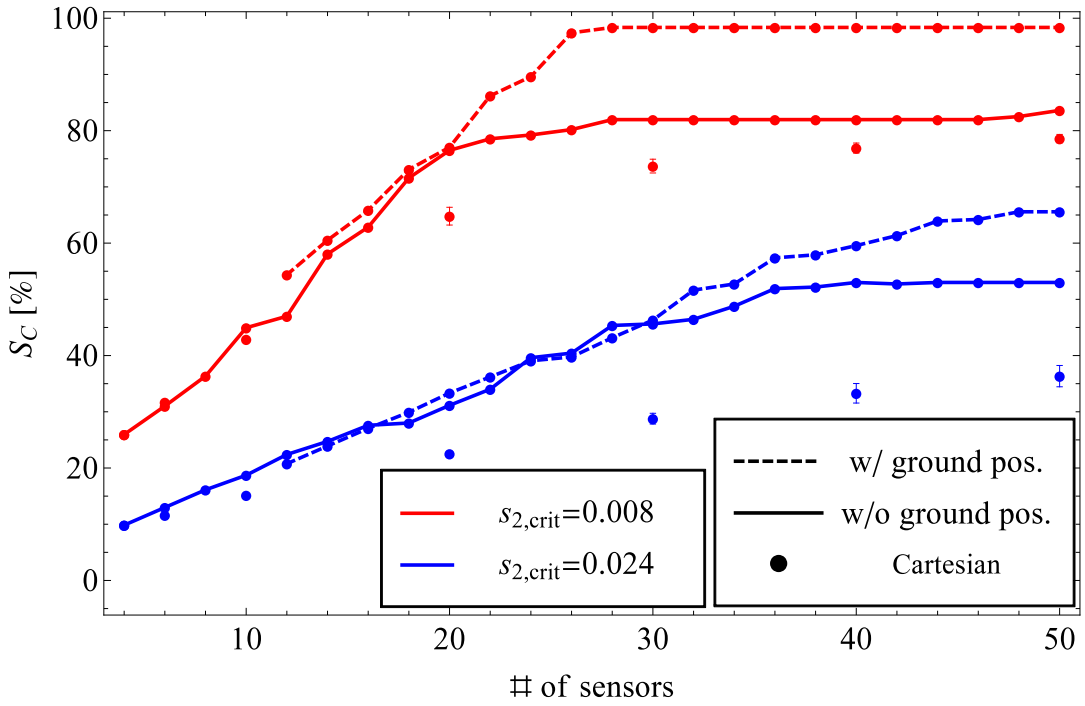

Figure 2.21.: Dipole detectability for sensor ensembles with positions inside the HV and ground electrodes and around the insulator rings, as well as various combinations of them. The behavior for $s_{2,\mathrm{crit}} = 0.008$ and $s_{2,\mathrm{crit}} = 0.024$ are compared. If all positions are allowed and the sensor noise is reduced, a detectability ratio of >99% is achieved for $N_{\mathrm{sen}} > 28$. By restricting the sensor positions to certain areas (e.g. position without the ground electrode), the final S_C is worse. The linear rise of S_C for $N_{\mathrm{sen}} < 20$ ($s_{2,\mathrm{crit}} = 0.008$) is caused by the increasing coverage of the insulator ring surfaces. For comparison, the results for the Cartesian grid (see figure 2.14) are also plotted.

3. Monte Carlo method based optimization of the active field compensation system (ACS)

This chapter deals with a system to compensate for and cancel magnetic fields in real-time for the nEDM experiment was designed, built and characterized. Due to the complexity of this system, the design was mainly driven by simulations and optimization processes. The concept of this "active compensation system" (ACS) is to use a set of coils to produce a magnetic field which counteracts external fields, continuously updating the applied field according to real-time measurements of the magnetic field. These external fields can arise from the magnetic field of the Earth, stray fields from neighboring experiments or the movement of magnetized machinery such as an indoor crane or a car moving next to the experimental hall.

The goal of the ACS is to counteract any external field change. An algorithm is used to automatically adjust the currents of the coils to any new measured field. Here the principles behind the real-time compensation algorithm are summarized, the technical requirements of the system are outlined and the implementation of the optimized system is presented. Finally, the effect on the nEDM experimental setup is presented.

3.1. Principles of external field compensation

The coils of the ACS surround the volume of the nEDM experimental setup and are used to minimize the magnetic field within the volume. All external fields are defined in $\mathbf{B}_{\text{ext}} = (B_{1,x}, B_{1,y}, B_{1,z}, ..., B_{n,z})$, where n is the number of magnetic field sensors and $B_{i,xyz}$ represents the components of the field at the position of the corresponding sensor. The m coils are powered separately by programmable unipolar power supplies. Similarly to $\mathbf{B}_{\text{ext}}$, $\mathbf{I} = (I_1, I_2, I_3, ..., I_m)$ is introduced to summarize the applied currents.

Each coil produces – proportional to the applied current I_j – a field B_i at the sensor i. This linear behavior is expressed in the so-called sensitivity matrix

$$A_{ij} = \left(\frac{\partial B_i}{\partial I_j}\right)_{ij} . \tag{3.1}$$

The superposition of the external field and the field of the coils $\mathbf{B} = A\mathbf{I} + \mathbf{B}_{\text{ext}}$ has to be minimized. This is done analogously to the least squares procedure. For

this purpose the derivative of the quadratic sum of $S = \sum_{i=1}^{n} (B_i)^2$ with respect to the each current I_j is built. This results in j equations:

$$\frac{\partial S}{\partial I_j} = 2 \sum_{i=1}^{n} A_{ij} \left(B_{i,\text{ext}} + \sum_{k=1}^{m} A_{ik} I_k \right) \stackrel{!}{=} 0 \tag{3.2}$$

or

$$\sum_{i=1}^{n} \sum_{k=1}^{m} {A^T}_{ji} A_{ik} I_k = - \sum_{i=1}^{n} {A^T}_{ji} B_{i,\text{ext}} \,. \tag{3.3}$$

Expressed in the matrix formalism, it follows $A^T A \mathbf{I} = -A^T \mathbf{B}_{\text{ext}}$ and the solution for the optimal current

$$\mathbf{I} = -(A^T A)^{-1} A^T \mathbf{B}_{\text{ext}} = F \mathbf{B}_{\text{ext}} \,, \tag{3.4}$$

with the so-called feedback matrix F. The matrix multiplication of the field $\mathbf{B}_{\text{ext}}$ with F yields the optimal current set $\mathbf{I}$ which has to be applied to the coils, resulting in the minimization of the magnetic field at the position of the sensors.

3.2. Design of the ACS

Before the ACS can be designed and optimized for the nEDM experiment, the experimental environment has to be determined and the requirements for the coils and the field sensors will be investigated.

3.2.1. Environment

The nEDM experiment is set up in the Neutron Guide Hall East (East Hall) at the site of the neutron source Heinz Maier-Leibnitz (FRM2) in Garching. Figure 3.1 gives an overview of all currently planned instruments in the East Hall. Before the first components of the nEDM experiment were installed, the concrete of the hall floor was removed and partially rebuilt with non-magnetic rebar. The reason for this modification was to install a 6.05 m × 8.90 m × 1.05 m large pit, called the "EDM hole", without highly magnetized materials in the structure around the nEDM experiment. As regular concrete contains iron rebar, it is magnetizable and acts as a source for stray fields (∼100-200 μT at a distance of ∼1 m), which are detrimental to the nEDM measurement.

The mechanical structure of the ACS encloses the passive shield which sits on a vibration stabilized table. The center of the passive shield is 2.55 m above the floor of the EDM hole (1.50 m above the floor of the hall). It is possible to lift the whole nEDM experiment by 1 m to shift the energy spectrum of the UCNs by 100 neV. In this case the center of the shield is elevated at 3.5 m. In order to have similar conditions for both scenarios, the height of the ACS is set to 6 m, resulting in a 50 cm offset from the center. The length and width are limited by the size of the pit and therefore the maximum size of the ACS is 6.00 m × 8.85 m × 6.00 m.

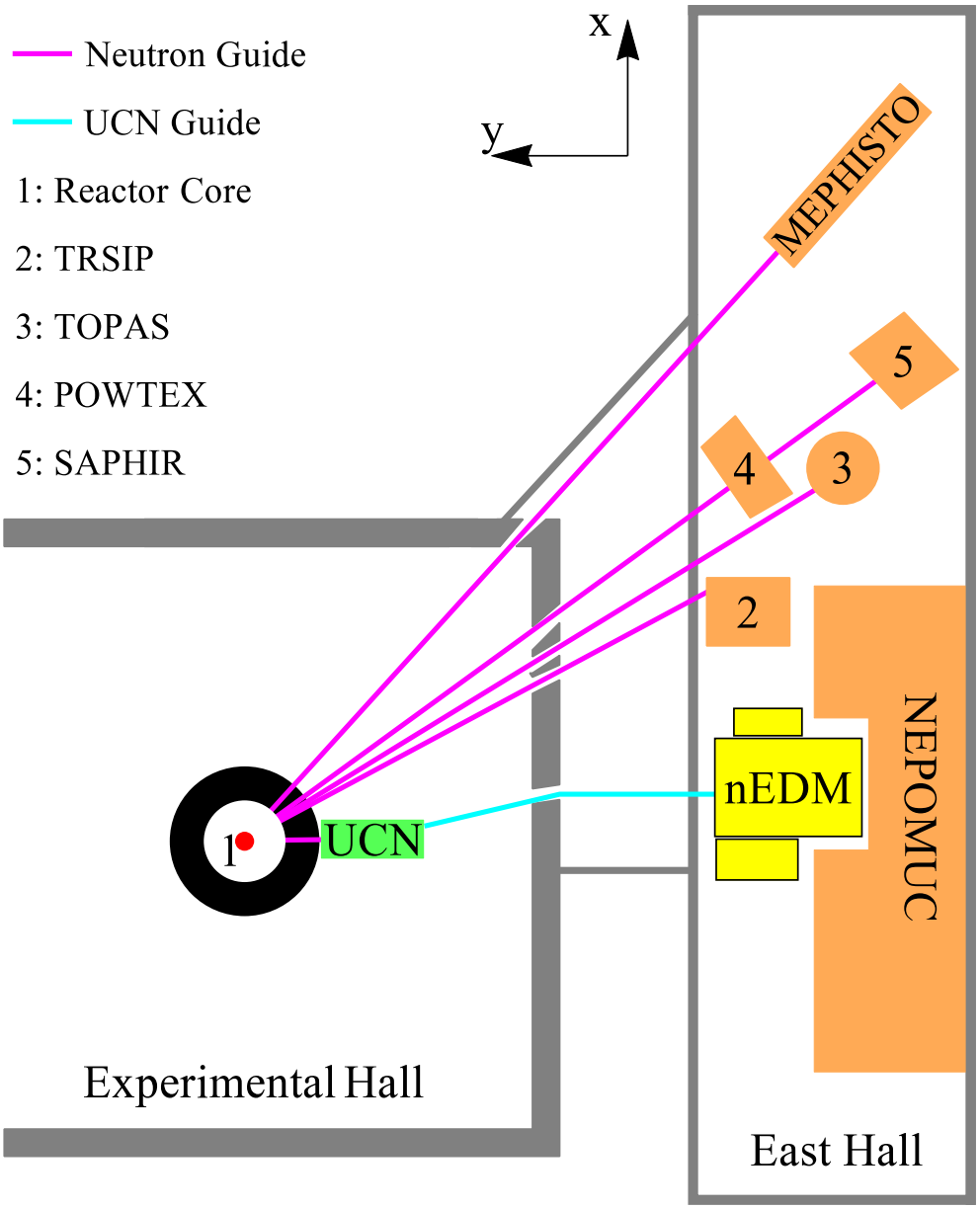

Figure 3.1.: Overview of the Neutron Guide Hall East: The East Hall is shown on the right side and houses the nEDM experiment and multiple other experiments (item 2-5 and NEPOMUC). The PERC experiment (positioned at the MEPHISTO instrument location) is the primary external concern for the ACS. Neutrons produced in the reactor core thermalize in the water surrounding the reactor core and are guided via neutron guides to the experiments. The UCN source converts thermal neutrons to UCNs. UCN guides are used to transport the UCNs to the nEDM experiment.

Stray fields from directly neighboring experiments are expected to be of high order ($m > 2$ in the multipole expansion, see e.g. equation 2.5) and therefore will be small at position of the nEDM experiment. Therefore they are neglected for the moment. The only exception is the PERC experiment positioned 40 m to the north. It consists of a solenoid magnet, which produces a field of 2.5 T in its center and is tilted by 45° relatively to the longitudinal axis of the nEDM experiment. This asymmetry has to be taken into account in the design of the ACS.

3.2.2. Determination of coil parameters

The optimization of the coils and their positions is based on the expected residual fields arising from the Earth's magnetic field $\mathbf{B}_\mathrm{E}$ and the PERC field $\mathbf{B}_\mathrm{PERC}$. Due to the large distance to the PERC experiment and its own magnetic shielding, $\mathbf{B}_\mathrm{E}$ will be the main contributor to the total field $\mathbf{B}$. At the time of the ACS design and construction the PERC magnet was not yet built. For this reason, in the calculation it was approximated as a bar magnet with strength and dimensions corresponding to the PERC design parameters (⌀1 m, 8 m length, 2 T field [85]).

To generate a homogeneous field over an extended volume, the dimensions of the coil pairs have to be larger than the considered volume. Each direction (e.g. x, y and z) was treated separately. If the maximum size is limited, additional coil pairs have to be used, with the downside of increasing complexity and costs. Hence the number of coil pairs per direction is set to three. The field generated in a particular direction is then determined by six positions $\mathbf{r}_j$ (center of the coil) and six currents I_j.

The figure of merit for the optimization is the field homogeneity H in the fiducial volume $V = 4\,\mathrm{m} \times 8\,\mathrm{m} \times 4\,\mathrm{m}$ around the center of the ACS. The volume is chosen to enclose both the passive shield and a region in front of it (see figure 3.2) to account for temporary removal of the inner passive shield. Thus the inner shield never passes through high field regions when it is moved out of the passive shield. The homogeneity H is defined by

$$H = \frac{1}{B_{mean}} \frac{1}{V} \int_V |\mathbf{B}(\mathbf{r}) - \mathbf{B}_\mathrm{mean}| d\mathbf{r} \tag{3.5}$$

with

$$\mathbf{B}_\mathrm{mean} = \frac{1}{V} \int_V |\mathbf{B}(\mathbf{r})| d\mathbf{r}\,. \tag{3.6}$$

Symmetry arguments can be used to reduce the parameter space of the field generation (six positions and six currents). First, there is one pair (for each direction) where both coils are placed at opposing edges of the field cage (see figure 3.2). Second, the position of the inner coils is symmetric to the center of the ACS ($r_{2,3} = -r_{5,4}$). Third, as H is independent of the absolute field value that is directly proportional to the current, the current of the outermost coils ($I_1 = I_6$) is arbitrarily set to 1 A. Last, due to symmetry, the currents of opposing coils have

coil direction	d_1 [m]	d_2 [m]	d_3 [m]	I_1 [A]	I_2 [A]	I_3 [A]	H [%]	$B_{x,y,z}$ [nT]
x,z	3.00	1.20	0.40	1	0.257	0.219	2.4	290
y	4.43	1.80	0.60	1	0.390	0.257	3.0	260
Helmholtz	1.5	-	-	1	-	-	50	240

Table 3.1.: Result of the coil optimization: index 1 represents the outermost coil pair and 3 the innermost.

the same value ($I_{1,2,3} = I_{6,5,4}$). Hence the parameter space reduces from twelve to four for a particular direction. Due to orthogonality of the coils, each direction can be treated separately.

The optimization procedure numerically varies the four parameters (two positions $r_{2,3}$ and two currents $I_{2,3}$) to find the minimum of H, indicating the most homogeneous field. The result of the numerical optimization is shown in table 3.1. For comparison, the homogeneity of a square Helmholtz coil, which would not be suitable for this extended volume, is shown. As an example for the tolerance on the construction accuracy, the position of the x coils are shifted by 10 cm. In that case the optimal currents change and the homogeneity slightly worsens from 2.4% to 2.5%. In order to generate a field on the order of B_E the currents I_j have to be scaled accordingly. For a homogeneous field, the result of the optimization (table 3.1) corresponds to a field reduction of $\sim 33 - 40$. Next to homogeneous fields, higher-order fields can also be generated to a certain degree (see appendix B).

In addition to the homogeneous fields, the gradient fields are crucial. However, the given coil geometry is only able to generate longitudinal gradients $\frac{\partial \mathbf{B}_i}{\partial \mathbf{r}_i}$. As neighboring experiments can produce transverse gradients $\frac{\partial \mathbf{B}_i}{\partial \mathbf{r}_i}$ with $i \neq j$, the coil geometry has to be extended to also account for them. In this case the outermost coils are split into two parts. When operated with the same current, these split coils act as one large coil, as the fields of the wires on the touching sides cancel each other out (see figure 3.2).

In order to produce a magnetic field with a magnitude of $\approx 2B_\mathrm{E}$ in the volume of interest, a maximal current $I_{max} = 300\,\mathrm{A}$ in the outermost coils would be needed. This value can be decreased by increasing the number of loops per coil $N_{\mathrm{coil},i}$. For the design the costs of the components (wires and power supplies) must also be optimized. This optimization is decoupled from the previous optimization. Wires with larger cross section A reduce the resistance R and therefore the total power consumption, but additional loops increase R. The result of this optimization yields $N = 15$ and $A = 6\,\mathrm{mm}^2$ for the outer coils and $N = 10$ and $A = 4\,\mathrm{mm}^2$ for the middle and inner coils . All parameters are shown in detail in appendix A.

Figure 3.3 shows the field cage (the mechanical structure of the ACS) after its construction. The mechanical skeleton is made of aluminum beams. The field cage is covered with PVC panels to isolate the inside from the outside environment. An air conditioning system (a preliminary version is shown in figure 3.3 in the right top corner) is used to stabilize the temperature and humidity inside. A few panels are non-transparent to protect the passive shield from direct sunlight (for details see

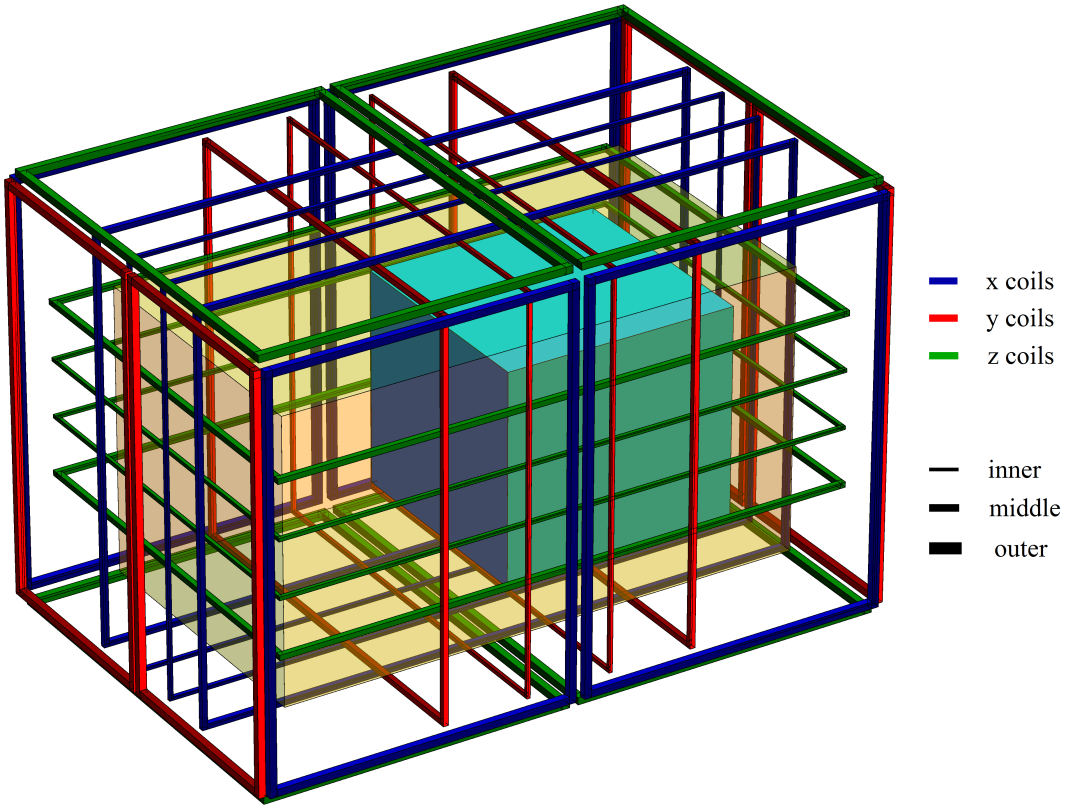

Figure 3.2.: Sketch of the ACS coils: The outer coils are split into two coils for transverse gradient generation. Also shown are the middle and inner coils, the passive shield (cyan) and the fiducial volume (yellow). The thickness of the lines indicates groups of symmetric coils (same current, opposing position). The coils are on the outside surfaces of the field cage.

Figure 3.3.: Photograph of the field cage after its construction: An aluminum structure supports the hull made of PVC panels and the cables of the coils (kept in place with PVC tubes).

appendix C). The wires of the coils are standard 5-wire cables (H07RN-f 5G4 and H07RN-f 5G6) which have been installed in the horizontally and vertically oriented white PVC tubes. In one corner of the coil loop, the wires are connected to switch from a parallel to a serial connection.

Using the now fixed coil geometry it is possible to extend the simulation to specific scenarios. Previously only a uniform field was assumed. Now more complex fields like the approximated PERC field or field deviations arising from the effect of the passive shield can be included. Therefore the previous numerical optimization, which was based on simple analytical functions, is replaced by a Finite Element Method (FEM) simulation, performed with Comsol Multiphysics[1]. The simulations are used to estimate the amount of sensors needed to operate the ACS and the requirements they have to fulfill.

[1]Comsol Multiphysics GmbH, Comsol Multiphysics v.4.0, `https://www.comsol.de/comsol-multiphysics`

3.3. Magnetic field probe and current supply requirements

The passive shield mainly consists of Magnifer®, an alloy with a very high magnetic permeability $\mu > 10^4$. The relative magnetic permeability μ can be interpreted as the conductivity of magnetic flux. Similar to electric current, magnetic flux also takes the path of minimal resistance. Air has μ=1 and is therefore a comparatively poor conductor for magnetic flux. In the presence of a piece of Magnifer® (or similar materials with a high magnetic permeability) the magnetic flux adjacent to its surface decreases. A consequence of this is that a sensor placed near the passive shield would measure an altered field, thus affecting the sensitivity matrix A.

Figure 3.4 illustrates the deformations of the magnetic field in the presence of a structure with a very high magnetic permeability (μ = 25000). Figure 3.5 shows the superposition of the Earth's magnetic field and the estimated field produced by the magnet of the PERC experiment, further referred to as the "combined ambient field". The field maps of all 24 coils and the combined ambient field are the basis for the sensor optimization.

In order to optimize the position of the 3-axis sensors and their quantity N_{Sen}, the volume inside the ACS is modeled by a grid of points with a spacing of 0.2 m. The field maps are used to determine the elements of the sensitivity matrix A_{ij} (i represents the position of the field/sensor and j the coil). Applying practical cuts (e.g. inside the passive shield, walkways, etc.) the number of positions reduces from 40000 to 7000. Assuming a total number of 50 sensors yields a total of $> 10^{127}$ possible sensor position configurations, meaning an analytical optimization is not possible within a reasonable amount of time. Hence the Monte Carlo method which has been introduced in chapter 2 is adapted to fit to this optimization task.

The procedure then follows as:

- A random set of sensor positions $C_{0,0}$ is chosen and the sensitivity matrix A (see equation 3.1) is determined via the field maps. With equation 3.4, the sensitivity matrix is transformed into the feedback matrix. The ambient field map is then used to extract the optimal current configuration $\mathbf{I}$ (equation 3.4). The indexes $(0, 0)$ represent the iteration status of the two level Monte Carlo optimization. The resulting magnetic field can then be calculated by

$$\mathbf{B}_{\mathrm{res}} = A\,\mathbf{I} + \mathbf{B}_{\mathrm{ext}}\,. \tag{3.7}$$

  At the end of this step the norm of this field $B_{0,0}$ is calculated.

- One randomly chosen sensor is removed from its position and moved to a new randomly chosen position, which is not yet occupied by other sensors. Again the norm is determined and compared to the previous one. In the case of a reduction the new sensor set $C_{0,n+1}$ is selected and the old set $C_{0,n}$ is discarded.

- The first two steps are repeated, until a maximal number of iterations n_{max}=1000 is reached. The procedure then starts again from the first step with a completely new set of sensors $C_{1,0}$ and is repeated m_{max} times. Without the restart

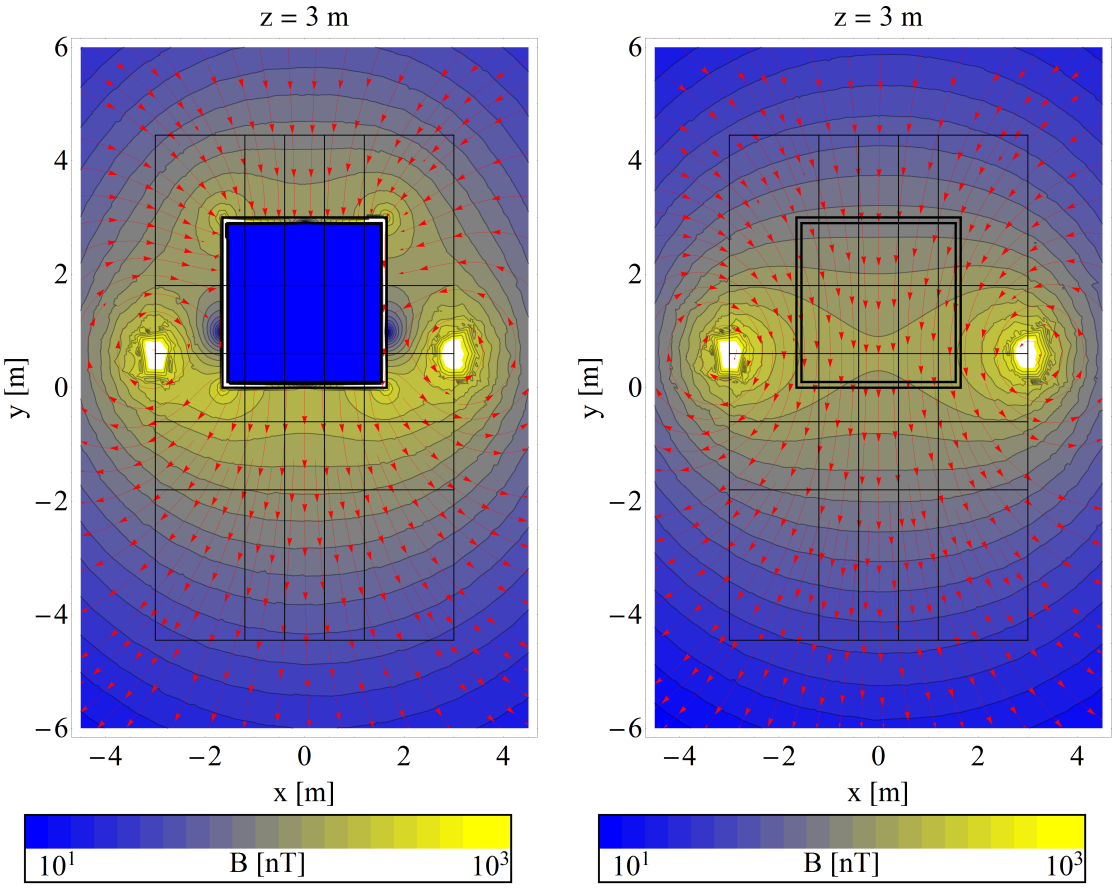

(a) with the passive shield

(b) without the passive shield

Figure 3.4.: Top view of the magnetic field produced by a coil and deformed by the passive magnetic shield for $\mu = 25000$ (a) and $\mu = 1$ (b). The MSR (indicated by the thick black lines) is modeled by a 5 cm thick shell. This thickness was chosen to get a mesh that is calculateable in a reasonable amount of time in the FEM software. The interior of the MSR is modeled by air ($\mu = 1$). The contours of the coils of the ACS are indicated by the thin black lines. The color scale is logarithmic.

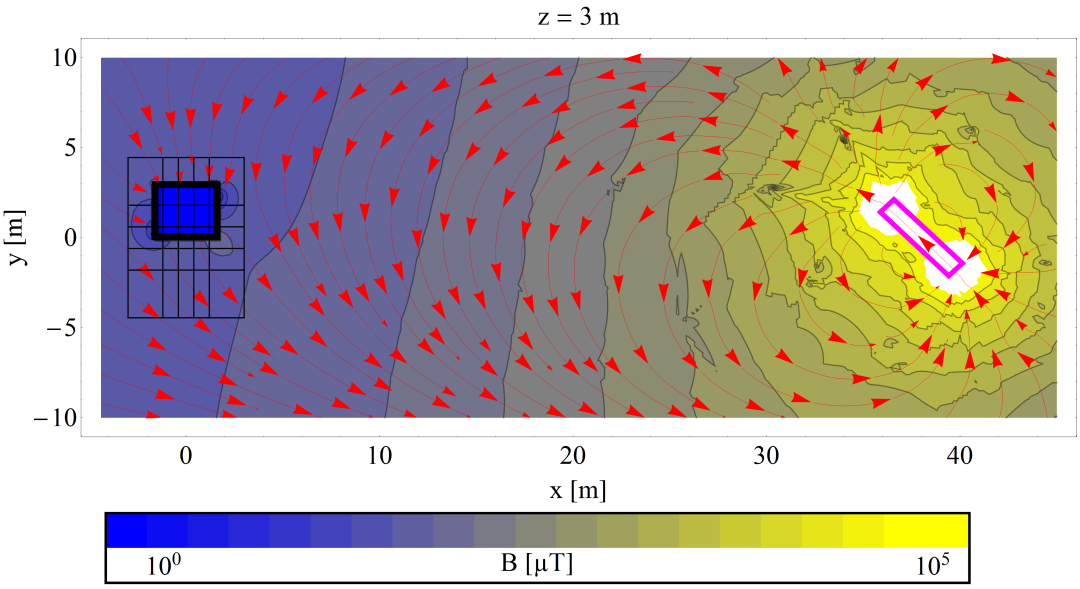

Figure 3.5.: Superposition of the Earth's magnetic field and the estimated magnetic field produced by the PERC magnet (indicated by the magenta lines) at the position of the ACS (thin black lines) and the passive shield (thick black lines). Values above >100 mT are not displayed (white). In the case that the PERC experiment would not magnetically shield its solenoid, the field at the position of the nEDM instrument is ∼50 μT, the same order as the Earth's field.

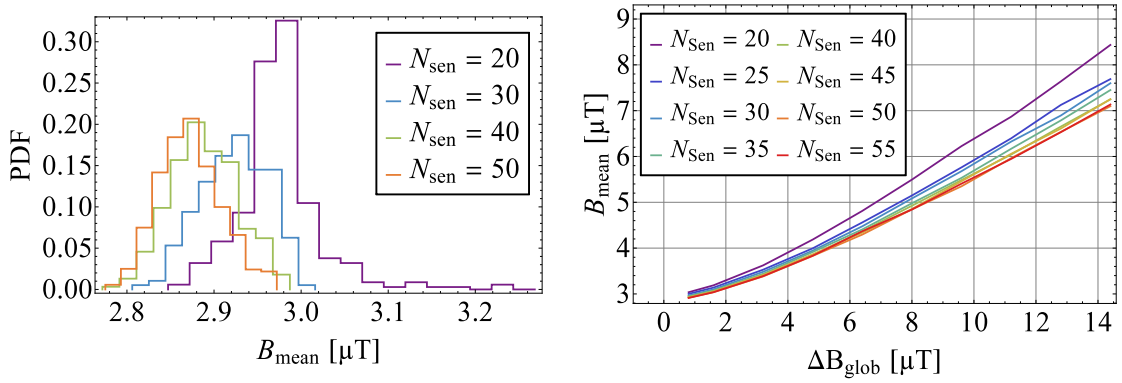

(a) Mean field distribution

(b) External field drift

Figure 3.6.: Mean field of the optimization result for the superposition of the Earth's magnetic and the PERC field: The probability density function (PDF) extracted from the various optimization results of the sensor positions (a) shows that the mean field is almost independent of the number of sensors. To study the performance of the ACS a homogeneous field change is added (b). The sensor positions are fixed to the scenario without an external field change. Sensor configurations with an increased number of sensors N_{sen} only show a slightly improved performance. Hence a different criterion needs to be defined to optimize N_{sen}.

the optimization process can get stuck in a local minimum and therefore not yields the optimal configuration.

This kind of optimization does not necessarily end up at the optimum configuration, but a large number of sets converging to a specific field value indicates that these solutions are close to the optimum. All optimized sets $C_{m,n_{max}}$ are compared in respect to the norm and homogeneity of the field. The sensor positions returned by the optimization process are not yet of importance as they need to be matched to the real ambient field later on.

In addition, the amount of sensors does not affect the performance of the ACS in terms of resulting field and homogeneity (see figure 3.6a), because the resulting field is only determined by the applied currents and the residual field. Criteria for the number of sensors will be given later.

To determine the optimal number of sensors N_{sen} as well as the requirements for the magnetic field probes and the current sources, external field changes, sensor noise and current source noise are included in the calculations. Due to the shielding factor of the passive shield, external fields are reduced by a factor of about 10^6. For integration times of ≈ 300 s the field at the nEDM experiment has to be stable to 10 fT. Therefore external effects have to be reducible to below 10 nT.

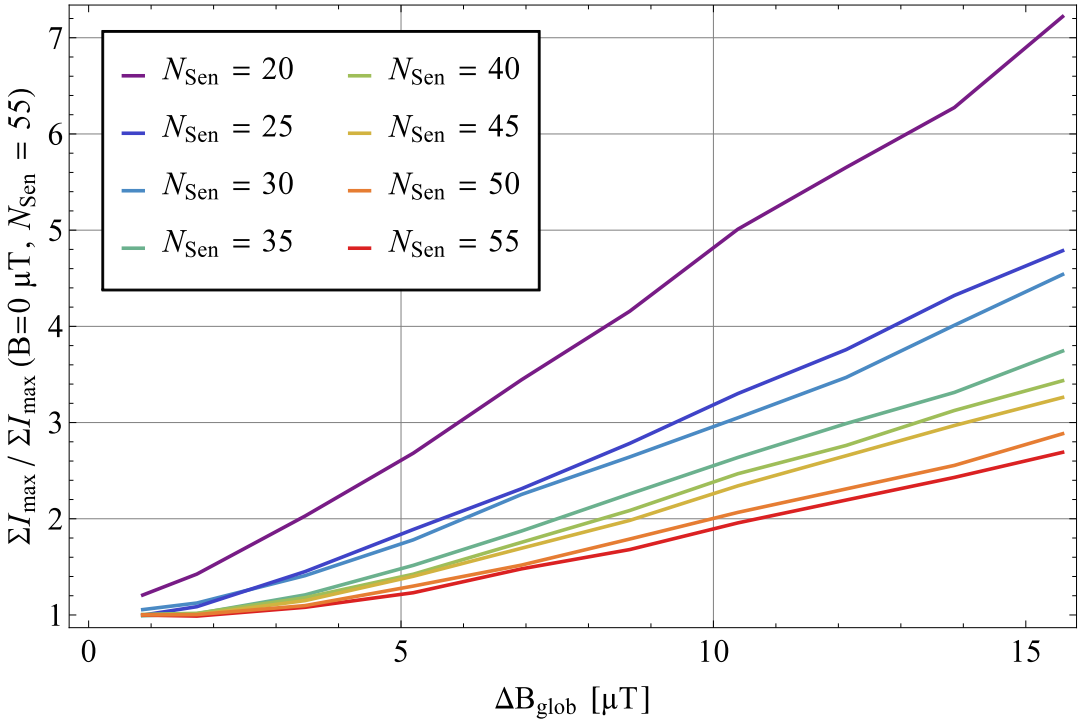

Figure 3.7.: Relative change of the total current consumption as a function of N_{sen} and $\mathbf{\Delta B}_{glob}$: With an increasing external field the current needed to compensate also increases. This could drive the current sources into their current limit which would stop the compensation algorithm.

Homogeneous field change

The behavior for a field change is shown in figure 3.6b. Here a homogeneous global field change $\mathbf{\Delta B}_{glob}$ is added to the ambient field. The sensor configuration is not changed, but equation 3.4 is used to find the new optimal current and afterward the mean field is determined. For the same sensor configuration the procedure is repeated multiple times. Each time a new $\mathbf{\Delta B}_{glob}$ is chosen, with the global field pointing to a randomly chosen direction. Increasing N_{sen} only slightly improves the situation. Therefore the mean field is not a good figure of merit to optimize N_{sen}.

Any field change measured by the sensors results in a change of $\mathbf{I}$ such that the field at the sensors is minimized. But the field in the volume of interest is not necessarily minimized, which can be seen in the total current consumption

$$\Sigma I_{max} = \sum_{i=1}^{N_{coil}} |I_i| \,. \tag{3.8}$$

ΣI_{max} is therefore a measure for the stability of the system in respect to external perturbations. Figure 3.7 shows the increase in the total current consumption of the ACS as a function of the external field change relative to the undisturbed case ($\mathbf{\Delta B}_{glob} = 0$). Hence a system with more sensors is more stable. This result,

combined with a bulk discount, sets the number of sensors to 50. Increasing the number of sensors only slightly increases the performance of the ACS and hence all following calculations and optimizations are performed with N_{sen}=50.

Sensor noise

Sensor noise is modeled almost the same as the field drift. The difference here is that a local field $\mathbf{B}_{\text{noise}}$ is added to each sensor individually for each iteration step i. The magnitude of the noise field is Gaussian distributed with the width B_{noise}. With equations 3.4 and 3.1 the currents are calculated and the resulting field is determined.

To quantify the response to sensor noise the field deviation

$$\sigma_B = \sqrt{\frac{1}{N}\sum_{i=1}^{N} |\mathbf{B} - \overline{\mathbf{B}}|^2} \tag{3.9}$$

is chosen as a figure of merit, with N the total number of iterations, $\mathbf{B}$ the resulting field at the center of the ACS and $\overline{\mathbf{B}}$ the mean of the resulting field series.

For the best 40 sensor configurations B_{noise} is varied and the average field deviation indicates that magnetic field probes with a maximal noise of 60 nT are needed to reach the overall 10 nT stability goal.

The system to measure the magnetic field consists of Mag-690 fluxgates[2], a custom made breakout-box and three analog-digital-converters (ADCs) XVME-564[3]. The sensitivity of the field measurement system is dominated by the noise of the sensors. It yields a sensitivity of 20 nT. The characterization of the measurement system can be found in appendix D.

Current noise

Analogous to the sensor noise, the figure of merit for the current noise study is the field deviation (equation 3.9). A randomly chosen current noise $\mathbf{I}_{\text{noise}}$ with independent components is added to the undisturbed current set. With equation 3.1 the resulting field is determined. Figure 3.8b shows that a current noise of 30 mA is needed to reach the stability goal of 10 nT. The current supplies are connected to coils with 10 or 15 loops. Therefore the requirement scales down to 2 mA. For this purpose the programmable power supplies CPX400DP[4] are used. They have a noise of $\approx$ 1 mA and their characterization is shown in chapter D.

[2]Bartington Instruments, `http://www.bartington.com/mag690-low-cost-three-axis-magnetic-field-sensor.html`

[3]Acromag Inc., XVME-564

[4]Thurlby Thandar Instrumends, Ltd.

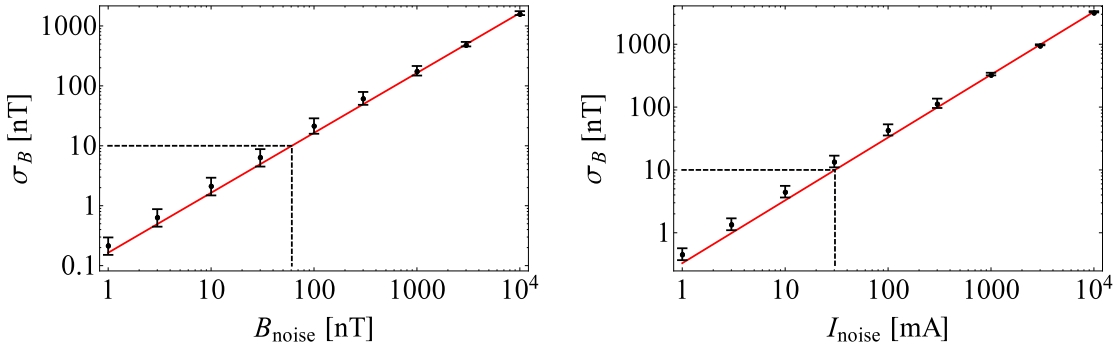

(a) Sensor noise (b) Current source noise

Figure 3.8.: Stability of the system with respect to sensor (a) and current source (b) noise. The dashed line indicates the requirement on a system stability of 10 nT and the resulting requirements of the sensors and current sources.

3.4. Data acquisition

The control system is the connection between the data acquisition (including the fluxgates) and the magnetic field generation systems. The hardware consists of twelve 2-channel current supplies, three ADC cards (64 channel, 16 bit), three breakout-boxes, a single board computer (SBC) and a control PC (Mac Mini). Figure 3.9 illustrates all of the components and shows the connections between them.

The breakout-boxes provide the power supply for the fluxgates and separate the power lines from the signal lines (for the cable configuration see appendix F). One breakout-box operates 20 fluxgates. The signal lines for each breakout-box are bundled into two 50-conductor twisted ribbon cable and connected to the input terminals of the ADC cards.

The ADC cards are mounted together with the SBC in a VME crate. The SBC is connected to a local network. The control PC accesses the ADCs via the SBC. To increase the magnetic field sensor sensitivity the fluxgate signals are averaged in the SBC code.

Each current supply is accessed via the local network and controlled by the control PC. As for higher frequencies the SF (shielding factor) of the passive shield also increases, the task of the ACS is solely to stabilize the slow field drifts ($f < 3$ Hz). Therefore the requirements for the communication speed are low and the connection via Ethernet is sufficient. Due to the inductive properties of the coils, the current ramps up in about 10-20 ms (estimation based on the inductance and resistance of the coils, see appendix A). The control system communicates with the current supplies via Ethernet. Its communication speed is limited to ∼14 Hz which is sufficient.

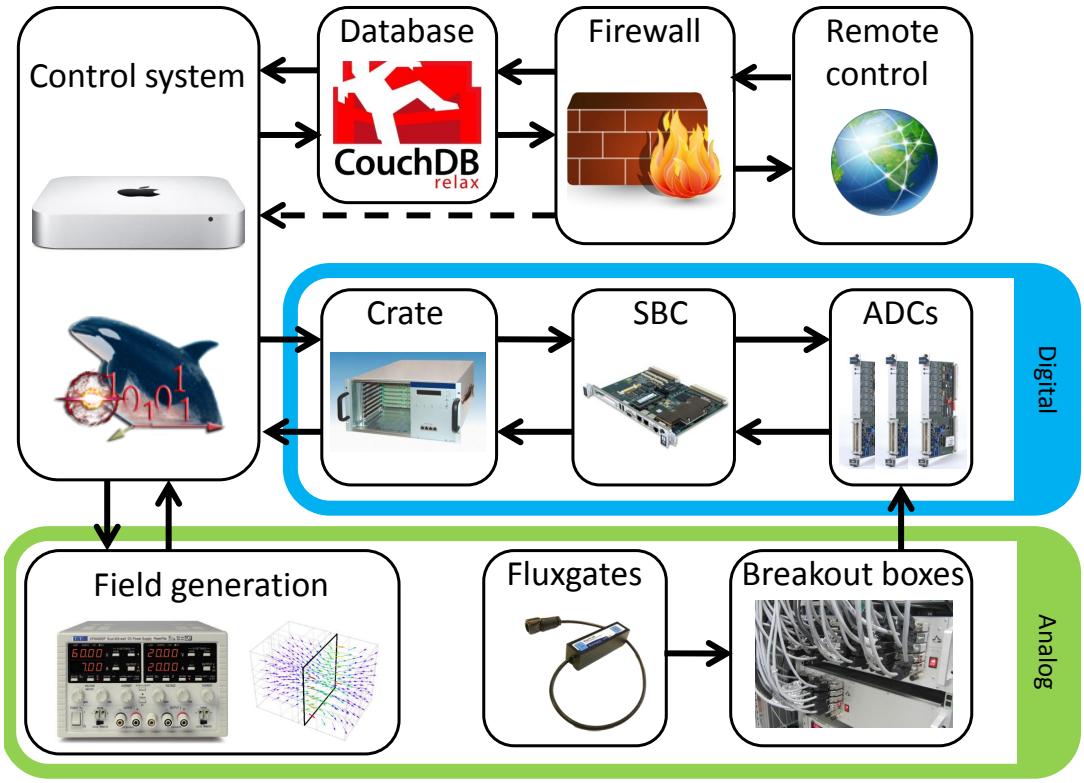

Figure 3.9.: Schematic overview of the ACS components and the connections between them.

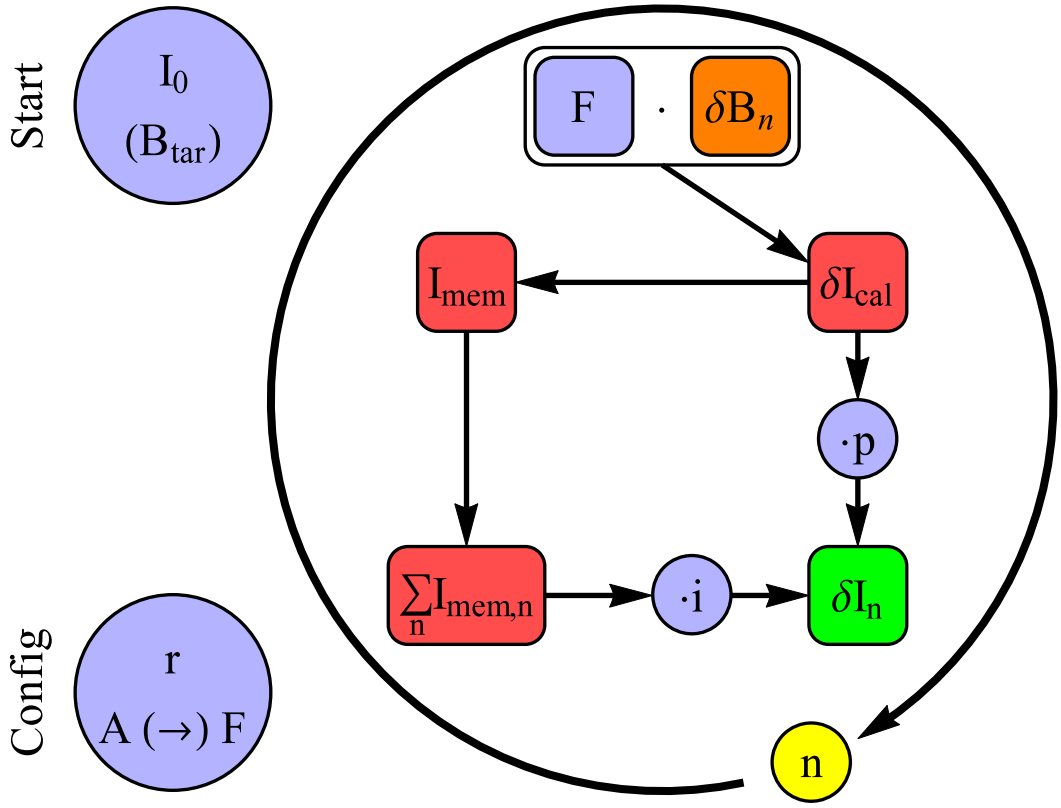

Figure 3.10.: Sketch of the ACS algorithm: Before the compensation loop starts, start parameters (start current I_0, target field B_{tar}) and configuration (regularization parameter r, sensitivity matrix A and feedback matrix F) are set. In each iteration step n, the change in magnetic field δB_n is measured and multiplied with the feedback matrix to determine the compensation current δI_{cal}. The set current value is composed of the sum of all previous current values (stored in the current memory I_{mem}) weighted with i and the current value of the current weighted with p.

3.5. Control system

The control system is able to read all 180 magnetometer channels (three ADC cards) with >80 Hz, which is limited by the communication with the SBC. The ADC reads the raw field values with $f_S \approx 50$ kHz. To determine the magnetic field of a sensor channel, N_{avg} raw values are averaged. Hence the maximal run frequency is dominated by the power supplies. During standard operation the run frequency f is usually set to values between 2 Hz and 3 Hz. A sketch of the ACS algorithm is shown in figure 3.10.

In addition to the run frequency, various other parameters can be set in the software. In some cases it is not reasonable to minimize the field to 0, but instead to a target field $\mathbf{B}_{tar}$. Therefore $\mathbf{B}_{ext}$ is replaced by $\mathbf{B}_{ext} - \mathbf{B}_{tar}$. There exist two ways to set $\mathbf{B}_{tar}$, either by reading the values from a map file or by setting an initial current

I_0. In the latter, $\mathbf{B}_{\text{tar}}$ is determined by a magnetic field measurement integrated over a long time at the beginning of the compensation algorithm to minimize the effect of sensor noise. This method has the advantage that the best magnetic field configuration – if determined beforehand – can be restored, even if the local field measured by the fluxgates changes. Due to the installation of magnetic equipment near a fluxgate, the magnetic field can change locally. In practice, this mode is favored over using the predefined $\mathbf{B}_{\text{tar}}$.

As the ACS acts like a closed loop control, an integral term i can be added to the proportional term p. With optimized p and i this standard method increases the stability of the system. Equation 3.4 is therefore expanded to

$$\mathbf{I}^{n+1} = p\mathbf{F} \cdot (\mathbf{B}^n - \mathbf{B}_{\text{tar}}) + i \sum_{j=0}^{n} \mathbf{I}^j \,. \tag{3.10}$$

Similar to $\mathbf{B}_{\text{tar}}$, there are two possibilities to include the feedback matrix $\mathbf{F}$. It can be read in with a map containing predefined values or it can be calculated directly in the software via the sensitivity matrix. As this process is slow compared to the run frequency, $\mathbf{F}$ can only be calculated while the compensation algorithm is not running.

3.5.1. Regularization

If integrated in the software, the calculation of $\mathbf{F}$ can be easily expanded to include matrix regularization [86, 87]. An alternate way to calculate $\mathbf{F}$ with a singular value decomposition:

$$\mathbf{A} = \mathbf{U} \cdot \mathbf{V} \cdot \mathbf{W}^T \Rightarrow \mathbf{W} \cdot \mathbf{V}^{-1} \cdot \mathbf{U}^T = \mathbf{A}^{-1} = \mathbf{F} \,. \tag{3.11}$$

In the case of ill-conditioned matrices, electronic noise measured by fluxgates can be amplified through the feedback system and then the ACS creates an additional field (for details see [87]). By applying a matrix regularization

$$V_{jj} = \frac{1}{v_j} \rightarrow \frac{v_j}{{v_j}^2 + {\beta_j}^2} \,, \tag{3.12}$$

the condition of the matrix can be improved. Here v_j are the singular values of $\mathbf{A}$ and $\beta = 10^r$ V/A ($10^r \cdot 10\mu$T/A). With increasing r the effect of the ACS vanishes and in the limit of $\beta \rightarrow \infty$ all entries in the $\mathbf{F}$ become 0, stopping the dynamic compensation completely. For small r the noise reduction of the regularization vanishes. Therefore a compromise has to be found. An estimate for r can be extracted from noise simulations.

As figures of merit, the general noise Γ produced by random sensor noise B_N and the response $R_{(h,g)}$ of the system in respect to homogeneous (h) and gradient (g) field changes are defined:

$$\Gamma(r, B_N) = \sqrt{\frac{1}{N_{\text{sen}}} \sum_{i=1}^{N_{\text{sen}}} (\partial {B_i}^{\text{sim}}(r, b_N))^2} \,, \tag{3.13}$$

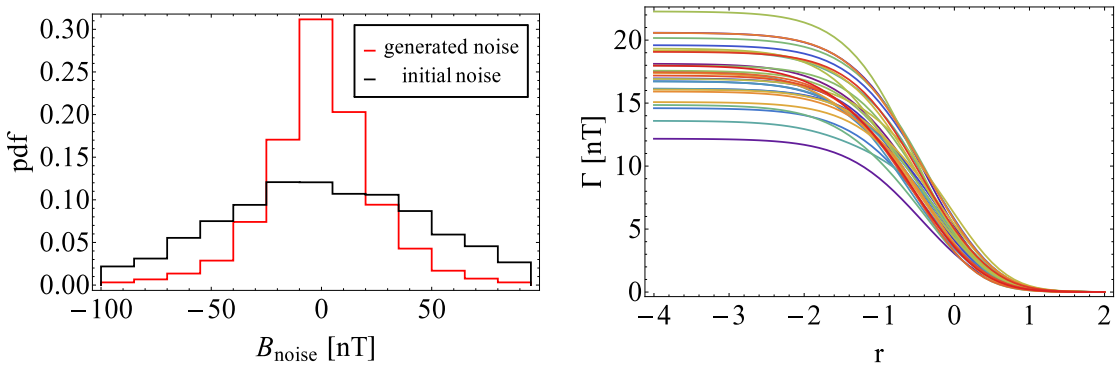

(a) Noise distribution

(b) Regularization effect

Figure 3.11.: Effect of the matrix regularization in respect to sensor noise. The initial electronic sensor noise distribution of $\sim$ 50 nT transforms into a real magnetic field noise with a width of $\sim$ 20 nT (a). The general noise (norm of the distribution) for different noise sets (rainbow colored lines) decreases with increasing regularization parameter r (b).

with

$$\partial B_i^{\text{sim}}(r, B_N) = [\mathbf{F}(r)\mathbf{B}_N]_i \quad \text{and} \quad \mathbf{B_N} = (B_{N,1}, B_{N,2}, ..., B_{N,N_{\text{sen}}}) \tag{3.14}$$

and

$$R_{(h,g)}(r, B_{(h,g)}) = \frac{\sqrt{\frac{1}{N_{\text{sen}}} \sum_{i=0}^{N_{sen}} (B_{(h,g),i} + [\mathbf{A}(\mathbf{F}(\mathbf{r})\mathbf{B}_{(h,g)})]_i)^2}}{\sqrt{\frac{1}{N_{\text{sen}}} \sum_{i=0}^{N_{\text{sen}}} (B_{(h,g),i})^2}} \tag{3.15}$$

with

$$\mathbf{B}_h = (B_x, B_y, B_z, ..., B_z) \quad \text{and} \quad \mathbf{B_g} = (B_x(x_1, y_1, z_1), B_y(x_1, y_1, z_1), ..., B_z(x_N, y_N, z_N)) \,. \tag{3.16}$$

The numerator of $R_{(h,g)}$ is effectively the compensated field and the denominator is the uncompensated field.

In order to model the noise, a Gaussian distribution with a width of 50 nT is used. Figure 3.11a shows this initial noise distribution and the field noise generated by the coils for a vanishing regularization ($r \to -\infty$). Multiple noise distributions (sets) are calculated to quantify the performance of the regularization. With increasing r the generated noise for these sets decreases (see figure 3.11b).

In terms of noise generation, $r \to \infty$ would be preferable. But in that case the compensation of a real field change would also vanish. Therefore the homogeneous and gradient field changes have to be simulated as a function of r. Figure 3.12 shows the response of the ACS to various homogeneous field changes. Each direction is randomly chosen, following a Gaussian distribution with a width of 2 μT. Without regularization ($r \to -\infty$) $R_h \approx 0.1$ is achieved, which means that only 10% of the

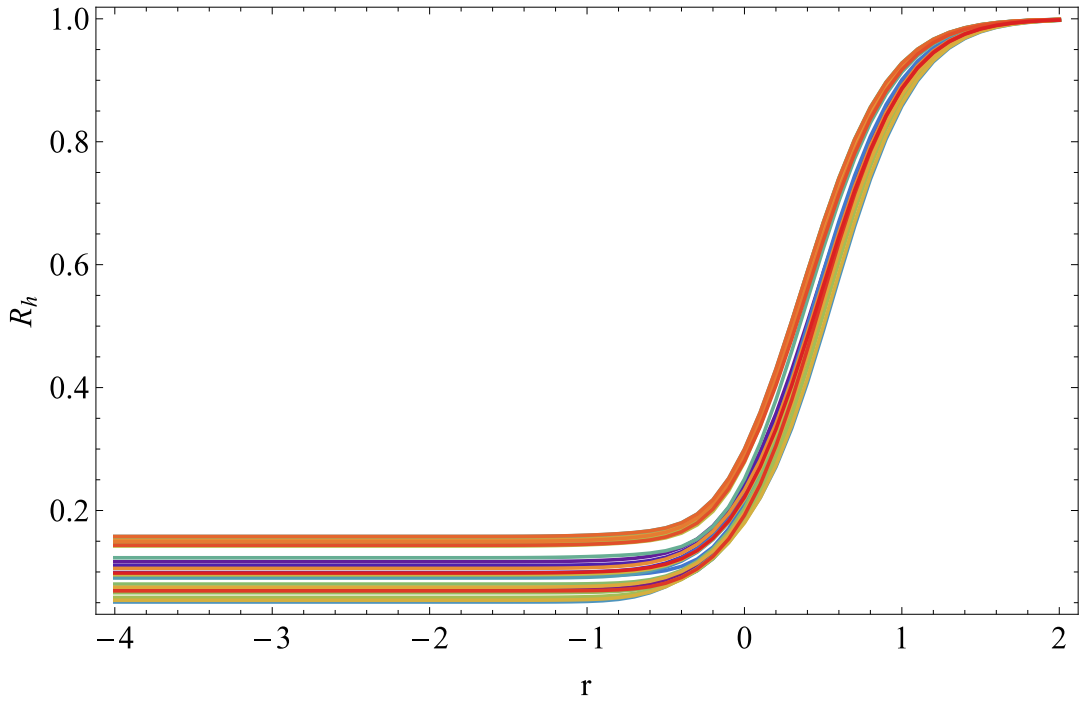

Figure 3.12.: Reduction of the field compensation as a function of the regularization parameter r.

field change is left due to the compensation. For a very strong regularization R_h converges to 1. In other words, the field change is not compensated at all.

The result of the gradient field compensation behaves similar. But on average a compensation of 75% ($R_g \approx 0.25$) is achieved.

A good noise suppression and good compensation properties cannot be fulfilled at the same time and hence a compromise has to be made. To compare Γ and $R_{(h,g)}$, both are normalized, as shown in figure 3.13. The intersection of the graphs indicates the optimal value for r. Due to the spread of Γ and $R_{(h,g)}$ (colored area), the range $-0.5 < r < 0$ is considered optimal.

It has to be pointed out that the response reduction for real field drifts does not mean that these fields are compensated. It rather means that the system needs more iterations to account for the field change. In other words it reduces the effective compensation frequency. With each iteration of the compensation algorithm the – not yet – compensated field change is further compensated (see solid lines in figure 3.14).

In contrast to it, electronic noise (dashed lines in figure 3.14) increases with each iteration, assuming the worst case ($p = 1$, $i = 0$, $r \to -\infty$). The evolution of the noise resembles a random walk problem and is proportional to the square root of the iteration number for $r \to -\infty$. Hence the preferred range $-0.5 < r < 0$ shifts to $-0.2 < r < 0.2$.

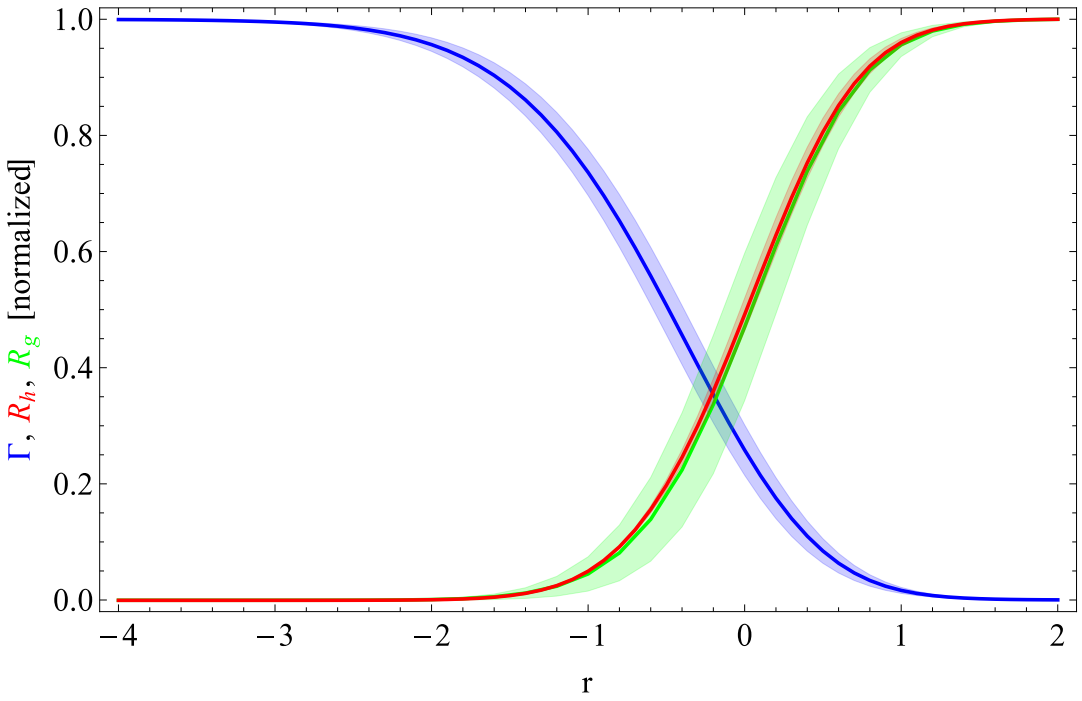

Figure 3.13.: Normalized noise amplification (blue) and response to homogeneous (red) and gradient (green) field changes as a function of r. The optimal range $-0.5 < r < 0$ ensures a good noise cancellation, without reducing the compensation of real fields. The colored shadow indicates the spread of Γ and $R_{(h,g)}$ with respect to the different sets of fields.

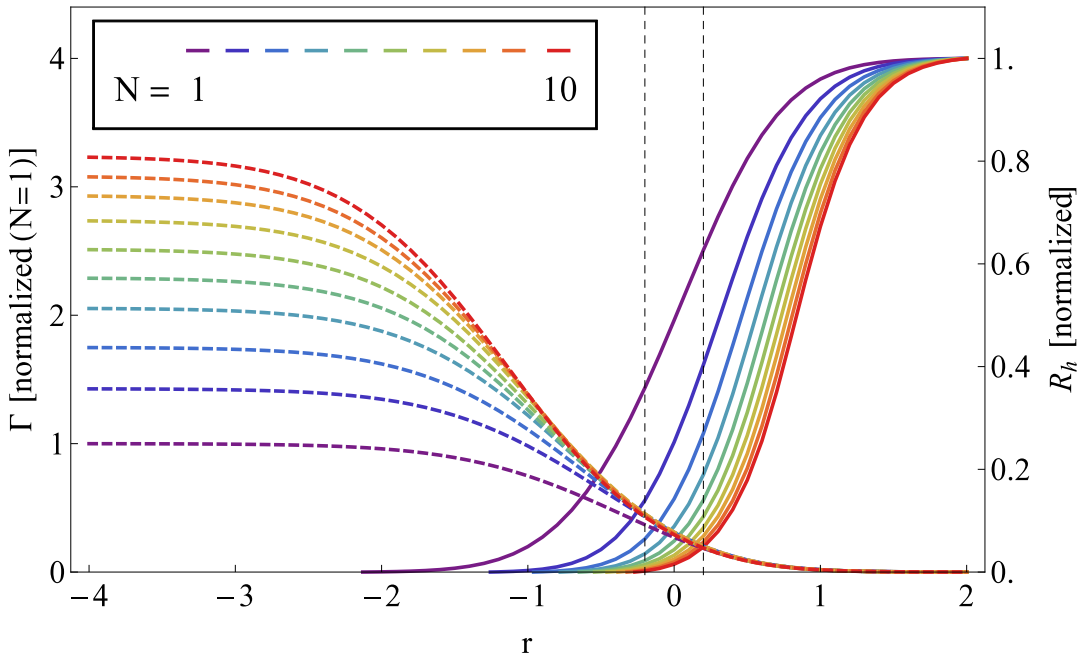

Figure 3.14.: Γ and R_h evolution: With each iteration the compensation power (solid colored lines) increases, but so does the noise (dashed colored lines). In the preferred range from r= -0.2 to 0.2 (dashed black lines) the noise increase is small.

3.5.2. Sensor correlation

In addition to the matrix regularization, there is a second way to reduce the noise amplification: signal correlations. If sensors close to each other measure a common noise, it is very likely that these signals are not just electronic sensor noise, but rather a real disturbance and therefore should be compensated. Accordingly the signals from these signals should be weighted more than those that have a smaller correlation (due to uncorrelated noise).

Next to the determination of the average magnetic field B_i, the raw signals read from the fluxgates can be used to calculate correlation coefficients $C_{i,j}$ (later defined in equation 3.19). Completely uncorrelated noise yields $C_{i,j} \to 0$ for long integration times ($N_{avg} \to \infty$). Correlated noise with a frequency f_n results in $C_{i,j} \approx 1$ for $f < f_n < f_S$. Since it is faster than the compensation frequency f, contribution from such noise sources cannot be reduced with this method. Noise with $F_n < f$ also gives $C_{i,j} \approx 1$, but in this case the field change can be compensated.

Anti-correlated signals yield $C_{i,j} = -1$, but they are treated the same as correlated signals. They represent a field gradient between the two corresponding channels i and j, which the compensation algorithm should also handle. Consequently the absolute value $|C_{i,j}|$ enters the calculation of the global correlation.

A fast way to calculate the correlation of the $N_{\mathrm{ch}} = 3 \cdot N_{\mathrm{sen}} \approx 150$ channels is to use a $N_{\mathrm{avg}} \times N_{\mathrm{sen}}$ matrix, $\mathbf{S}$. It combines the time series for all channel. The mean

values of the channels can then be easily expressed with a vector $\boldsymbol{\mu}$:

$$\boldsymbol{\mu} = \frac{1}{N_{\text{avg}}} \mathbf{1}^T \mathbf{S}\,, \tag{3.17}$$

with $\mathbf{1}^T$ a row vector of length N_{avg}, of which all elements are 1. By subtracting $\boldsymbol{\mu}$ from $\mathbf{S}$, the relative signal matrix $\mathbf{S}'$ is determined. The standard deviation is then calculated by

$$\boldsymbol{\sigma} = \sqrt{\frac{1}{N_{\text{avg}}} \mathbf{S}'^T \mathbf{S}'}\,. \tag{3.18}$$

The square root represents here an operator, which takes the square root of all elements of the matrix. The elements of the correlation matrix $\mathbf{C}$ can then be expressed by

$$C_{i,j} = \frac{1}{N_{\text{avg}} - 1} \frac{(\mathbf{S}'^T \mathbf{S}')_{i,j}^{\;2}}{\sigma_i \sigma_j}\,. \tag{3.19}$$

By definition the diagonal elements of $\mathbf{C}$ are 1, as these are the correlation of the channels with themselves. They should not contribute to the correlation based compensation and are therefore set to 0. Also the correlation of the three channels in the same sensor are set to 0, because they could share common noise. Hence $\mathbf{C}$ has the form

$$\begin{pmatrix}
0 & 0 & 0 & * & * & * & . & . & . & * & * & * \\
0 & 0 & 0 & * & * & * & . & . & . & * & * & * \\
0 & 0 & 0 & * & * & * & . & . & . & * & * & * \\
* & * & * & 0 & 0 & 0 & . & . & . & * & * & * \\
* & * & * & 0 & 0 & 0 & . & . & . & * & * & * \\
* & * & * & 0 & 0 & 0 & . & . & . & * & * & * \\
. & . & . & . & . & . & . & . & . & . & . & . \\
. & . & . & . & . & . & . & . & . & . & . & . \\
. & . & . & . & . & . & . & . & . & . & . & . \\
* & * & * & * & * & * & . & . & . & 0 & 0 & 0 \\
* & * & * & * & * & * & . & . & . & 0 & 0 & 0 \\
* & * & * & * & * & * & . & . & . & 0 & 0 & 0
\end{pmatrix}. \tag{3.20}$$

The normalized norm of the elements of the correlation matrix $\mathbf{C}$ is used to scale the proportional term p of the PI control, which then transforms to p' :

$$p' = p \cdot \frac{\sum_{i}^{N_{\text{sen}}} \sum_{j}^{N_{\text{sen}}} C_{i,j}}{(N_{\text{sen}} - 3)^2}\,. \tag{3.21}$$

Thus uncorrelated field changes yield a small p' and are not compensated.

However, there is still a problem, because a constant field offset has a correlation of 0. Therefore the correlation mechanism – as it is now – would stop the compensation of time independent field offsets. If a deviation to the target field, represented by $\boldsymbol{\mu}$, is large in comparison to the noise of the channels, represented by $\boldsymbol{\sigma}$, the effect

of the correlation mechanism has to be removed. Therefore the quadratic mean of noise-weighted offset

$$\eta = \sqrt{\frac{1}{N_{\text{sen}}} \sum_{i}^{N_{\text{sen}}} (\frac{\mu_i - B_{i,\text{tar}}}{\sigma_i})^2} \tag{3.22}$$

is used to control the correlation mechanism. The proportional term of the PI control is therefore transformed:

$$p \to e^{-\frac{\eta^2}{2}} p' + (1 - e^{-\frac{\eta^2}{2}}) p \,. \tag{3.23}$$

The new p is also a quantity to study the reduction of noise and the compensation of field changes. The Gaussian weighting of p through η results in improved behavior for $B > B_{\text{noise}}$ and hence is preferred to a $e^{-\eta}$-weighting. For example, white noise and $N_{\text{avg}} = 250$ results in $p \propto \sqrt{\frac{1}{N_{\text{avg}}}} \approx 0.06$, which means that the noise amplification is reduced by 94%. On the other hand, the correlation of real field changes is independent of N_{avg}. To quantify this behavior linear field drifts (slow field change $B_i(t) = \frac{B}{T} \cdot t$ and T corresponds to the time needed to take N_{avg} data points), instantaneous field changes (field jump $B_i(t) = B$) and gradient drifts ($B_i(t) = \frac{B}{TR} \cdot rt$ with R representing the dimensions of the field cage) are combined with a white noise signal, of which the magnitude relative to the real field change is varied. The proportional term p is used as the figure of merit as it reflects the performance of the compensation.

Figure 3.15 shows the effect of the correlation on p. With increasing noise $\mathbf{B}_{\text{noise}}$, p decreases monotonically. In order to compare different field types, the magnitude of the noise is normalized by the mean value of the real field. The performance is very similar for all three scenarios. Vanishing noise results in $p \to 1$, which means that the field change is compensated with the full potential.

In a case where the noise is on the same order as the real field change, 70% of the noise is reduced while only 30% of the real field is compensated. In the limit of a vanishing field change ($B_{\text{noise}}/B \to \infty$), p converges to the predicted value 0.06. Here N_{avg} was set to 250 to speed up the calculation. Due to the noise amplification effect of the feedback method (see figure 3.11), B_{noise}/B is favored over B/B_{noise} to not be misinterpreted as the signal-to-noise ratio (B_{noise}/B) which would not fit here.

As the method of the sensor signal correlation affects only p and the method of the matrix regularization modifies the feedback matrix $\mathbf{F}$, both are independent and can be applied at the same time. In general the matrix regularization reduces all kinds of signals and acts as a damping mechanism. Real field changes are simply compensated after a few more iterations.

The sensor correlation method dynamically reduces signals if they are not correlated. During the compensation of a large field change, the uncorrelated noise is not reduced either. For a constant field with just electronic sensor noise, the sensor correlation very effectively reduces the undesirable noise amplification property of the ACS. Therefore its main advantage is to prevent the ACS from adding unnecessary noise to a stable field.

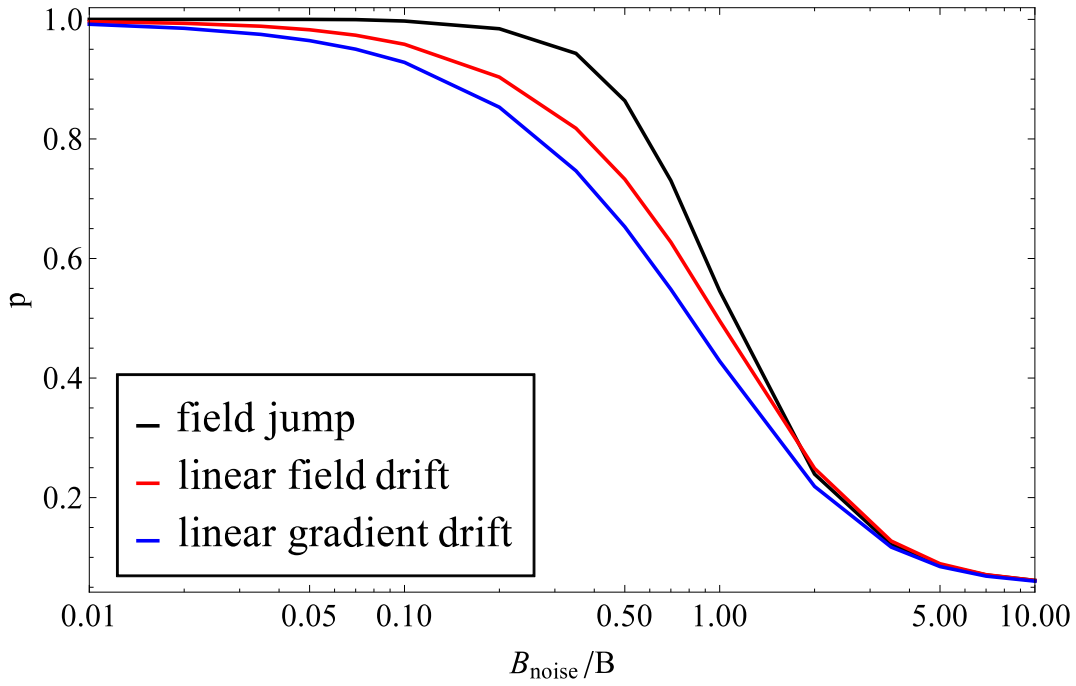

Figure 3.15.: Correlation corrected proportional term p for an instantaneous field jump, a linear temporal field and a gradient drift as a function of the sensor noise B_{noise}. Here is B the amplitude of the corresponding field change.

3.6. Static field compensation

The ambient field at the position of the nEDM instrument was measured before the passive shield was installed. In addition, the field map of each coil was taken by ramping the individual coils from 0 A to 10 A in 1 A steps. These data were then used to determine the sensitivity matrix A (see equation 3.1). This yields information on positions which later are blocked by other equipment (e.g. passive shields). The data was taken on a grid with a spacing of 1 m inside the volume of the ACS, in a total of 270 positions. Figure 3.16 shows the ambient field on the three central planes. As the two planes not shown are above and below the final position of the MSR, they play a minor role. For reference the silhouette of the passive shield is also indicated in red and black lines.

Near the ground there are large stray fields arising from magnetized concrete at the edges of the EDM hole. The hole is surrounded by a layer of 1 m non-magnetic concrete. Without this special concrete, the stray fields would be stronger (a comparable area next to the nEDM instrument has been measured). With increasing height the stray fields decrease and the Earth's magnetic field becomes dominant, which is indicated by the homogeneous field map at z=4 m.

Due to the measured coils and ambient field maps, equation 3.4 can be used to calculate the optimal current set I_0 for a given environment. The optimal current set I_0 is obtained by restricting the fiducial volume to a cuboid spanned by $-2\,\mathrm{m} < x < +2\,\mathrm{m}$, $-4\,\mathrm{m} \leq y \leq +4\,\mathrm{m}$ and $+1\,\mathrm{m} < z \leq +4\,\mathrm{m}$. For reference, I_0 is shown in table A.1. The asymmetric current distribution is attributed to the stray fields.

Applying this current set yields a reduced field almost everywhere around the MSR, except for the northwest corner (x=2.5 m, y=4 m, z=2 m). The uncompensated ambient field was already quite low in this area and now is overcompensated. As the field geometry of the stray field is highly non linear, the ACS is not capable of reducing such a high-order inhomogeneity. In order to do so, additional coils would be required, which would increase the complexity of the system. However, no decreased performance of the passive shield due to this slightly increased field has been observed, so there is no need to install additional coils.

On the other hand, the well compensated area ($B < 10\,\mu\mathrm{T}$) extends around the MSR and the area in front it, which is dedicated to the interim position of the insert. Therefore all components of the passive shield can be kept in a low magnetic environment during maintenance of the nEDM apparatus.

In terms of average field inside the fiducial volume, the static compensation yields a reduction from $43\,\mu\mathrm{T}$ to $6\,\mu\mathrm{T}$. Assuming a purely homogeneous field (e.g. that caused by the Earth's field) the ACS achieves a reduction to $1\,\mu\mathrm{T}$, but the above discussed inhomogeneities are the reason for the non-optimal performance. Nevertheless the measured values of the compensated field match within 8% to the field predicted by the calculation based on the coil and the ambient field maps.

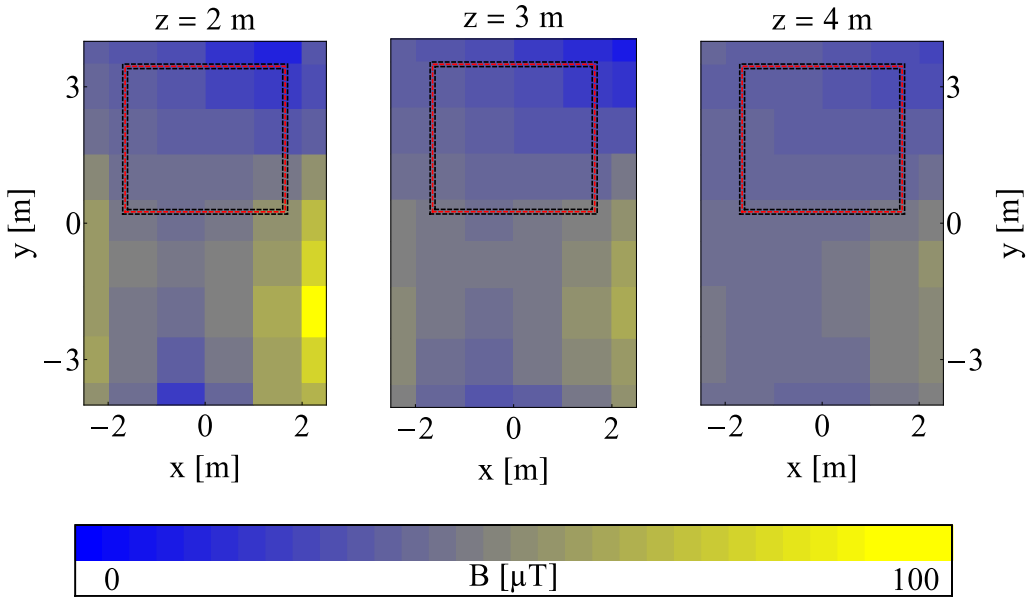

(a) Uncompensated field

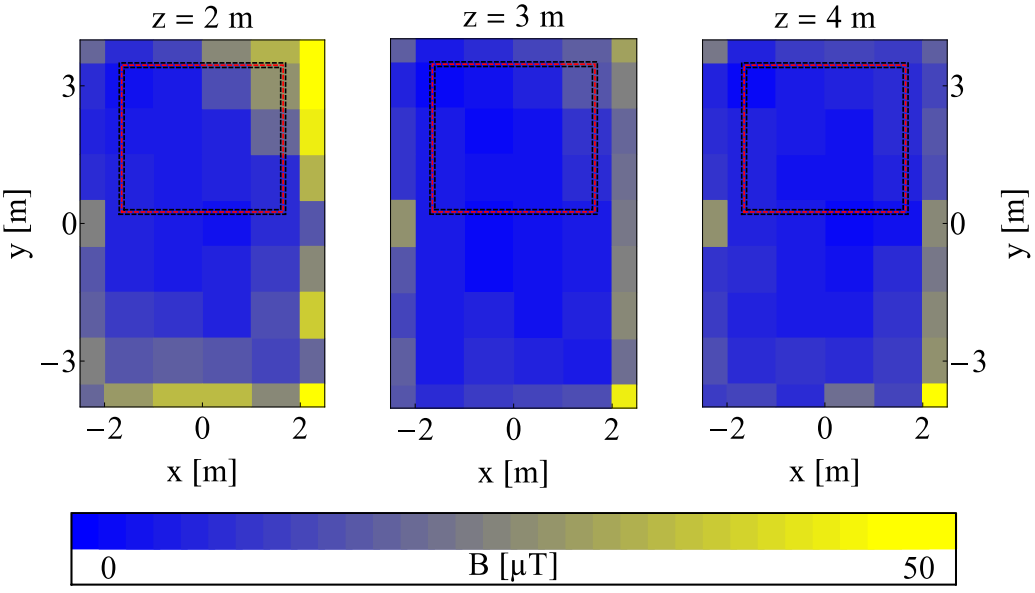

(b) Compensated field

Figure 3.16.: Static compensation of the ambient field inside the ACS: The average field in the area around the MSR is reduced from 43 μT (a) to 6.4 μT (b). Due to internal stray fields arising from magnetized concrete near the edges of the EDM hole, the predicted field reduction factor of ~ 40 (see section 3.2.2) is not reached. The position of the MSR is indicated by the black and red dashed lines.

3.7. Dynamic field compensation and drift reconstruction

While the main benefit of a low magnetic field around the MSR is to avoid the magnetization of sensitive nEDM experiment components, the value of the field itself is less important. With degaussing techniques the passive shield can be brought into an equilibrium state, featuring a field inside of it almost independent of the outside field [70]. On the other hand, slow external field drifts change the magnetization of the passive shield, taking it away from its equilibrium state. Therefore the main feature of any ACS is to provide a temporally stable field around the passive shields.

The magnetic field is read out in the three spatial directions at 59 positions located around the MSR. The large number of field values have to be combined to a figure of merit to quantize the performance of the ACS. Following the above argumentation, only the field change $\Delta B_i(t) = B_i(t) - B_i(0)$ is taken into account and all of the values are combined as

$$\Delta B(t) = \frac{1}{\sqrt{N_{\text{sen}}}} \sqrt{\sum_{i=1}^{N_{\text{sen}}} \Delta B_i^2(t)} \,. \tag{3.24}$$

The quadratic sum intrinsically weights large field deviations stronger and therefore is considered to be a conservative estimate for the stabilization quality.

Next to the magnetic field values, the current values are also recorded while the compensation algorithm is running. This gives the possibility to calculate the field drift that would have occurred without the dynamic compensation. The uncompensated field is determined by

$$B_{i,\text{unc}}(t) = B_i(t) - \sum_j A_{ij} I_j \,. \tag{3.25}$$

Figure 3.17 shows the compensated and uncompensated field of a long-term measurement performed over the course of a night. Eleven hours after the start of the measurement a field change happened that the ACS successfully compensated. At that time regular operation in the experimental hall started. The spread of the uncompensated field is slightly higher than that of the compensated field. In other words, there are small field changes on short time scales that the ACS compensates.

A standard way to illustrate the temporal stability of clocks is to plot them as an Allan deviation. This concept also can be applied to the temporal stability of an environmental parameter, here the magnetic field. The Allan deviation [88] originally was used to quantize the stability of atomic frequency standards, but it can be used to check any system for its temporal characteristics. The Allan deviation is the square root of the Allan variance, which is essentially a moving window of length τ for a waveform. Within each time interval the variance is determined and afterward all values corresponding to τ are averaged. The Allan deviation is dominated by noise for small τ and by drifts for large τ. Typically the minimum

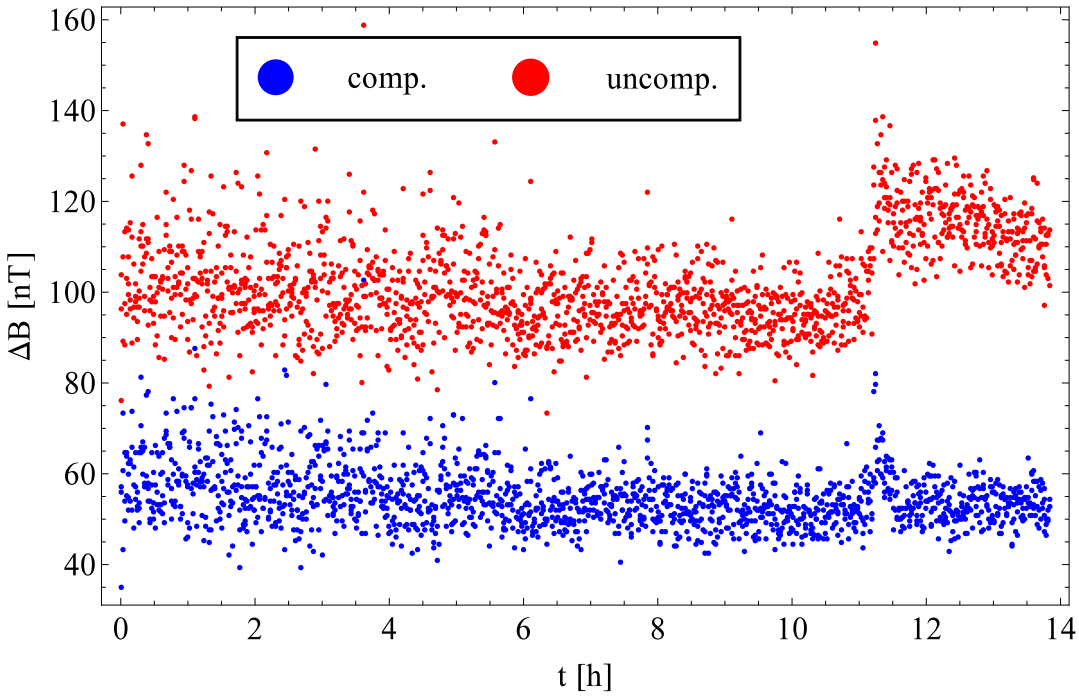

Figure 3.17.: Long-term measurement of the external field: All field values are determined according to equation 3.24. The uncompensated field (red) experiences a permanent field drift 11 hours after the start. The compensated field (blue) is also affected by the same field change, but reaches its previous level shortly after. The time of the disturbance corresponds to the start of regular operation in the experimental hall. For t <7 h (until midnight), the noise level is higher than in the second half measurement. The reason for this noise reduction is not known. For illustrative purposes, the uncompensated field is shifted by +30 nT.

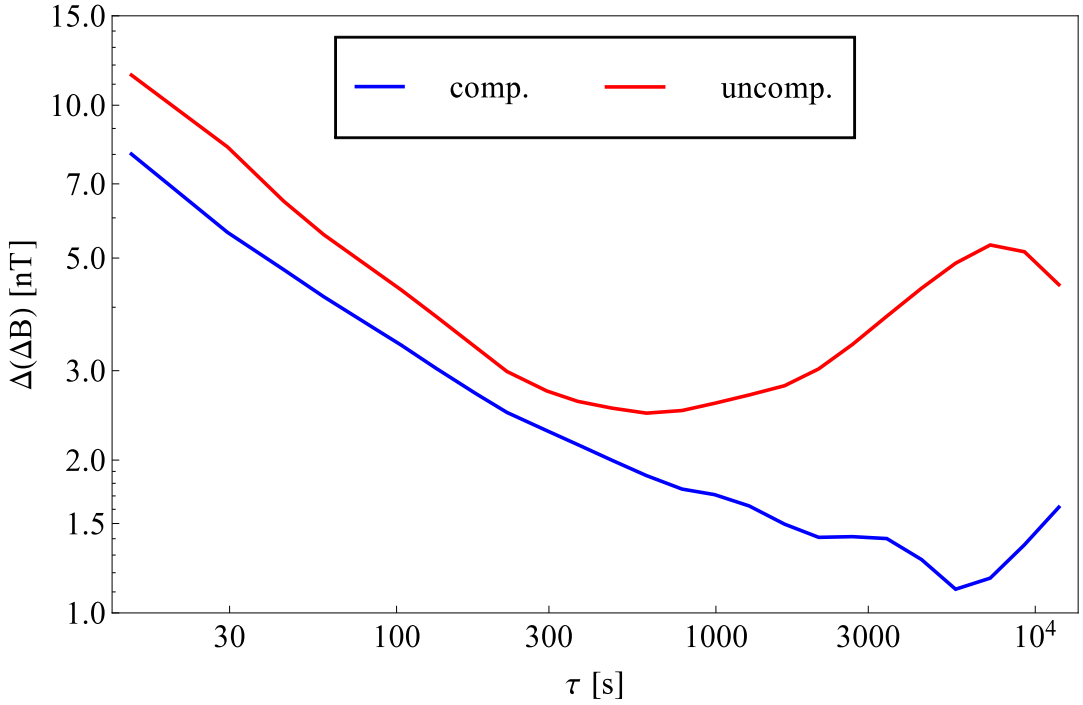

Figure 3.18.: Allan deviation of the compensated and uncompensated field: The uncompensated (red) field has a slightly higher noise and is dominated for τ >1000 s by the field drift. It reaches a minimum of 2.5 nT at 370 s. The field jump at t=11 h in the time series (figure 3.17) causes a reduced stability for longer integration times τ. The ACS compensates for this jump and hence the stability is significantly improved. The compensated field is more stable and has its minimum of 1.1 nT at 5600 s.

of the Allan deviation indicates the optimal integration time for the most sensitive measurement.

Figure 3.18 shows the temporal stability of ΔB, corresponding to the long-term measurement. The compensated field feature an overall increased field stability compared to the uncompensated field. For an integration time of $t \approx 6000$ s the compensated field is stable to 1.1 nT. The uncompensated field is strongly influenced by the permanent field jump, resulting in worse stability at longer integration times. The best stability of the uncompensated field is reached at 360 s with 2.5 nT.

4. Stability of the magnetic field inside the nEDM apparatus

The internal fields of the apparatus consist of the uncompensated parts of the external field, the remanent field of the shield and any artificially generated field (e.g. B_0-coil). These internal fields are more important than the external fields. In this work only the first two contributions are discussed, as the artificial fields easily can be disentangled. Passive shields show a good performance in shielding high frequency noise [72], so typically any Allan deviation is dominated by the noise of the sensor used. Therefore field measurements with fluxgates and SQUIDs are performed to characterize the passive shields.

4.1. The magnetically shielded room (MSR)

The basics of a temporal stability measurement are fairly simple. One or multiple magnetometers are placed at the center of the shield and during magnetically "quiet" times (e.g. nights and weekends) long time series of data are taken. In parallel, environmental parameters are recorded to correlate them with a potential field change. Before a long-term measurement, the MSR has to be degaussed, otherwise the first portion of the data is dominated by the drift of the passive shield to its new equilibrium.

4.1.1. Fluxgate-based shield characterization

Figure 4.1 shows a night measurement using three low noise fluxgates (Mag-03IEHVL70[1]) positioned at the center of the MSR. Fluxgates usually have an offset B_{off}, which shifts the real magnetic field B. As this offset is dependent on various parameters (e.g. supply voltage, temperature of sensor electronics and sensing element of the sensor), it does not drop out by analyzing relative field drifts $\Delta B(t) = B(t) - B(t = 0)$. In order to disentangle the offset from a real field change, two of the fluxgates are aligned parallel along the y-direction and the third one is arranged antiparallel to them. The fluxgates have the same power supply and are read out simultaneously with the same electronics. Therefore it can be assumed that their offset drifts comparably.

[1] Bartington Instruments, `http://www.bartington.com/mag-03-three-axis-magnetic-field-sensor.html`

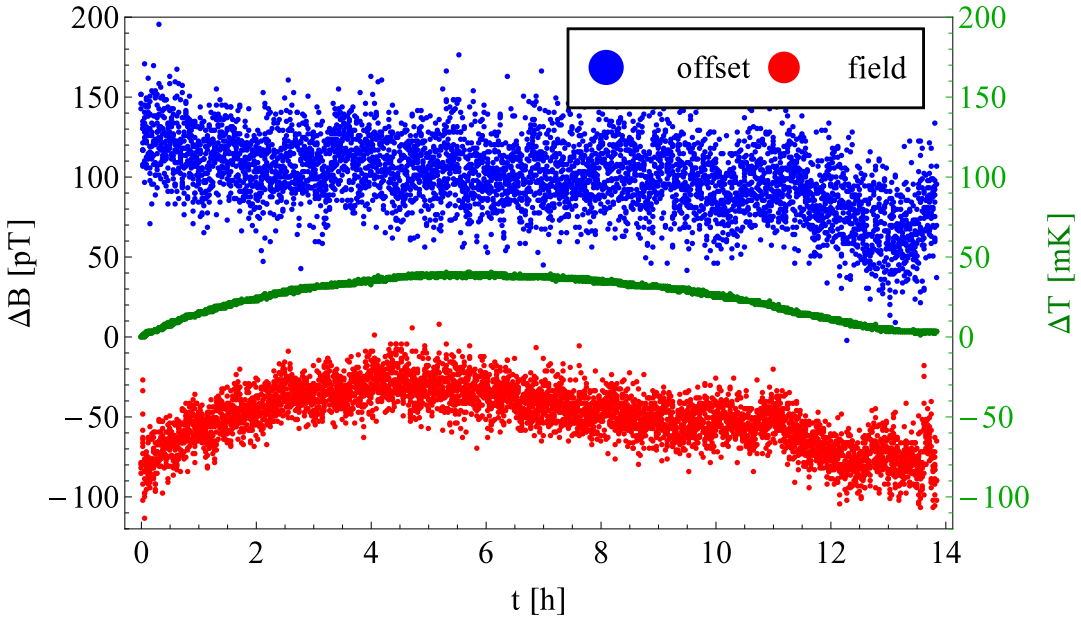

Figure 4.1.: Field drift at the center of the MSR: Three fluxgates in a parallel and antiparallel arrangement along the y-direction (for reference, see figure 3.1) are used to disentangle between electronic offset drift (blue) and field drift (red). The temperature (green) of the Magnifer® is recorded to perform a temperature correction. The field is clearly correlated to the temperature. Field and offset are arbitrarily shifted for illustration purposes.

The difference between the parallel and antiparallel converts to the drift-subtracted field signal, while their sum provides the offset drift. During the 50000 s measurement the offset changes by (-53 ± 1) pT and the field shows a clear correlation to the temperature of the Magnifer® (measured with a PT-1000). The magnetic permeability of the shielding material changes as a result of the temperature change and consequently the magnetization of the shield also changes. Assuming a linear correlation of the field and temperature changes, the correlation factor can be fitted. By neglecting all drift sources except the temperature change, the variation of the correlation factor yields an optimum for the temporal stability. Hence a scaling factor of $\frac{\partial B}{\partial T} = (1.1 \pm 0.1)\,\frac{\mathrm{pT}}{\mathrm{mK}}$ is extracted. The error arises from the 1σ confidence level ($\frac{\chi^2}{dof} = \frac{1578}{1398-2} = 1.13$).

Figure 4.2 is the Allan deviation of the dataset shown in figure 4.1. Up to integration times $\tau < 1000\,\mathrm{s}$ the graphs are dominated by the intrinsic noise of the fluxgates. The noise of the offset is twice as high as that of the field and indicates a correlated noise of the individual fluxgates. Assuming the temperature drift could be avoided, the stability of the field shifts from 2.2 pT at 620 s to 2.1 pT at 1530 s.

4.1.2. SQUID measurements

In case of uncorrelated noise, any Allan deviation scales with the noise level of the applied measurement device. Therefore the use of a more sensitive magnetometer (here a SQUID) is necessary to further characterize the temporal stability of the MSR. SQUIDs are superconducting devices, which measure the magnetic flux [68]. As they are not able to measure the absolute value of the field, they can be seen as a magnetic flux interferometer. In order to measure the magnetic field, it is necessary to keep them constantly below their superconducting transition temperature. Usually this is ensured by submerging them in a bath of liquid helium, housed in a dewar.

The applied SQUID [89, 90] is a multi-channel SQUID with six channels mounted on a cube with a side length of 3 cm. Channels on opposing sides measure the field in anti-parallel directions. By adding (subtracting) opposing channels, the field gradient (value) can be determined. The reservoir of the dewar contains a few liters of liquid helium and offers a maximal operation time of about 16 hours. Figure 4.3 illustrates the dewar and the mounting of the SQUIDs.

The SQUID is positioned in the center of the MSR on a rotation table. The rotation table is operated from the outside of the MSR with strings. By slowly rotating the SQUID back and forth by 180°, the absolute value of the x and y field component can be determined. However, rotating too quickly results in fast field change that could cause the SQUID to lose its lock. After relocking, any previous field information is lost and consequently no absolute field values can be extracted. During a typical night measurement the SQUID does intermittently lose its lock, but the field is not expected to change within such small time scales and therefore the resulting field jumps (so-called Φ_0 jumps) can be corrected for.

Figure 4.4 shows a night measurement performed with the SQUID. The calibra-

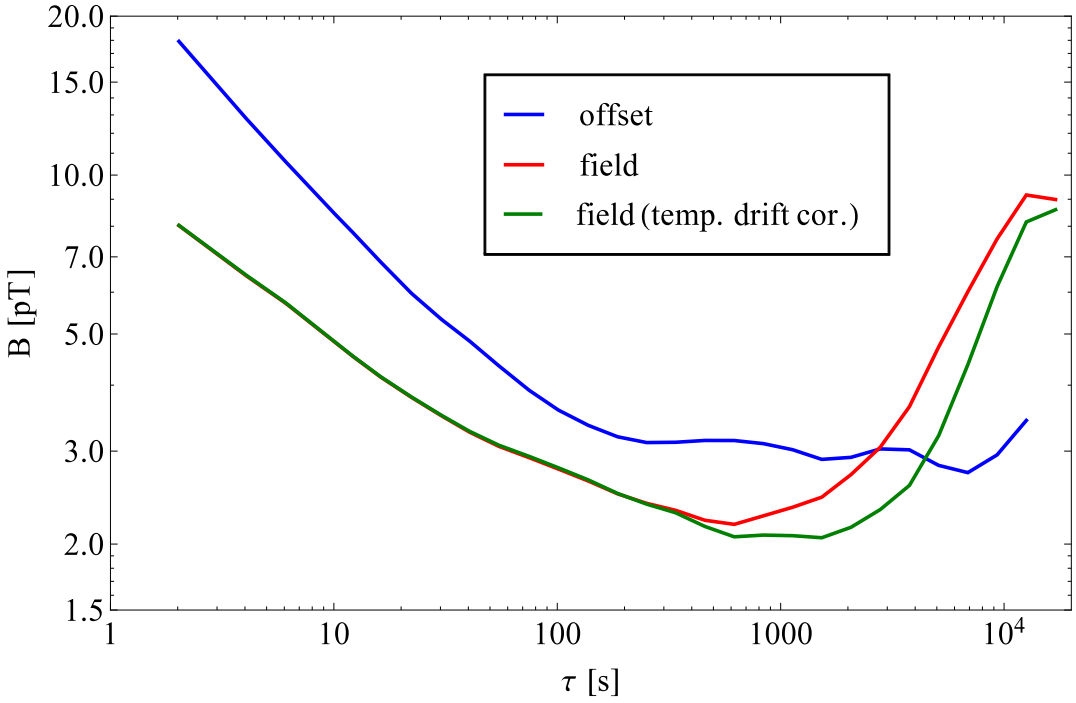

Figure 4.2.: Allan deviation of the fluxgate measurement of figure 4.1. By linearly correcting the field with the temperature change ΔT ($\frac{\partial B}{\partial T} = 1.1 \frac{\mathrm{pT}}{\mathrm{mK}}$), the long-term drift of the field can be suppressed, resulting in an improved stability for τ >500 s. The stability has an optimum of 2.2 pT at τ =620 s for the non-corrected field and 2.1 pT at τ =1530 s for the temperature-corrected field. The fact that the minimum of the temperature-corrected field is not at arbitrary high integration times, indicates that either there are higher-order correlations between temperature and field or other drift sources are present. The electronic offset is mainly dominated by noise. The drift of the offset becomes dominant for $\tau > 10^4$ s and therefore it is not crucial for the characterization of the MSR.

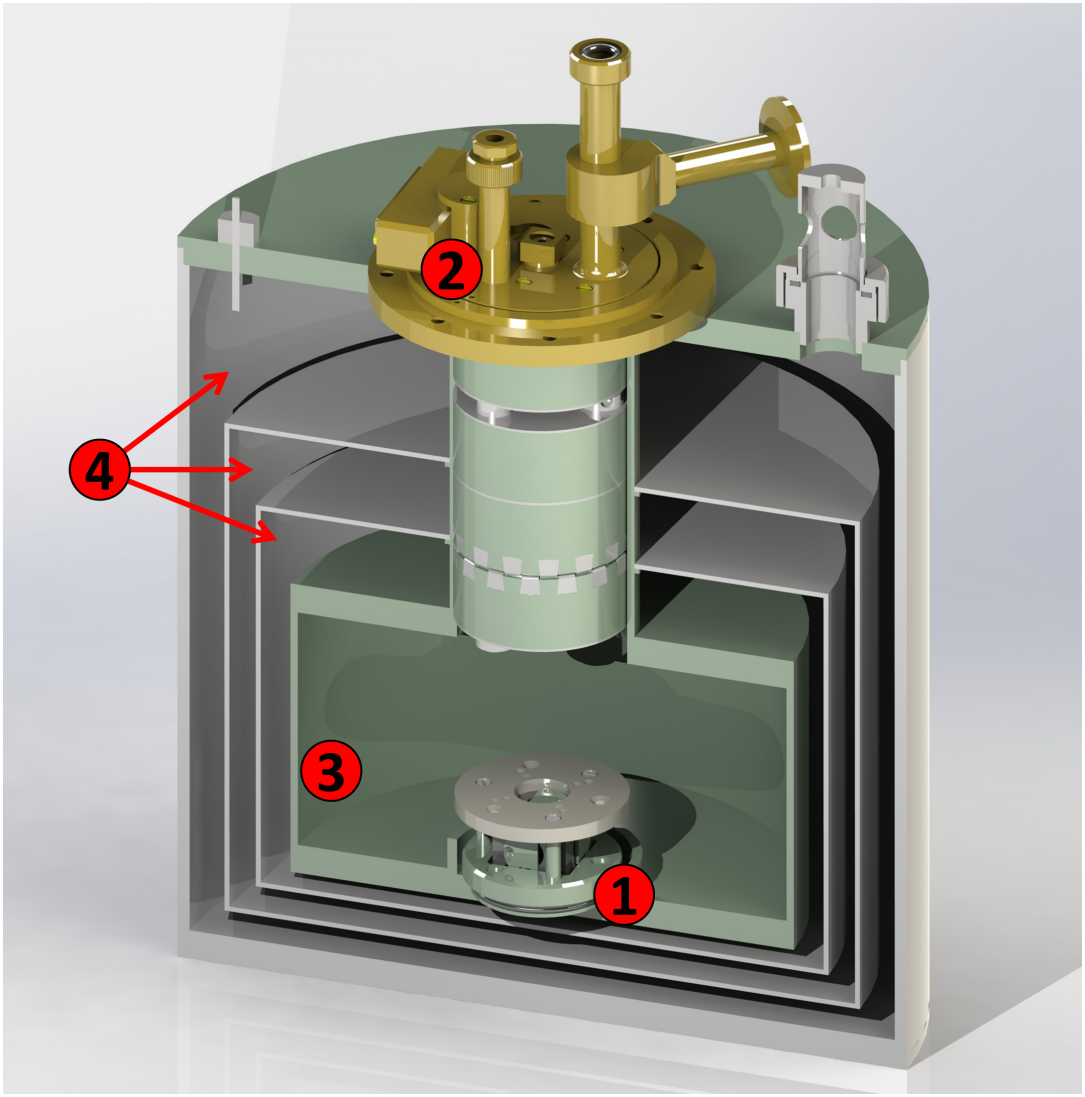

Figure 4.3.: Cut-away view of the SQUID dewar: The SQUIDs are mounted on the six sides of a cube (gray) which is positioned inside in a cylindrical structure (1) at the bottom of the dewar. Item 2 shows the connection to the electronics and the vacuum system. Three evacuated volumes (4) surrounding the liquid helium storage volume (3) reduce the thermal connection to the helium for an operation time of about 16 hours.

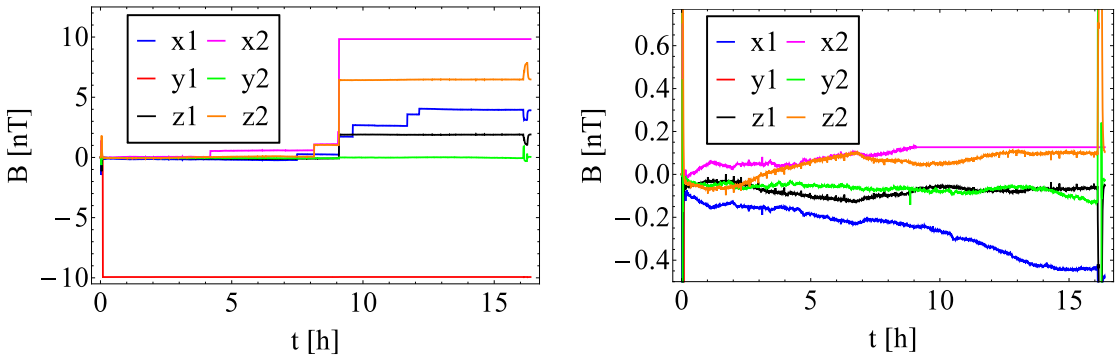

(a) Raw data

(b) Corrected for Φ_0 jumps

Figure 4.4.: Raw data (a) of a long-term measurement with the SQUID inside the MSR: In multiple channels Φ_0 jumps occur, with x2 and y1 railing after 9 hours respectively directly after the calibration rotation. The first character of the label corresponds to the field component the channel is measuring and the second character indicates the relative orientation (1 is parallel, 2 anti-parallel). The Φ_0 jump corrected data are shown in (b).

tion rotations at the beginning and at the end of the measurement show a temporary field change in *all* channels, which is not expected as the z1 and z2 should be invariant to this rotation. This behavior is likely attributed to the helium sloshing inside the dewar. The dewar is not aligned with gravity and therefore rotation of the dewar can cause some internal parts to lose their contact with the helium. Consequently their temperature increases, which could result in a change in the magnetic field. The calibration for the other directions yields an absolute field of $B_x = -0.69\,\mathrm{nT}$ and $B_y = -0.42\,\mathrm{nT}$ at the start of the measurement, respectively $B_x = -0.33\,\mathrm{nT}$ and $B_y = -0.15\,\mathrm{nT}$ at the end. By comparing the drift extracted from the signal sequence ($dB_x = -0.32\,\mathrm{nT}$ and $dB = -0.05\,\mathrm{nT}$), it is shown that both drift determinations yield different values, even with different signs. This is an additional indication that the change in helium level causes unpredictable effects and the presented calibration technique is not sensitive enough for the drift characterization of long-term stability measurements of the MSR. For all further measurements the calibration measurement was omitted and only the signal sequence was analyzed, without any corrections.

At random times the signals of individual channels perform a discrete field jump in integers of $(0.48 \pm 0.01)\,\mathrm{nT}$, which is in good agreement with the specification of the SQUID $0.46\,\mathrm{nT}/\Phi_0$ [90]. The discrete nature of these field changes allows for an easy correction by adding the negative jump height to the signal after the field jump. As the field change within this time scale is negligible compared to the field jump, the Φ_0 correction does not have an observable effect on the following analysis.

Channel y1 reached the over-range limit of 10 nT directly at the end of the calibration procedure. The same happened to x2 at around 9 hours after the start of the measurement. When a channel is in an over-range status, it constantly measures

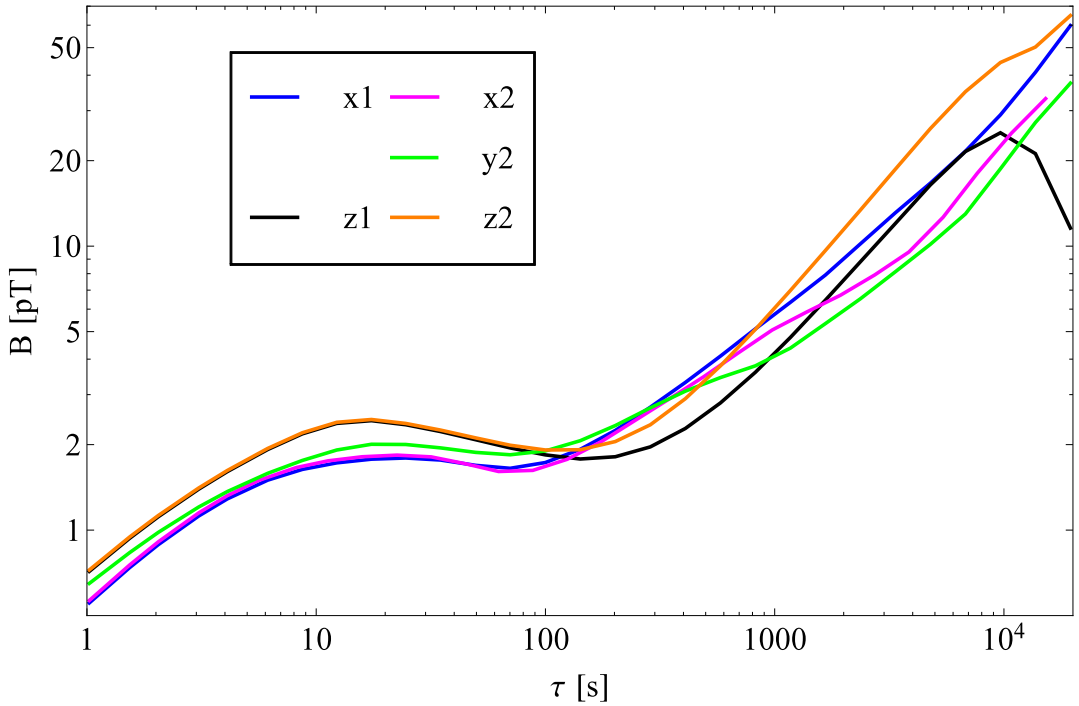

Figure 4.5.: Allan deviation of the SQUID measurement of figure 4.4b. The temporal stability is mainly dominated by the drift of the SQUID system. There also must be a noise source with a period of ∼20 s. This is indicated by the local maximum at 20 s. For longer integration times the noise contribution of this source averages out. As y1 went into the over-range limit at the beginning of the measurement, the stability of y1 cannot be determined and thus is not shown here.

only the maximum value and all potential field changes become invisible. The Φ_0 correction does not work in this case and the data of that specific channel can only be used up to the point reaching the over-range.

Figure 4.5 shows the Allan deviation for all channels, except y1. They all are dominated by drift processes, as the overall trend is increasing. The local maximum at 20 s indicates a periodic noise source which averages out for larger integration times. The local minima are 1.65 pT at 70 s, 1.83 pT at 70 s and 1.78 pT at 140 s for the x, y and z components of the field. Compared to the results of the fluxgate measurement the absolute value of minima are almost the same, but their positions are shifted. As expected the fluxgates show a better long-term drift behavior, but the SQUIDs are more sensitive for short integration times.

Both measurements are combined in figure 4.6. For each integration time τ, the best value for the temporal stability is taken, with the fluxgate measurement covering long integration times (τ >250 s) and the SQUID measurement covering short integration times (τ <250 s). It still is not possible to disentangle the temporal stability of the MSR from the drift and noise characteristics of the applied magne-

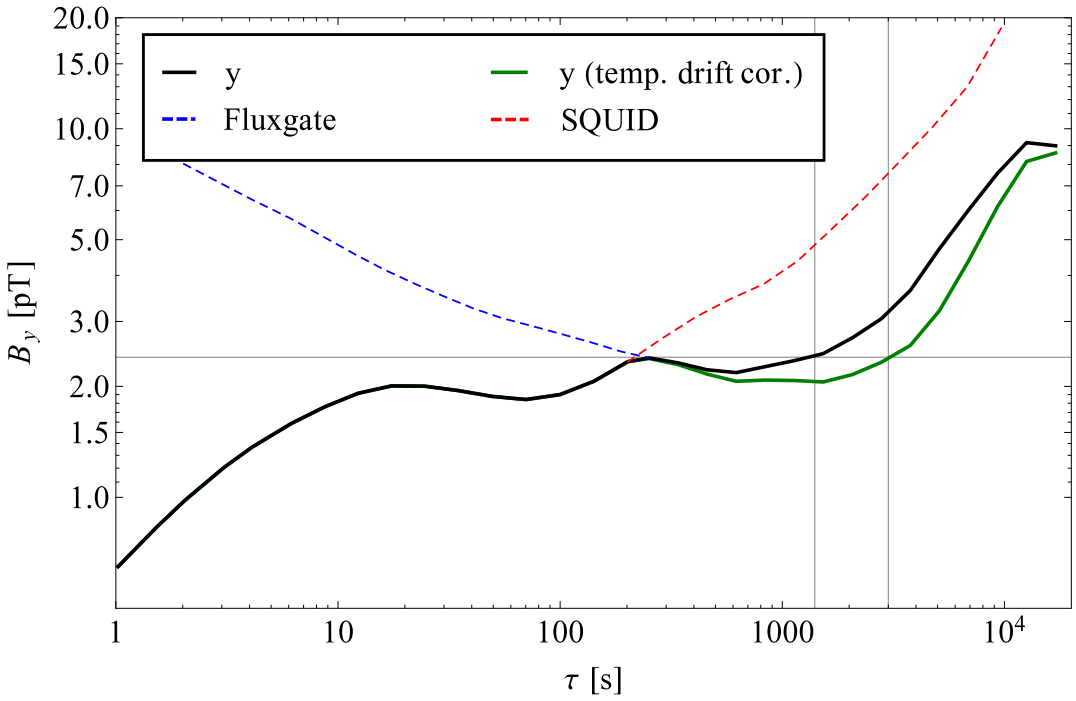

Figure 4.6.: Combined Allan deviation of the MSR measurements: The fluxgate (figure 4.2) and SQUID (figure 4.5) measurements are plotted in one plot and the best of the two stability values for the corresponding integration time τ is shown in black (green, assuming the temperature drift could be avoided) for the y-direction. The portion of the measurements that does not contribute to the combined value is also shown (dashed lines). Both measurements complement each other in terms of noise and drift behavior, resulting in a temporal stability of <2.4 pT for τ <1400 s or τ <3000 s assuming the temperature is stabilized.

tometers. They do however cover different integration time regimes and therefore the field of the MSR is stable to approximately 2.4 pT for integration times $\tau < 1400\,\mathrm{s}$ without and $\tau < 3000\,\mathrm{s}$ with temperature correction. Though both measurements have not been performed simultaneously, environmental conditions – like temperature drift and night measurement – have been similar. The temperature drift during the SQUID measurement followed a linear behavior with $\sim 5\,\mathrm{mK/h}$ for $t < 9\,\mathrm{h}$ and $\sim 15\,\mathrm{mK/h}$ for $t > 9\,\mathrm{h}$. Although the drift was worse compared to the fluxgate measurement, the stability for short integration times ($\tau < 200\,\mathrm{s}$) is not significantly influenced, as temperature drifts are slow and therefore mainly contribute to the stability for long integration times ($\tau > 200\,\mathrm{s}$). The local maximum is defined by crossing point of the fluxgate and the SQUID measurements.

4.2. Field stability of the full nEDM shield

After the installation of the insert inside the MSR, similar long-term measurements to characterize the temporal stability of the full shield (MSR + insert) were performed. At that time a second SQUID system [91] was borrowed and used in parallel to the previously presented SQUID. It features 16 channels, of which 12 (4 per direction) are used for the analysis. To distinguish between the two SQUIDs, going forward, the 6-channel SQUID will be called "SQUID-6" and the borrowed SQUID "SQUID-16". The channels that were not used showed very little response to external changes It was assumed that these 4 channels were not operating properly and were therefore excluded.

Fluxgates were not used during the measurement, as they are not expected to be sensitive enough for this kind of measurement. The temperature of the insert was monitored indirectly by measuring the temperature inside the MSR, which shows a linear drift of $14\,\mathrm{mK\,h^{-1}}$. Though the MSR and insert were not not thermally coupled, the temperature inside the insert is expected to follow a similar trend, dampened in amplitude and delayed in time. The increased complexity of the shield and the presence of SQUID-16 makes a calibration (rotating) measurement almost impossible and therefore a calibration was not performed. Hence no corrections are applied to the raw signals, except the correction for Φ_0 jumps.

Figure 4.7 shows a long-term night measurement, during which both SQUID systems were used to measure the magnetic field. The first hour of both measurements are dominated by large drifts. While the SQUID-16 stabilizes after this drift period to an overall field change of $< 5\,\mathrm{pT}$ in 8 h, the SQUID-6 drifts in some channels up to 50 pT. Both devices showed Φ_0 jumps during their operation, though with reduced frequency of occurrence compared to the measurements with only the MSR. The data are shown has already been corrected for these steps.

The SQUID-6 experiences a quick field change in the y and z channel at $t \approx 5.5$ h. In order to quantize the stability of the shield and avoid the effect of this jump, a time interval of 3 h ($2\,\mathrm{h} < t < 5\,\mathrm{h}$) is analyzed. This is still much larger than a typical EDM run ($T_{\mathrm{EDM}} \sim 250\,\mathrm{s}$). For the SQUID-16 the interval is set to ($3\,\mathrm{h} < t < 6\,\mathrm{h}$), as it showed there the highest stability. The relative drift of the temperature of

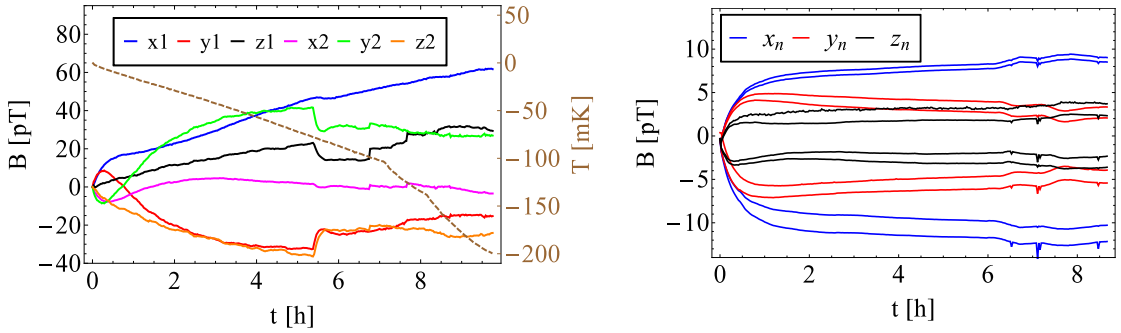

(a) SQUID-6 (b) SQUID-16

Figure 4.7.: Φ_0 jump corrected field measurement inside the full nEDM shield: The SQUID-6 (a) and the SQUID-16 (b) are operated simultaneously, with the latter showing almost an order of magnitude smaller drift. Due to the indistinguishability of the individual SQUID channels per direction of SQUID-16, those channels are labeled in the groups x_n, y_n and z_n. For reference, the temperature of the MSR is shown by the dashed brown line in (a). The temperature of the insert was not measured, but is expected to follow the temperature of the MSR with a temporal delay and a dampened amplitude. Further explanation can be found in the text.

the MSR was similar for both intervals the (assuming the temperature of the insert follows the temperature of the MSR). The fact that all environmental conditions were constant up to the time when regular technical operations started ($t \approx 6\,\mathrm{h}$), indicates that the change of the magnetic field is still dominated by the drift characteristics of the SQUIDs. Hence the freedom in choice of the time interval is justified. One of the z channels of the SQUID-16 showed an increased noise with an amplitude that is not observed in any other channel. This noise was therefore considered to be of electronic nature.

As before, the temporal stability is illustrated through the Allan deviation, shown in figure 4.8. Both SQUIDs feature a monotonic rise, with the SQUID-6 having a temporal stability of 300 fT (100 fT for x2) for an integration time of 250 s, respectively 10 fT measured by the SQUID-16. One of the z channels of SQUID-16 (see figure 4.7b upper black line) measures an increased noise compared to the other z channels. This channel then also shows a different behavior in the Allan deviation, resulting in a poor stability for τ <1000 s. However, only one channel measures this increased noise and hence it attributed to the intrinsic noise of that specific channel and not to the stability of the shield.

Similar to the previous section, the presented measurements of the full nEDM shield are very likely dominated by the characteristics of the applied magnetometers. In other words, these measurements of the temporal stability of the shield provide only a conservative estimate of the shield's capabilities.

Both SQUIDs have multiple channels per direction and therefore the determina-

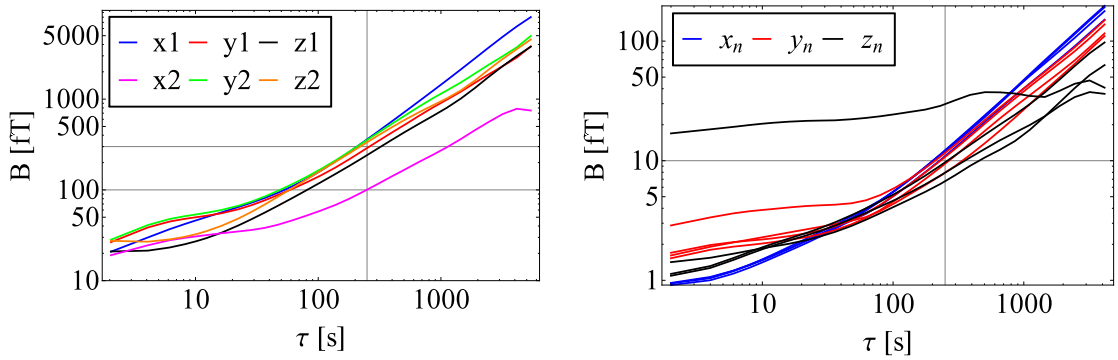

(a) SQUID-6

(b) SQUID-16

Figure 4.8.: Temporal stability of the full nEDM shield: Both Allan deviations are mainly dominated by drifts, which is very likely attributed to the drift behavior of the SQUIDs. The SQUID-16 shows an almost 10-times improved performance compared to the SQUID-6, resulting in a temporal stability of about 10 fT in 250 s.

tion of the local field gradient is possible. Environments with very low and stable magnetic field gradients are required by many applications. For example geometric phases and spin depolarization rates are strongly influenced by gradients.

The SQUID loops are separated by 3 cm for the SQUID-6 and 5 cm for the SQUID-16. The malfunctional channel of the SQUID-16 is not used to determine the gradient. Figure 4.9 shows the temporal stability of the field gradient expressed through the Allan deviation. Both SQUIDs seem to be dominated by their drift characteristic and the results are considered a conservative estimate for the performance of the shield.

The SQUID-6 measurement yields a field gradient $\frac{dB}{dr}$ stability of 2.6 pT/m for the y direction and 12.2 pT/m for the z direction, with the value for the x direction in between. With a range of 135 fT/m to 300 fT/m SQUID-16 improves upon the SQUID-6 result by about a factor of 20. As with the measurement of the field stability, the gradient stability is also considered to be an upper limit, as the measurements are very likely dominated by the drift characteristics of the magnetometers.

During one of the long term measurements, the ACS was switched from *static* to *dynamic* mode every 1000 s. The reason for this approach was to test under similar conditions the influence of the ACS on the field stability. For every 1000 s interval the Allan deviation is calculated and the average of Allan deviations is shown in figure 4.10. The measurements of both SQUIDs do not reveal a difference between the compensation modes. As the drift characteristics of the magnetometer conceal the real field stability, any effect of the ACS – be it negative or positive – does not influence the temporal stability on a verifiable level.

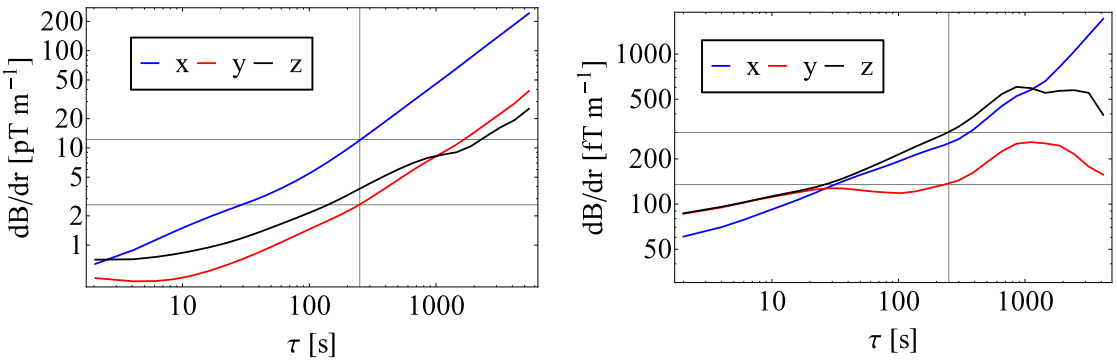

(a) SQUID-6 (b) SQUID-16

Figure 4.9.: Temporal gradient stability of the full nEDM shield: The stability measured with the SQUID-6 ranges from 2.6 pT m^{-1} to 12.2 pT m^{-1} for a integration time of 250s, respectively 135 fT m^{-1} to 300 fT m^{-1} measured with the SQUID-16. It has to be pointed out that the range of the y-axes in the plots for SQUID-6 (a) and SQUID-16 (b) are different.

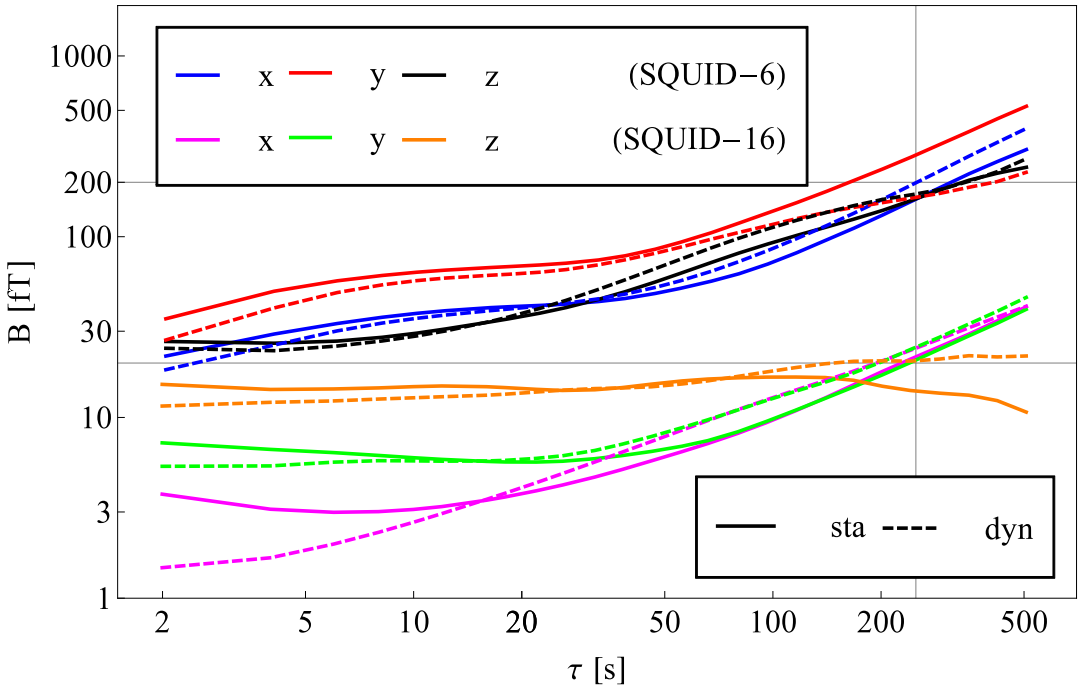

Figure 4.10.: Temporal field stability with alternating ACS compensation mode: During the measurement the compensation mode of the ACS was switched between static and dynamic every 1000 s. The resulting Allan deviations are averaged. No difference between modes is observable.

4.3. Conclusion

To further characterize other properties of the insert (ambient field and B_0 homogeneity), it was taken out of the MSR. As no magnetometer with better drift behavior was available at the time of the removal, the full potential of the field and gradient stability could not be determined. Nevertheless the presented stability regarding field and gradient is remarkable, given that the temporal stability in similar shields, e.g. the "Berlin Magnetic Shield Room 2" (BMSR-2) at the Physikalisch-Technische Bundesanstalt (Berlin, Germany), is about an order of magnitude worse [92].

The nEDM experiment uses a double chamber approach and therefore the field gradients induce a frequency shift equivalent to a false EDM. Hence the gradient stability is directly connected to the systematic error of an EDM run.

The design parameters for the nEDM experiment are an electric field of $E \approx 20\,\mathrm{kV\,cm^{-1}}$ and a distance between both chambers of $l \approx 10$ cm. With the magnetic moment $\mu_n \approx 60\,\mathrm{neV\,T^{-1}}$ equation 1.8 yields

$$d_{n,\mathrm{sys}} = \frac{\mu}{2E}\frac{\partial B}{\partial r} l = 3 \cdot 10^{-26}\,\mathrm{e \cdot cm}\,, \tag{4.1}$$

assuming a temporal gradient stability of $\frac{\partial B}{\partial r} \approx 200\,\mathrm{fTm^{-1}}$. As a side note, the temporal field stability of about 10 fT leads to a comparable sensitivity for a single chamber.

As a typical EDM run takes about 250 s, around 100 runs per night can be performed. By measuring 100 nights, a total number of 10^4 is a rough estimate for the data taking of a year. Assuming that there is no correlation between the switching of the magnetic field (which reverses the symmetry of the experiment and is done to check for systematics) and the direction of the field drift, the field drift can be considered to behave stochastically. Hence by averaging the 10^4 runs, magnetic field drifts yield an error contribution of $3 \cdot 10^{-28}\,\mathrm{e \cdot cm}$ to nEDM sensitivity.

With this sensitivity the current limit for the neutron EDM could be improved by almost two orders of magnitude. The application of various magnetometer systems makes it possible to measure the field and gradient drifts. Because of this capability, each measurement run can be corrected for, yielding a decreased systematic error per EDM run. With regards to the magnetic field and gradient stability, the sensitivity goal of a few $10^{-28}\mathrm{e \cdot cm}$ at a 90% confidence level is feasible.

5. Search for magnetic monopoles

Due to its extremely high shielding factor, the nEDM shield on its own is a highly applicable instrument for high precision experiments, providing a very low magnetic noise environment. Next to its primary purpose for the search for the neutron EDM, other system can also be investigated for EDM signals. Other, non-EDM-related exotic physics can be studied. As noted in the previous chapter, SQUIDs are ideal magnetic flux detectors with a very high sensitivity. Placed in a highly shielded magnetic environment, they can be used to search for spontaneous field changes. A moving particle carrying a magnetic charge – a so-called magnetic monopole – could be the source for such a field change. Therefore SQUID data can be analyzed to search for potential monopole signals. On the example of the search for magnetic monopoles, the high capability of the presented magnetic shield will be demonstrated.

In this chapter a brief overview of the theory of magnetic monopoles (hereafter referred to as simply "monopoles") and the previous attempts to measure them is given. The general concept of using SQUIDs as monopole detectors is presented, with data taken with a SQUID within the nEDM shield providing an example implementation of these techniques. Finally, the sensitivity of such detectors is discussed and compared to other types of monopole searches, with an outlook for further future improvements.

5.1. Magnetic monopoles in theory and experiment

In order to symmetrize Maxwell's equations of electromagnetism, Dirac introduced in 1948 the concept of magnetic monopoles [93]. Gauss's law for magnetism $\nabla \cdot \mathbf{B} = 0$ is replaced by $\nabla \cdot \mathbf{B} = \mu_0 \rho_m$, which is symmetric to $\nabla \cdot \mathbf{E} = \frac{\rho_e}{\epsilon_0}$ [94]. Together with $\nabla \times \mathbf{B} = \epsilon_0 \mu_0 \frac{\partial \mathbf{E}}{\partial t} + \mu_0 \mathbf{J}_e$ and $\nabla \times \mathbf{E} = -\frac{\partial \mathbf{B}}{\partial t} - \mu_0 \mathbf{J}_m$, they form the Maxwell equations with magnetic monopoles, with ϵ_0 and μ_0 the vacuum permittivity and the vacuum permeability, $\mathbf{J}_e$ and $\mathbf{J}_m$ the electric and magnetic currents, and $\mathbf{E}$ and $\mathbf{B}$ the electric and magnetic field.

Many grand unified theories (GUT) naturally include magnetic monopoles [95, 96]. A monopole defined within the framework of a particular GUT does not necessarily have the charge of a Dirac monopole. However, in the frame of this work, for simplicity only monopoles with the Dirac charge are taken into consideration. The mass of the monopole is strongly model dependent, ranging from 10^{14} GeV up to 10^{22} GeV [96]. Thus their direct production in collider experiments is impossible with current technology and unlikely ever to be achieved.

A simple illustration for a monopole is a semi-infinitely long, infinitely thin solenoid of magnetic flux, with magnetic field lines pointing isotropically in all directions from its finite end. The form of the field lines is then equivalent to the electric field of a point charge, meaning this end of the solenoid may be interpreted as a magnetic point charge ("monopole").

Dirac modified the equation of electromagnetism and argued that if magnetic monopoles exist, the magnetic flux crossing any closed surface has to be zero, except for *one* point on any surface, resulting in a string extending outward from the pole [93]. Dirac further motivated that the string itself is "unphysical" [93]. In addition, the electric charge e and magnetic charge g are quantized (for details see e.g. [93, 96]): $\frac{1}{4\pi}\frac{eg}{\epsilon_0 c} = \frac{1}{2}\hbar c$ (the factor $\frac{1}{4\pi\epsilon_0 c}$ occurs through the transformation from the cgs system to the SI system). In SI units the charge of the Dirac pole is $g_D = 3.29 \cdot 10^{-9}$ Am.

Next to the symmetrization of electric and magnetic nature and the quantization of e and g, the discovery of monopoles could answer fundamental questions and provide proof of physics beyond the SM. Monopoles only interact weakly with regular matter, making them also potential dark matter candidates. Cosmological arguments (e.g. the total mass of all monopoles must be smaller than the mass of the universe and consistency with the cosmological constant) can be used to derive an upper limit for the particle flux of monopoles: 10^{-16} to 10^{-13} $\mathrm{cm}^{-2}\mathrm{s}^{-1}\mathrm{sr}^{-1}$ [97].

There have also been a few attempts to search for magnetic monopoles directly. Monopoles should have been produced in large numbers after the Big Bang. Assuming the conservation of magnetic charge, they cannot decay into lighter particles. (There may be multiple particles carrying the magnetic charge, but for simplicity "monopoles" only refer to the lightest of these particles.) The only process to decrease the total number of monopoles is annihilation with anti-monopoles. After the inflationary epoch their density should have decreased dramatically and therefore the collision rate between monopole and anti-monopoles is strongly reduced. As of now, no monopole signal has ever been found and only upper limits for the monopole flux have been extracted. Monopoles trapped in matter have also been sought, e.g. in lunar material [98] or deep-sea sediments [99], yielding null or inconclusive results.

There are three processes which can be used to detect magnetic monopoles [96].

- **Induction**: The magnetic field of a moving magnetic charge can be measured with a SQUID. As the monopole passes through the superconducting ring of the SQUID, the flux permanently increases by $2g$. A monopole which only passes nearby and not through the ring, evokes a temporary field change. In both cases the monopole is observed by the measurement of its most basic properties: the magnetic flux and the magnetic field.

- **Ionization**: Like electrically charged particles, magnetically charged particles may also ionize matter. This process is velocity dependent and in addition hard to quantify as the interaction of slow magnetic monopoles with matter (e.g. energy transfer) is not well understood. It is assumed that the field change of a monopole with $v < 10^{-4}c$ is slower than the velocity of the electrons.

Therefore the field change is adiabatic and no energy is transferred.

- **Catalysis**: In the vicinity of magnetic monopoles, nucleon processes at the GUT scale are possible and could then trigger the decay of nucleons. Hence a monopole moving through a dedicated detector would leave a trace of decaying nucleons, which then may be detected by searching for the corresponding decay products.

In 1982, B. Cabrera employed the induction process to search for monopoles, using a SQUID detector with a $20\,\mathrm{cm}^2$ superconducting ring with 4 loops [100]. In this case a 8 $\Phi_{0,C}$ jump is expected, with the flux quantum $\Phi_{0,C} = \frac{h}{2e}$. The C indicates that Cooper pairs [101] are used as the charge for the more general flux quantum $\Phi_0 = \frac{h}{n \cdot e}$. (The value of the flux quantum is important to extract the expected signals of monopoles in section 5.3.) The experiment was shielded from external field changes with a passive magnetic shield, similar to the shield of the nEDM experiment, only smaller in size and also with a higher shielding factor (smaller shields typically suppress external fields better). In 151 days of live-time only one candidate event was recorded, but it was not identified as a monopole, as it also could have been an internal stress release of the magnetic shield. The experiment resulted in an upper limit of $6.1 \cdot 10^{-10}\,\mathrm{cm}^{-2}\mathrm{s}^{-1}\mathrm{sr}^{-1}$.

The MACRO collaboration [102] put very good limits on the flux of monopoles for the two other processes, Ionization and Catalysis. MACRO is an underground experiment at the "Laboratori Nazionali del Gran Sasso" lab (Gran Sasso Mountain, Italy). It consists of liquid scintillators, "streamer tubes" (gaseous ionization detectors) and nuclear track detectors arranged in a ~ 9000 m^3 area. An upper limit of $1.5{-}2{\cdot}10^{-16}\,\mathrm{cm}^{-2}\mathrm{s}^{-1}\mathrm{sr}^{-1}$ ($3{\cdot}10^{-4} < \beta < 1$) for ionization and $3{-}4{\cdot}10^{-16}\,\mathrm{cm}^{-2}\mathrm{s}^{-1}\mathrm{sr}^{-1}$ ($10^{-4} < \beta < 6 \cdot 10^{-3}$) for the catalysis process.

By comparing the limits, the MACRO experiment is shown to be greatly superior to the Cabrera experiment and it is very unlikely that future induction-based experiments would be able to reach the sensitivity of the MACRO measurements. Nevertheless, the search for monopoles using the induction method is attractive as it is model independent.

A very important parameter is the expected velocity window of monopoles. As no monopole has ever been found, their typical velocities are unknown and therefore theoretical arguments have to be used to confine the velocity regime. Monopoles are massive particles and therefore affected by gravity. A characteristic v may then be estimated using e.g. the escape velocities of planets, solar systems or galaxies. For the earth this results in $v \approx 10^{-4} - 10^{-3}c$. Next to gravity, magnetic gradients accelerate or decelerate monopoles, but for monopoles with mass $m < 10^{17}\,\mathrm{GeV}$ gravitation is the dominant force [96]. In addition, monopoles can lose energy through interaction with matter. Taking these factors into consideration, it is reasonable to expect a velocity window of $10^{-5}c - 10^{-2}c$ to be of interest for the search of free monopoles.

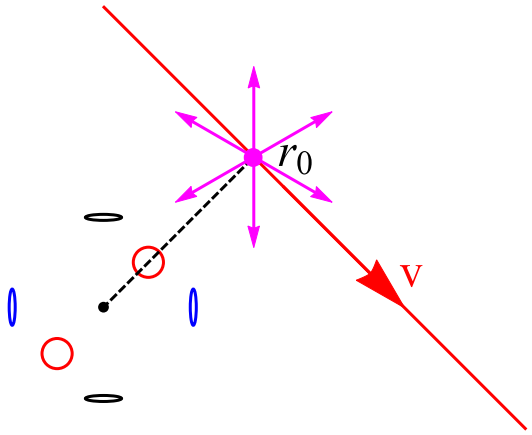

(a) Illustration

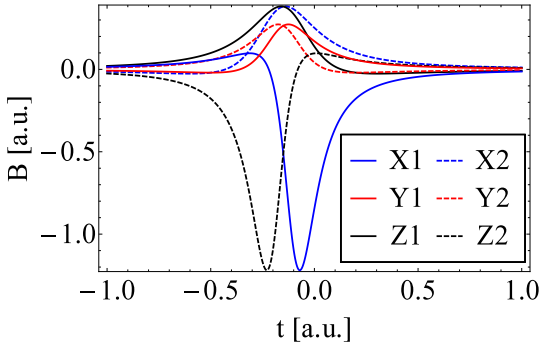

(b) Detector signals

Figure 5.1.: Illustration of a monopole passing by the SQUID detection system (a). The blue, black and red colored circles indicate the superconducting rings of the SQUID system. The expected field profile (b) is asymmetric with respect to the field strength in channel 1 and 2, because the monopole approaches one of them more closely.

5.2. Time-resolved field induction method

A moving monopole can be regarded as a small magnetic field distortion, where the center of the distortion moves along a linear path. Even if there are strong scattering mechanisms, the high mass of monopoles would suppress a noticeable change in path direction on length scales of laboratory experiments. In analogy to the point-like field of the electron the local field of a monopole can be expressed as:

$$\mathbf{B}_m(\mathbf{r}) = \frac{\mu_0 g}{4\pi}\frac{\mathbf{r}}{r^3} = \frac{\mu_0 g}{4\pi}\frac{\mathbf{r}-(\mathbf{r}_0+\mathbf{v}\cdot t)}{|\mathbf{r}-(\mathbf{r}_0+\mathbf{v}\cdot t)|^3}\,, \tag{5.1}$$

with $\mathbf{r}_0$ an arbitrary point along the flight path (here chosen to be the point closest to the center of the SQUID system). (This technique is not restricted to a SQUID magnetometer, but the requirements on the bandwidth and sensitivity make them superior compared to other magnetometer types.) Figure 5.1 shows an illustration of the detection system and an example detector signal.

5.2.1. Detection principle

The illustration (figure 5.1b) shows an ideal signal profile with an infinite time resolution and without noise, but real signals are recorded with the SQUID system and a digitizer card (operated at 1 MHz with 6 channels and 16-bit)[1]. As a result, a very fast particle would possibly be measured with only a few data points recorded,

[1] D-TACQ Solutions Ltd., ACQ425ELF, `http://www.d-tacq.com/acq400ds/acq425elf-product-specification.pdf`

or even just single point. In addition, the signal has to be distinguished from noise. Both the recording frequency f and the noise level $\mathbf{B}_n$ are the main contributors to the measurement sensitivity. Signals $\mathbf{B} < \sigma\mathbf{B}_n$ are considered as noise and rejected. σ is used to tune the acceptance efficiency of the detection algorithm. Passing events are handled in an offline analysis.

In contrast to monopoles, external noise sources produce a signature in all channels. This allows a discrimination, further discussed in section 5.2.3. To calculate the contribution of decay particles, cosmic particles and thermal neutrons (produced at the FRM2) to false signals, the field generated by dipole at a distance of r is compared to the noise level of the detection system ($|\mathbf{B}_n| = 0.3\,\mathrm{pT}$). The maximal field of a dipole is

$$|\mathbf{B}| = \frac{\mu_0 m}{2\pi r^3} \tag{5.2}$$

with m the magnetic moment of the particle, approximated here by the Bohr magneton ($\sim 10^{-24}\,\mathrm{J\,T^{-1}}$). The characteristic distance is then

$$r = \left(\frac{\mu_0 m}{2\pi|\mathbf{B_n}|}\right)^{\frac{1}{3}} \approx 1\,\mu\mathrm{m}\,. \tag{5.3}$$

Assuming an effective detection area $A = 4\pi r R_{\mathrm{SQUID}} = 10^{-8}\,\mathrm{m}^2$ defined by the superconducting ring of the SQUID (radius $R_{\mathrm{SQUID}} \approx 0.7\,\mathrm{mm}$), a cosmic muon flux of $\sim 100\,\mathrm{s^{-1}m^{-2}}$ [5] corresponds to 1 expected event in 14 days. Due to the r^{-3} dependency dipole events can be distinguished from monopole events ($\propto r^{-2}$), as the signal width is much smaller for dipoles. In addition, natural sources (cosmic radiation and decay) mostly produce "dipoles" with high velocities $\beta > 10^{-3}$.

Neutrons (with a magnetic moment of $\mu_{\mathrm{N}} = -9.662 \cdot 10^{-27}\,\mathrm{J\,T^{-1}}$ [5]) produce a field of 1 pT at a distance of ≈ 100 nm. UCN typically have velocities of $\sim 5\,\frac{\mathrm{m}}{\mathrm{s}}$ and hence a UCN moving through or close to a SQUID yields a signal with a length of about 20 ns. Consequently, neutrons are not resolvable by the presented SQUID.

Following the above argumentation, the noise is assumed to be mainly Gaussian with a probability density function $e^{-\frac{(B-\overline{B})^2}{2(B_n)^2}}$. The probability that white noise produces n consecutive data points with $\mathbf{B} > \sigma\mathbf{B}_n$, which might be misinterpreted as a real signal, is set to the inverse number of recorded events $\frac{1}{f\cdot T}$. This then defines the needed threshold

$$\sigma = \sqrt{\mathrm{Log}(f \cdot T)\frac{2}{n}}\,. \tag{5.4}$$

Table 5.1 shows examples for a few parameter sets.

Data will typically be taken during nights and weekends to reduce external disturbances. For example, people walking close to the magnetic shield or the operation of the indoor crane may produce false signals or changes in the noise. The threshold is set to $\sigma = 7$, which corresponds to 1 event in 12 hours (the typical time scale of a night measurement). This is mainly done for practical reasons. The measurement is automated via a script taking data in 60 ms intervals. Parallel to the recording, the data is analyzed by extracting the histogram, the mean value, minimum and

n	1	2	3	5	10	1	1	1
T	12 h	12 h	12 h	12 h	12 h	151 d	1 yr	10 yr
σ	7.0	5.0	4.0	3.1	2.2	7.8	7.9	8.2

Table 5.1.: Noise thresholds for the monopole search. The threshold is dynamic and scales with σ to the RMS-noise of the waveform of length $f \cdot T$ (measurement time T and sampling frequency f =1 MHz). An excess in n consecutive data points reduces σ.

maximum and the standard deviation. For each interval in which the threshold is exceeded, the whole 1 MHz waveform is also saved. The expected 1 event per night then has to be analyzed offline.

Noise with a characteristic frequency has a recurrent structure and hence is distinguishable from monopole signals. However, these noise sources increase the overall noise and can reduce the overall sensitivity of the experiment.

To estimate the effective detector area and the speed sensitivity, it is sufficient to consider only one SQUID channel. By setting $\mathbf{B}_n = \sigma \mathbf{B}_m$ equation 5.1 transforms into a characteristic length scale

$$r = \sqrt{\frac{\mu_0 g}{4\pi\sigma B_n}} \approx (\sigma B_n)^{-\frac{1}{2}} \cdot \left(1.8\,\mathrm{cm} \cdot \mathrm{pT}^{\frac{1}{2}}\right) \tag{5.5}$$

and a characteristic velocity $v = \frac{r}{n} \cdot f$. By expanding, it turns out that $v \propto n^{-3/4}$ and $r \propto n^{1/4}$. Without the need of optimization, it is clear that $n = 1$ should be favored. However, the bandwidth of the detector must be considered, and for the employed SQUID detector $n = 1$ is indeed not an ideal choice. This will be further discussed in section 5.2.2.

Before taking a closer look on the hardware, the signal profiles will be studied in more detail. By assuming Gaussian distributed noise of 0.3 pT and varying the speed, direction, and position of the monopoles, different signal profiles occur. Figure 5.2 shows a few examples for different parameter sets.

Example (a) is a fast monopole flying by one of the SQUID channels with a distance of 1 cm. The distance to the other channels is much larger. The term *fast* means that the field of the particle surpasses the 7σ threshold for a single measured ADC value.

Slower monopoles are measured multiple times (see (b)), but by increasing the distance to the SQUID the signal decreases and therefore the threshold is not reached as seen in example (c). Below a method will be shown that nevertheless enables the detection of such signals.

As the coupling constant of the monopole (its charge) is not known, it will be a free parameter in the analysis. Example (d) shows a particle carrying a magnetic charge four times larger than the Dirac charge g_D. The peak field is almost the same as the slow monopole of example 2, but the signal profile is much broader. In the unlikely case of detecting a monopole, this could be used to extract some information on the detected particle.

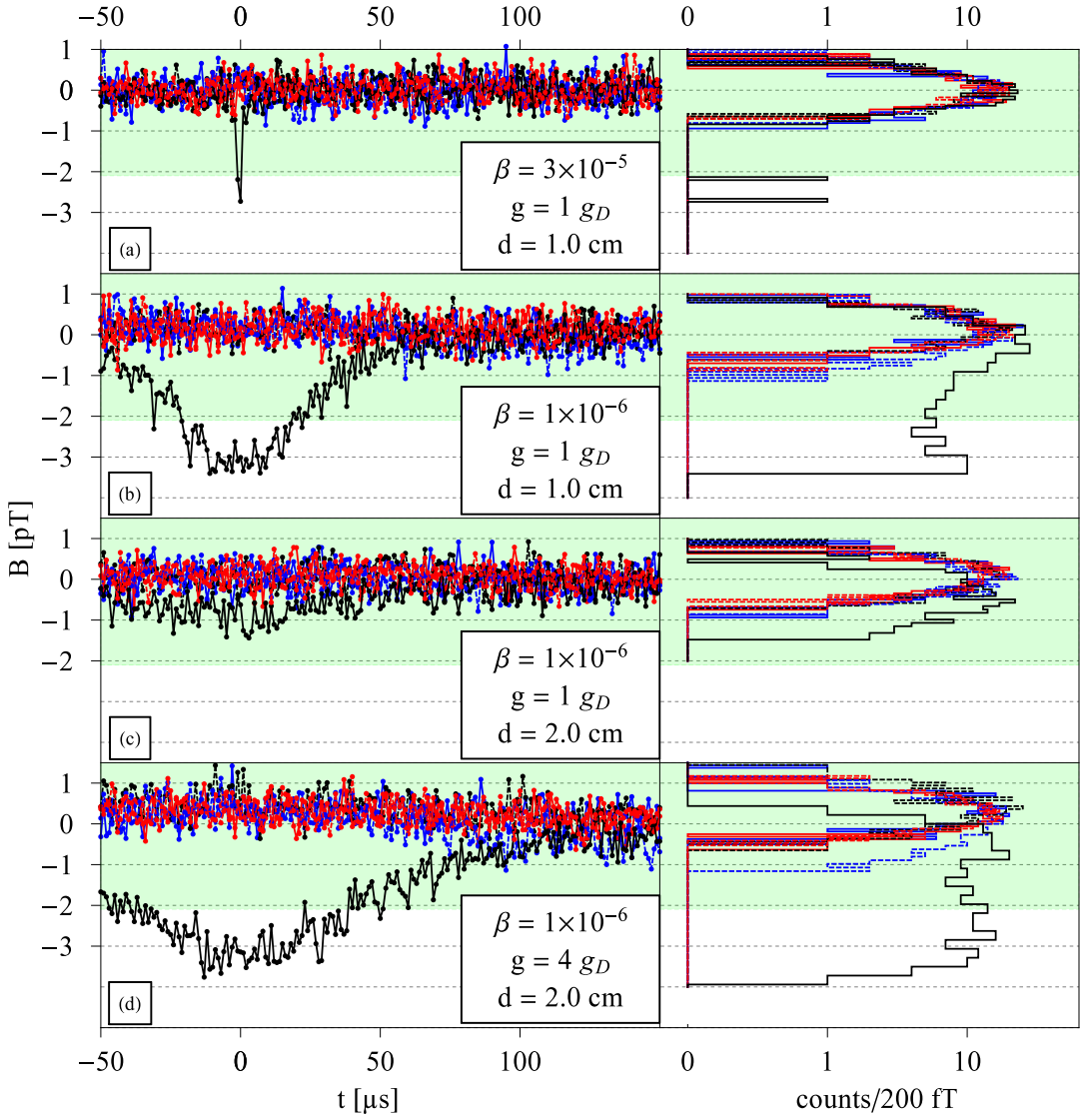

Figure 5.2.: Simulated expected signal of a monopole passing by the SQUID system for different distances, speed, and monopole charge in units of the Dirac charge g_d. On the left side the waveform is displayed and on the right side the histogram that is generated by projecting the points onto the y-axis. The color code is equivalent to figure 5.1b. The green area represents the 7σ threshold. Further description can be found in the text.

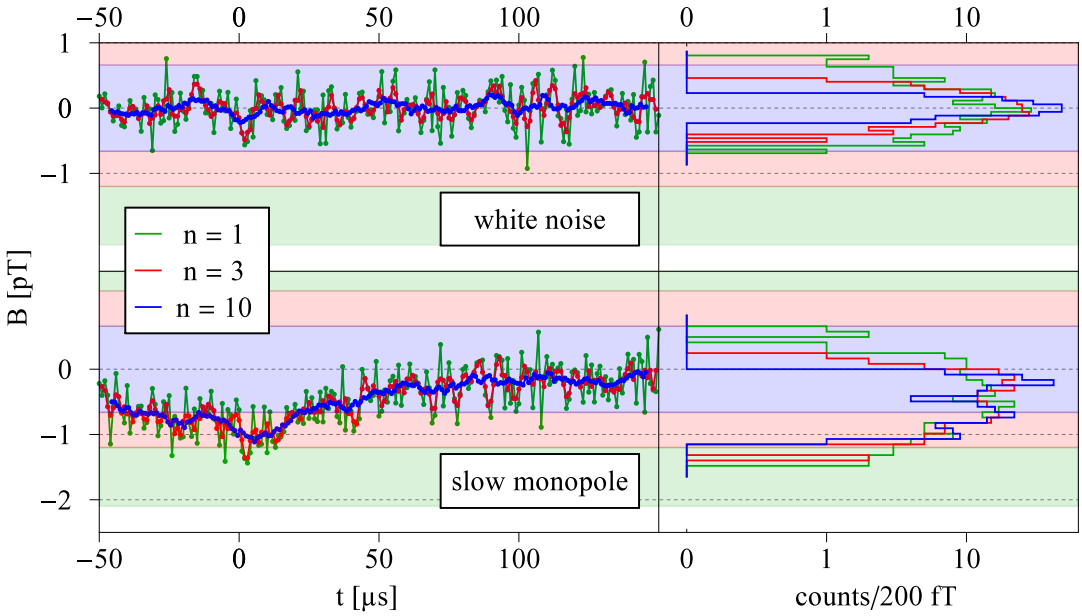

Figure 5.3.: Moving average technique: by smoothing the waveform with a moving average window with the width of n data points, the threshold can be reduced, as statistical fluctuations of uncorrelated noise (top) flatten out, but a real signal (bottom) surpasses the reduced threshold. The colored areas represent the thresholds corresponding to its n.

In order to extend the reach for slow monopoles, a moving average is applied to the waveform:

$$B_m = \frac{1}{n} \sum_{j=m}^{m+n} B_j \,, \tag{5.6}$$

with m the index of the waveform and n the width of the averaging window. For all n up to $n_{\max}$ this method is used and parameters from before (minimum, maximum, mean and standard deviation) are extracted. The needed threshold for different n is specified in table 5.1. If for any n-average class an extreme value exceeds the corresponding threshold, the whole waveform is recorded for offline analysis. Therefore the detection radius (equation 5.5) increases for slower monopoles. In figure 5.3 this technique is applied on example (d) of figure 5.2 and compared to a waveform solely consisting of white noise. The histogram of the white noise becomes more narrow than the real signal with increasing n.The threshold for the real signal is not exceeded for $n = 1$, but for $n = 10$.

With the procedure set up as described, this technique can be studied in detail by simulating various signals. That is, paths and velocities of monopoles are randomized and a white noise of 0.3 pT (RMS) is added to the signals. The resulting waveforms are analyzed using the moving average technique. The outcome is shown in two contour plots, which span the monopole speed range $10^{-7} < \beta = \frac{v}{c} = 10^{-3}$

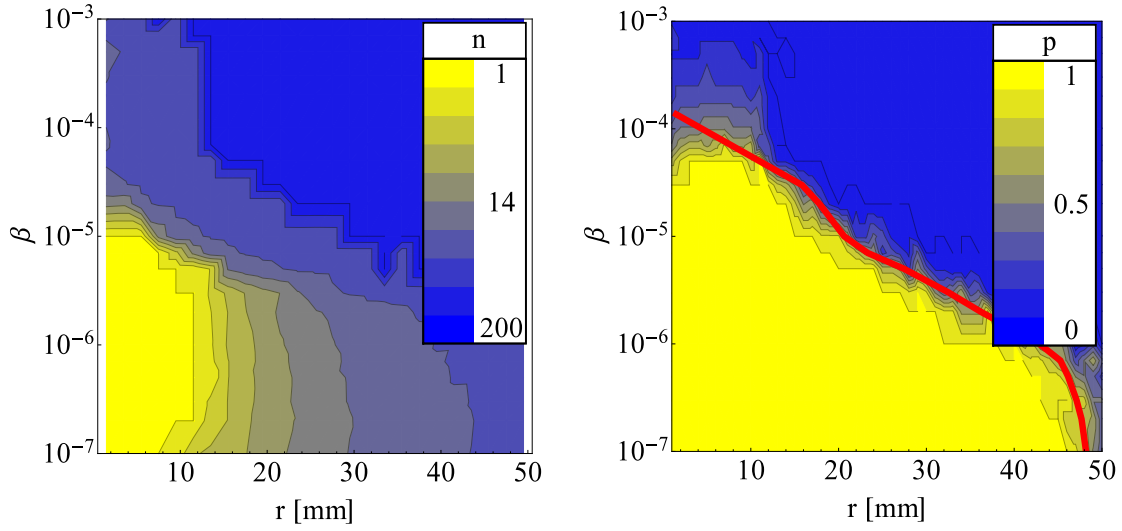

(a) moving average window width

(b) detection probability

Figure 5.4.: Average signal detectability of monopoles with randomly distributed start parameters categorized by the required moving average window width n (a) and the detection probability p (b). The detection radius for slow monopoles ($\beta < 10^{-5}$) is increased by the moving average method. The detectability of fast monopoles ($\beta > 3 \cdot 10^{-5}$) decreases rapidly and becomes $< 1\%$ for $\beta > 10^{-3}$. The red line in (b) indicates the average reach. More details on the detection probability and the average reach can be found in the text.

and the closest distance of the monopole to the SQUID. In figure 5.4a the necessary window width n for a positive event recognition is shown and in figure 5.4b the probability p of a successful detection. A particle is considered as detected when the average signal exceeds the threshold ($\sigma(n)$) for $n < n_{\max} = 200$. Though the restriction to $n < n_{\max} = 200$ is chosen arbitrarily, larger average windows ($n > 200$) only improve the detectability of very slow particles ($\beta < 10^{-7}$) and there is little theoretical motivation to prove their existence. Particles with $v > r \cdot f$ are detected with a chance of about $\frac{r \cdot f}{v}$, just due to relative time they are inside the detection volume. Velocities $\beta > 10^{-3}$ are effectively not detectable and for $\beta < 10^{-5}$ the probability becomes effectively 1. By weighting the detection radius r with the detection probability p an average reach r_{avg} for the corresponding velocity can be determined (the red line in figure 5.4b):

$$r_{\text{avg}}(\beta) = \int_0^\infty p(\beta, r) dr \,. \tag{5.7}$$

This velocity-dependent reach is a key ingredient to extract sensitivity of the experiment and will be used later.

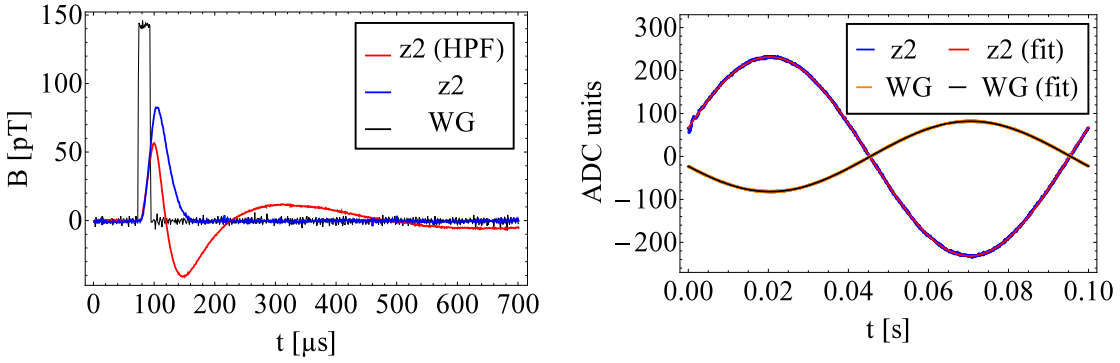

(a) Calibration pulse

(b) Amplitude calibration

Figure 5.5.: SQUID calibration: In (a) the response of the SQUID to a 20 μs calibration pulse applied by a waveform generator (WG) is shown with (blue) and without a 1 kHz high pass filter (HPF). In (b) the calibration measurement to determine the absolute amplitude is displayed. It has been performed without the HPF and with a 10 Hz sine wave.

5.2.2. SQUID calibration

In order to make sure that the described detection system is suitable for the measurement of monopoles, it has to be calibrated. Therefore a small coil – consisting of only one wire – is brought in close proximity to the SQUID and various magnetic field signals are created with a waveform generator (WG). The calibration system was tested with different electric circuits (change of the resistance) to check that the bandwidth of the calibration system is not limiting the calibration. The response of the detection system was independent of the components used for the calibration system.

The waveform of an expected monopole signal is approximated by a rectangular pulse with varying pulse width. Figure 5.5 shows the first part of the calibration procedure. In figure 5.5b a sine signal with a 10 Hz frequency is applied. In this low frequency regime the SQUID system is not limited to its bandwidth and therefore the set signal voltage of the WG can be translated to the field amplitude (here shown in adc units). In figure 5.5a one example for a calibration pulse is displayed. Here a 20 μs wide, 140 pT high pulse yields a $\approx$ 80 pT field signal measured with the SQUID (blue). In this frequency regime (50 kHz) a noticeable effect of the bandwidth limitation is visible. The amplitude is reduced by a factor of about 60% and the width is also increased. By using a high pass filter (HPF), the signal is shaped into an even broader waveform with slightly higher amplitude. The HPF is mainly used to reduce low frequency noise, which worsens the efficiency of event detection algorithm and hence increases the false event rate.

Figure 5.6 shows the bandwidth of the SQUID system, with and without the 1 kHz HPF. As for a sensitivity estimation the reduction of the signal amplitude is important, the bandwidth $b(f)$ is here expressed in amplitudes, not as usual in powers. Together with the results shown in figure 5.3 the bandwidth determines the

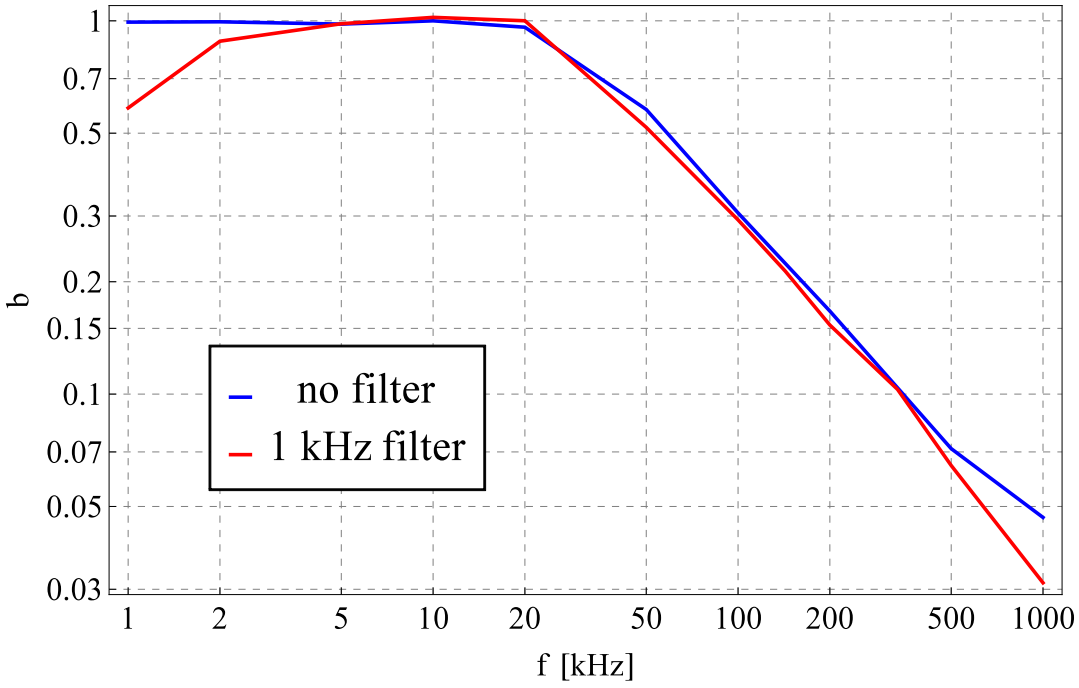

Figure 5.6.: Bandwidth b of the SQUID detection system including the readout system: The field amplitude reduction is normalized by the height of the initial field step.

monopole detection efficiency per unit time. Both the detection area ($A \propto r(f)^2$) and the speed resolution ($v = r(f) \cdot f$) are frequency dependent due to the detection radius (see equation 5.5)

$$r \propto (\sigma B_n)^{-\frac{1}{2}} \cdot \sqrt{g} \longrightarrow r \propto (\sigma B_n)^{-\frac{1}{2}} \cdot \sqrt{g \cdot b(f)}\,, \tag{5.8}$$

as the monopole charge is effectively scaled by the bandwidth b. Also A and v are linked together and therefore an analytic expression is difficult to extract and relies on approximations. Hence the final sensitivity estimate will be done numerically at the end of the next section.

5.2.3. Data analysis

In order to test this measurement concept, data has been taken during several nights and over a weekend. The data are only partially of use, as errors occurred during some runs. In total approximately 23 hours of usable data was acquired. Measurements during daytime on regular working days are avoided as external disturbances can make the analysis more difficult than needed for a proof of principle measurement. These external influences (e.g. magnetic field outside the MSR or mechanical vibrations) are constantly recorded.

Figure 5.7 shows the time series of five SQUID channels (x2 was broken at the time of the measurement). Here the output of x1 is filtered with the HPF, resulting

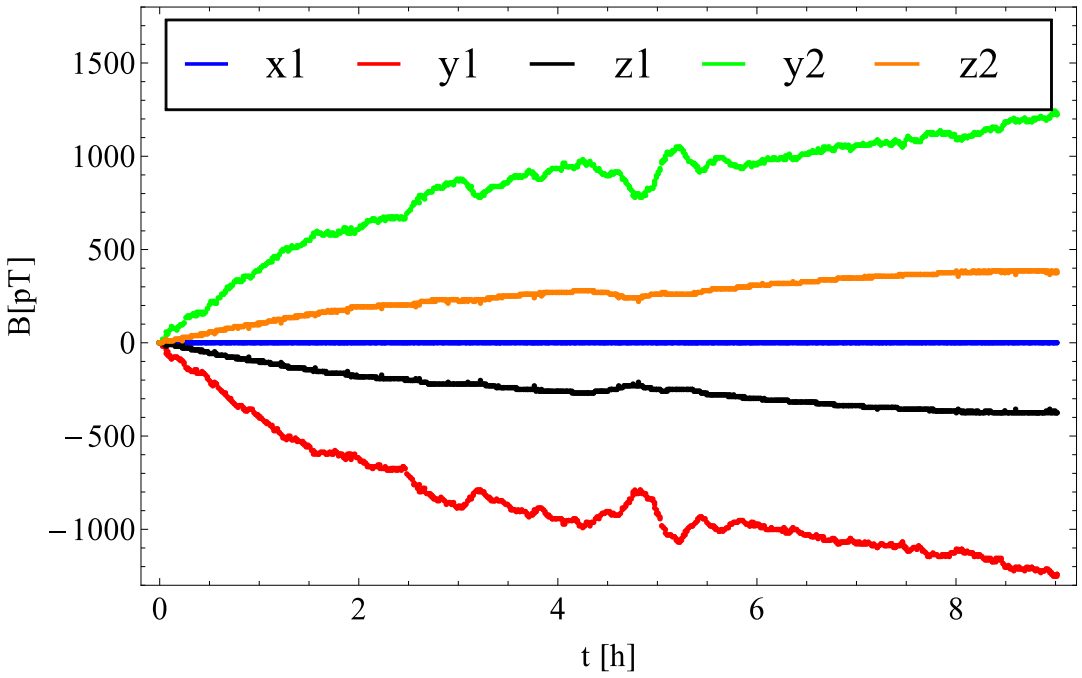

Figure 5.7.: Long-term monopole measurement using the field induction method. All channels except x1 show a field drift which is common for the applied SQUID magnetometer. The x1 channel was read out in combination with a 1 kHz HPF which eliminates any low-frequency drift. The channel x2 is not shown, as it was broken at the time of the measurement. The data have been recorded over the course of a night (starting at 9pm).

in a flat line without drift. The other channels experienced a large drift of more than 1 nT. The drift is symmetric in opposite channels which therefore has to be interpreted as a real field drift. This is mainly attributed to the SQUID itself. With a dropping helium level, the magnetization inside the SQUID cryostat changes. The y channels are mostly influenced by this behavior. The drift seems to be high, but on the typical timescales for the monopole detection, which has a time window of about 60 ms, the drift is negligible. The measurement was performed inside the MSR without the insert.

Of greater importance is the noise level, as any significant change of it indicates a failure of a subsystem or a change in the external conditions. Figure 5.8 shows the noise levels corresponding to the above time series. It is determined by the standard deviation (rms) of the individual 50 ms long signal waveforms. All non-filtered channels measure a similar noise on the order of >1 pT, while x1 has only 350 fT noise. The large difference is caused by the elimination of 50 Hz noise and its harmonics.

About 4 hours and 15 minutes after the start of the measurement the noise in x1 rises for a short amount of time and afterward drops again. The reason for this behavior is a failure in the power supply of the HPF. The HPF is an active filter

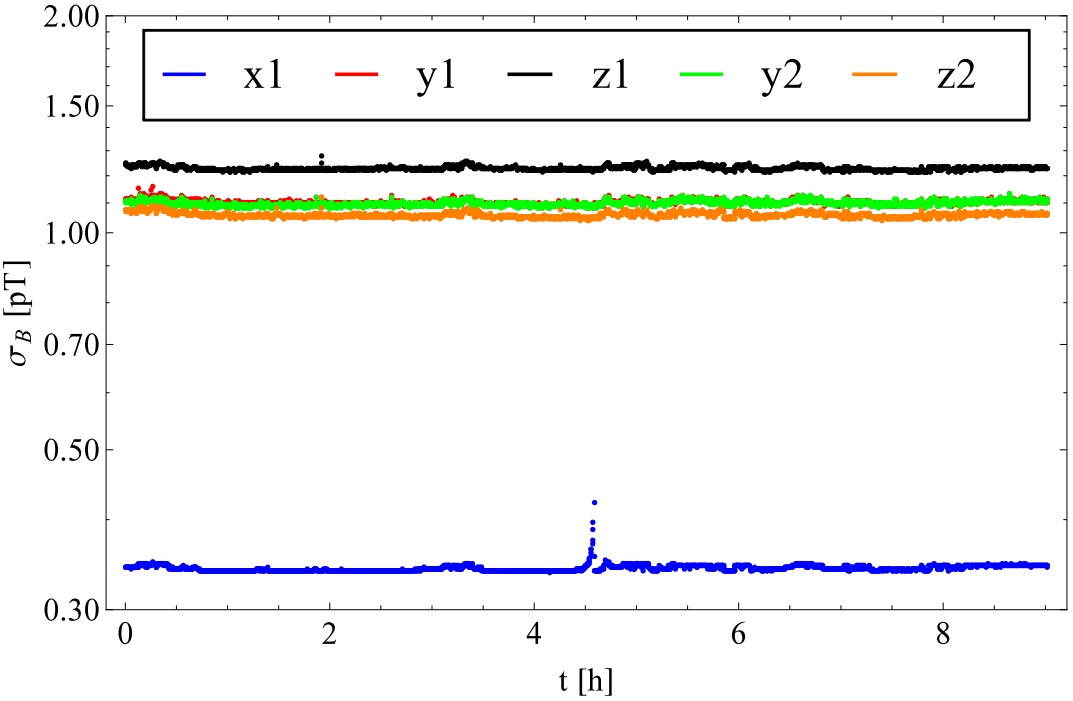

Figure 5.8.: Noise level of a night measurement (corresponding to figure 5.7): Unfiltered channels show a noise level of 1.1 pT to 1.2 pT. x1 with the HPF has a reduced noise of about 0.35 pT. y1 is barely visible as it is covered by y2.

which is powered by a battery pack. At the time of assumed failure one of the connection cables broke and the HPF was not functional afterward. Consequently, only about 4 hours of data can be used for the analysis. To exclude a non-functional filter the voltage of the battery pack is measured at the beginning and the end of each measurement run.

As a very short field peak with a width of a few microseconds changes the standard deviation of 50 ms waveform by only a small value, the noise level alone can not be used for a sensitivity determination. Parallel to the data taking process, a second process analyzes the data (as in the above section introduced) and saves the complete waveforms of all channels to the hard disk if one of the detection algorithm determines an excess in the waveform of one channel.

Assuming the monopole charge is not much larger than the Dirac monopole ($g \gtrsim g_D$), a monopole producing a large field in one of the channels is very unlikely to also produce a large field in a second channel. Therefore it would have to move very close to the center of the SQUID. A signal occurring in all three channel has an even lower probability, as the large mass of the monopole ensures a linear path of the particle. Therefore at least one of the three signals has to be smaller compared to the others. The same argument yields an even lower probability for signals measured in more than three channels.

This expected signal distribution can be used in the data analysis, as a signal in

all (or a majority) of the channels is most likely a global field change. For the shown noise level (350 fT with the HPF, 1100 fT without the filter) the detection range of the individual channels becomes even smaller (10 μs signal width, here equivalent to n = 10) 2 cm, respectively 1 cm. This is less than the distance between the SQUID channels. In other words, a real monopole signal is expected to occur in a single channel, or at most in two.

For very strong monopoles ($g \gg g_D$) the effective detection range rises to a point at which it becomes larger than the distance between the SQUIDs. In this case all SQUIDs experience a field change within a short time window. Depending on the speed of the monopole, its direction could be extracted as the individual signals are shifted in time. A fast monopole, which gives a signal at the same time in all channels and is only measured within a few microseconds ($n \approx 1$), still gives a different signal height in the different channels. Both characteristics make them distinguishable to a global field change or noise.

On average, an 8 hour long measurement results in approximately 1 event, as is expected based on the white noise assumption (see section 5.2.1). These events are recurrent and therefore they can be categorized. Here an example of each category will be shown (figures 5.9 and 5.10) and discussed.

- **Noise pulse event**: For a short amount of time the noise level increases. These events can occur repeatedly with short intervals between them. These events are caused by either a noise source outside the MSR, as it is seen by all channels with a similar signal strength, or electronic noise picked up in the cable connecting the SQUID with the readout system. The presented example is mainly electronic noise. This behavior can be studied by either subtracting (field noise) or adding (electronic noise) from two opposing channels (one measuring in positive and the other one in negative direction.)

- **Multi-peak event**: One of the most common false events is a waveform with increased noise over the whole 60 ms period. They begin and end very rapidly without any indication. In addition, their nature can be completely electronic noise (figure 5.9b) or an equal mixture of field and electronic noise (figure 5.9c).

- **Digitizer reset**: These events occur only after the digitizer used to convert the analog signals from the SQUID resets. As the digitizer is operated at almost the maximal sampling rate,the buffer can become corrupted. If this occurs, the software detects an error and resets the digitizer readout. The different signal height in the x-, y- and z-direction and also the opposing trend of opposing channels indicate a field like signal.

- **Single noise pulse event**: Very short pulses are seen by all channels. In connection with the HPF the signal is reduced compared to the other channels. The example in figure 5.10b is a purely electronic noise dominated event.

- **Extended noise pulse event**: In this case, the signal was a combination of electronic and magnetic noise, with the electronic contribution being slightly dominant.

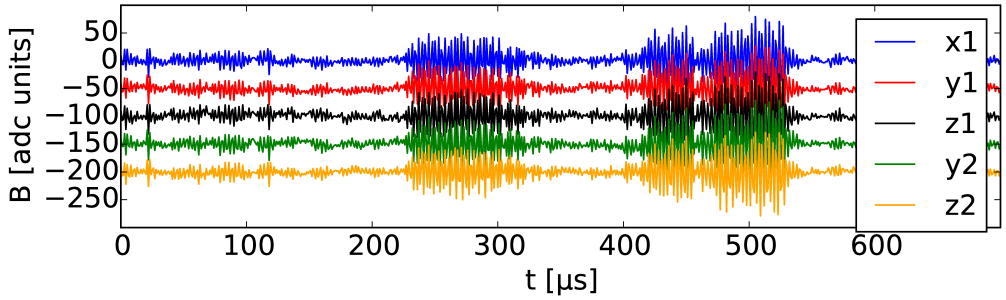

(a) Several noise pulse events

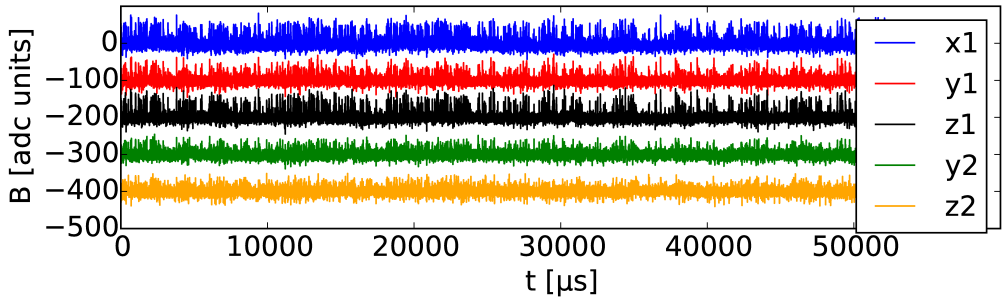

(b) Multi-peak event

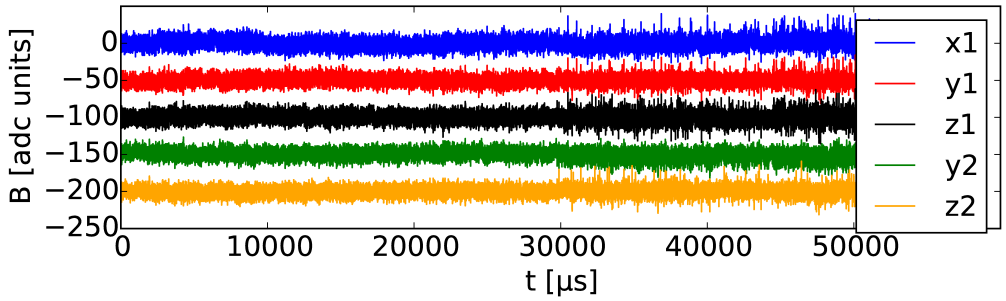

(c) Start of a multi-peak event

Figure 5.9.: Typical false signals: The most common false signals that trigger an event detection are increased noise signals measured simultaneously in all channels. It can be a short noise pulse, which vanishes after a few microseconds (a) or a constantly elevated noise over a whole waveform and even extending beyond it (b, c). These signals occur spontaneously with full strength. Here no filter is applied. The individual waveforms are also shifted by an arbitrary offset for visualization purpose.

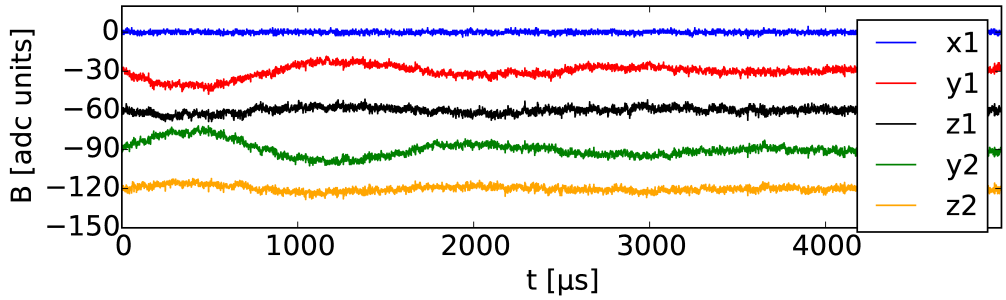

(a) Digitizer reset event

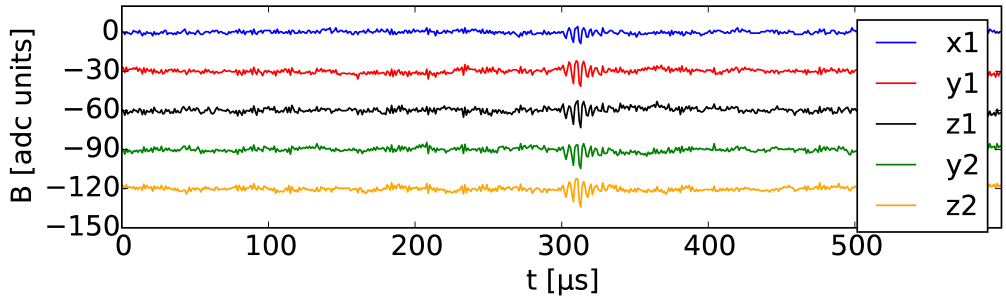

(b) Single noise pulse event

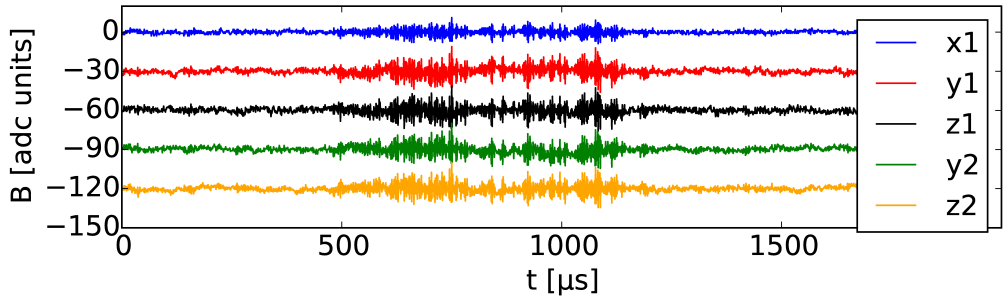

(c) Extended noise pulse event

Figure 5.10.: False signals (x1 with HPS): A buffer error of the readout card typically triggers a false event (a). Also spontaneously occurring noise pulses of different time scales (b, c) are measured in all channels. The plotting style is equivalent to figure 5.9.

By having two opposing channels, the nature of the event can be studied. All measured events were detected in all channels and hence no real monopole signal was identified. Therefore a detailed signal study is not necessary.

5.2.4. Sensitivity

As no real event has been seen within the combined 23 hours of data, an upper limit for the monopole flux can be given. This limit is strongly dependent on the speed of the monopoles, as shown above. The result here is compared to the limit that has been set in the Cabrera experiment [100]. To express the full sensitivity level of the presented method, the measurement time is scaled to the measurement time of the Cabrera experiment. In addition, it is assumed that all six channels are read out in combination with a HPF. The result is shown in figure 5.11. It is shown for two choices of monopole charge (1 Dirac charge and 10 Dirac charges). The flux limit has a minimum of $1.1 \cdot 10^{-8}\,\mathrm{cm^{-2}s^{-1}sr^{-1}}$ at $v = 10^{-5.7}c$. By assuming a higher monopole charge g or extrapolating to a longer measurement time T, the limit scales to $\sqrt{\frac{g_D}{g}}$, $23\mathrm{h}/T$, and $\frac{1}{N}$, with N the number of channels with a HPF. The low velocity regime is only limited by the high pass filter and the high velocity regime by the bandwidth of the SQUID system. Velocities can be converted to frequencies by using the velocity-reach correlation:

$$\nu = \frac{v}{r(v)}\,. \tag{5.9}$$

In contrast to the Cabrera experiment, the time resolved induction technique is more sensitive for higher monopole charges, as they directly change the detection reach. In addition, more information about a potential event – like the velocity and direction – can be extracted.

This is also a downside to this technique. The detection reach drops very rapidly for high monopole velocities. An increased performance in the high velocity regime is difficult to achieve, as it is difficult to extend the bandwidth of the SQUID system by more than an order of magnitude. The main potential for improvements therefore is given by the reduction of the noise level, as it affects the detection area and the velocity reach.

5.3. Flux induction method

The previously shown field induction method has advantages and disadvantages compared to the method that Cabrera used (referred to hereafter as the flux induction method). However, it is possible to apply both methods simultaneously with the same SQUID system. In the following section, the upgrade of the applied SQUID to an flux induction based monopole detector will be shown. The detection principle will be explained, the design of the modifications will be illustrated and a limit estimation based on recorded data will be given.

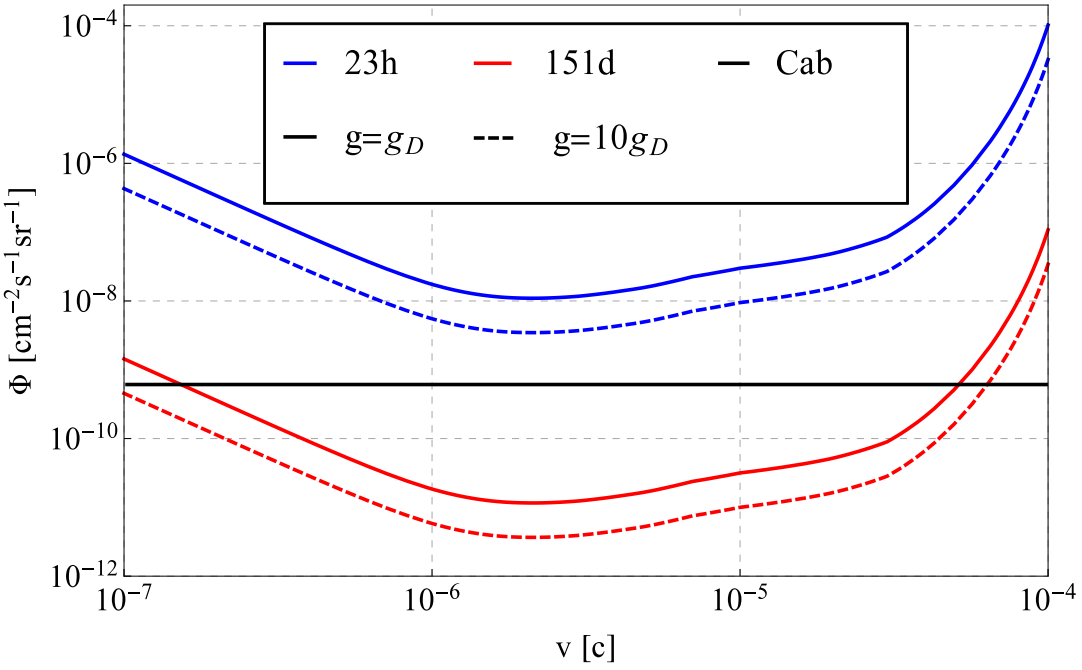

Figure 5.11.: Monopole flux limit estimation of the time resolved induction method: The combination of the measurement time, the bandwidth of the SQUID system and the velocity-reach correlation yields an upper limit for the monopole flux. It is shown for two choices of the monopole charge: 1 g_D (solid line) and 10 g_D (dashed line). The result is given for the data which has been taken with one filtered channel (blue) and an extrapolation is shown for six filtered channels and 151 days of data (red) which corresponds to the measurement time of the Cabrera experiment (black).

5.3.1. Detection principle

Inside the SQUID cryostat an additional coil system made of a 50 μm thick Niobium wire is installed. It consists of a large pickup coil at the bottom of the cryostat, a small transfer coil and a section of twisted wire pairs to connect both coils. The coil system is made from one single piece of wire, which is connected electrically at an arbitrary position on the pickup coil by pressing both wire ends against each other. The inner volume of the cryostat limits the diameter of the pickup coil to 19 cm. To reduce the pickup of noise in the connection section, the two portions of the wire are twisted together. The transfer coil is directly mounted back-to-back to one of the initial SQUID channels.

In analogy to Cabrera's experiment, a monopole moving through the large pickup ring would induce a permanent current in the superconducting wire. This can be derived by using Maxwell's generalized equations [100]. The flux through the ring is given by the flux of the monopole Φ_g and the flux of the induced current $\Phi_S = -I(t) \cdot L$, with L the self inductance of the whole wire. The time dependent

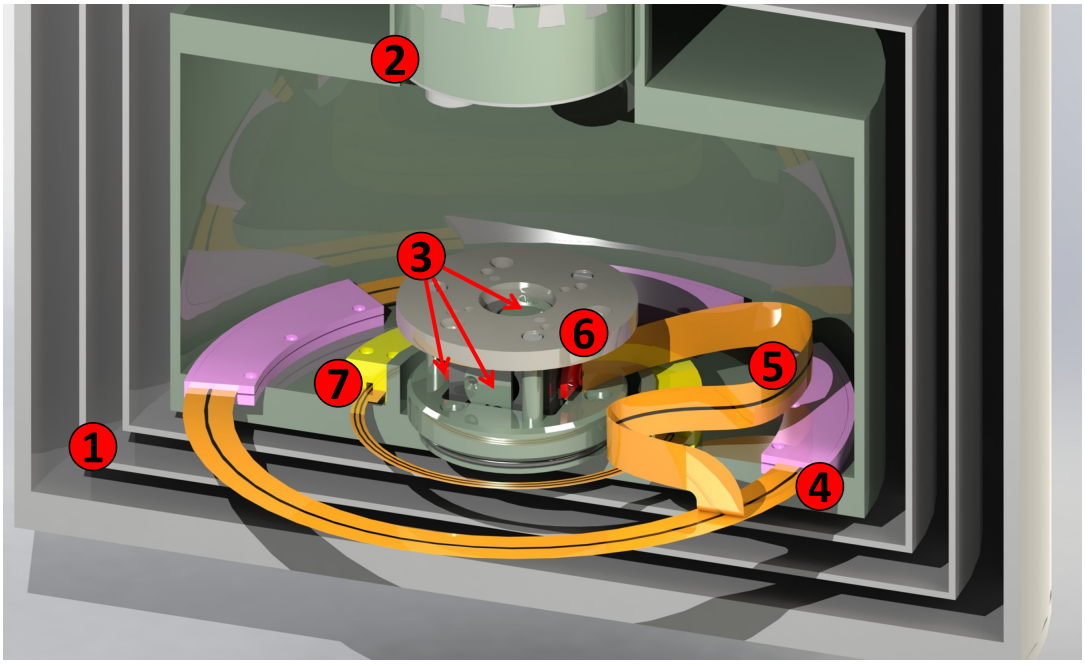

Figure 5.12.: Sketch of the modified SQUID system: The six SQUID channels (3) are mounted on a sides of a cube, which is screwed into the bottom of the cryostat (1). Thin cables (not shown) reach from the SQUID cube to the insulation plug (2). An additional ∅180 mm coil – called the pickup coil (4) – offers a large area for monopole detection. The induced current generates a magnetic field in the y1 channel via the transfer coil (6), which is connected with a twisted pair wire (5) to item 4. Item 7 is a second pickup coil with ∅90 mm and 2 loops, a not yet implemented upgrade.

current I can be expressed as [100]:

$$I(t) = \frac{\Phi_0}{L}\left[1 + \frac{\gamma v t}{[(\gamma v t)^2 + b^2]^{1/2}}\right]. \tag{5.10}$$

Here is v the velocity of the monopole, γ and b are characteristics of the coil. The exact form of the signal is not of importance, as a permanent current change of $\Delta I = 2\Phi_0/L$ results from the passage of the monopole. A monopole missing the ring does only temporarily change the flux. In other words, only monopoles moving through the area of the ring leave a permanent flux. It can be described figuratively by imagining a monopole as a particle, of which radially magnetic flux is emitted. A property of superconductors is that it prevents magnetic flux to enter it. Therefore the magnetic field lines of the monopole have to break up at the position of the ring and reform from new after the passage. This is only possible by leaving a flux vortex behind. Due to the nature of Cooper pair, a flux change of $2N\Phi_0$ results, with $\Phi_0 = \frac{h}{2e}$ the flux quantum and N the number of loops of the coil.

Figure 5.12 illustrates the experimental setup. The flux change in the pickup loop generates a constant current in the whole wire. Consequently, the current creates via

the transfer coil a magnetic field that is measured at the SQUID channel (here y1). The transfer coil is rigidly mounted to the SQUID channel. The inductance of the coils is proportional to their surfaces and to N^2. As the flux change is linear to N and the self inductance is linear to N^2, the optimal number of loops is 1. Compared to the pickup coil (L_{pc}) the self inductance of the twisted wire connection part (L_{tw}) is much smaller and therefore neglected for the moment. The dimensions of the transfer coil affect its inductance (L_{tc}) and the generated field. Consequently, they have to be optimized by maximizing the generated field at the position of the SQUID channel. The inductance of each individual coil can be calculated numerically [103] and the inductance of the coil system is given by the sum of its parts $L = L_{\mathrm{pc}} + L_{\mathrm{tw}} + L_{\mathrm{tc}}$.

The transfer coil is mounted back-to-back to the SQUID channel and therefore has the smallest possible distance to it. As the SQUID channels have a very small active surface, the transfer coil also can be small. Hence the parameter range of the coil optimization reaches from radius $2\,\mathrm{mm} < r < 10\,\mathrm{mm}$ and number of loops $1 \leq n \leq 100$. The result of this particular case is a coil with $n = 6$ loops and the minimal radius $r = 2$ mm. An even smaller radius would slightly increase the performance, but becomes very difficult to build due to the fact that the coils are manually wound. Henceforth the pickup-transfer-coil system will be referred to as the *monopole coil* or *monopole channel*.

A long twisted wire connection is inevitable due to the assembly process. While the SQUID cryostat is at room temperature, the pickup coil needs to be placed manually at the bottom of the cryostat. As the access hole (⌀70 mm) is much smaller than the pickup coil, the coil itself has to unfold at its final position. Therefore the wire of the coil is glued to a 50 μm thin Kapton ring stabilized by small segments made of plastic (purple parts in figure 5.12). During this first step of assembly, the SQUID cube is outside the cryostat. And as the transfer coil has to mounted to it, a connection at least as long as the length of the access hole is necessary.

In the sketch a second monopole coil is also shown, which can be neglected for now. It will be discussed at the end of this chapter. Similar to the first monopole coil it has a segmented design, in order to enable the assembly inside the cryostat.

5.3.2. Calibration of the pickup and transfer coil system

Similar to the time-resolved field induction method, the detector has to be calibrated in order to extract a monopole sensitivity estimate. But here the bandwidth has a subordinate role. The calibration mainly eliminates some uncertainties of the monopole coil. For example, the inductance of both coils could be underestimated, as a non perfect circular shape results in an increased inductance. Also the neglected inductance of the twisted wire connection could be larger than expected. The second major uncertainty is the distance between the transfer coil and the SQUID channel. The dimensions of all parts are known, but the effect of the manual coil winding and thermal expansion due to the liquid helium are difficult to determine.

The actual calibration is done similarly to before, except that the 1-wire coil is exchanged through a Helmholtz coil. The Helmholtz coil and the waveform generator

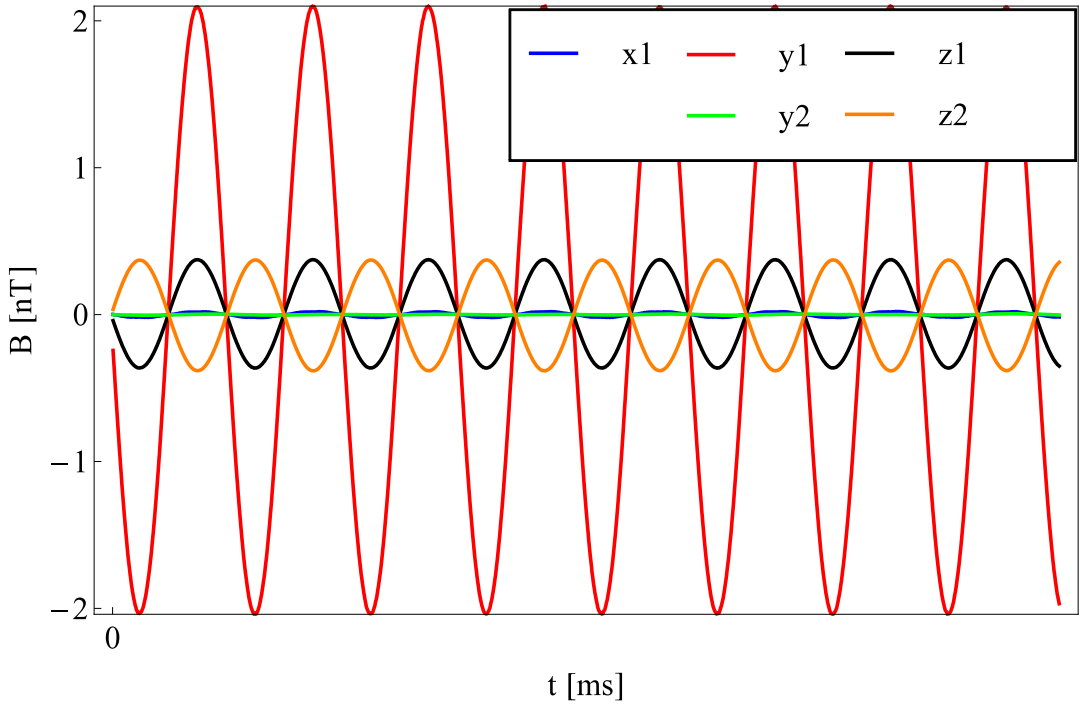

Figure 5.13.: Calibration of the monopole coil: All channels (except the broken x2 channel) measure a 10 Hz signal, which has been applied with a Helmholtz coil, driven by a waveform generator. The amplitude of the monopole channel (y1) is 5.552 ± 0.001 larger than the amplitude of the z channels.

are used to generate a uniform field in the z direction with variable amplitude and frequency. Figure 5.13 shows the 10 Hz calibration signal. The amplitude measured by the monopole channel is 5.552 ± 0.001 times higher than the z channels, which have the same orientation. This number will be later referred to as the scaling factor s_z. The amplified signal is caused by the larger pickup area of the monopole coil and the flux transformer effect of the whole coil. But this seeming advantage has its downside, as magnetic noise is also amplified by the same factor.

The scaling factor s_z can also be determined using simulations, which include the numerical treatment of the coil. The flux through the pickup coil is determined by $\Phi = AB_z$, with A the area of the coil and B_z the z component of the field measured by both z channels. The resulting current $I = \Phi/L$ is used to calculated the field at the y1 channel, which ends up being about a factor 6 larger than measured. By replacing Φ with the evoked flux change of a monopole $2\Phi_0$, the expected monopole signal $B_{mon} = (1.11 \pm 0.11)$ pT can be calculated. The error arises from the uncertainty of the area of the pickup coil, which occurs due to manual installation of the coil and the thermal contraction in the liquid helium. The relative error of the area is estimated to be about 10%. In comparison to the area error, the error of s_z is negligible.

By comparing the measured and the simulated s_z, it is possible to extract infor-

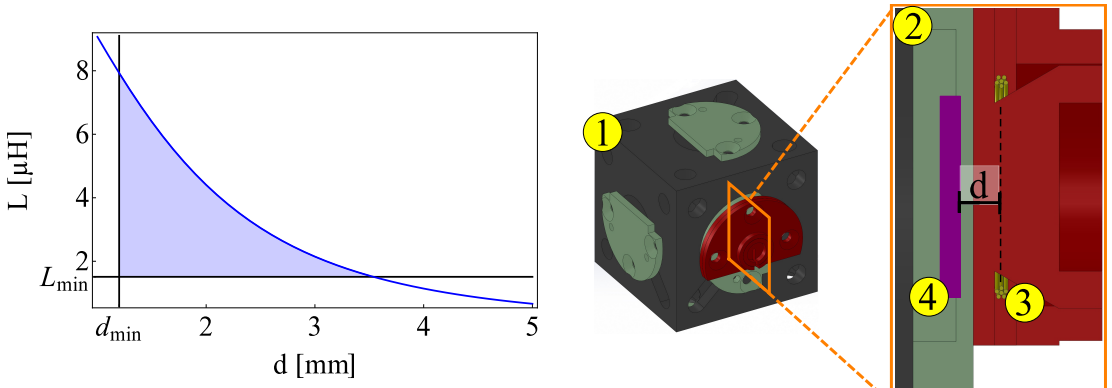

(a) Inductance

(b) Cut-away view of the SQUID cube

Figure 5.14.: Improvement potential of the monopole coil: The result of the calibration measurement gives only a degeneracy of the inductance L of the whole coil system and the distance d between the transfer coil (3, yellow tubes) and the SQUID channels (4, purple rectangle) is not optimal (a). The shaded area between the degeneracy line of L and d (blue line) and the limitation to the best possible $L = L_{\text{min}}$ and $d = d_{\text{min}}$ indicates the range for improvement. For clarity a cut-away view of the SQUID cube (1) is shown in (b) to illustrate the mounting of the transfer coil.

mation about the real inductance L and the distance d between the transfer coil and the SQUID channels. As one number cannot have enough information to determine L and d, only a degeneracy of both parameters can be determined, which is shown by the blue line in figure 5.14. It has to be pointed out that there is *no* dependency between L and d.

The plot also shows the improvement potential of this method, as L and d are not at their best possible value L_{min} and d_{min}. Decreasing both parameters results in a larger scaling factor, which also increases B_{mon}. With the current cryostat the full potential cannot be achieved, as the long twisted wire connection between the transfer and the pickup coil is indispensable. In order to reduce d, an automated coil winding process needs to be implemented, as the manual winding results in an undefined pitch of the transfer coil. In general, a cryostat dedicated for a monopole measurement with higher accessibility for assembly has the best potential for improvements.

On a side note: an idea was suggested to use the increased signal of the monopole coil to measure the precession signal of cells containing spin-polarized helium and xenon [104]. Helium and xenon precess at their Larmor frequencies and a potential shift due to a electric field has to be only measured in close proximity of the Larmor frequency. Hence the signal-to-noise ratio (SNR) is of interest.

For this purpose the decaying signal of a test cell containing helium and xenon has been measured simultaneously with the monopole coil and the z coils. The

extracted SNR determined with the monopole coil is equivalent to the SNR of the one z coils, which is closer to the cell. The reason for this is that proportional to the signal the noise is also increased. Consequently, the noise is mainly dominated by magnetic field noise than rather by noise of the electronics. As a result, the big pickup-coil in combination with the transfer coil neither improves nor worsens a helium-xenon-EDM experiment.

5.3.3. Noise and drift cancellation

A crucial ingredient for a sensitive monopole measurement is a low noise environment, as a too high noise floor conceals any real signal with a low amplitude. In contrast to the time-resolved field induction method, a monopole here creates a permanent field change. Therefore high frequency noise can be reduced by using a low pass filter (here 1 kHz with -18 dB/octave). Thus the sampling rate of the ADC card can be reduced and the previously used digitizer is replaced by another digitizer with 24-bit resolution and a sampling rate from 10 kHz to 250 kHz (here operated with the minimal rate).

Another noise reduction approach makes use of the other SQUID channels. As the monopole coil is orientated in the z direction, y1 measures

$$B_{\mathrm{y1}} = s_z \cdot B_z + B_y + B_{\mathrm{mon}} \tag{5.11}$$

with $B_{y,z}$ the magnetic field in the corresponding direction. By incorporating the orientation of y2 and z2, the non-monopole channels (z1, y2 and z2) can be used to correct for noise and for a potential drift. Hence the corrected monopole signal is expressed by:

$$B_{\mathrm{mon}} = B_{\mathrm{y1}} - s_z \cdot (B_{\mathrm{z1}} - B_{\mathrm{z2}}) + B_{\mathrm{y2}}\,. \tag{5.12}$$

Figure 5.15 shows the raw y1 channel and the noise and drift corrected monopole channel. It is clearly visible that the initial drift with a complex structure is almost completely removed, with only a linear drift of 20 fT/s remaining. This drift is mainly attributed to drift between z1 and z2. Compared to the remaining noise this drift is negligible for the monopole detection, which uses a time window of 20 ms for the permanent field jump detection.

On average the noise – here expressed by the rms standard deviation – is reduced from 1.4 pT to 1.0 pT. A reason for the weak reduction could be that the noise of the individual channels is partially uncorrelated or that correlated high frequency noise is measured with a phase shift, which is difficult to correct for with numerical methods. The previously mentioned low pass filter was not built at the time of the measurement. Shortly before it was finished, a major incident happened, which will be discussed later that prevented to measure a potential improvement of the signal.

In equation 5.12, s_z has been taken from the calibration measurement, but an offline analysis with varying s_z can also be used to determine an optimal scaling factor for the drift and noise cancellation. In order to do so, a night measurement is divided into chunks with a length of 5.8 s. This is the time window on which the

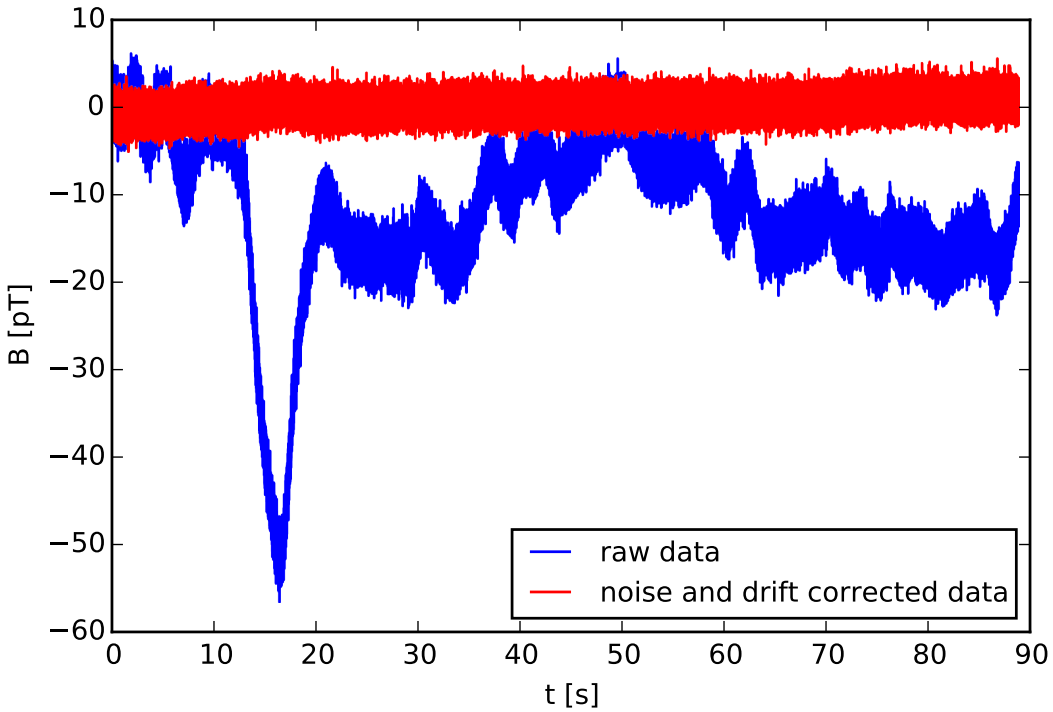

Figure 5.15.: Drift and noise cancellation: y1 (blue) is corrected by z1, y2 and z2 to separate a potential monopole signal from the change in the ambient magnetic field. The corrected signal (red) has a negligible drift and a slightly reduced noise, which indicates a mainly uncorrelated nature of the noise sources.

detection algorithm operates. A randomly chosen scaling factor is used for each time interval individually and the improvement on the detection algorithm is extracted.

In order to detect a potential monopole signal a differential moving average window is convolved with the dataset (here the corrected signal). The window has a length of N and the first half of its entries are $-1/N$ and the second half $+1/N$. The result of the convolution is proportional to the step height inside the window. The maximal value of a 5.8 s interval is then a measure for the highest step that the algorithm detected, hereafter this maximum is referred to as SV. The width N does practically not influence SV, as long as the width of the window is larger than the rise time of the field jump, which is dominated by the bandwidth of the SQUID.

The result of the simulation (see figure 5.16) is $s_z = 5.34 \pm 0.15$, which is consistent with the value of the calibration measurement. Even if SV does not show a quadratic shape within the error bars, a quadratic fit is still a good approximation. The minimal value of SV is connected to the noise level and therefore SV is a benchmark for the noise floor of the environment, next to being a measure for step height. Given that the error on the calibration measurement is much smaller than that of this approach, s_z is set to 5.552 for all real monopole measurements.

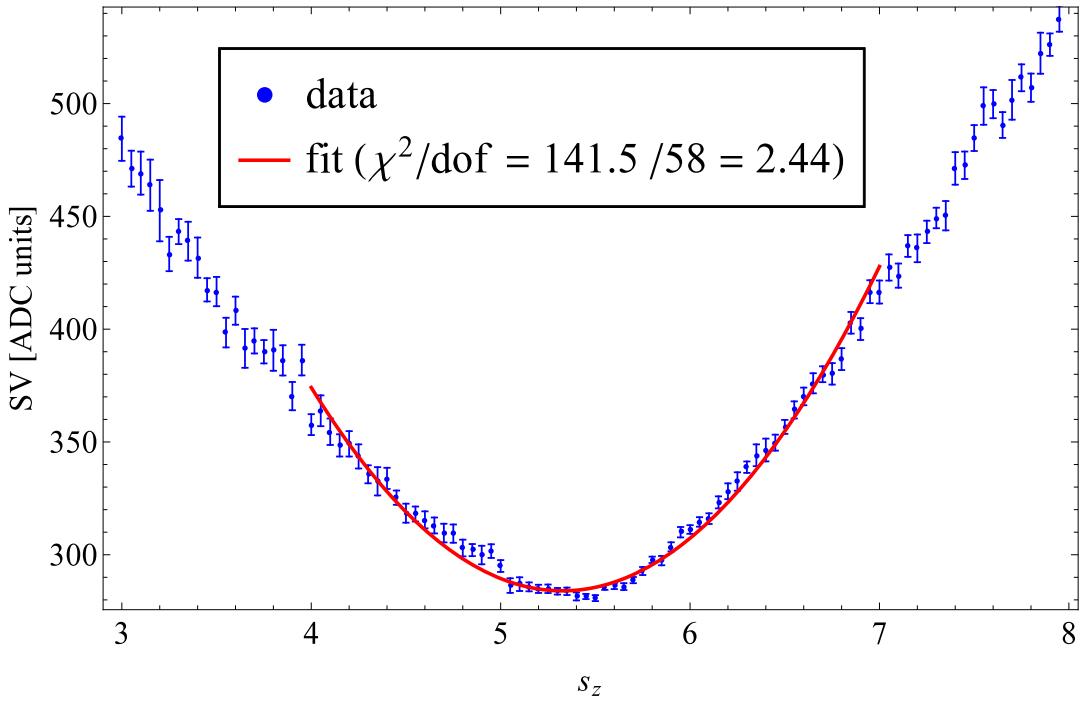

Figure 5.16.: Determination of the scaling factor s_z via the optimization of the noise cancellation method. A quadratic fit (red) is used to determine the optimal s_z for a minimal SV. Even though the fit does not match well to the data points (blue) within the error bars, it is still a good approximation to determine the optimal s_z.

5.3.4. Detection algorithm efficiency

As SV has been chosen to be the figure of merit, a threshold SV_{min} needs to be introduced to discriminate between a clean waveform and a waveform containing an event. To do so, a few datasets are modified with simulated events. At a random time a permanent field step dB with a randomly chosen height is added to the waveform. The resulting SV distribution is shown in figure 5.17a. The shaded area indicates the range of (dB, SV)-tuples. Without the drift and noise cancellation, the range of SV starts at 800 and begins to rise for $dB > 3$ pT. In other words, up to that field step height, the detection algorithm is dominated by noise and consequently would conceal events with $dB < 3$ pT. This also includes the field jump expected by a Dirac monopole. In contrast to the result for the raw signal, the corrected signal allows a threshold of $SV_{\text{min}} = 350$ to be set, which separates noise-only events ($dB = 0$) and real events ($dB > 0$).

The ratio of the area above SV_{min} to the whole area of the interval $dB \pm \delta B$ gives the detection probability p for an event including a field step dB (see figure 5.17b). For illustration purposes, the SV_{min} has been set to 1000 for the uncorrected signal. According to this result, it is obvious that without the cancellation method, the detection of a Dirac monopole using this experimental setup is impossible, as the detection probability is too small. The corrected signal yields a monopole identifica-

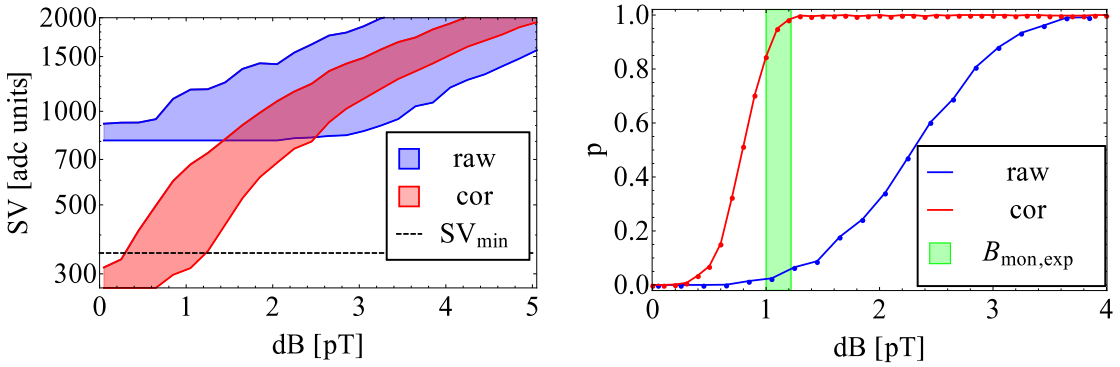

(a) SV distribution

(b) Detection efficiency

Figure 5.17.: Determination of the field step detection efficiency: In (a) the simulated result of the detection algorithm for the raw (blue) and corrected (red) signal is plotted. The shaded area indicates the range of results. The ratio of events with SV $>$ SV$_{min}$ to all events gives the detection probability of the field step dB (b).

tion probability of about $> 85\%$ and hence enables the search for Dirac monopoles. Monopoles with a fraction of the Dirac charge g_D become unlikely to be found and particles carrying a higher magnetic charge ($g > g_D$) quickly reach a detectability of 100%.

While the real measurement runs are performed, all events with SV $>$ SV$_{min}$ are exported to a ROOT tree for offline analysis. Events with SV $<$ SV$_{min}$ are considered to be mainly dominated by noise. In this case a simulation routine is started, which adds simulated field steps at a random position and height to the waveforms. In order to increase statistics, this process is applied multiple times to the clean waveform. Using this technique the detector efficiency can be checked continuously.

5.3.5. Data analysis

The measurement procedure of the flux induction method is very similar to the time-resolved field induction technique. Parallel to the SQUID measurement, environmental parameters like external field and mechanical vibration of the MSR are recorded.

Data has been taken in two phases. The first phase took place during eight consecutive days, including eight night measurements and five day measurements. All events with SV $>$ SV$_{min}$ are analyzed offline. As the surface of the monopole coil is large compared to the coils of the other channels, a monopole is very likely to only pass through the monopole coil. As previously discussed, a signal in multiple channels is an indicator for an external field change and consequently this event can be discarded. A field jump in one of the correction channels also induces a field jump in the corrected monopole channel, so this event can also be discarded. A

typical measurement of about 10 h produces around 100 events which have to be analyzed offline. The data only include events with a recurrent characteristic and therefore these events can be categorized as follows:

- **Noise in multiple channels**: Similar to the time-resolved field induction method, events with temporary peaks are detected. Most of them leave a signal in multiple or all channels and can be discarded. The detection algorithm is nevertheless written conservatively to record these events for offline analysis.

- **Permanent field drift in multiple channels**: A new feature of this method is the ability to detect all permanent field drifts. Like before, multiple channels measure a field change and their magnitudes are similar and hence these events are also discarded. The detection algorithm of the time-resolved field induction method did not register such events, as the field drifts are less visible in a 60 ms time window. Also a drift only broadens the distribution and hence the previous trigger criteria would not have been fulfilled.

- **Increased noise in a correction channel**: Compared to the previous two types, here the noise level of a channel, which is used for the noise and drift cancellation is increased for a short time or for the whole waveform. The convolved waveform shows a higher scattering and sometimes surpasses the SV_{min} threshold. As this happens randomly, not necessarily all consecutive waveforms trigger these events. The increased noise is transferred via the cancellation method to the monopole channel and therefore a false event is induced. All events of this kind are consequently discarded. Also due to the broadened field distribution, the previous method was not able to detect these kind of events.

- **SQUID jump**: A common characteristic of the SQUID is that its lock is lost sometimes. This is typically caused by either a large or a fast field change. When this happens the SQUID electronics are unable to follow the field change. The consequence is a voltage jump, which corresponds to Φ_0 or multiples of it. The convolved waveform then shows a very large peak. All of these events are discarded.

- **Double jump**: Shortly after a first field jump, a second jump happens. As it is very unlikely that two monopoles are observed within such a short time interval or that one monopole reenters the pickup loop from the opposite direction, these events are discarded. The double jump event can be induced by a correction channel or by the raw monopole channel.

- **Single jump**: The last type of events are the most interesting to observe. Here only the raw monopole (y1) and corrected monopole channel (Mon) experience a very quick rise of the field. All of these events showed a jump with a negative amplitude. Despite this asymmetry of the field jump direction, this type of event is marked as a monopole-like event. The next section is dedicated to a detailed analysis of these events.

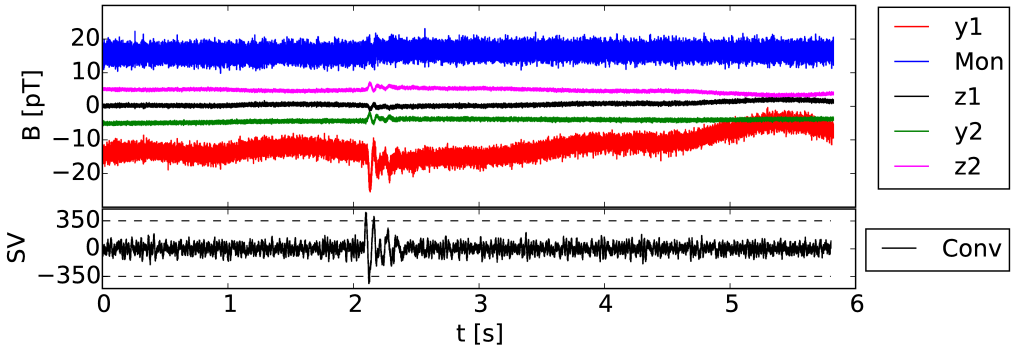

(a) Noise in multiple channels

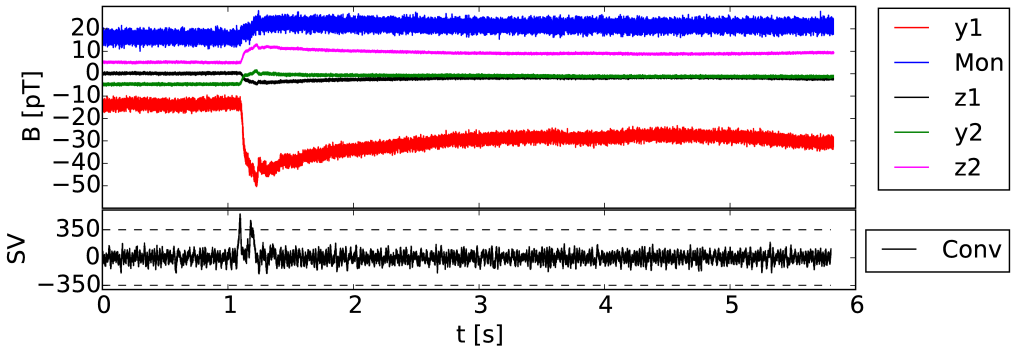

(b) Drift in multiple channels

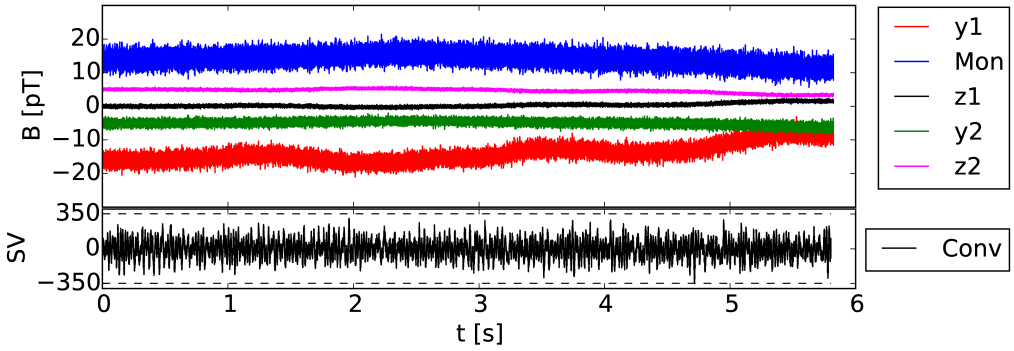

(c) Increased noise in a correction channel

Figure 5.18.: Recurrent noise and drift signals: Almost all false events are measured in multiple or all channels and show a temporary noise pulse (a) or a permanent field drift (b). Also increased noise in a channel which is used for the cancellation method triggers false events (c). For illustration purpose a shift is added to each waveform. The lower part of the plot shows the trigger value SV, extracted by the convolution of the monopole channel with the moving differential average window.

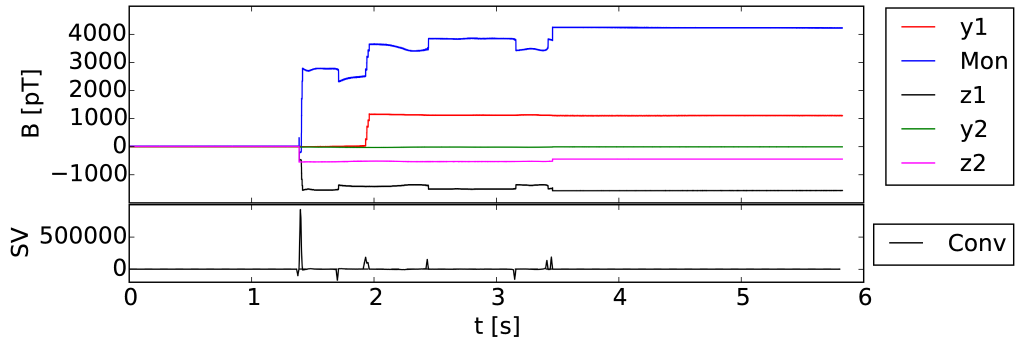

(a) SQUID jump

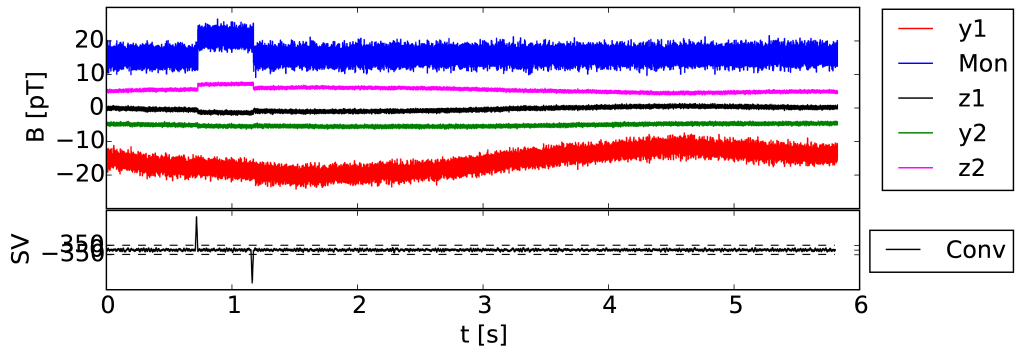

(b) Double jump

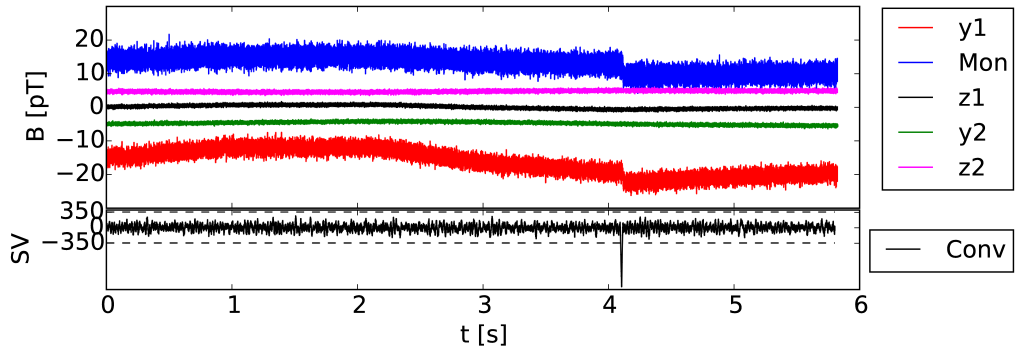

(c) Single jump

Figure 5.19.: Recurrent jump signals: The minority of the triggered events are jump events. They show a large amplitude, and occur if the SQUID loses its lock (a). Here usually multiple channels measure a jump. The case of two field steps shortly after each other (b) indicates a false event. Single jump events only seen in the monopole channel are considered as monopole-like events and are analyzed separately (see text for details). The plotting style is equivalent to figure 5.18.

5.3.6. Monopole-like signals

The result of the first measurement phase yields 21 monopole-like events. Before these events enter the next analysis phase based on a closer look on the waveform, the correlation to the environmental parameters, external field and mechanical vibration, are checked. The external field is measured by the $N_{\mathrm{Sen}} = 177$ field channels (B_i) of the ACS. The information of it is concentrated in

$$dB_e(t) = \frac{1}{\sqrt{N_{\mathrm{Sen}}}} \sqrt{\sum_{i=1}^{N_{\mathrm{Sen}}} (B_i(t) - B_i(t = t_0))^2}\,. \tag{5.13}$$

All fluxgate values are written to the experiment database every 2 or 3 seconds, depending on the time set in the software.

Mechanical vibrations are measured with an accelerometer (Endevco Model 86[2]). The raw data is sampled with a rate of 50 kHz and the maximum value is recorded with 50 Hz to reduce the amount of data.

In order to check for a non-stable environment, the 5 minutes before and after the monopole-like event are looked at. Figure 5.20 shows the environmental check on the example of the 13th event, which has been marked as monopole-like. Both environmental waveforms are centered to the starting time of the monopole waveform. Also the other SQUID channels (x1 and x2), which are not used at all for the monopole search are clear of field jumps. An induced signal via crosstalk is consequently excluded. In this example no peculiar environmental behavior is observed at the event time and not even in the whole time interval of 5 min before and after. Hence this event will not be discarded. All 21 events behave as the sample event shown and therefore all events enter the next analysis phase.

The convolved waveform does not only trigger the event detection, it also provides the event time. By taking the average of the field for the interval 0.3 s before and after the field jump, the field jump is determined with a precision of about 50 fT. The intervals starting 0.01 s before and ending 0.01 s after the jump are excluded from the height determination to avoid artifacts, which could occur due to an imprecise event time determination. Linear drifts which have been discussed previously have a negligible effect at these time scales. In figure 5.21 the signal amplitude (field jump) is illustrated on the example of the above shown waveform.

To check whether the event detection is independent of the detection algorithm and its only parameter N, each event waveform is convolved with variating N. If the maximum of the resulting convolved waveforms does not change its value in respect with N, the event is considered to be a real event and not as a numerical artifact. This check is important for signal amplitudes that are smaller than or similarly as large as the noise. All of the 21 monopole-like events passed this check.

Figure 5.22 shows the histogram of the signal amplitudes. All events have a negative amplitude and there is a peak visible at 1.8±0.1 pT, containing 7 events. This uncertainty is not extracted from a fit to the data, it is the spread of the

[2]Meggit Sensing Systems, Endevco Model 86, `https://www.endevco.com/datasheets/86.pdf`

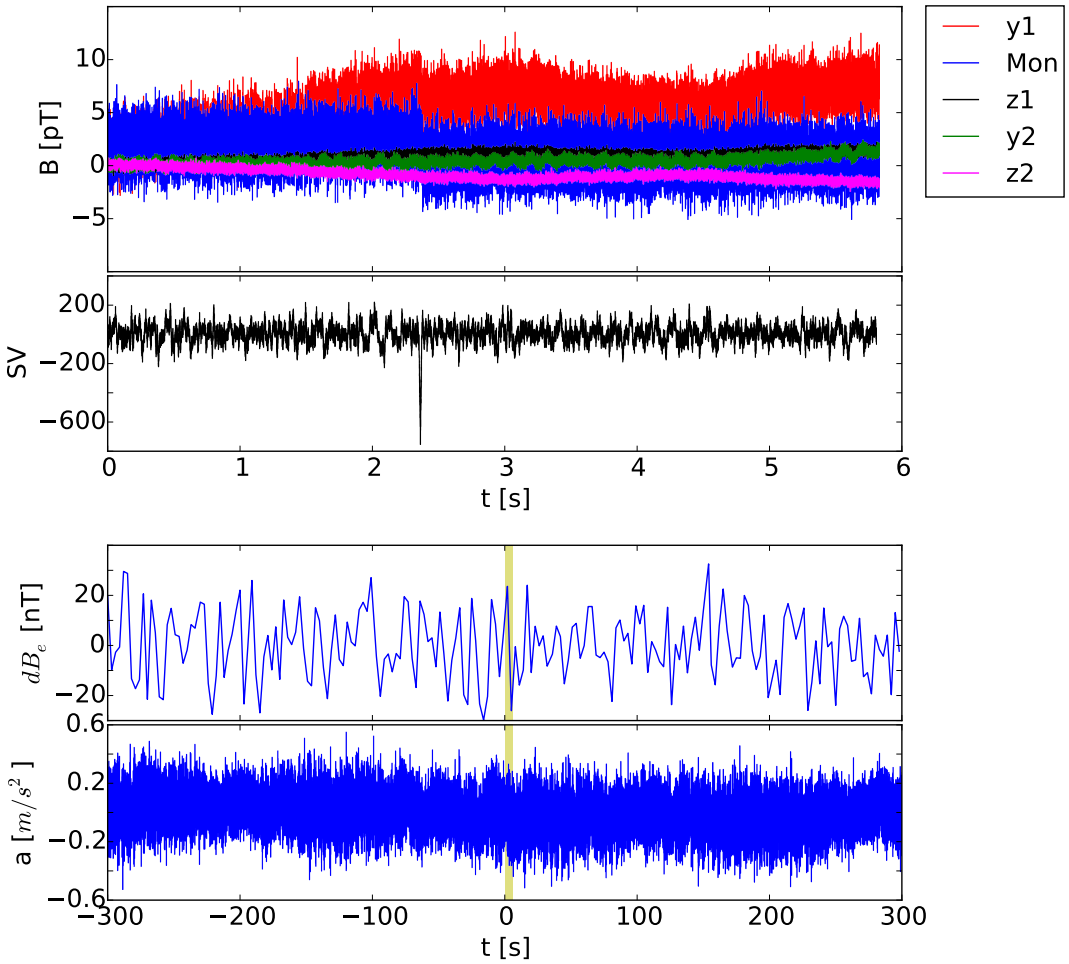

Figure 5.20.: Environmental check of monopole-like event #13: Here the monopole signal shows a small field jump on the order of a few picotesla, while the correction channel only show a small drift and no jump. At the time of the jump, the convolved waveform shows a clear peak with an absolute height of >600 and elsewhere <200. The 5.8 s long interval of the waveform is indicated by the shaded area in the external field dB_e and vibration data a. Both do not show a peculiar behavior and consequently this event will not be discarded.

event peak by the variation of binning parameter. For this kind of experiment no background was expected. The fact that monopole-like events are measured at all and that in particular the events peak near the expected value of Dirac monopoles ($dB \approx 1.1$ pT), is very puzzling.

Assuming monopoles are particles, which move freely through the universe, they should enter the detection system from an arbitrary direction. In the case that they are bound by a celestial body, a preferred direction is possible, but the exact opposite direction should have the same probability due to the oscillatory movement. The direction, from which the particle moves through the superconducting ring the

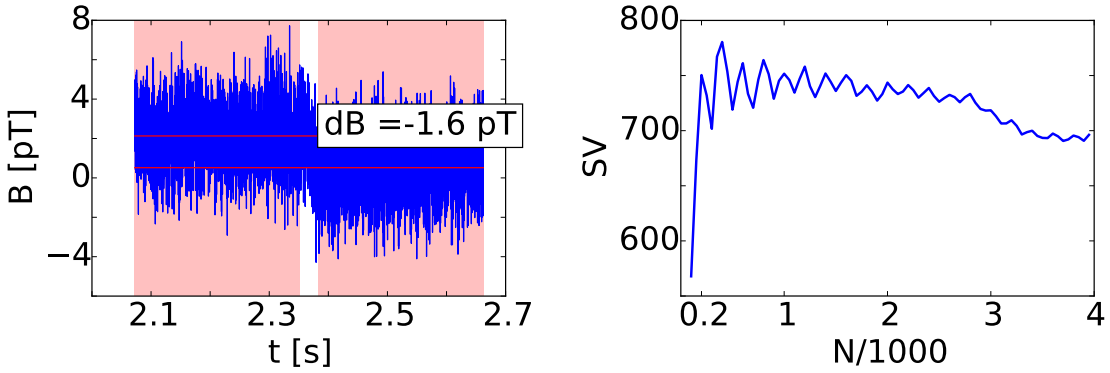

(a) Determination of the signal amplitude (b) Variation of the detection algorithm

Figure 5.21.: Signal verification and amplitude determination: The event of figure 5.20 is tested in respect to the detection algorithm parameter N (b). It shows that the variation of the convolution window width N yields an almost constant maximum of SV. So it is very unlikely to be a numerical artifact. (a) illustrates the time intervals used to determine the signal amplitude.

determines direction of the field jump, as either a positive or a negative flux is induced. Hence field jumps which originate from monopoles should peak at $\pm B_{\text{mon}}$. As this is not the case here, the observed events are very likely *not* signals generated by monopoles.

By analyzing the other SQUID channel, only y2 measured one similar event. It was a field jump of -0.5 pT with no other channel having a field excess at the same time. Comparing the amount of events, it is clear that the field jumps are connected to the monopole coil.

While the first measurement phase was running in parallel to other experiments at the nEDM instrument, the analysis showed that the nature of these events has to be investigated. Therefore all other activities inside the nEDM instrument have been stopped to decrease the noise level. Only devices which are necessary for the monopole experiment were running.

On the weekend after this shutdown two monopole like-events were detected, one with an amplitude matching the peak of the first phase. The first phase took data for 124 hours and the second phase for 42 hours. As the rate of events decreases with the reduction of environmental noise, this gives even more indication that the signals were not based on monopoles.

The next phase of the experiment was dedicated to improving the quality of the experiment. Two changes were made:

- The transfer coil of the monopole was inverted. In the case of a purely electronic nature of the events, the asymmetry of the detected events should not be influenced, while a magnetic nature would switch the sign of the field jumps.

- A second monopole coil (also shown in 5.12) was installed to measure in co-

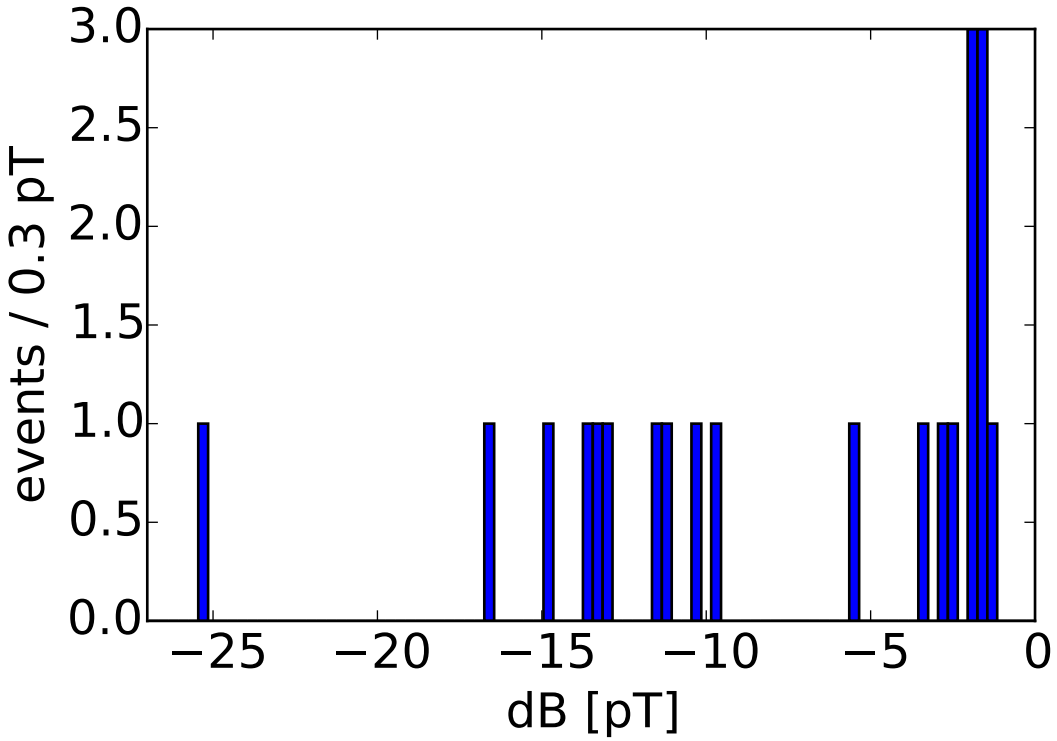

Figure 5.22.: Signal amplitude histogram of the 21 monopole-like events: The peak of events at around 1.8 pT is independent of the choice of the binning parameter. None of the events have a positive amplitude.

incidence to the first monopole coil. The second monopole coil features two loops with half the diameter of the larger coil. All other parts are equivalent to the first monopole coil and hence the inductance is expected to be the same. As induced current scales with the number of loops, a monopole generates a signal with double the amplitude (the monopole flux is independent of the coil surface), while a field change results in a halved amplitude. Consequently, a quarter of all events should be measured at the same time with a two times larger amplitude in the small coil.

The potential improvement of the 2-monopole channel upgrade is very large. It does immediately discriminate between monopole ($\propto 2$) and field ($\propto 1/2$) induced signals and also provides a clear signature in the event histogram. Due to the larger surface a peak measured by the large coil would be 4-times higher than the peak at the doubled field jump amplitude (measured by the small coil).

Unfortunately both monopole channels were damaged beyond repair during the final assembly inside the SQUID cryostat. The Kapton foil, carrying the twisted wire part of the coil, wrapped around one of the tools that are necessary to assemble the SQUID cube inside the cryostat. To avoid damage to the SQUID, the cryostat was opened and this revealed that the superconducting wire had been ripped off the transfer coil.

A rebuild of both coils is possible, but the orientation of the transfer coil to the SQUID channel is arbitrary and therefore two measurement runs would be necessary to discard the potential electronic nature of the field steps. The geometry of the SQUID cryostat does not allow a safer assembly of the monopole coils and hence future assembly attempts would likely result again in the destruction of the monopole coils. Consequently, this failure ended the monopole experiment.

5.3.7. Sensitivity

Even with the false events measured by the monopole coil, an upper limit for the monopole flux can be estimated. Equivalent to the previous measurement, the flux limit is determined by

$$\Phi = \frac{N(B)p(B)}{2\pi AT}\,, \tag{5.14}$$

with the detection surface $A \approx 280\,\mathrm{cm}^2$, the measurement time T, the detection efficiency $p(B)$ and the number of events $N(B)$ at the corresponding amplitude. The discarded events with $\mathrm{SV} > \mathrm{SV}_{\mathrm{min}}$ do not contribute to the measurement time. The expected signal amplitude scales linearly with the monopole charge g and therefore can be directly converted:

$$\frac{g}{g_D} = \frac{B}{B_{\mathrm{mon}}}\,. \tag{5.15}$$

In order to take the found events into account, their signal amplitude is binned with a width of 0.3 pT. From the variation of the start bin, an average distribution is extracted and fitted to multiple Gaussian peaks. There is no discrimination between regions with $N(B) = 0$ events/0.3 pT and $N(B) = 1$ events/0.3 pT in the process of the limit calculation. The detection efficiency (see figure 5.17b) can be modeled well with an error function.

Figure 5.23 shows the upper limit of the monopole flux, extracted from the data (124 hours). It is also extrapolated to 151 days of data, to be able to compare it with the current limit [100]. Even without decreasing the noise level, the presented method has the potential to improve the current limit in terms of sensitivity per day. The improvement is solely connected to the 14 times larger detection area. The major problem is the unidentified nature of the monopole-like events, as they peak very close to the expected Dirac monopole signal. The 124 hours of data result in an upper limit of $1.3 \cdot 10^{-9}\,\mathrm{cm}^{-2}\mathrm{sr}^{-1}\mathrm{s}^{-1}$, which is about a factor of 2 worse than the current limit.

5.4. Conclusion and outlook

Two methods to search for a potential dark matter particle have been described in the sections above. The first one is a completely new technique, which relies on the direct measurement of the field of a magnetic monopole. The advantage of this method is to be able to detect the direction and velocity of the magnetic charge carrying particle. But at the same time, this dependency strongly limits the

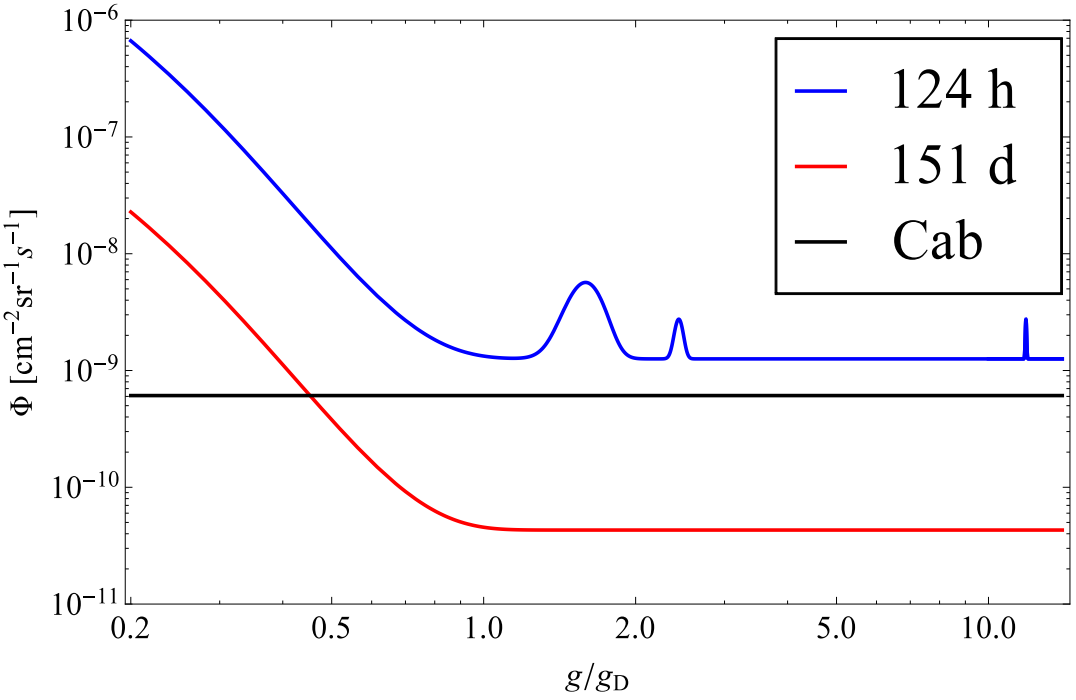

Figure 5.23.: Upper flux limit estimation: For low $g < g_D$ the upper limit is dominated by the noise level of the monopole coil. Neglecting the measured false events and assuming a similar measurement time, the presented method (blue) has the potential to improve the current limit [100] (black) by a factor 14, which solely caused by the larger detection area. The 124 hours of data set a limit (red), which is by a factor of 2 worse than current limit. Due to the false events, peaks in the upper flux at $1.6g_D$, $2.3g_D$ and $10.7g_D$ arise.

measurement at high velocities. In the astro-physically interesting velocity regimes it is statistically not yet competitive to other experiments. But nevertheless the widely unexplored parameter space of magnetic monopoles encourages further improvement of this technique. The main focus has to be put on the reduction of the noise level and an increased bandwidth of the detection system.

As no modifications on a common multi-channel SQUID are necessary, this measurement technique can be applied on all SQUIDs. In general, every kind of highly sensitive magnetometry can be used for this type of monopole search. The requirements on low noise and high bandwidth currently make SQUIDs the only suitable detector candidates. This method is complementary to the second technique, as the monopole mass can be extracted from the velocity. The mass determination is model dependent and therefore the uncertainty in this parameter is large.

The second method has been used previously and the presented implementation of it is a modification of the used SQUID. The installed monopole coil has a 14 times larger surface than the predecessor experiment of Cabrera [100] and consequently the potential to improve the current limit by the same factor. However the

analyzed dataset suffers from an unresolved background noise. The highly risky installation inside the SQUID cryostat makes it unreasonable to further measure with this cryostat.

This technique cannot easily be applied to other SQUIDs. Other magnetometer systems cannot be used at all, as the detection is based on the characteristics of the superconducting wire. In a different way, it also measures directly the main property of monopole, the magnetic charge. The approach to use multiple channels not only allows for drift and noise corrections, it also acts as a low level veto detection system. This is a large improvement in terms of the measurement quality. In the case of a positive particle identification, the monopole charge can be extracted. In contrast to the first method the detection rate is independent of the magnetic charge.

For both methods, datasets to successfully test the proof of principle have been taken. Due to the short measurement time, both yield a non-competitive limit ($1.1 \cdot 10^{-8}\,\mathrm{cm}^{-2}\mathrm{sr}^{-1}\mathrm{s}^{-1}$ and $1.3 \cdot 10^{-9}\,\mathrm{cm}^{-2}\mathrm{sr}^{-1}\mathrm{s}^{-1}$), but they have the potential to improve the current limit. Induction based experiments are the cleanest measurements to search for monopoles, as they are independent of any theoretical description of the nature of monopoles.

Based on the presented results, a cryostat which is dedicated to a monopole search experiment is the best way to continue. The application of multiple SQUIDs for field correction and veto discrimination is essential. By applying multiple monopole pickup coils with various sizes and orientations in a geometry that allows a coincidental detection, the quality of the measurement could be greatly improved.

6. Conclusion

The many open questions in fundamental physics along with the non-discovery of a BSM particle at the LHC makes high precision experiments even more important. Such experiments can test nature up to energy scales that are currently beyond the reach of collider based experiments. These sophisticated approaches rely on the precise control of the systematic effects connected to the experimental conditions. For some of these experiments controlling magnetic effects is a leading systematic. This thesis presented a set of such experiments with a particular focus on the magnetic field requirements.

The Munich nEDM instrument offers excellent conditions for various precision physics experiments. It features the current best magnetic shield, with residual fields of a few 100 pT over an extended volume. The modular composition of the shield enables custom-made solutions for the development and characterization of highly sensitive magnetometer systems.

Such a potential application is the 4π magnetometer concept which has been introduced here. It features a general way to measure magnetic fields at the position of the nEDM apparatus without disturbing the actual measurement. In addition, it has the unique possibility to spot local magnetic contaminations, like dipoles. Dipoles and linear gradients are the main source of systematic errors for the current nEDM experiment. Hence the comprehensive knowledge of them and of their temporal characteristics provides a good handle on the systematics.

In addition, a large-scale active shield has been built and characterized. A custom dynamic algorithm was implemented to handle the complex system of 180 field probes fed back on 24 compensation coils. The active field compensation system reduces the static field surrounding the passive shields by almost a factor of 10. The dynamic mode improves the temporal stability by more than one order of magnitude.

The temporal stability of the passive shielding has been measured using various magnetometer systems. The results show an unprecedented temporal quality of the field and of the field gradient, enabling the search for a neutron EDM with a sensitivity of a few 10^{-26} e $\cdot$ cm per measurement run. Consequently, the goal of 10^{-28} e $\cdot$ cm is feasible.

The excellent magnetic environment offered by the nEDM instrument also allows other exotic experiments. Two experiments searching for a hypothetical particle – the magnetic monopole – demonstrated the capability of the magnetic shield. Both of the experiments used a multichannel SQUID; the time-resolved field induction method is a totally new approach and the flux induction method is based on previous approaches. The proof of principle measurement for the time-resolved field induction method produced an upper limit estimate 20 times worse than the current

limit, but with 150 times fewer statistics. The full potential of this method, using six independent SQUIDs, yields an improvement of a factor of about 50 compared to the current limit in a specific part of the parameter space. This method is very versatile and can be implemented using any other multichannel magnetometer system that has a high bandwidth and sensitivity. The flux induction method extends the technique that was used to set the current experimental limit. Adding a flux transformer significantly increases the effective detection area, and the multichannel SQUID allows noise and drift cancellation. The multichannel design also allows for a veto mechanism that improves the discrimination between false and real events. Due to the smaller data set, the limit estimate is two times worse than the current limit. The effective detection area is 14 times larger than the experiment that set the current limit. Hence the sensitivity potential is also increased by 14. Unresolved background problems were discussed in detail and a concept to further increase the measurement quality was presented. The methods are complementary, with the time-resolved field induction technique being able to measure the velocity of the monopole and the flux induction technique being able to determine the monopole charge.

A. Parameters of the field cage system

coil label	$\mathbf{r_0}$ [m]	L x B [m^2]	N	$A\,[mm^2]$	$R\,[\Omega]$	L [mH]	I_0 [A]
z-BW	(0.0, +2.2, 0.0)	4.5 x 6.0	15	6	0.95	2.50	-5.78
z-BE	(0.0, -2.2, 0.0)	4.5 x 6.0	15	6	0.94	2.81	11.21
z-TW	(0.0, +2.2, +6.0)	4.5 x 6.0	15	6	1.07	3.03	4.58
z-TE	(0.0, -2.2, +6.0)	4.5 x 6.0	15	6	1.05	2.96	10.68
x-SW	(-3.0, +2.2, +3.0)	4.5 x 6.0	15	6	0.96	2.71	-3.23
x-SE	(-3.0, -2.2, +3.0)	4.5 x 6.0	15	6	1.04	2.56	-4.84
x-NW	(+3.0, +2.2, +3.0)	4.5 x 6.0	15	6	1.06	2.40	-3.24
x-NE	(+3.0, -2.2, +3.0)	4.5 x 6.0	15	6	1.04	3.05	-8.85
y-WS	(-1.5, +4.4, +3.0)	4.5 x 6.0	15	6	0.83	2.46	2.10
y-WN	(+1.5, +4.4, +3.0)	3.0 x 6.0	15	6	0.83	2.48	0.17
y-ES	(-1.5, -4.4, +3.0)	3.0 x 6.0	15	6	0.84	2.42	4.49
y-EN	(+1.5, -4.4, +3.0)	3.0 x 6.0	15	6	0.85	2.44	4.58
z-1	(0.0, 0.0, +1.8)	8.9 x 6.0	10	4	1.68	2.90	4.99
z-2	(0.0, 0.0, +2.6)	8.9 x 6.0	10	4	1.65	3.10	1.55
z-3	(0.0, 0.0, +3.4)	8.9 x 6.0	10	4	1.52	2.69	2.03
z-4	(0.0, 0.0, +4.2)	8.9 x 6.0	10	4	1.53	2.82	3.91
x-1	(-1.2, 0.0, +3.0)	8.9 x 6.0	10	4	1.48	3.03	-0.97
x-2	(-0.4, 0.0, +3.0)	8.9 x 6.0	10	4	1.47	2.93	0.33
x-3	(+0.4, 0.0, +3.0)	8.9 x 6.0	10	4	1.47	2.90	-2.99
x-4	(+1.2, 0.0, +3.0)	8.9 x 6.0	10	4	1.46	3.01	-1.66
y-4	(0.0, +1.8, +3.0)	6.0 x 6.0	10	4	1.18	2.30	-2.46
y-3	(0.0, +0.6, +3.0)	6.0 x 6.0	10	4	1.19	2.15	-2.89
y-2	(0.0, -0.6, +3.0)	6.0 x 6.0	10	4	1.19	2.27	-1.54
y-1	(0.0, -1.8, +3.0)	6.0 x 6.0	10	4	1.18	2.43	-0.46

Table A.1.: Coil parameters of the active field compensation system.

Sensor index	$\mathbf{r_0}$ [m]	sensor orientation
1	(0.1, 4.0, 4.2)	(-x, -z, -y)
2	(0.7, 4.0, 4.6)	(-x, -z, -y)
3	(1.5, 3.8, 4.6)	(+z, -x, -y)
4	(2.1, 3.8, 4.2)	(-y, -x, -z)
5	(2.1, 3.8, 4.6)	(-y, -x, -z)
6	(0.5, 3.6, 4.4)	(-x, -z, -y)
7	(-1.7, 3.4, 4.6)	(+z, +y, -x)
8	(-1.5, 3.4, 4.2)	(-z, +y, +x)
9	(-1.3, 3.4, 4.4)	(+x, +y, +z)
10	(+2.3, 3.4, 4.6)	(+x, -y, -z)
11	(-2.1, 3.2, 3.8)	(-y, -z, +x)
12	(-2.1, 3.2, 4.0)	(-x, -z, -y)
13	(-1.9, 3.2, 2.6)	(+y, +x, -z)
14	(2.3, 3.2, 4.0)	(+x, -z, +y)
15	(2.5, 3.2, 4.8)	(+y, -z, -x)
16	(0.3, 3.0, 4.2)	(+x, -y, -z)
17	(-1.1, 2.8, 4.4)	(+x, -y, -z)
18	(1.9, 2.8, 4.0)	(+x, -y, -z)
19	(2.5, 2.8, 3.8)	(-y, +z, -x)
20	(-1.7, 2.2, 1.2)	(+x, -y, -z)
21	(-1.7, 1.8, 1.6)	(+x, -y, -z)
22	(-1.7, 1.6, 3.6)	(+y, -x, +z)
23	(2.5, 1.4, 4.2)	(+y, -z, -x)
24	(-1.7, 1.0, 1.8)	(-x, -z, -y)
25	(-1.9, 0.8, 1.4)	(-y, -z, +x)
26	(-1.7, 0.8, 1.8)	(+x, -z, +y)
27	(1.9, 0.8, 2.4)	(-y, -x, -z)
28	(-1.7, 0.6, 1.4)	(-x, -z, -y)
29	(-1.7, 0.6, 3.4)	(-y, -x, -z)
30	(0.5, 0.4, 4.6)	(+x, -y, -z)

Table A.2.: Sensor parameters of the active field compensation system (part 1).

Sensor index	$\mathbf{r_0}$ [m]	sensor orientation
31	(0.9, 0.4, 4.5)	(+x, -y, -z)
32	(1.9, 0.4, 2.6)	(-y, -x, -z)
33	(1.3, 0.2, 4.4)	(+x, -y, -z)
34	(2.1, -1.8, 3.2)	(+x, -z, +y)
35	(2.1, -2.0, 3.2)	(+x, -z, +y)
36	(-2.5, 2.0, 4.0)	(-y, -z, +x)
37	(-0.5, -2.6, 4.0)	(+x, -y, -z)
38	(-1.5, -2.8, 3.6)	(-x, -y, +z)
39	(0.5, 0.8, 5.0)	(+x, -y, -z)
40	(-0.3, -2.8, 3.8)	(-x, -z, -y)
41	(1.5, -3.2, 3.2)	(+x, -y, -z)
42	(-2.5, -3.4, 3.6)	(-y, -z, +x)
43	(-2.1, -3.4, 3.6)	(+y, -z, -y)
44	(-1.7, -3.4, 4.0)	(-x, +y, -z)
45	(-2.3, -3.6, 3.6)	(-y, -z, +x)
46	(-1.5, -3.6, 4.0)	(-x, +y, -z)
47	(-0.7, -3.6, 3.8)	(+y, -z, -x)
48	(-0.3, -3.8, 3.6)	(+x, -z, +y)
49	(-1.5, -4.0, 3.8)	(+x, -z, +y)
50	(1.9, -4.0, 3.4)	(+x, -z, +y)
51*	(-0.5, 1.75, 4.75)	(-y, -x, -z)
52*	(0.0, -0.45, 4.62)	(+y, +x, -z)
53*	(0.55, 3.84, 3.05)	(-x, -z, -y)
54*	(-2.4, 2.0, 3.0)	(-y, -z, +x)
55*	(2.4, 2.0, 3.05)	(+y, -z, -x)
56*	(-2.4, -0.8, 3.0)	(+y, +z, +x)
57*	(-0.8, 1.9, -0.3)	(-x, +y, -z)
58*	(-0.75, 1.9, 0.75)	(-x, -z, -y)
59*	(0.75, -0.8, 0.75)	(-x, -z, -y)

Table A.3.: Sensor parameters of the active field compensation system (part 2): Sensors labeled with * only monitor the magnetic field and do not contribute to the dynamic compensation.

B. Multipole field generation by the ACS coils

With its six (outermost are combined to one) coils per spatial direction, the ACS is able to generate higher-order fields along the coil axis (perpendicular to the coil area). The x-direction is exemplarily shown for all directions. To quantize the quality of the generated field in respect to the target field, the field homogeneity (equation 3.5) is obviously not suitable. Therefore it is modified to

$$H_x = \frac{1}{V}\frac{1}{B_{\text{mean}}}\int_V |B_x(x) - x^n| dV \tag{B.1}$$

with the order of the field n, the fiducial volume V and

$$B_{\text{mean}} = \frac{1}{V}\int_V |B_x(x)| dV\,. \tag{B.2}$$

In figure B.1 the target fields are compared to the fields the ACS generates. The field averaged over the y and z direction

$$\bar{B}_x(x) = \frac{1}{L_y L_z}\int_{-\frac{L_y}{2}}^{\frac{L_y}{2}}\int_{-\frac{L_z}{2}}^{\frac{L_z}{2}} B_x(x,y,z) dy\, dz \tag{B.3}$$

is used to illustrated the multipole fields. With increasing order n, the generates field match less to the target field. This behavior also observable by the modified homogeneity H_x, which is 2.4 % (10.5 % / 53.6 %) for a constant (linear / quadratic) field. The high values of H_x are caused by the fields off the central line ($y = 0\,\text{m}$ $z = 3\,\text{m}$).

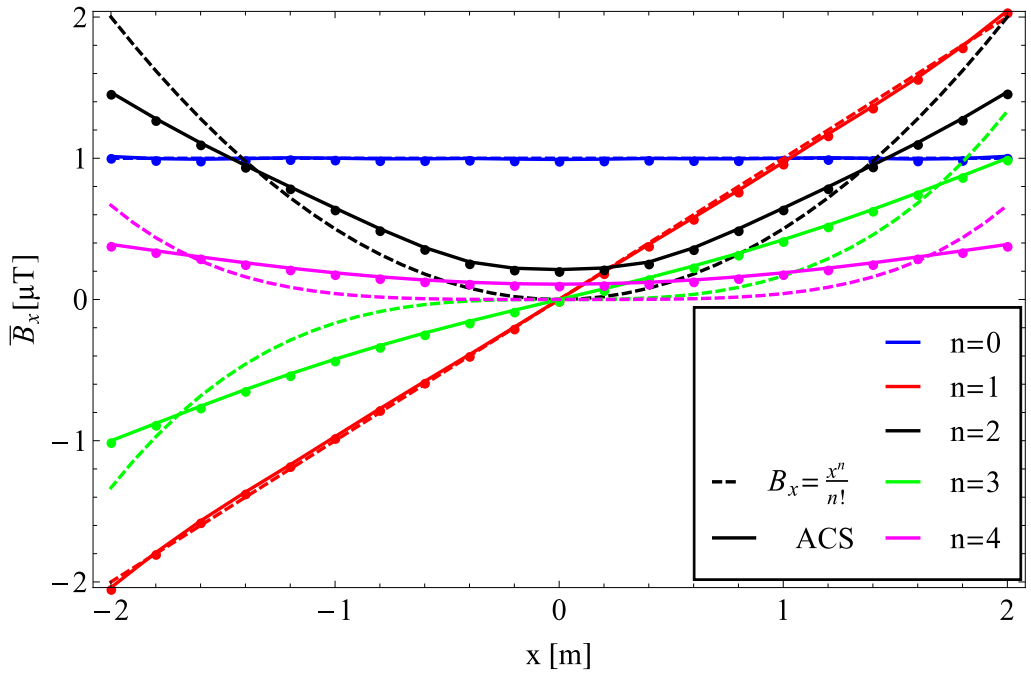

Figure B.1.: Generation of higher-order fields with the ACS coils: With increasing order the field generated by the ACS (soild lines) deviates from the target field (dashed lines).

C. Protection from sunlight for the passive shield

To protect the outer passive shield from direct sunlight, the shell of the field cage is partially made of non-transparent polyvinyl chloride (PVC) panels. A total coverage with non transparent panels makes the working place around the passive shield very dark and therefore the installation of artificial light would be needed. These could produce disturbing magnetic fields and hence the distribution of the panels have to be optimized.

The only sources for direct sunlight in the experimental hall are 4 rows of windows. They are on the East and West side of the building and range in height from 2 m to 3 m and from 8 m to 9 m. On the east side of the field cage there will be the NEPOMUC experiment[105], which has a height of ≈ 4 m. Consequently the east side of the field cage does not need sun protection on the lower panels. The angle of incidence which occurs in Munich during the year is shown in figure C.1[106].

The angle of incidence is transformed to a direction vector

$$\mathbf{v} = \begin{pmatrix} \sin(\theta) \cdot \cos(\phi) \\ \sin(\theta) \cdot \sin(\phi) \\ \cos(\theta) \end{pmatrix} . \tag{C.1}$$

Together with the starting points $\mathbf{r}$ which are located on the surfaces of the windows they form the equation of a line. The crossing points $\mathbf{r_c}$ of these lines with the surfaces of the passive shield can be calculated with

$$\mathbf{r_c} = \mathbf{r} + \mathbf{v} \cdot \frac{(\mathbf{r_S} - \mathbf{r}) \cdot \mathbf{n_S}}{\mathbf{v} \cdot \mathbf{n_S}} . \tag{C.2}$$

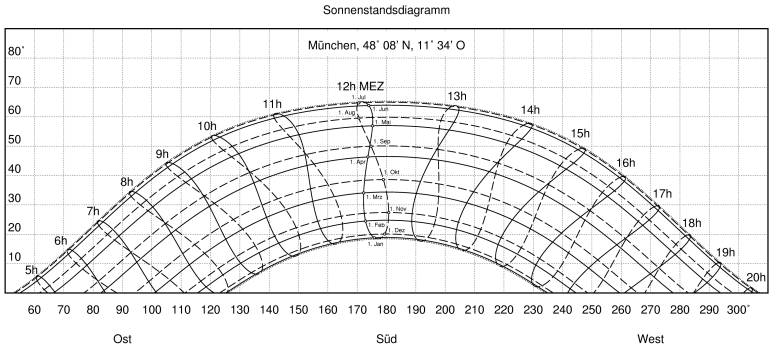

Figure C.1.: The angle of incidence of the sun light for Munich [106].

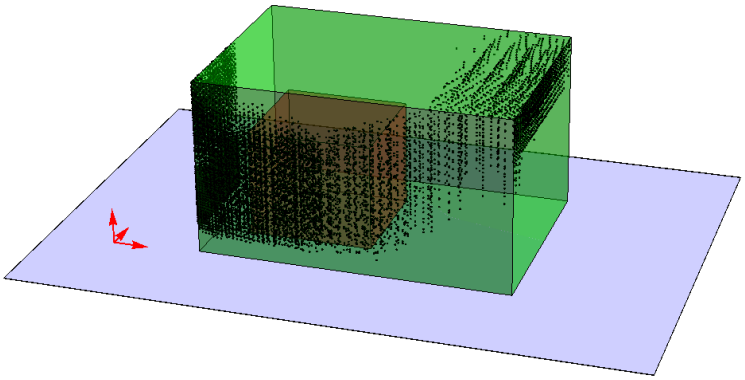

Figure C.2.: Crossing points of direct sunlight through the shell of the fieldcage on to the passive shield.

$\mathbf{r_S}$ is a point on one surface of the passive shield and $\mathbf{n_S}$ is the normal of the associated surface. The result of this numeric calculation is shown in figure C.2. The non-transparent PVC panels which have a maximum size of $1\,\mathrm{m}^2$ are installed at the places with the black dots.

D. Noise characterization

D.1. Current source - CPX400DP

The current output of the current source CPX400DP[1] has been measured via the voltage drop on a 1 Ω resistance with an oscilloscope. The measured current noise is < 1.3 mA over the whole current range (0-20 A). Figure D.1 shows the current noise and the used voltage scaling that was set in the oscilloscope. There is a clear correlation of the voltage scaling to the current noise. Therefore the measurement is very likely limited by the sensitivity of the oscilloscope and 1.3 mA may be overestimated.

D.2. Fluxgate - Mag690

The Mag-690[2] are installed in the ACS and read out with the analog-digital-converter (ADC) card XVME-564[3]. The average of 300 samples which are read out with a sample rate of ∼2kHz are combined to the determine the measured field value. The combined noise of the readout system including 30 m long cables is exemplary for one channel of one sensor shown in figure D.2. It follows a Gaussian distribution and is on the order of ∼10 nT. The sensitivity of the individual sensors vary from 5 nT to 650 nT (see figure D.3). Most sensors measure a noise <20nT. The few fluxgates with >20 nT are located near other electronic components and therefore measure the noise produced by these devices. Hence the sensitivity of the magnetic field measurement device is assumed to be ∼20 nT.

D.3. Resonant noise increase of the current supply coil circuit

The combination of the used current supplies and the coils (see A) produce an increased noise. This has been determined by measuring the magnetic field with the fluxgates and varying all currents simultaneously. For ∼0.5 A to 1.6 A the noise almost reaches 3μT (see figure D.4).

[1] Thurlby Thandar Instrumends, Ltd.

[2] Bartington Instruments, `http://www.bartington.com/mag690-low-cost-three-axis-magnetic-field-sensor.html`

[3] Acromag Inc., XVME-564

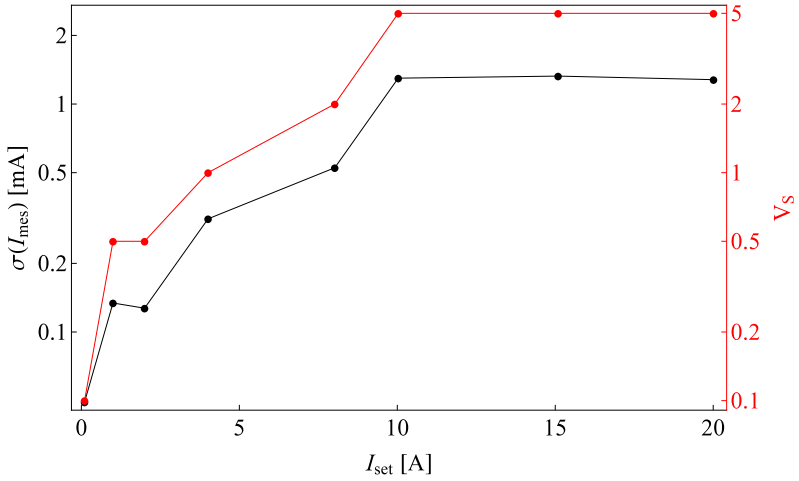

Figure D.1.: Current noise as function of the applied current (black) and the voltage scaling (red) used for the measurement with the oscilloscope.

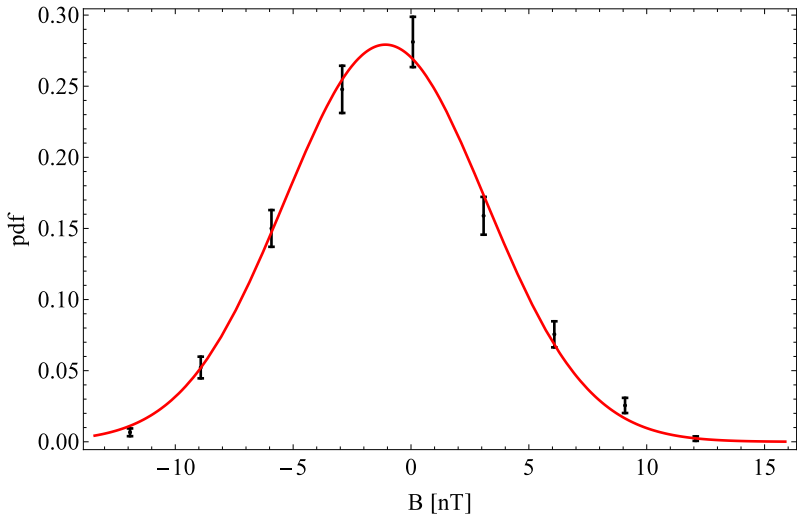

Figure D.2.: Probability distribution function (pdf) of a channel of the Mag-690 fluxgate. The distribution is Gaussian, with a full width of 8.5 nT.

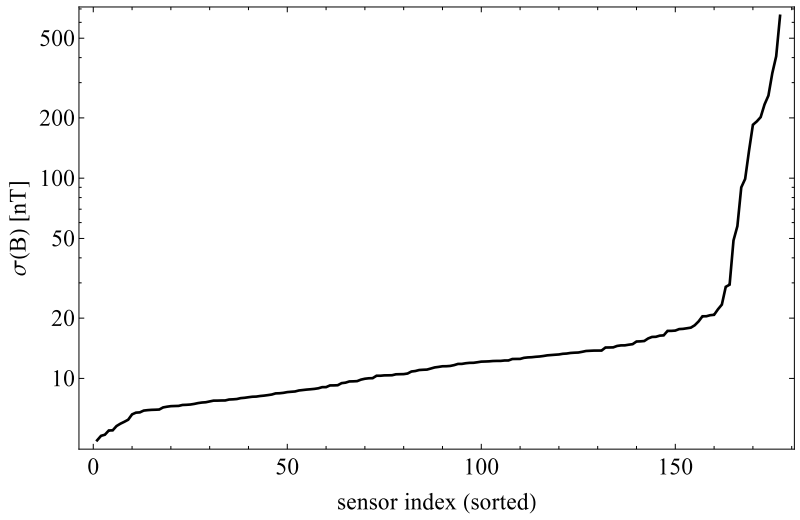

Figure D.3.: Full width of all sensor channels used, sorted by increasing width: The right part of the plot is attributed to the ambient field noise produced by neighboring electric devices of other nEDM components rather than to the intrinsic sensor sensitivity.

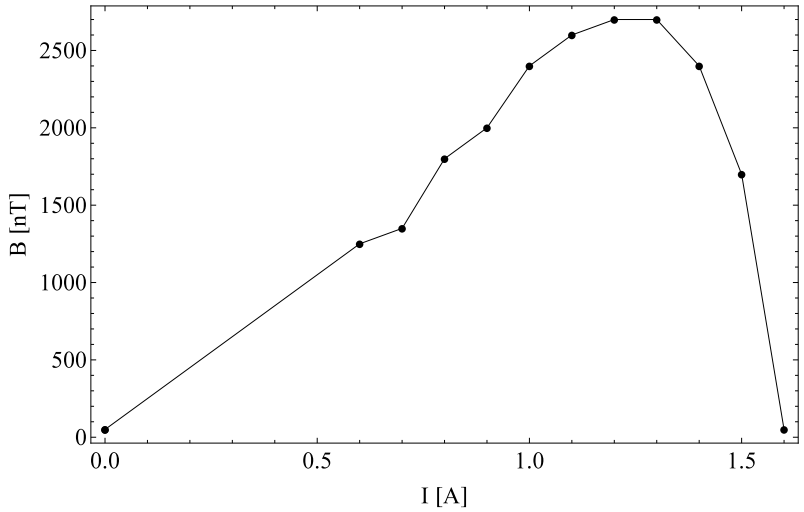

Figure D.4.: Measured field noise as a function of the applied coil current in the low current regime.

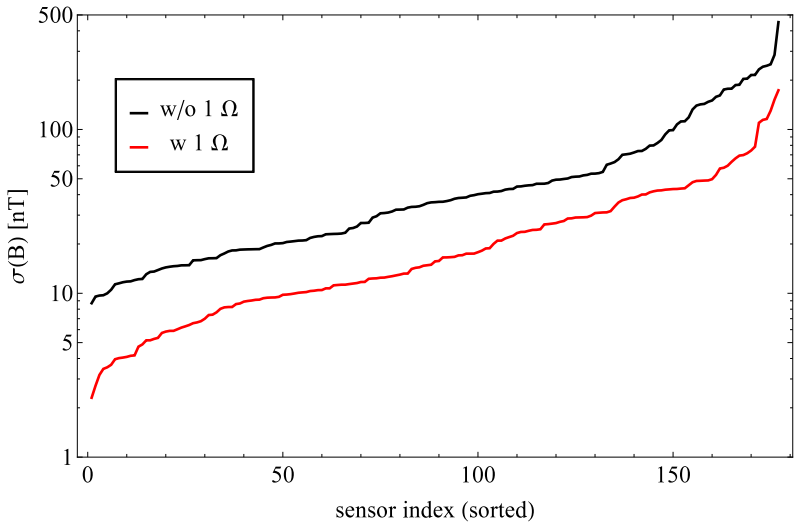

Figure D.5.: Noise reduction of the 1 Ω installation.

The origin of this noise behavior can be found in the interplay between the resistance and inductance of the coils and the internal electronics of the current supplies. Adding a series resistor of 1 Ω solves this problem. Figure D.5 shows the noise reduction resulting from the installation of a 1 Ω series resistor to the coil-current-source circuit. To quantify the improvement the standard current set I_0 (see A) is applied and the field noise of every sensor channel is measured.

E. ACS software

The ACS is controlled via a custom-written program based on ORCA[1]. ORCA is an object-orientated real time control and acquisition system written in objective-C. The software is divided into three parts: the graphical user interface (GUI), the controller and the model.

The model includes the compensation algorithm, the communication with the devices (ADC, SBC and power supplies) and the database. It handles all important system variables (e.g. the field vector **B**, the current vector **I**, the feedback matrix **F** and many more). Almost all calculations are based on matrix multiplication. CBLAS[2] routines are used to perform these multiplications very efficiently. The code by itself is straight forward, but very long. Hence it is not shown here. If a system variable is changed by the code, a notification is sent to a separate notification thread.

The controller recognizes the change and updates the GUI. It operates also in the reverse direction. So if a change is made by a user in the GUI, a notification is sent and the controller updates the corresponding system variable. Model and controller are written in objective-C.

The GUI offers full control of the system. The main window features 4 tabs: Controls, power supplies, ADCs and basic configuration.

In the upper part of the control (see figure E.1) page system values for the database (see tableE.1) and parameter of the compensation are specified. By checking the "Post to DB" box the current field and current values are saved in the database every "Period" seconds. Only the current value is saved and not the values of the intermediate iterations. In other words, if the run frequency ("Refresh rate") is higher than the period, not all data is saved. This is done to reduce the data size needed in the database. A "run comment" can be given which also will be written into the database.

When the "Start Process" button is activated it changes to "Stop Process". If the "Dynamic mode" check box is not checked, the algorithm is in the static mode (all currents are fixed). By checking the box, the dynamic mode is activated and the target field is set to the current field. The dynamic mode should be turned off, while large field changes are done (e.g. the degaussing process or the opening of the passive shield). A "feedback threshold" can be used to modify the compensation algorithm. Only current changes larger than the threshold are applied by the power supplies. The threshold is usually set to zero.

The lower part of control page features 4 sub-tabs. "Channel map" shows the

[1]ORCA, Mark Howe, `http://orca.physics.unc.edu/~markhowe/Orca_Help/Home.html`
[2]C Basic Linear Algebra Subprograms

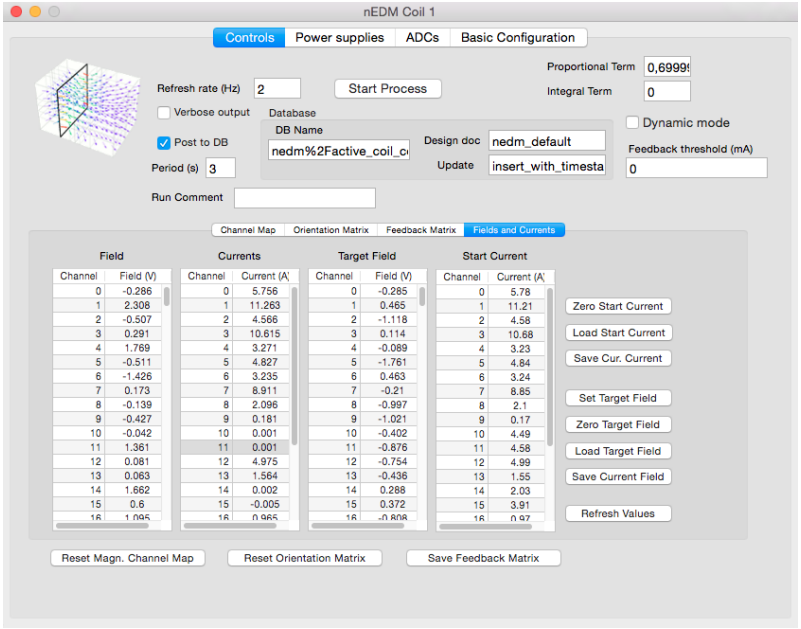

Figure E.1.: Main window of the ACS GUI.

Name	Value
DB Name	nedm%2Factive_coil_compensation
Design doc	nedm_default
Update	insert_with_timestamp

Table E.1.: Database specification.

mapping of the ADC channel to the field channel. The "Orientation Matrix" corrects for the polarity of the coils. The "feedback matrix" displays the feedback matrix which is calculated in the "Basic Configuration" tab. The "Fields and Currents" sub-tab displays the current field and current and the target field and the start current. The individuals lists are stored in property lists (PList). These can be loaded with new ones, saved to the hard drive or reseted. The "Refresh button" updates the display of the fields and currents.

In the "power supplies" tab (see figure E.2a) an overview of the power supplies is given. Next to basic operations, each power supply can be selected to open its configuration page (figure E.2b). If the "Fluxgate ONLY mode" box is checked, the power supplies are excluded from the algorithm. This mode can be set manually (if only the magnetic field has to be measured) or is set by the code, if a communication error with the power supplies happens. This ensures that in the case of a network failure the currents stay at their last value and the magnetic field continues being recorded. If the "Fluxgate ONLY mode" is active, a warning text is displayed in the "Controls" tab.

In the "Basic configuration" tab (see figure E.3) the sensitivity map (matrix A of equation 3.1) and the list of active channel are set, both by PLists. The "Regular-

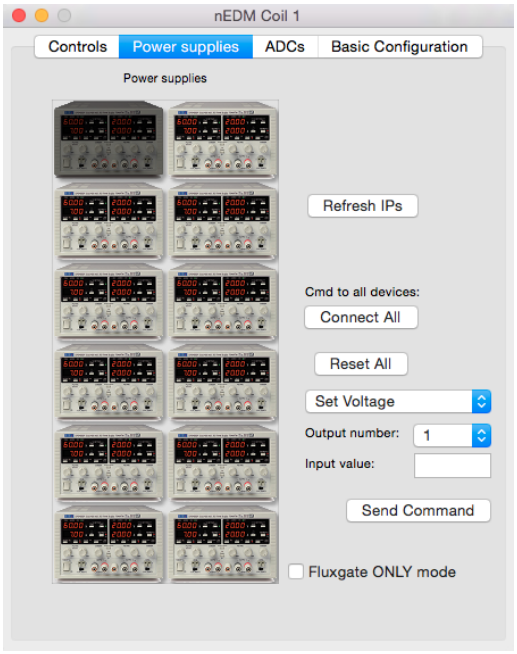

(a) Overview

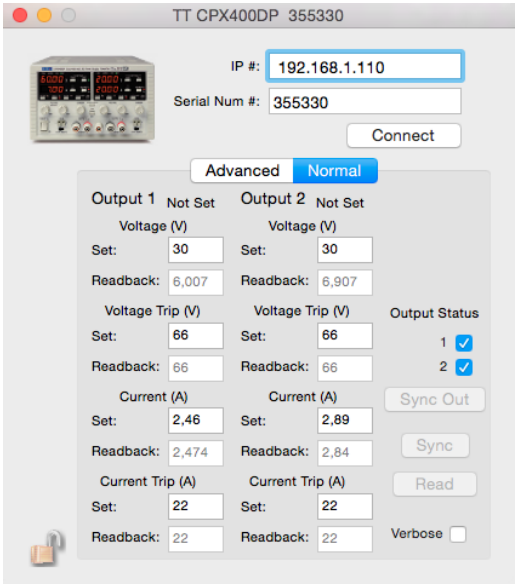

(b) Power supply interface

Figure E.2.: Power supply window.

ization parameter" r is used to transform ("Build new Feedback Matrix" button) A to the feedback matrix. The active channel map defines the sensors that contribute to the compensation algorithm and the sensors that are only used for monitoring the field.

The sensitivity map is determined by a ORCA script and a standalone Mathematica (see figure E.4) procedure. ORCA features a script environment that enables quickly programmed applications. In this case the coils are individually ramped from 0 A to 10 A in 1 A steps and all field values are recorded.

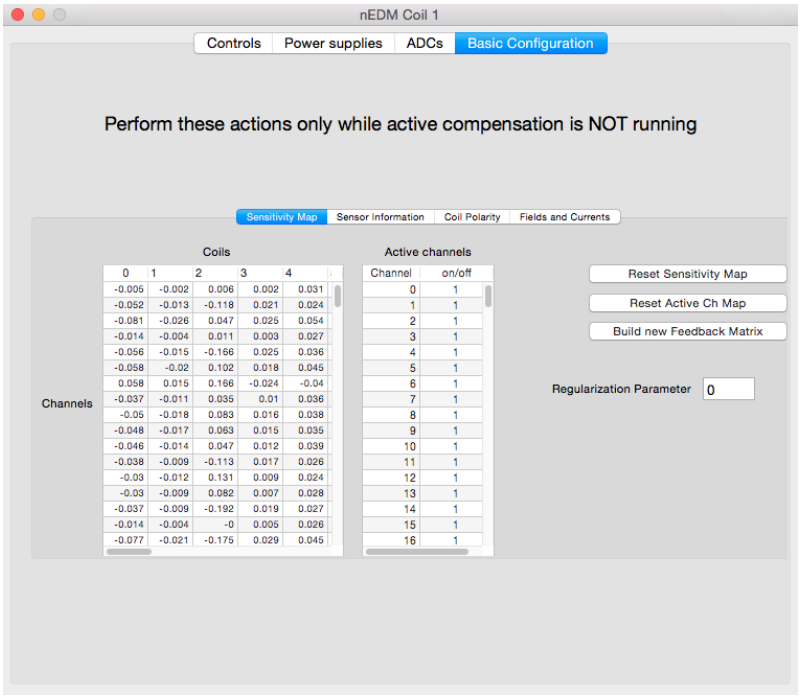

Figure E.3.: Basic configuration window.

```
Table2PList[tab_] := Module[{prefix, core, suffix},
  prefix = {{"<?xml version=\"1.0\" encoding=\"UTF-8\"?>"},
    {"<!DOCTYPE plist PUBLIC \"-//Apple//DTD PLIST 1.0//EN\" \"http://www.apple.com/DTDs/PropertyList-1.0.dtd\">"},
    {"<plist version=\"1.0\">"}, {"<array>"}};
  suffix = {{"</array>"}, {"</plist>"}};
  core = Flatten[Table[Join[{{"", "<array>"}}, Table[
       {"", "",
        If[StringQ[tab[[i, j]]], "<string>", "<real>"] <>
         If[StringQ[tab[[i, j]], tab[[i, j]], ToString[1.0 * If[Abs[tab[[i, j]] > 10^-5, tab[[i, j]], Sign[tab[[i, j]] * 0.00001]]] <>
         If[StringQ[tab[[i, j]]], "</string>", "</real>"]}, {j, 1, Length[tab[[i]]]}], {{"", "</array>"}}], {i, 1, Length[tab]}], 1];
  Join[prefix, core, suffix]
 ]
coilmapraw = Import["name_coilramp.txt", "Table"];
nsen = 3 * Length[coilmapraw[[All, -7]] // DeleteDuplicates];
ncoil = 24;
nsteps = 11;
coilmapraw2 = Flatten[
   Table[{
     Drop[Drop[c, {-1}], {-1}],
     Drop[Drop[c, {-1}], {-2}],
     Drop[Drop[c, {-2}], {-2}]}
    , {c, coilmapraw}], 1];
coilmapraw2 = Select[coilmapraw2, Total[#[[Range[4, 3 + ncoil]]]] ≠ 0 &];
coilmapraw3 = Partition[coilmapraw2, nsen * (nsteps - 1)];
coilmap = Transpose[Table[Table[cc[[Range[c, Length[cc], nsen]]], {c, 1, nsen}], {cc, coilmapraw3}]];
res = Table[
   Table[
    ramfit = NonlinearModelFit[coilmap[[n, c, All, -1]], aa + bb * x, {aa, bb}, x];
    {ramfit["ParameterTable"][[1, 1, 2, 2]],
     ramfit["ParameterTable"][[1, 1, 3, 2]],
     Abs[ramfit["ParameterTable"][[1, 1, 3, 3]] / ramfit["ParameterTable"][[1, 1, 3, 2]]}
    , {c, 1, ncoil}]
   , {n, 1, nsen}];
aij = res[[All, All, 2]];
b0 = Mean[Transpose[res[[All, All, 1]]]];
Export["name_aij.plist.txt", aij // Table2PList, "Table"];
```

Figure E.4.: Mathematica code for the Aij extraction.

F. Cable configuration of the ACS sensor system

Each breakout box connects 20 fluxgates to one ADC card. The pin configuration is shown in figure F.1. C indicates the channel number, AGD is the analog ground, PGD the power ground, TRG the trigger input, X, Y and Z the signals from the x, y and z channels, Vs the voltage supply and NC is not connected.

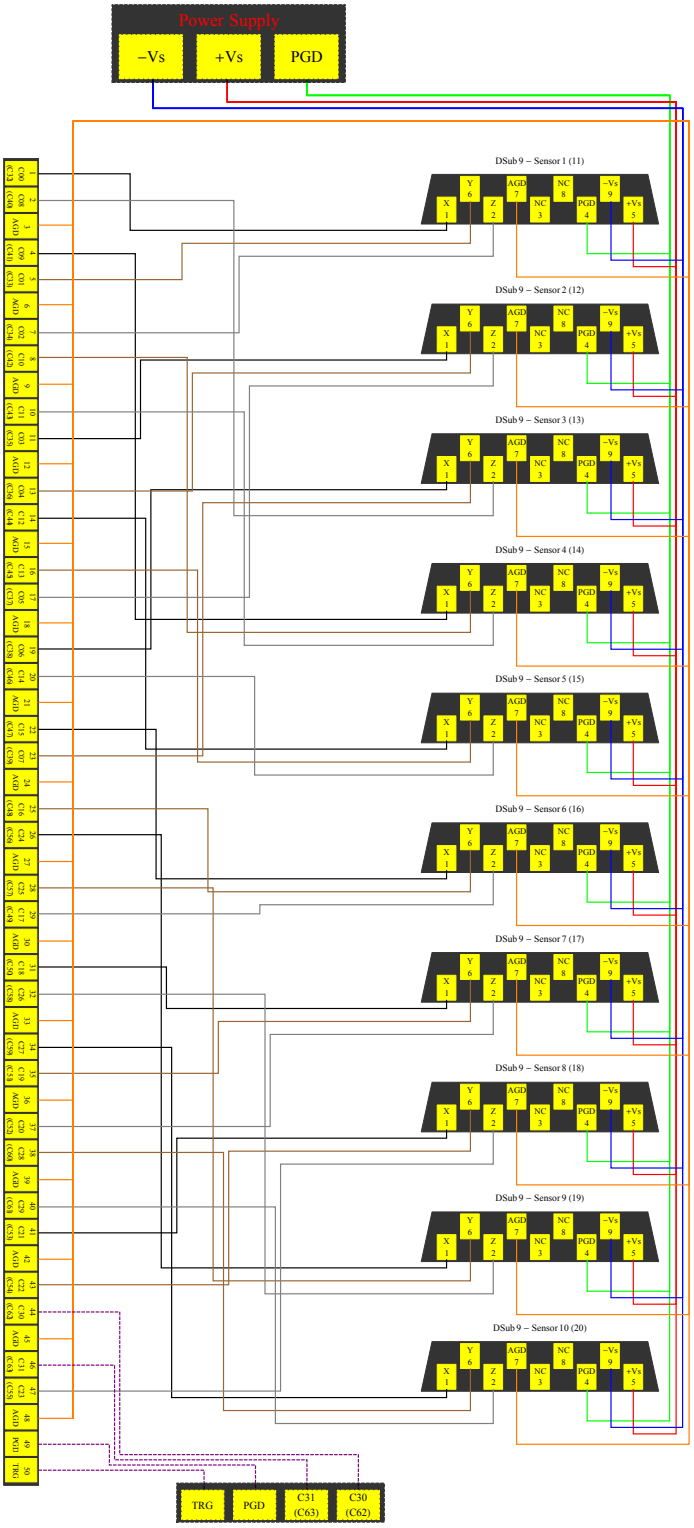

Figure F.1.: Pin configuration of the breakout box.

G. Expression for arbitrary magnetic fields in spherical coordinates

The magnetic field $\mathbf{B}(x, y, z)$ expressed in spherical coordinates can used to model problems with a radial symmetry. If only the radial distance is needed, the angular components can be neglected, independently of their complexity.

Every magnetic field can be expressed by the curl of vector potential $\mathbf{A}$:

$$\mathbf{B} = \nabla \times \mathbf{A}\,. \tag{G.1}$$

In spherical coordinates $\mathbf{A}$ can be expressed as a series [107]:

$$\mathbf{A}(\mathbf{r}) = a \sum_{n,l} {g_n}^l \frac{1}{n} \Big(\frac{a}{r}\Big)^{n+1} {\boldsymbol{\alpha}_n}^l(\theta, \phi) \tag{G.2}$$

with the reference radius a, which can be identified as typical length scale of magnetic source to the position $\mathbf{r}$, ${g_n}^m$ a constant and $\boldsymbol{\alpha}(\theta, \phi)$ the surface function of $\mathbf{A}$. Even if a length scale for point-like source (e.g. a dipole) does not make sense, this model still can be used for them, because a can always be absorbed in to the strength of the source.

With the expression for the curl in spherical coordinates and equation G.2 the magnetic field (equation G.1) can be written as

$$\mathbf{B}(\mathbf{r}) = \nabla \times \mathbf{A}(\mathbf{r}) = \frac{1}{r \sin\theta} \Big[\frac{\partial}{\partial\theta}(A_\phi \sin\theta) - \frac{\partial A_\theta}{\partial\phi}\Big] \hat{\mathbf{e}}_r \tag{G.3a}$$

$$+ \Big[\frac{1}{r \sin\theta} \frac{\partial A_r}{\partial\phi} - \frac{1}{r} \frac{\partial}{\partial r}(r A_\phi)\Big] \hat{\mathbf{e}}_\theta + \frac{1}{r} \Big[\frac{\partial}{\partial r}(r A_\theta) - \frac{\partial A_r}{\partial\theta}\Big] \hat{\mathbf{e}}_\phi\,. \tag{G.3b}$$

Here $A_{r,\theta,\phi}$ are the r, θ and ϕ components of $\mathbf{A}$ and $\hat{\mathbf{e}}_{r,\theta,\phi}$ unit vectors in the corresponding direction. With

$$\frac{\partial}{\partial r}(r A_{\theta,\phi}) = -a \sum_{n,l} {g_n}^l \frac{1}{n} {\boldsymbol{\alpha}_n}^l \Big(\frac{a}{r}\Big)^{n+1} \tag{G.4}$$

follows

$$\mathbf{B}(\mathbf{r}) = \sum_{n,l} a {g_n}^l \frac{1}{n}\Big(\frac{a}{r}\Big)^{n+1}\frac{1}{r}\Bigg[\frac{1}{\sin\theta}\Big[\Big(\frac{\partial}{\partial\theta}\big(({\boldsymbol{\alpha}_n}^l(\theta,\phi))_\phi \sin\theta\big)\Big) - \frac{\partial({\boldsymbol{\alpha}_n}^l)_\theta}{\partial\phi}\Big]\hat{\mathbf{e}}_r \quad \text{(G.5a)}$$

$$+\Big[\frac{1}{\sin\theta}\frac{\partial({\boldsymbol{\alpha}_n}^l(\theta\phi))_r}{\partial\phi} + n\Big]\hat{\mathbf{e}}_\theta \quad \text{(G.5b)}$$

$$+\Big[-n({\boldsymbol{\alpha}_n}^l(\theta\phi))_\theta - \frac{\partial({\boldsymbol{\alpha}_n}^l)_r}{\partial\theta}\Big]\hat{\mathbf{e}}_\phi\Bigg]. \quad \text{(G.5c)}$$

The equation now can be separated in a r-dependent and a (θ,ϕ)-dependent part. The latter is summarized in ${\boldsymbol{\beta}_n}^l(\theta,\phi)$. $\mathbf{B}(\mathbf{r})$ then simplifies to

$$\mathbf{B}(\mathbf{r}) = \sum_n a\frac{1}{n}\frac{1}{r}\Big(\frac{a}{r}\Big)^{n+1}\sum_l {g_n}^l {\boldsymbol{\beta}_n}^l(\theta,\phi) = \sum_n \Big(\frac{a}{r}\Big)^{n+2}\mathbf{b}_n(\theta,\phi)\,. \quad \text{(G.6)}$$

$\mathbf{b}_n(\theta,\phi)$ incorporates constants and the θ- and ϕ-dependent parts.

H. Analytic determination of gradient parameters

In order to extract the five parameters of the gradient field ($G_{1,1}$, $G_{1,2}$, $G_{1,3}$, $G_{2,2}$ and $G_{2,3}$, see equation 2.8) the two vector magnetometers have to be used. They form an equation system with six equations and five unknowns. For a purely analytical solution only five equations are needed and hence one component of one magnetometer is discarded, yielding in total six solutions for $G^{(}_{i,j}x, y, z)$ (x, y and z indicate here the discarded component). Three of the six solution are listed below. The other six can be extracted by exchanging the index of the sensor number ($1 \rightarrow 2$ and $2 \rightarrow 1$).

$$
\begin{aligned}
G^{(x)}_{1,1} = & \Big[x_2^2 \left(y_1^2 + z_1^2\right) B_{1,x} \\
& - x_2 \big(2x_1 \left(y_1 y_2 + z_1 z_2\right) B_{1,x} + \left(y_1^2 + z_1^2\right) \left(-y_2 B_{1,y} - z_2 B_{1,z} + y_1 B_{2,y} + z_1 B_{2,z}\right) \big) \\
& + x_1 \big(x_1 \left(y_2^2 + z_2^2\right) B_{1,x} - y_1 \left(y_2^2 B_{1,y} + z_2^2 B_{1,y} - 2 z_1 z_2 B_{2,y} - 2 y_2 z_1 B_{2,z}\right) \big) \\
& + x_1 \big(y_1^2 \left(y_2 B_{2,y} - z_2 B_{2,z}\right) - z_1 \left(y_2^2 B_{1,z} + z_2^2 B_{1,z} + y_2 z_1 B_{2,y} - z_1 z_2 B_{2,z}\right) \big) \Big] \\
& \times \left[x_1 \left(x_2^2 \left(y_1^2 + z_1^2\right) + \left(y_2 z_1 - y_1 z_2\right)^2 - 2 x_1 x_2 \left(y_1 y_2 + z_1 z_2\right) + x_1^2 \left(y_2^2 + z_2^2\right) \right) \right]^{-1}
\end{aligned}
$$

$$
\begin{aligned}
G^{(x)}_{1,2} = & \Big[x_1 z_2 \left(-y_2 z_1 + y_1 z_2\right) B_{1,x} + x_2 \left(-z_2 \left(z_1 \left(y_1 B_{1,x} + x_1 B_{1,y}\right) + x_1 y_1 B_{1,z}\right)\right) \\
& + x_1 \left(y_2 \left(z_1^2 B_{1,x} - x_1 y_1 B_{1,y} + x_1 z_1 B_{1,z} \right) + x_1 \left(y_1^2 + z_1^2\right) B_{2,y} \right) \\
& + z_1 \left(y_2 z_1 - y_1 z_2\right) \left(y_2 B_{1,y} + z_2 B_{1,z} - y_1 B_{2,y} - z_1 B_{2,z}\right) \\
& + x_1^2 \left(y_2^2 B_{1,y} + z_2 \left(z_2 B_{1,y} - z_1 B_{2,y} + y_1 B_{2,z}\right) - y_2 \left(y_1 B_{2,y} + z_1 B_{2,z}\right) \right) \Big] \\
& \times \left[x_1 \left(x_2^2 \left(y_1^2 + z_1^2\right) + \left(y_2 z_1 - y_1 z_2\right)^2 - 2 x_1 x_2 \left(y_1 y_2 + z_1 z_2\right) + x_1^2 \left(y_2^2 + z_2^2\right) \right) \right]^{-1}
\end{aligned}
$$

$$
\begin{aligned}
G^{(x)}_{1,3} = & \Big[x_1 y_2 \left(y_2 z_1 - y_1 z_2\right) B_{1,x} + y_1 \left(-y_2 z_1 + y_1 z_2\right) \left(y_2 B_{1,y} + z_2 B_{1,z} - y_1 B_{2,y} - z_1 B_{2,z}\right) \\
& + x_1^2 \left(y_2^2 B_{1,z} + z_2^2 B_{1,z} + y_2 z_1 B_{2,y} - y_1 z_2 B_{2,y} - \left(y_1 y_2 + z_1 z_2\right) B_{2,z} + x_2 y_1 z_2 B_{1,y} \right) - \\
& + x_2 \left(-y_1 \left(y_2 \left(z_1 B_{1,x} + x_1 B_{1,z}\right)\right) + y_1^2 \left(z_2 B_{1,x} + x_1 B_{2,z}\right) + x_1 z_1 \left(-y_2 B_{1,y} - z_2 B_{1,z} + z_1 B_{2,z}\right) \right) \Big] \\
& \times \left[x_1 \left(x_2^2 \left(y_1^2 + z_1^2\right) + \left(y_2 z_1 - y_1 z_2\right)^2 - 2 x_1 x_2 \left(y_1 y_2 + z_1 z_2\right) + x_1^2 \left(y_2^2 + z_2^2\right) \right) \right]^{-1}
\end{aligned}
$$

$$
\begin{aligned}
G_{2,2}^{(x)} =& \Big[-x_2^2\left(z_1^2 B_{1,x} - x_1 y_1 B_{1,y} + x_1 z_1 B_{1,z}\right) + 2x_1 x_2 z_1 z_2 B_{1,x} \\
&+ x_1\left(-x_1 z_2^2 B_{1,x} + y_1 z_2^2 B_{1,y} + z_1 z_2^2 B_{1,z} + x_1^2 y_2 B_{2,y} + y_2 z_1^2 B_{2,y}\right) \\
&+ x_1\left(-2y_1 z_1 z_2 B_{2,y} - \left(x_1^2 + z_1^2\right) z_2 B_{2,z}\right) \\
&+ x_2\left(x_1^2\left(-y_2 B_{1,y} + z_2 B_{1,z} - y_1 B_{2,y} + z_1 B_{2,z}\right) + z_1^2\left(-y_2 B_{1,y} - z_2 B_{1,z} + y_1 B_{2,y} + z_1 B_{2,z}\right)\right)\Big] \\
&\times\Big[x_1\left(x_2^2\left(y_1^2 + z_1^2\right) + \left(y_2 z_1 - y_1 z_2\right)^2 - 2x_1 x_2\left(y_1 y_2 + z_1 z_2\right) + x_1^2\left(y_2^2 + z_2^2\right)\right)\Big]^{-1}
\end{aligned}
$$

$$
\begin{aligned}
G_{2,3}^{(x)} =& \Big[x_2^2\left(x_1 z_1 B_{1,y} + y_1\left(z_1 B_{1,x} + x_1 B_{1,z}\right)\right) \\
&+ x_1\left(z_2\left(y_2\left(x_1 B_{1,x} - y_1 B_{1,y} - z_1 B_{1,z}\right) + \left(x_1^2 + y_1^2\right) B_{2,y}\right) + y_2\left(x_1^2 + z_1^2\right) B_{2,z}\right) \\
&+ x_2\left(-x_1\left(y_2 z_1 + y_1 z_2\right) B_{1,x} - x_1^2\left(z_2 B_{1,y} + y_2 B_{1,z} + z_1 B_{2,y} + y_1 B_{2,z}\right)\right) \\
&+ x_2\left(y_1 z_1\left(y_2 B_{1,y} + z_2 B_{1,z} - y_1 B_{2,y} - z_1 B_{2,z}\right)\right)\Big] \\
&\times\Big[x_1\left(x_2^2\left(y_1^2 + z_1^2\right) + \left(y_2 z_1 - y_1 z_2\right)^2 - 2x_1 x_2\left(y_1 y_2 + z_1 z_2\right) + x_1^2\left(y_2^2 + z_2^2\right)\right)\Big]^{-1}
\end{aligned}
$$

$$
\begin{aligned}
G_{1,1}^{(y)} =& \Big[x_2\left(y_1^2 + z_1^2\right)\left(-y_2 B_{1,x} + y_1\ B_{2,x}\right) \\
&+ x_1\left(y_1\left(y_2^2 + z_2^2\right) B_{1,x} + \left(-y_1^2 y_2 + y_2 z_1^2 - 2y_1 z_1 z_2\right) B_{2,x}\right) \\
&- \left(y_2 z_1 - y_1 z_2\right)\left(y_2\left(z_1 B_{1,y} + y_1 B_{1,z}\right) + z_2\left(-y_1 B_{1,y} + z_1 B_{1,z}\right) - \left(y_1^2 + z_1^2\right) B_{2,z}\right)\Big] \\
&\times\Big[y_1\left(x_2^2\left(y_1^2 + z_1^2\right) + \left(y_2 z_1 - y_1 z_2\right)^2 - 2x_1 x_2\left(y_1 y_2 + z_1 z_2\right) + x_1^2\left(y_2^2 + z_2^2\right)\right)\Big]^{-1}
\end{aligned}
$$

$$
\begin{aligned}
G_{1,2}^{(y)} =& \Big[x_2^2\left(y_1^2 + z_1^2\right) B_{1,x} + y_1\left(x_1 z_2^2 B_{1,y} + y_2\left(-z_2\left(z_1 B_{1,x} + x_1 B_{1,z}\right) + \left(x_1^2 + z_1^2\right) B_{2,x}\right)\right) \\
&+ y_1^2 z_2\left(z_2 B_{1,x} - z_1 B_{2,x} + x_1 B_{2,z}\right) + x_1 z_1 z_2\left(-y_2 B_{1,y} - z_2 B_{1,z} + x_1 B_{2,x} + z_1 B_{2,z}\right) \\
&- x_2\left(x_1\left(\left(y_1 y_2 + z_1 z_2\right) B_{1,x} + \left(y_1^2 + z_1^2\right) B_{2,x}\right)\right) \\
&- x_2\left(+z_1\left(-y_2\left(z_1 B_{1,y} + y_1 B_{1,z}\right) + z_2\left(y_1 B_{1,y} - z_1 B_{1,z}\right) + \left(y_1^2 + z_1^2\right) B_{2,z}\right)\right)\Big] \\
&\times\Big[y_1\left(x_2^2\left(y_1^2 + z_1^2\right) + \left(y_2 z_1 - y_1 z_2\right)^2 - 2x_1 x_2\left(y_1 y_2 + z_1 z_2\right) + x_1^2\left(y_2^2 + z_2^2\right)\right)\Big]^{-1}
\end{aligned}
$$

$$
\begin{aligned}
G_{1,3}^{(y)} =& \Big[x_1^2\left(-y_2 z_1 + y_1 z_2\right) B_{2,x} + y_1\left(y_2^2 z_1 B_{1,x} + z_2\left(x_2\left(y_1 B_{1,y} - z_1 B_{1,z}\right) + y_1^2 B_{2,x}\right)\right) \\
&- y_1\left(y_2\left(x_2 z_1 B_{1,y} + y_1\left(z_2 B_{1,x} + x_2 B_{1,z} + z_1 B_{2,x}\right)\right) + x_2\left(y_1^2 + z_1^2\right) B_{2,z}\right) \\
&+ x_1\left(x_2\left(y_2 z_1 - y_1 z_2\right) B_{1,x}\right) \\
&+ x_1\left(y_2\left(y_2\left(z_1 B_{1,y} + y_1 B_{1,z}\right) + z_2\left(-y_1 B_{1,y} + z_1 B_{1,z}\right) - \left(y_1^2 + z_1^2\right) B_{2,z}\right)\right)\Big] \\
&\times\Big[y_1\left(x_2^2\left(y_1^2 + z_1^2\right) + \left(y_2 z_1 - y_1 z_2\right)^2 - 2x_1 x_2\left(y_1 y_2 + z_1 z_2\right) + x_1^2\left(y_2^2 + z_2^2\right)\right)\Big]^{-1}
\end{aligned}
$$

$$
\begin{aligned}
G_{2,2}^{(y)} =& \Big[x_2^2 y_1 \left(y_1 B_{1,y} - z_1 B_{1,z}\right) - x_1^3 y_2 B_{2,x} + x_2 z_1^2 \left(y_2 B_{1,x} - y_1 B_{2,x}\right) \\
&+ \left(y_2 z_1 - y_1 z_2\right)\left(y_2 z_1 B_{1,y} - y_1 z_2 B_{1,y} + z_1 z_2 B_{1,z} - z_1^2 B_{2,z}\right) \\
&+ x_1^2 \left(y_2 \left(y_2 B_{1,y} + z_2 B_{1,z}\right) + x_2 \left(y_2 B_{1,x} + y_1 B_{2,x}\right) - \left(y_2 z_1 + y_1 z_2\right) B_{2,z}\right) \\
&- x_1 \left(x_2^2 y_1 B_{1,x} + y_1 z_2^2 B_{1,x} + z_1 \left(y_2 z_1 - 2 y_1 z_2\right) B_{2,x} + 2 x_2 y_1 \left(y_2 B_{1,y} - z_1 B_{2,z}\right)\right)\Big] \\
&\times \left[y_1 \left(x_2^2 \left(y_1^2 + z_1^2\right) + \left(y_2 z_1 - y_1 z_2\right)^2 - 2 x_1 x_2 \left(y_1 y_2 + z_1 z_2\right) + x_1^2 \left(y_2^2 + z_2^2\right)\right)\right]^{-1}
\end{aligned}
$$

$$
\begin{aligned}
G_{2,3}^{(y)} =& \Big[-x_1^3 z_2 B_{2,x} \\
&- x_1 \left(x_2^2 z_1 B_{1,x} + x_2 \left(\left(y_2 z_1 + y_1 z_2\right) B_{1,y} + \left(y_1 y_2 + z_1 z_2\right) B_{1,z}\right) + y_1 z_2 \left(-y_2 B_{1,x} + y_1 B_{2,x}\right)\right) \\
&+ x_1 x_2 \left(-y_1^2 + z_1^2\right) B_{2,z} + x_1^2 \left(z_2 \left(y_2 B_{1,y} + z_2 B_{1,z}\right) + x_2 \left(z_2 B_{1,x} + z_1 B_{2,x}\right) + \left(y_1 y_2 - z_1 z_2\right) B_{2,z}\right) \\
&+ y_1 \left(x_2^2 \left(z_1 B_{1,y} + y_1 B_{1,z}\right) + x_2 z_1 \left(-y_2 B_{1,x} + y_1 B_{2,x}\right) + \left(y_2 z_1 - y_1 z_2\right)\left(-z_2 B_{1,z} + z_1 B_{2,z}\right)\right)\Big] \\
&\times \left[y_1 \left(x_2^2 \left(y_1^2 + z_1^2\right) + \left(y_2 z_1 - y_1 z_2\right)^2 - 2 x_1 x_2 \left(y_1 y_2 + z_1 z_2\right) + x_1^2 \left(y_2^2 + z_2^2\right)\right)\right]^{-1}
\end{aligned}
$$

$$
\begin{aligned}
G_{1,1}^{(z)} =& \Big[x_2 \left(y_1^2 + z_1^2\right)\left(-z_2 B_{1,x} + z_1 B_{2,x}\right) + x_1 \left(z_1 \left(y_2^2 + z_2^2\right) B_{1,x} + \left(-2 y_1 y_2 z_1 + \left(y_1^2 - z_1^2\right) z_2\right) B_{2,x}\right) \\
&+ \left(-y_2 z_1 + y_1 z_2\right)\left(-y_1 \left(y_2 B_{1,y} + z_2 B_{1,z}\right) + y_1^2 B_{2,y} + z_1 \left(-z_2 B_{1,y} + y_2 B_{1,z} + z_1 B_{2,y}\right)\right)\Big] \\
&\times \left[z_1 \left(x_2^2 \left(y_1^2 + z_1^2\right) + \left(y_2 z_1 - y_1 z_2\right)^2 - 2 x_1 x_2 \left(y_1 y_2 + z_1 z_2\right) + x_1^2 \left(y_2^2 + z_2^2\right)\right)\right]^{-1}
\end{aligned}
$$

$$
\begin{aligned}
G_{1,2}^{(z)} =& \Big[x_1^2 \left(y_2 z_1 - y_1 z_2\right) B_{2,x} + z_1 \left(z_2 \left(-x_2 z_1 B_{1,y} + y_1 \left(z_2 B_{1,x} - x_2 B_{1,z} - z_1 B_{2,x}\right)\right)\right) \\
&+ z_1 \left(y_2 \left(-x_2 y_1 B_{1,y} + z_1 \left(-z_2 B_{1,x} + x_2 B_{1,z} + z_1 B_{2,x}\right)\right) + x_2 \left(y_1^2 + z_1^2\right) B_{2,y}\right) \\
&+ x_1 \left(x_2 \left(-y_2 z_1 + y_1 z_2\right) B_{1,x}\right) \\
&+ x_1 \left(z_2 \left(y_1 y_2 B_{1,y} + z_1 z_2 B_{1,y} - y_2 z_1 B_{1,z} + y_1 z_2 B_{1,z} - \left(y_1^2 + z_1^2\right) B_{2,y}\right)\right)\Big] \\
&\times \left[z_1 \left(x_2^2 \left(y_1^2 + z_1^2\right) + \left(y_2 z_1 - y_1 z_2\right)^2 - 2 x_1 x_2 \left(y_1 y_2 + z_1 z_2\right) + x_1^2 \left(y_2^2 + z_2^2\right)\right)\right]^{-1}
\end{aligned}
$$

$$
\begin{aligned}
G_{1,3}^{(z)} =& \Big[x_2^2 \left(y_1^2 + z_1^2\right) B_{1,x} + y_2^2 \left(z_1^2 B_{1,x} - x_1 y_1 B_{1,y} + x_1 z_1 B_{1,z}\right) + \left(x_1^2 + y_1^2\right) z_1 z_2 B_{2,x} \\
&+ y_2 \left(-z_2 \left(z_1 \left(y_1 B_{1,x} + x_1 B_{1,y}\right) + x_1 y_1 B_{1,z}\right) + y_1 \left(x_1^2 - z_1^2\right) B_{2,x} + x_1 \left(y_1^2 + z_1^2\right) B_{2,y}\right) \\
&- x_2 \left(x_1 \left(\left(y_1 y_2 + z_1 z_2\right) B_{1,x} + \left(y_1^2 + z_1^2\right) B_{2,x}\right)\right) \\
&- x_2 \left(y_1 \left(-y_1 \left(y_2 B_{1,y} + z_2 B_{1,z}\right) + y_1^2 B_{2,y} + z_1 \left(-z_2 B_{1,y} + y_2 B_{1,z} + z_1 B_{2,y}\right)\right)\right)\Big] \\
&\times \left[z_1 \left(x_2^2 \left(y_1^2 + z_1^2\right) + \left(y_2 z_1 - y_1 z_2\right)^2 - 2 x_1 x_2 \left(y_1 y_2 + z_1 z_2\right) + x_1^2 \left(y_2^2 + z_2^2\right)\right)\right]^{-1}
\end{aligned}
$$

$$
\begin{aligned}
G_{2,2}^{(z)} = & \Big[x_1^3 z_2 B_{2,x} - x_1^2 \left(z_2 \left(y_2 B_{1,y} + z_2 B_{1,z} \right) + x_2 \left(z_2 B_{1,x} + z_1 B_{2,x} \right) - \left(y_2 z_1 + y_1 z_2 \right) B_{2,y} \right) \\
& + x_1 z_1 \left(x_2^2 B_{1,x} + z_2 \left(-z_2 B_{1,x} + z_1 B_{2,x} \right) + 2 x_2 \left(z_2 B_{1,z} - y_1 B_{2,y} \right) \right) \\
& + z_1 \left(x_2^2 \left(y_1 B_{1,y} - z_1 B_{1,z} \right) + x_2 z_1 \left(z_2 B_{1,x} - z_1 B_{2,x} \right) + \left(y_2 z_1 - y_1 z_2 \right) \left(-z_2 B_{1,y} + z_1 B_{2,y} \right) \right) \Big] \\
& \times \left[z_1 \left(x_2^2 \left(y_1^2 + z_1^2 \right) + \left(y_2 z_1 - y_1 z_2 \right)^2 - 2 x_1 x_2 \left(y_1 y_2 + z_1 z_2 \right) + x_1^2 \left(y_2^2 + z_2^2 \right) \right) \right]^{-1}
\end{aligned}
$$

$$
\begin{aligned}
G_{2,3}^{(z)} = & \Big[-x_1^3 y_2 B_{2,x} + x_1^2 \left(y_2 \left(y_2 B_{1,y} + z_2 B_{1,z} \right) + x_2 \left(y_2 B_{1,x} + y_1 B_{2,x} \right) + \left(-y_1 y_2 + z_1 z_2 \right) B_{2,y} \right) \\
& + z_1 \left(x_2^2 \left(z_1 B_{1,y} + y_1 B_{1,z} \right) + x_2 y_1 \left(-z_2 B_{1,x} + z_1 B_{2,x} \right) + \left(y_2 z_1 - y_1 z_2 \right) \left(y_2 B_{1,y} - y_1 B_{2,y} \right) \right) \\
& - x_1 \left(x_2^2 y_1 B_{1,x} + y_2 z_1 \left(-z_2 B_{1,x} + z_1 B_{2,x} \right) \right) \\
& - x_1 \left(x_2 \left(y_1 \left(y_2 B_{1,y} + z_2 B_{1,z} \right) - y_1^2 B_{2,y} + z_1 \left(z_2 B_{1,y} + y_2 B_{1,z} + z_1 B_{2,y} \right) \right) \right) \Big] \\
& \times \left[z_1 \left(x_2^2 \left(y_1^2 + z_1^2 \right) + \left(y_2 z_1 - y_1 z_2 \right)^2 - 2 x_1 x_2 \left(y_1 y_2 + z_1 z_2 \right) + x_1^2 \left(y_2^2 + z_2^2 \right) \right) \right]^{-1}
\end{aligned}
$$

The solution for the superposition of a homogeneous and a gradient field requires 3 vector magnetometers (nine equations). The field can be described with eight parameters and hence nine solutions can be extracted analytically with the above described method. As the solutions are much more complex, they will not be shown.

List of Figures

List of Tables

Bibliography

[1] Peter W. Higgs. Broken symmetries and the masses of gauge bosons. *Phys. Rev. Lett.*, 13:508–509, Oct 1964.

[2] F. Englert and R. Brout. Broken symmetry and the mass of gauge vector mesons. *Phys. Rev. Lett.*, 13:321–323, August 1964.

[3] G. S. Guralnik, C. R. Hagen, and T. W. B. Kibble. Global conservation laws and massless particles. *Phys. Rev. Lett.*, 13:585–587, Nov 1964.

[4] Guido Altarelli and Martin W. Grunewald. Precision electroweak tests of the standard model. *Phys. Rept.*, 403-404:189–201, 2004.

[5] K. A. Olive et al. Review of Particle Physics. *Chin. Phys.*, C38:090001, 2014.

[6] F. Abe, H. Akimoto, A. Akopian, et al. Observation of top quark production in $\overline{p}p$ collisions with the collider detector at fermilab. *Phys. Rev. Lett.*, 74:2626–2631, Apr 1995.

[7] Paul Langacker. Structure of the standard model. *Adv. Ser. Direct. High Energy Phys.*, 14:15–36, 1995.

[8] Ben Gripaios. Lectures on Physics Beyond the Standard Model, 2015. arXiv:1503.02636.

[9] Guido Altarelli. The Standard electroweak theory and beyond. In *Neutrinos in physics and astrophysics from 10**(-33) to 10**28 CM. Proceedings, Conference, TASI'98, Boulder, USA, June 1-26, 1998*, pages 27–93, 1998.

[10] V. C. Rubin and W. K. Ford, Jr. Rotation of the Andromeda Nebula from a Spectroscopic Survey of Emission Regions. *apj*, 159:379, February 1970.

[11] Schumann, Marc. Dark matter 2014. *EPJ Web of Conferences*, 96:01027, 2015.

[12] Joel R. Primack. Dark matter and galaxy formation. *AIP Conference Proceedings*, 1192(1):101–137, 2009.

[13] AlisonL. Coil. The large-scale structure of the universe. In TerryD. Oswalt and WilliamC. Keel, editors, *Planets, Stars and Stellar Systems*, pages 387–421. Springer Netherlands, 2013.

[14] Adam G. Riess et al. Observational evidence from supernovae for an accelerating universe and a cosmological constant. *Astron. J.*, 116:1009–1038, 1998.

[15] S. Perlmutter, G. Aldering, G. Goldhaber, et al. Measurements of ω and λ from 42 high-redshift supernovae. *The Astrophysical Journal*, 517(2):565, 1999.

[16] Patrick Huet and Eric Sather. Electroweak baryogenesis and standard model cp violation. *Phys. Rev. D*, 51:379–394, Jan 1995.

[17] G. Steigman. Neutrinos and big bang nucleosynthesis. *Advances in High Energy Physics*, 2012, 2012.

[18] A.D. Sakharov. Violation of CP Invariance, c Asymmetry, and Baryon Asymmetry of the Universe. *Pisma Zh.Eksp.Teor.Fiz.*, 5:32–35, 1967.

[19] Michael Dine and Alexander Kusenko. Origin of the matter-antimatter asymmetry. *Rev. Mod. Phys.*, 76:1–30, Dec 2003.

[20] Mihoko M. Nojiri. Beyond the Standard Model. In *Proceedings, 1st Asia-Europe-Pacific School of High-Energy Physics (AEPSHEP)*, pages 137–149, 2014.

[21] Frank E. Paige. Determining SUSY particle masses at LHC. *eConf*, C960625:SUP114, 1996. [,710(1996)].

[22] Georges Aad et al. Summary of the ATLAS experiment's sensitivity to supersymmetry after LHC Run 1 — interpreted in the phenomenological MSSM. *JHEP*, 10:134, 2015.

[23] B. K. Gjelsten, D. J. Miller, and P. Osland. Determining masses of supersymmetric particles. In *2nd Southeastern European Workshop on Challenges Beyond the Standard Model (BW2005) Vrnjacka Banja, Serbia, Nis, Serbia, May 19-23, 2005*, 2005.

[24] Kingman Cheung, Ran Huo, Jae Sik Lee, and Yue-Lin Sming Tsai. Dark Matter in Split SUSY with Intermediate Higgses. *JHEP*, 04:151, 2015.

[25] Jonathan Engel, Michael J. Ramsey-Musolf, and U. van Kolck. Electric dipole moments of nucleons, nuclei, and atoms: The standard model and beyond, 2013. arXiv:1303.2371.

[26] Tarek Ibrahim, Ahmad Itani, and Pran Nath. Electron electric dipole moment as a sensitive probe of PeV scale physics. *Phys. Rev.*, D90(5):055006, 2014.

[27] David E. Morrissey and Michael J. Ramsey-Musolf. Electroweak baryogenesis, 2012. arXiv:1206.2942.

[28] V. Alan Kostelecky. CPT and Lorentz tests in the standard model. In *Proceedings, 6th International Symposium on Particles, strings and cosmology (PASCOS 1998)*, pages 392–399, 1998.

[29] V. W. Hughes, H. G. Robinson, and V. Beltran-Lopez. Upper limit for the anisotropy of inertial mass from nuclear resonance experiments. *Phys. Rev. Lett.*, 4:342–344, Apr 1960.

[30] D. Bear, R. E. Stoner, R. L. Walsworth, et al. Limit on lorentz and *CPT* violation of the neutron using a two-species noble-gas maser. *Phys. Rev. Lett.*, 85:5038–5041, Dec 2000.

[31] V. Alan Kostelecký and Charles D. Lane. Constraints on lorentz violation from clock-comparison experiments. *Phys. Rev. D*, 60:116010, Nov 1999.

[32] I. Altarev, C. A. Baker, G. Ban, et al. Test of lorentz invariance with spin precession of ultracold neutrons. *Phys. Rev. Lett.*, 103:081602, Aug 2009.

[33] D. Hanneke, S. Fogwell, and G. Gabrielse. New measurement of the electron magnetic moment and the fine structure constant. *Phys. Rev. Lett.*, 100:120801, Mar 2008.

[34] Tatsumi Aoyama, Masashi Hayakawa, Toichiro Kinoshita, and Makiko Nio. Tenth-Order QED Contribution to the Electron g-2 and an Improved Value of the Fine Structure Constant. *Phys. Rev. Lett.*, 109:111807, 2012.

[35] Thomas Blum, Achim Denig, Ivan Logashenko, et al. The muon (g-2) theory value: Present and future, 2013. arXiv:1311.2198.

[36] Robert Bluhm, V. Alan Kostelecký, and Neil Russell. CPT and lorentz tests in penning traps. *Phys. Rev. D*, 57:3932–3943, Apr 1998.

[37] Frederick Gray. Muon g-2 Experiment at Fermilab. In *12th Conference on the Intersections of Particle and Nuclear Physics (CIPANP 2015) Vail, Colorado, USA, May 19-24, 2015*, 2015.

[38] RobertoD. Peccei. The strong cp problem and axions. In Markus Kuster, Georg Raffelt, and Berta Beltrán, editors, *Axions*, volume 741 of *Lecture Notes in Physics*, pages 3–17. Springer Berlin Heidelberg, 2008.

[39] Jihn E. Kim and Gianpaolo Carosi. Axions and the Strong CP Problem. *Rev. Mod. Phys.*, 82:557–602, 2010.

[40] A. Ringwald. Axions and axion-like particles, 2014. arXiv:1407.0546.

[41] Peter W. Graham, Igor G. Irastorza, Steven K. Lamoreaux, et al. Experimental searches for the axion and axion-like particles. *Annual Review of Nuclear and Particle Science*, 65(1):485–514, 2015.

[42] Dmitry Budker, Peter W. Graham, Micah Ledbetter, et al. Proposal for a cosmic axion spin precession experiment (casper). *Phys. Rev. X*, 4:021030, May 2014.

[43] Peter W. Graham and Surjeet Rajendran. New observables for direct detection of axion dark matter. *Phys. Rev. D*, 88:035023, Aug 2013.

[44] Tatsuya Nakada. Review on cp violation. *AIP Conference Proceedings*, 302(1):425–463, 1994.

[45] J. Boucrot. Oscillations of neutral b mesons systems. *Nuclear Physics B - Proceedings Supplements*, 75(3):261 – 266, 1999.

[46] G. J. Feldman, J. Hartnell, and T. Kobayashi. Long-baseline neutrino oscillation experiments. *Advances in High Energy Physics*, 2013(1):425–463, 2013.

[47] M. G. Aartsen et al. Measurement of Atmospheric Neutrino Oscillations with IceCube. *Phys. Rev. Lett.*, 111(8):081801, 2013.

[48] S. Fukuda et al. Determination of solar neutrino oscillation parameters using 1496 days of Super-Kamiokande I data. *Phys. Lett.*, B539:179–187, 2002.

[49] S. M. Bilenky and Carlo Giunti. Neutrinoless double-beta decay: A brief review. *Mod. Phys. Lett.*, A27:1230015, 2012.

[50] The EXO-200 Collaboration. Search for majorana neutrinos with the first two years of exo-200 data. *Nature*, 510:229–234, Sep 2014.

[51] M. Agostini, M. Allardt, E. Andreotti, et al. Results on neutrinoless double-β decay of ^{76}Ge from phase i of the gerda experiment. *Phys. Rev. Lett.*, 111:122503, Sep 2013.

[52] M. Baldo-Ceolin, P. Benetti, T. Bitter, et al. A new experimental limit on neutron-antineutron oscillations. *Zeitschrift für Physik C Particles and Fields*, 63(3):409–416, 1994.

[53] David Milstead. A new high sensitivity search for neutron-antineutron oscillations at the ESS. In *Proceedings, 2015 European Physical Society Conference on High Energy Physics (EPS-HEP 2015)*, 2015.

[54] J. E. Moody and Frank Wilczek. New macroscopic forces? *Phys. Rev. D*, 30:130–138, Jul 1984.

[55] W. A. Terrano, E. G. Adelberger, J. G. Lee, and B. R. Heckel. Short-range, spin-dependent interactions of electrons: A probe for exotic pseudo-goldstone bosons. *Phys. Rev. Lett.*, 115:201801, Nov 2015.

[56] Hideki YUKAWA. On the interaction of elementary particles. i. *Proceedings of the Physico-Mathematical Society of Japan. 3rd Series*, 17:48–57, 1935.

[57] Maxim Pospelov and Adam Ritz. Electric dipole moments as probes of new physics. *Annals Phys.*, 318:119–169, 2005.

[58] S K Lamoreaux and R Golub. Experimental searches for the neutron electric dipole moment. *Journal of Physics G: Nuclear and Particle Physics*, 36(10):104002, 2009.

[59] The ACME Collaboration. Order of magnitude smaller limit on the electric dipole moment of the electron. *Science*, 343(6168):269–272, 2014.

[60] Maxim Pospelov and Adam Ritz. Electric dipole moments as probes of new physics. *Annals of Physics*, 318(1):119 – 169, 2005. Special Issue.

[61] C. A. Baker, D. D. Doyle, P. Geltenbort, et al. Improved experimental limit on the electric dipole moment of the neutron. *Phys. Rev. Lett.*, 97:131801, Sep 2006.

[62] W. C. Griffith, M. D. Swallows, T. H. Loftus, et al. Improved limit on the permanent electric dipole moment of ^{199}hg. *Phys. Rev. Lett.*, 102:101601, Mar 2009.

[63] A. Frei, K. Schreckenbach, B. Franke, et al. Transmission measurements of guides for ultra-cold neutrons using {UCN} capture activation analysis of vanadium. *Nuclear Instruments and Methods in Physics Research Section A: Accelerators, Spectrometers, Detectors and Associated Equipment*, 612(2):349 – 353, 2010.

[64] A. Frei, E. Gutsmiedl, C. Morkel, et al. Understanding of ultra-cold–neutron production in solid deuterium. *EPL (Europhysics Letters)*, 92(6):62001, 2010.

[65] M. Daum, B. Franke, P. Geltenbort, et al. Transmission of ultra-cold neutrons through guides coated with materials of high optical potential. *Nuclear Instruments and Methods in Physics Research A*, 741:71–77, March 2014.

[66] I. Altarev, D. H. Beck, S. Chesnevskaya, et al. A next generation measurement of the electric dipole moment of the neutron at the frm ii. *Il nuovo cimento*, 4:122–127, 2012.

[67] B. Taubenheim. *in preperation*. PhD thesis, Technische Universtät München, 2016.

[68] J. Clarke and A. I. Braginski. *The SQUID Handbook*, volume 1. Wiley-VCH, 2004.

[69] D. Budker and M. Romalis. Optical magnetometry. *Nature Physics*, 3:227–234, 2007.

[70] S. Stuiber. *in preperation*. PhD thesis, Technische Universtät München, 2016.

[71] I. Altarev, E. Babcock, D. Beck, et al. A magnetically shielded room with ultra low residual field and gradient. *Review of Scientific Instruments*, 85(7), 2014.

[72] I. Altarev, M. Bales, D. H. Beck, et al. A large-scale magnetic shield with 106 damping at millihertz frequencies. *Journal of Applied Physics*, 117(18), 2015.

[73] Norman F. Ramsey. A molecular beam resonance method with separated oscillating fields. *Phys. Rev.*, 78:695–699, Jun 1950.

[74] Norman F. Ramsey. Experiments with separated oscillatory fields and hydrogen masers. *Rev. Mod. Phys.*, 62:541–552, Jul 1990.

[75] I. Altarev, G. Ban, G. Bison, et al. An improved measurement of the electric dipole moment of the neutron. *Nuclear Physics A*, 844(1–4):47c – 52c, 2010. Proceedings of the 4th International Symposium on Symmetries in Subatomic Physics.

[76] F. M. Piegsa, M. Fertl, S. N. Ivanov, M. Kreuz, K. K. H. Leung, P. Schmidt-Wellenburg, T. Soldner, and O. Zimmer. New source for ultracold neutrons at the Institut Laue-Langevin. *Phys. Rev.*, C90(1):015501, 2014.

[77] J. M. Pendlebury, W. Heil, Yu. Sobolev, et al. Geometric-phase-induced false electric dipole moment signals for particles in traps. *Phys. Rev. A*, 70:032102, Sep 2004.

[78] Rainer Schönberger. Simulation of the transport and storage of ultracold neutrons. Bachelor thesis, Technische Universität München, 2012.

[79] K. Green, P.G. Harris, P. Iaydjiev, et al. Performance of an atomic mercury magnetometer in the neutron {EDM} experiment. *Nuclear Instruments and Methods in Physics Research Section A: Accelerators, Spectrometers, Detectors and Associated Equipment*, 404(2–3):381 – 393, 1998.

[80] J. M. Pendlebury, W. Heil, Yu. Sobolev, et al. Geometric-phase-induced false electric dipole moment signals for particles in traps. *Phys. Rev. A*, 70:032102, Sep 2004.

[81] Guillaume Pignol and Stéphanie Roccia. Electric-dipole-moment searches: Reexamination of frequency shifts for particles in traps. *Phys. Rev. A*, 85:042105, Apr 2012.

[82] Christian Velten. Electric Field Strength and Stability Measurement Using the Linear Electro-Optic Effect in Quartz. Master thesis, Technische Universität München, 2015.

[83] B. Patton, E. Zhivun, D. C. Hovde, et al. All-optical vector atomic magnetometer, 2014. arXiv:1403.7545.

[84] S. N. Balashov, K. Green, M. G. D. van der Grinten, et al. A proposal for a cryogenic experiment to measure the neutron electric dipole moment (nedm), 2007. arXiv:0709.2428.

[85] D. Dubbers, H. Abele, S. Baeßler, et al. A clean, bright, and versatile source of neutron decay products. *Nuclear Instruments and Methods in Physics Research Section A: Accelerators, Spectrometers, Detectors and Associated Equipment*, 596(2):238 – 247, 2008.

[86] G. Golub and W. Kahan. Calculating the singular values and pseudo-inverse of a matrix. *Journal of the Society for Industrial and Applied Mathematics: Series B, Numerical Analysis*, 2(2):pp. 205–224, 1965.

[87] S. Afach, G. Bison, K. Bodek, et al. Dynamic stabilization of the magnetic field surrounding the neutron electric dipole moment spectrometer at the paul scherrer institute. *Journal of Applied Physics*, 116(8):–, 2014.

[88] D.W. Allan. Statistics of atomic frequency standards. *Proceedings of the IEEE*, 54(2):221–230, Feb 1966.

[89] M. Burghoff, H. Schleyerbach, D. Drung, et al. A vector magnetometer module for biomagnetic application. *Applied Superconductivity, IEEE Transactions on*, 9(2):4069–4072, June 1999.

[90] Dietmar Drung. High-performance {DC} {SQUID} read-out electronics. *Physica C: Superconductivity*, 368(1–4):134 – 140, 2002.

[91] J. Voigt, S. Knappe-Grüneberg, Gutkelch, et al. Development of a vector-tensor system to measure the absolute magnetic flux density and its gradient in magnetically shielded rooms. *Review of Scientific Instruments*, 86(5), 2015.

[92] M. Burghoff. Hardware developments at ptb for high resolution spin precession investigations. 2nd Status Meeting of the DFG Priority Program 1491 (Wildbad Kreuth, Germany), 2015.

[93] P. A. M. Dirac. The theory of magnetic poles. *Phys. Rev.*, 74:817–830, Oct 1948.

[94] Ricardo S. Leite, Nicolau C. Saldanha, and Carlos Tomei. Reconstruction of tridiagonal matrices from spectral data, 2005. arXiv:math/0508099.

[95] G.'t Hooft. Magnetic monopoles in unified gauge theories. *Nuclear Physics B*, 79(2):276 – 284, 1974.

[96] J Preskill. Magnetic monopoles. *Annual Review of Nuclear and Particle Science*, 34(1):461–530, 1984.

[97] Michael S. Turner, E. N. Parker, and T. J. Bogdan. Magnetic monopoles and the survival of galactic magnetic fields. *Phys. Rev. D*, 26:1296–1305, Sep 1982.

[98] Philippe H. Eberhard, Ronald R. Ross, Luis W. Alvarez, and Robert D. Watt. Search for magnetic monopoles in lunar material. *Phys. Rev. D*, 4:3260–3272, Dec 1971.

[99] Henry H. Kolm. Search for magnetic monopole in deep-sea sediment. *Physics Today*, 20(10):69–70, 1967.

[100] Blas Cabrera. First results from a superconductive detector for moving magnetic monopoles. *Phys. Rev. Lett.*, 48:1378–1381, May 1982.

[101] Leon N. Cooper. Bound electron pairs in a degenerate fermi gas. *Phys. Rev.*, 104:1189–1190, Nov 1956.

[102] M. Ambrosio et al. Final results of magnetic monopole searches with the macro experiment. *The European Physical Journal C - Particles and Fields*, 25(4):511–522, 2002.

[103] R. Dengler. Self inductance of a wire loop as a curve integral, 2012. arXiv:1204.1486.

[104] F. Kuchler. *Electric dipole moment searchesusing the isotope 129-xenon*. PhD thesis, Technische Universtät München, 2014.

[105] The NEPOMUC experiment. http://www.sces.ph.tum.de/research/positron-physics/experimental-facilities/nepomuc/, Sep 2014.

[106] Wikipedia. http://de.wikipedia.org/wiki/sonnenstandsdiagramm, Sep 2014.

[107] F.J. Lowes and B. Duka. Magnetic multipole moments (gauss coefficients) and vector potential given by an arbitrary current distribution. *Earth, Planets and Space*, 63(12):i–vi, 2011.

Acknowledgement

First of all I want thank Prof. Dr. Peter Fierlinger, who cordially received me in his group and gave me the opportunity to work on very interesting projects. His never ending flow of genial ideas feeds the whole group with exiting projects and his friendly nature creates an enjoyable working environment.

In particular, I thank Mike Marino. He set up the framework for almost all software development in our group. He guided me through software programming of the ACS and helped whenever I got stuck. In addition, I want to thank him for reading through my thesis and giving me constructive comments.

I also want to thank Amanda Boomer for reading my thesis and helping me improve its style.

I am very grateful that my colleagues supported me in the mechanical construction of the field cage: Igor Altarev, Vitaly Andreev, Wolfhart Feldmeier, Katharina Fierlinger, Peter Fierlinger, Andreas Himpsl, Florian Kuchler, Mike Marino, Max Newrzella, Gerd Pezoldt, Johannes Rothe, Rainer Schoenberger, Andreas Seiler, Thomas Stolz, Stefan Stuiber, Bernd Tabubenheim and David Wurm. Without this team effort, it would have been impossible to assemble the field cage.

I also want to thank the students who helped with characterizing the performance of the field cage: Vitaly Andreev, Florian Kasper, Florian Niederreiter and Johannes Rothe.

A special thank is addressed to the mechanical workshop, especially to Michael Novotny. Even in busy times in which the workshop actually didn't have free capacity, he managed to produce urgent parts.

My parents and my sisters always supported me through the course of my studies. I deeply thank you very much for your love and encouragement in all the years.

Last but not least, I want to thank Eva who accompanied me in the last year of my thesis and greatly enriched my life.